Miniaturization and Integration of Measurement Systems for Space Electromagnetic Environments

Hajime Fukuhara

Acknowledgements

I would like to express my gratitude to Professor Hiroshi Yamakawa for his fruitful comments and suggestions whenever I faced a problem in the present study. I would also like to thank him for his concise and clear guidance throughout my research. In addition, his work as the Japanese space exploration strategic headquarter secretary has aroused my enthusiasm about the further evolution of the space exploration industry and a desire to contribute to it.

I am most grateful to Dr. Hirotsugu Kojima for his kind advice. I am thankful for the wide knowledge he has shared with me about instrumentation for space science, the design of analog and digital circuits, space plasma physics, and other subjects. His attitude regarding achieving goals and solving problems was a morale booster as well as a loadstar for completing objectives in the present research and development. I deeply appreciate his thoughtful support in entrusting most of the development of the ASIC to me. The present thesis could never have been published without his great support.

I greatly appreciate Professor Masao Kitano for our fruitful discussions and for reviewing this thesis. I also sincerely thank him for his many helpful comments and astute suggestions. I deeply thank Professor Naoki Shinohara for his helpful suggestions and positive encouragement and for reviewing this thesis and providing helpful and fruitful comments.

I am grateful to Professor Hirokazu Ikeda at the Institute of Space and Astronautical Science/Japan Aerospace Exploration Agency for his helpful comments for designing ASICs. I appreciate very much being able to examine the source code of the Ray tracing program and the helpful support of Prof. Yoshiya Kasahara and Dr. Yoshitaka Goto at Kanazawa University and Professor Emeritus Iwane Kimura at Kyoto University.

I would like to express my acknowledgments to Professor Yoshiharu Omura, Dr. Yusuke Ebihara, and Dr. Tomohiko Mitani for their great encouragement and helpful suggestions and advice on the present study. I greatly thank Dr. Yoshikatsu Ueda for his thoughtful suggestions and support in the present study and for creating a stimulating environment in the laboratory . I also deeply thank Dr. Yohei Miyake and Dr. Masafumi Shoji for their heartfelt advice and support. I sincerely appreciate the work done completing the present project of developing the ASIC by Mr. Hiroshi Imakubo, Mr. Takashi Matsumoto, Mr. Yuto Saito, Mr. Yuta Mizuochi, Mr. Satoshi Okada, Mr. Hiromune Ishii, and Mr. Kensuke Hangyo.

Special thanks to Ms. Megumi Ogawa, secretary of Prof. Yamakawa, for her careful support. I wish to thank Dr. Keiichiro Kashimura, Dr. Masaki Nakamiya and all the students in the space group laboratories for their kind support and encouragement. I also deeply thank Mr. Mitsuru Watanabe, Mr. Kenshi Saho, Mr. Kazunori Kimura, Dr. Seita Iwahashi, Mr. Satoru Nakagawa, and Mr. Yoshinori Fujiwara for their assistance during the early period when I entered Kyoto University.

I gratefully appreciate the financial support of JSPS Research Fellow that made it possible to complete my thesis. The present study was supported in part by the VLSI Design and Education Center (VDEC) of the University of Tokyo in collaboration with Cadence Design Systems, Inc. and SiliConsortium Ltd. The mask layout used in the present thesis was designed in collaboration with Digian Technology Inc. The design and fabrication of the printed circuited board was supported by Meiwa System Corporation. Additional support was provided by Grants-in-Aid for Scientific Research A (19204048, 23244097) and a JAXA Grant-in-Aid for Fundamental Development and Experimentation of On-board Instruments. Partial support was also provided by the Yamada Science Foundation.

Finally, I would also like to express my heartfelt appreciation for the moral support and warm encouragement of my parents, Hideki and Takako, and my dear wife, Tomoko.

Abstract

Our exploitation of space is increasing and space systems such as GPS and climate satellites have become indispensable in our lives. It is hence very important to understand physical phenomena that occur in space. Space is filled with collisionless plasmas generated by the solar wind and the ionized upper atmosphere. The interaction between the solar wind and the Earth's magnetism forms the region called the magnetosphere. Space plasmas show different characteristics in the solar wind and the magnetosphere. The magnetosphere is divided into several regions depending on the plasmas' characteristics. The radiation belt region is the part of the magnetosphere that lies typically at geocentric distances of around 2 to 4 Earth radii. Highly energetic plasmas of protons and electrons exist in the radiation belts and can negatively influence space systems and human health. However, the mechanism of the generation and disappearance of the radiation belts is not yet clearly understood.

Plasma waves are an important physical phenomenon for understanding the behavior of space plasmas since the kinetic energy of the plasmas is transferred through the plasma waves. The phase of a plasma wave is related to the plasma's velocities and is important in the interaction between plasma waves and particles. The present thesis focuses on instruments for investigating plasma waves and wave–particle interactions.

A plasma wave consists of only an electric field or electromagnetic field. Sensors for plasma waves include dipole antennas for the electric field components and search coils or loop antennas for the magnetic field. The signals detected by the sensors are input to the electronics of the receiver for signal processing and data transmission through the telemetry. The electronics of the plasma wave receiver has been highly integrated and miniaturized by replacing analog components with digital hardware and software. This has been very effective for integration, though there is a trade-off between power consumption and processing speed. However, analog electronics are still used at the front-end of the receiver due to high performance requirements i.e., low noise, high sensitivity, wide-dynamic range, and wide-band frequency. Recently, multiple exploration missions have been planned and high performance miniaturized analog electronics would greatly benefit these missions.

In this thesis, the analog electronics for plasma wave observations are developed with application specific integrated circuit (ASIC) technology in order to greatly reduce the size and mass of the instruments. A plasma wave receiver can be either a waveform receiver or a spectrum analyzer. A waveform receiver observes instant electric and magnetic fields while a spectrum analyzer provides the time evolution of the intensity in each frequency band. Only a waveform receiver contains phase information of the plasma waves. The target components for miniaturization of the waveform receiver are a band-limiting filter, a variable gain differential amplifier with low, medium, and high gains, and an anti-aliasing filter. The G_m–C filter is a commonly used active filter for communication front-end with low noise and can be applied to the band-limiting filter. A multi-gain differential amplifier is realized with switching resistors to obtain each appropriate gain. Since the anti-aliasing filter must be manufactured accurately, a switched capacitor filter is suitable. However, extra G_m–C filters are necessary in the front and back of the switched capacitor for noise elimination. The spectrum analyzer has an advantage in that it can provide an overview of plasma waves and their variations. The sweep frequency analyzer (SFA) is one type of spectrum analyzer which sweeps the observation frequency range finely. The SFA has poor time resolution and fine frequency resolution. The target SFA in the present thesis has an improved time resolution without losing frequency resolution. The SFA is a double super heterodyne receiver. Because of frequency conversion, unnecessary signals at image frequency is to be rejected. Thus, a frequency synthesizer, mixer, and band pass filter must be developed for the ASIC. These circuits for both receivers are tested after manufacturing and their feasibility is evaluated.

The developed components are integrated into one chip. For the waveform receiver, a six-channel circuit of filters and amplifiers is laid on the chip. After the layout design, the chips are manufactured using the TSMC 0.25μm CMOS process. A circuit board is also designed for mounting the chip. A power supply, clock generator, divider, and six A/D converters are implemented on the circuit board. The area of the analog components is reduced to a twentieth the size of previously developed instruments.

Applications using the miniaturized plasma wave receiver are proposed. A sensor network for plasma wave observation is introduced, consisting of a distribution of several sensor nodes with small plasma wave receivers where observation data are collected at each node. This application can obtain the spatial distribution of plasma waves. The second application consists of a constellation of satellites, used to determine the position of the plasmapause with Faraday rotation. One satellite in the constellation actively emits radio waves of linear polarization. The other satellites receive the emitted radio waves with small wave receivers and detect the variation of the polarization direction from the expected value. The principle and system design of the satellites are discussed.

Moreover, a direct measurement system for energy transfer between plasmas and plasma waves is presented. The time derivative of the kinetic energies of plasmas is proportional to the inner product of the electric field vector of the plasma waves and velocity of the plasmas. The principle is based on the different kinds of instruments and preprocessing working together before the actual calculation. The calibration of the waveform data and time correction for synchronization of the particle data with the waveform are described. The one-chip system is realized in the FPGA with real-time processing.

Concluding the present thesis, the miniaturization and integration are conducted successfully, with a few suggestions for future works.

Contents

Acknowledgments **i**

Abstract **iii**

List of Figures **ix**

List of Tables **xv**

1 General Introduction **1**

1.1 Introduction 1
1.2 Space Electromagnetic Environment Sensors 5
1.3 Scope and Contribution of the Present Study 7

2 Miniaturization and Integration Techniques and Targets **11**

2.1 Introduction 11
2.2 Plasma Wave Receiver 12
  2.2.1 Brief Summary of Instrument 12
  2.2.2 Typical Plasma Wave Receiver 12
2.3 Miniaturization and Integration Approach 13
  2.3.1 Digital Components 13
  2.3.2 Analog Components 15
2.4 Analog ASIC Technology 16
  2.4.1 Summary of ASIC 16
  2.4.2 ASIC for Space Science 17
2.5 Target of Miniaturization 18
  2.5.1 Waveform Receiver 18
  2.5.2 Spectrum Analyzer 22
2.6 Summary 25

3 Component Designs and Evaluations of the Plasma Wave Receiver **27**

3.1 Introduction 27

3.2 Attention to Radiation Tolerance 28
3.3 G_m–C Filters 30
  3.3.1 Fully Differential Band-limiting G_m–C Filter 30
  3.3.2 Single-ended Noise Rejection G_m–C Filters 33
3.4 Temperature Compensation for the G_m–C filters 38
  3.4.1 Design Policy 38
  3.4.2 Compensation Scheme 39
  3.4.3 Temperature Compensation Current Source 40
  3.4.4 Implementation 42
3.5 Differential Amplifier 47
3.6 Switched Capacitor LPF 54
3.7 Switching Capacitor BPF 57
3.8 Mixer 62
3.9 Phase-Locked Loop 66
  3.9.1 Voltage Controlled Oscillator 68
  3.9.2 Phase Frequency Comparator and Divider 74
  3.9.3 Loop Filter 75
  3.9.4 Closed-Loop Operation 79
3.10 Conclusions 82

4 Miniaturized Plasma Wave Receivers 83
4.1 Introduction 83
4.2 Specifications 83
4.3 Integrated Waveform Receiver 84
4.4 Overall Evaluation 87
4.5 Conclusions 89

5 Applications with Miniaturized Receivers 91
5.1 Introduction 91
5.2 Sensor Network System in Space 92
5.3 Plasmapause Location Determination 99
  5.3.1 Outline 99
5.4 Radio Wave Propagation in Space Plasma 101
5.5 Polarization Calculation 106
5.6 System Design of Satellites 109
5.7 Conclusion and Future Works 112

6 One-chip Wave-Particle Interaction Analyzer 113
6.1 Introduction . . . 113
6.2 Principle and significance of the WPIA . . . 115
6.3 Wave-Particle Interaction Analyzer (WPIA) . . . 118
  6.3.1 Interconnections with necessary sensors . . . 118
  6.3.2 Blocks to be implemented . . . 120
6.4 One-Chip WPIA . . . 124
  6.4.1 Advantages of the One-Chip WPIA . . . 124
6.5 Design of the One-chip WPIA . . . 125
  6.5.1 Waveform Calibration . . . 125
  6.5.2 Coordinate Transformation . . . 128
6.6 Time Correction . . . 129
  6.6.1 Calculation of $\boldsymbol{E}_w \cdot \boldsymbol{v}$/Accumulation . . . 131
6.7 Performance . . . 133
  6.7.1 Operational Accuracy . . . 133
  6.7.2 Calibration errors . . . 134
  6.7.3 Power consumption . . . 136
6.8 Conclusion . . . 137

7 Concluding Remarks 139
7.1 Summary and Conclusions . . . 139
7.2 Suggestions for Future Work . . . 142

References 143

Publication List 151

List of Figures

1.1 Cutaway diagram illustrating the three-dimensional magnetosphere [*Russell*, (2001)]. 2

1.2 *L–t* diagram for electron flux, represented by color coded Kp and Dst indices during the 3 November 1993 storm [*Miyoshi et al.*, (2003)]. 4

1.3 Design of a fluxgate magnetometer [*Acuna and Pellerin*, (1969)]. 5

1.4 Cross section of a toroidal electrostatic analyzer [*Young et al.*, (1988)]. . . 6

1.5 GEOTAIL satellite mounting electric and magnetic field sensors. 7

1.6 Typical intensities and frequency band of plasma waves with the sensitivities of the sensors onboard BepiColombo/MMO [*Kasaba et al.*, 2010]. . . . 8

2.1 System block diagram of the plasma wave receiver of SCOPE [*SCOPE Working Group*, 2008]. 13

2.2 Number of transistors on a single processor. 14

2.3 System block diagram of the WFC onboard KAGUYA [*Kasahara et al.*, 2008]. 15

2.4 Block diagram of the system chip for the waveform receiver. 19

2.5 Block diagram of the MCA onboard GEOTAIL [*Matsumoto et al.*, (1994)]. 22

2.6 Block diagram of the SFA onboard GEOTAIL [*after Matsumoto et al.*, (1994)]. 23

2.7 Block diagram of the SFA with improvement of time resolution. 24

2.8 Proposal to maintain frequency resolution with the short sweep time. . . . 25

2.9 Allocation of time. 26

3.1 Photograph of packages including an ASIC. 28

3.2 Unintended PNPN junction in the CMOS circuit. 29

3.3 Via holes between the bottom metal layer and p-substrate/n-well layer exist in blue/red color areas. 30

3.4 Circuit diagram of the first block, fully differential G_m–C low pass filter. . 30

3.5 Circuit schematic of OTA for the fully differential G_m–C LPF. 32

3.6 Circuit schematic of CMFB of OTA shown in Fig. 3.5. 33

3.7 Measurement and simulation results of frequency response of differential gain of the fully differential $\mathrm{G_m}$–C filter. 34
3.8 Equivalent input noise voltage densities of the fully differential $\mathrm{G_m}$–C filter, obtained from the measurement and simulation. 35
3.9 Simulation results of the equivalent input noise voltage densities of the fully differential $\mathrm{G_m}$–C filter at the temperature of $-30, 25$, and 60 °C. 36
3.10 Circuit diagram of the single-end second-order $\mathrm{G_m}$–C filter. 36
3.11 Circuit schematic of OTA for the single-ended $\mathrm{G_m}$–C filter. 37
3.12 Measurement and simulation results of frequency response gain of the single-ended Gm-C filter. 37
3.13 The temperature compensation current source I_{TC} is fed to OTAs which consist of the $\mathrm{G_m}$–C filter. 40
3.14 Circuit schematic of PTAT current source. 41
3.15 Circuit to generate I_{pl} which has piecewise-linear temperature characteristics. 42
3.16 Circuit schematic to generate current I_{TC}. 43
3.17 Characteristics of I_{TC} versus temperature with combinations of R_{ext1} and R_{ext2}. 44
3.18 Fully differential first-order $\mathrm{G_m}$–C LPF with current source for temperature compensation. 44
3.19 Measured temperature dependence of the cutoff frequency of $\mathrm{G_m}$–C LPF with the compensation circuits compared with that of the $\mathrm{G_m}$–C LPF without the compensation circuit. 45
3.20 Relative temperature dependence of cutoff frequencies of the measurement and simulation results. 46
3.21 Temperature dependence of cutoff frequencies of the measurement and simulation results. 46
3.22 Circuit diagram of the main amplifier. 47
3.23 Circuit schematic of the OP1. 48
3.24 Simulated gain of the frequency response of the Op-amp for the differential amplifier circuit. 49
3.25 Circuit schematic of the OP2. 50
3.26 Simulated gain of the frequency response of the Op-amp for the non-inverting amplifier for high gain. 51
3.27 Resistors for gain switching of the main amplifiers. 52
3.28 Measured results of the frequency response gains of the overall differential amplifier. 53
3.29 Circuit diagram of the sixth-order switched capacitor filter. The clock generating circuit is not shown. 54

3.30 Frequency response gains for the measured result (solid line), and the theoretical transfer function calculated from the capacitance ratios (broken line). 56

3.31 Circuit diagram of the unit switched capacitor band pass filter. 57

3.32 Circuit diagram of the total switched capacitor band pass filter. 58

3.33 Capacitances of thirteen and seventeen units realized with the Yiannoulos path. 60

3.34 Layout design of the BPF of Unit 6 with checkered capacitances. 61

3.35 Frequency response gains for the measured results of individual chips (solid lines), the theoretical transfer function calculated from the capacitance ratios (dotted line), and interpolated simulation results with transient analysis (broken line). 61

3.36 Circuit diagram of the Gilbert cell mixer. 63

3.37 Measured spectra of the IF signals for $V_{\mathrm{RF}} = 8$ mV (solid line), and $V_{\mathrm{RF}} =$ 20 mV (dotted line). $f_{\mathrm{RF}} = 55$ kHz, $f_{\mathrm{LO}} = 250$ and kHz. 64

3.38 Input versus output amplitude characteristics. 65

3.39 Circuit diagram of the Gilbert cell mixer which has independent the gain and the output common-mode voltage to improve the linearity. 65

3.40 Block diagram of the PLL. 66

3.41 Half circuit schematics of variable G_{m} OTA [*after Sato et al.*, (2005)]. . . . 68

3.42 Controlled G_{m} by the control voltage V_{C} of the OTA. 70

3.43 Variable G_{m} OTA with cancelling V_{tn} variation circuit. 70

3.44 Circuit diagram of the VCO with V_{tn} cancelling circuit. 71

3.45 Output frequency versus input voltage characteristics of the VCO. 72

3.46 Controlled G_{m} by the control voltage $V_C{}'$ of the OTAs for the modified VCO. 73

3.47 Output frequency versus input voltage characteristics of the modified VCO. 73

3.48 Circuit diagram of the phase frequency comparator. 74

3.49 Simulation result of the pulse width of the detection pulse signals to phase delay of the input signal. 75

3.50 Simulation result of the phase delay versus the mean voltage of the phase comparator output. 76

3.51 Circuit schematics of *RC* lag, lag-lead, and lag-lead-lag filters. 76

3.52 Frequency response of the lag-lead-lag-filter. Upper panel: Gain, and lower panel: phase. 77

3.53 Frequency response of the $H_{\mathrm{VCO-PC}}(s)$. Upper panel: Gain, and lower panel: phase. 78

3.54 Circuit diagram of the loop filter. 79

3.55 Simulation result of the frequency response gain (upper panel) and phase (lower panel) of the loop filter under the each corner condition. 80
3.56 Simulation result of the frequency response gain (upper panel) and phase (lower panel) of the open-loop in the PLL under the each corner condition. 80
3.57 Time evolution of f_{OUT} for two conditions of $f_{\mathrm{REF}} \times N$: (a) 5kHz × 64, and (b) 6kHz × 32. 81
3.58 Time evolution of the loop filter output for the conditions of (a) and (b). . 82

4.1 Block diagram of the system chip for the waveform receiver (Reprint of Fig. 2.4). 84
4.2 Layout design of the system chip. 85
4.3 Photograph of the system chip enclosed in the package. 86
4.4 Gains and phases for the frequency response of the chip on the waveform receiver module. The pass band gain can be set to three different values: low (0 dB), medium (20 dB), and high (40 dB) gain. 87
4.5 Block diagram of the waveform receiver. 88
4.6 Percentages for power loss of the devices on the waveform receiver module. 88
4.7 Photographs of both surfaces of the fabricated waveform receiver. 89
4.8 Crosstalk of the waveform receiver and the system chip from channel 6 to channels 1 and 5. 90
4.9 Sensitivities of the circuit board. 90

5.1 Schematic illustration of the MSEE sensor network system. The system consists of several small sensor nodes. 93
5.2 Schematic illustration of the MSEE sensor node. 94
5.3 Block diagram of the MSEE sensor node in the current design. 95
5.4 Equivalent input noise of the preamplifier for the electric field component. 95
5.5 Second prototype of the MSEE sensor node. 97
5.6 Summary of the sensitivities of electric field sensors (red line: MSEE, black lines: GEOTAIL and BepiColombo MMO) compared with the intensities of typical plasma waves observed in the terrestrial magnetosphere (green and gray boxes), and the electric field radiation from the breadboard model of the sensor node (blue line). 98
5.7 The schematic illustration of the nanosatellite constellation to observe the plasmasphere structure with a radio wave. 100
5.8 The z_{B0} axis is parallel to $\boldsymbol{B_0}$, and $\boldsymbol{k}$ exists in x_{B0}-z_{B0} plane. 102
5.9 The square refractive index versus normalized frequency with plasma frequency. 104

5.10 The electron density model for the geocentric radial direction which has peaks. 106
5.11 Rotation angle for six magnetic latitudes. 107
5.12 Upper panel: Electron density. Middle panel: refractive index difference. Lower panel: Rotation Angle (solid line: total, broken line: the first term in Eq. (5.29), and dotted line: the second term in Eq. (5.29). 108

6.1 Classical method in studying wave-particle interactions. The phase relation of the plasmas and plasma waves disappear in the reduced velocity distributions. 116
6.2 Principle of the WPIA. The WPIA calculates $\boldsymbol{E}_w \cdot \boldsymbol{v}$ before accumulating the observed data. 118
6.3 Interconnection of the WPIA with other instruments. 119
6.4 Data flow diagram of the WPIA. 121
6.5 Relation between the coordinate system of the spacecraft and the ambient magnetic field. 122
6.6 Relation between the coordinate system of the spacecraft and the coordinate system of a particle detector on a spacecraft which has a constant angle ξ relative to the r_x-axis. A particle with velocity v comes from a direction at angle θ to the $r_x r_y$-plane. 123
6.7 Schematic illustration indicating that a waveform is sampled and held at a sampling frequency although the particles are asynchronously caught by the particle detector. 123
6.8 Evaluation board for developing the one-chip WPIA. It contains the FPGA device (located in the center of the figure) and peripheral circuits including simple plasma wave receivers and simulators of plasma and magnetic field sensors. 124
6.9 State transition diagram of the “Waveform Calibration” block. 126
6.10 Block diagram of the “Waveform Calibration”. 126
6.11 Block diagram of the “Coordinate Transformation” for the ambient magnetic field coordinate system. 129
6.12 Block diagram of the “Coordinate Transformation” for the spacecraft coordinate system. 130
6.13 Timing chart for the time correction. After the first input of waveform data, calculations of the waveform calibration and coordinate transformation start while the second input starts. The first particle data set is written in RAM0 and waits for the end of the calculations of the first waveform data set. When the calculations are finished, RAM0 transfers the first data set and RAM1 takes the role of RAM0. 130

6.14 Block diagram of the “Time Correction”. 131
6.15 Data v and θ are captured when the incoming pulse becomes ‘High’. It takes seven clock cycles to transform v and θ into $v_{\perp 1}$, $v_{\perp 2}$, and $v_{\parallel}$. The incoming pulse is held in seven clock cycles to save information about time. Thus, the “Reference Clock” is reset and the RAM select signal is inverted seven clock cycles behind the reset of the “Write Clock.” 132
6.16 Block diagram of the “$\boldsymbol{E}_w \cdot \boldsymbol{v}$ Calculation”. 132
6.17 Ten results of $I(t) = \sum \boldsymbol{E}(t) \cdot \boldsymbol{v}(t)$. There is only a time distinction between the curves. 134
6.18 Average errors in the “Waveform Calibration” are plotted against the signal-to-noise ratio at the frequencies of the input waveform of 3.90625 kHz, 5 kHz, 10 kHz, 15 kHz, and 20 kHz. 135
6.19 Standard deviation of the errors in the “Waveform Calibration” are plotted against the signal-to-noise ratio at the frequencies of the input waveform of 3.90625 kHz, 5 kHz, 10 kHz, 15 kHz, and 20 kHz. 136

List of Tables

1.1 Typical plasma and cyclotron frequencies of protons and electrons at each region. 6

2.1 Advantages and disadvantages of ASIC technology. 16
2.2 Specifications of the integrated magnetic field sensor with ASIC [*Magnes et al.*, (2008)]. 18
2.3 Specifications of the waveform receivers. 21
2.4 Frequency configuration of the SFA. 24

3.1 Specifications of the designed first block, fully differential Gm-C low-pass filter. 31
3.2 Correspondence of the gain to switch configuration. 50
3.3 Type of the resistance, width, length, number of series element of the resistors for the differential amplifier. 51
3.4 Gains of the differential amplifier under different conditions of the internal Op-Amp. 52
3.5 Capacitance ratios based on the unit capacitance (25 fF) of the switched capacitor LPF. 55
3.6 Specifications of the anti-aliasing filter. 56
3.7 Ratios of each capacitance to the unit capacitance of 25 fF, and characteristic values in the each unit switched capacitor BPF. 58
3.8 Frequencies and their expression of the output of the mixer. 64
3.9 Specifications of the PLL. 67
3.10 Parameters for design of the loop filter. 77

4.1 Specifications of the waveform receiver. 83
4.2 Gain and dynamic range at 1 and 100 kHz with correspond gain that causes aliasing. 85
4.3 Device model, current and power consumption of peripheral circuitries. . . . 86

5.1 Specifications of the MSEE sensor node. 96

5.2 Orbital elements of “Emitter” and “Receivers.” 109
5.3 Assumptions in transmitter and receiver. 110

6.1 Logic cells of Virtex-II XC2V1000 FG456. 125

Chapter 1

General Introduction

1.1 Introduction

Beginning in the previous century, human beings have extended their activity onto outer space and have benefited greatly from applications utilizing spacecraft, such as weather forecasting and global positioning. The space environment that spacecraft are exposed to is completely different from the environment on Earth. For example, there is no atmosphere in space, the temperature on the surface of an object varies because of exposure to solar rays, gravity is either more or less intense and radiation exposure is considerably stronger. Most of the conditions of the space environment are deeply related to space plasmas.

Space is filled with essentially collisionless plasmas. Circumterrestrial plasmas are mostly generated by the solar wind and the Earth's atmosphere. The solar wind is an energy source released from the sun as well as solar radiation and is composed mostly of protons and electrons. A magnetic field accompanies the solar wind, the so-called interplanetary magnetic field (IMF). Each proton or electron in the solar wind obeys equations of motion with an external electric and magnetic force and travels in space with a gyro motion. The density and temperature in the solar wind are typically 10^7 m^{-3} and 10 eV, respectively. The solar wind velocity at 1 A.U. is approximately between 300 and 900 km/s. However, the density, temperature, plasma velocity, and magnetic field intensity in the solar wind change continually. These quantities are observed by the ACE (Advanced Composition Explorer) satellite of NASA (the National Aeronautics and Space Administration) and the real time data from the ACE satellite are made available to the public [1]. The Earth has an innate magnetic field approximated by a dipole moment of 8 $\times 10^{15}$ Am^2. The solar wind interacts with the Earth's magnetic field, forming the terrestrial magnetosphere. Figure 1.1 shows an illustration of a cutaway of the magnetosphere. The incoming solar wind is bent and forms a shock wave, the so-called bow shock (not indicated in Fig. 1.1). The bent plasma flows around the Earth

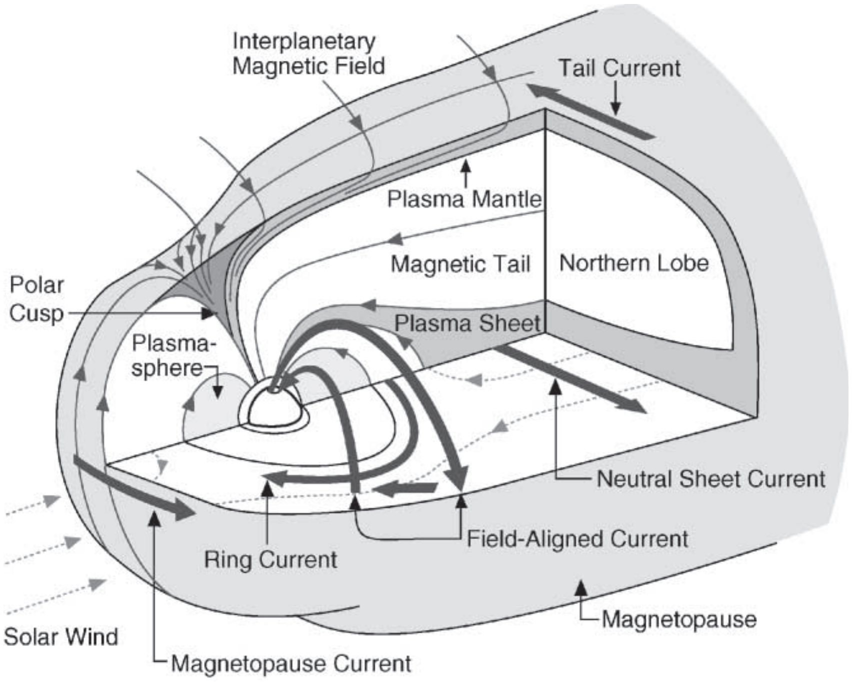

Figure 1.1: Cutaway diagram illustrating the three-dimensional magnetosphere [*Russell*, (2001)].

and stretches the Earth-derived magnetic field toward the night side of the Earth. Hence, the magnetosphere is steadily formed unsymmetrically at the day and night sides of the Earth. The night side expanded region is called the magnetic tail. The boundary between the solar wind and magnetosphere is called the magnetopause. The magnetosphere has various regions with different features due to differences in the plasma parameters and magnetic field intensity. For example, the low latitude region where hot plasmas are injected from the magnetotail is the plasma sheet. The hot plasma flow is thought to be caused by energy release when magnetic reconnection occurs at the magnetic tail. A ring current is generated by drift motion of ions and electrons in opposite directions (the ions drift westward and the electrons drift eastward). The ring current decreases the magnetic moment. In the plasmasphere, there exist more cold and dense plasmas than in other regions. The upper boundary of the plasmasphere is called the plasmapause. The lower boundary contacts the upper ionosphere.

The Earth's atmosphere is commonly defined as the region at altitudes lower than 80 to 120 km. The higher region, up to almost 800 km altitude, is called the ionosphere. Atoms and molecules of nitrogen and oxygen, which exist in the adjacent lower layer of the ionosphere, are ionized by absorbing solar radiation (visible light, ultraviolet, and higher energy rays). The densities of ions and electrons increase at higher altitudes in the ionosphere. Based on the differences in electron density, the ionosphere is classified into two (E, F) or four (D, E, F1, and F2) layers. The electron density depends on the amount of solar radiation exposure, and hence the aspect of the ionosphere and the classification at the night side differ from those at the day side. The ionosphere affects propagation of radio waves. At the day side, the D layer absorbs radio waves in the LF band while the MF and HF band waves are reflected at the D and F layer, respectively. At the night side, the LF and MF waves are reflected at the E layer and the HF waves are reflected at the F layer, though the propagation is different from that at the day side. Although radio waves in the VHF or upper band can propagate through the ionosphere, a propagation delay occurs and can cause errors in the global positioning system.

Applications utilizing spacecraft, e.g., communication and GPS, and the spacecraft themselves are affected by the space plasmas. The most critical problems are caused in the radiation belts. The terrestrial magnetosphere has regions where electrons and protons have relativistic kinetic energies, the so-called radiation belts. The radiation belts typically exist from 4 to 6 R_E in geocentric distance, where R_E (Earth's radii) is equal to 6337 km. The radiation belts were discovered by Dr. James Van Allen in 1958 [2], and were then collectively called the "Van Allen Belt." Spacecraft in a geostationary orbit must be designed to tolerate hard radiation, i.e., extremely energetic particles, which would otherwise cause a fatal error. The mechanism of generation and the characteristics of the radiation belts are not thoroughly understood. It has been reported that the particle flux in the radiation belts is correlated with magnetic storms and magnetospheric substorms. Magnetic storms are global substantial fluctuations of the Earth's magnetism. Typically, decreases in the Earth's geomagnetism take place over a few hours to a day in the main phase, and the magnetism recovers to the prior level in the recovery phase. Most magnetic storms are triggered by contact of the coronal mass ejection (CME) with the southward IMF from the sun. Figure 1.2 shows the energetic electron flux measured by the NOAA-12 and Exos-D (Akebono) [3], where L is the equatorial distance. Panels (a) and (b) indicate the electron fluxes in the dawn side of the northern hemisphere with the NOAA-12. The energy ranges of the fluxes in (a) and (b) are 30–1100 keV, and 300–1100 keV, respectively. Panel (c) shows electrons measured with the Exos-D ($>$ 2500 keV). The spectral index derived by NOAA-12 is represented in panel (d). The Kp and Dst indices shown in panels (e) and (f) denote the degree of disturbance of the Earth's magnetism. When the Dst index decreases, the Earth's magnetism is largely perturbed and the magnetic storm occurs. Up to day 308, energetic electrons in the radiation belts were located at $L > 3 \sim 7$. The peaks of the electron fluxes disappeared synchronously with the downside variation of the Dst index, indicating the radiation belts vanished. The electron flux then grew and eventually exceeded the prior level in proportion, as the Dst index approached zero. The magnetospheric substorms, triggered by the high-speed solar wind with southward IMF, are also considered to affect the radiation belt since the Earth's magnetism is also

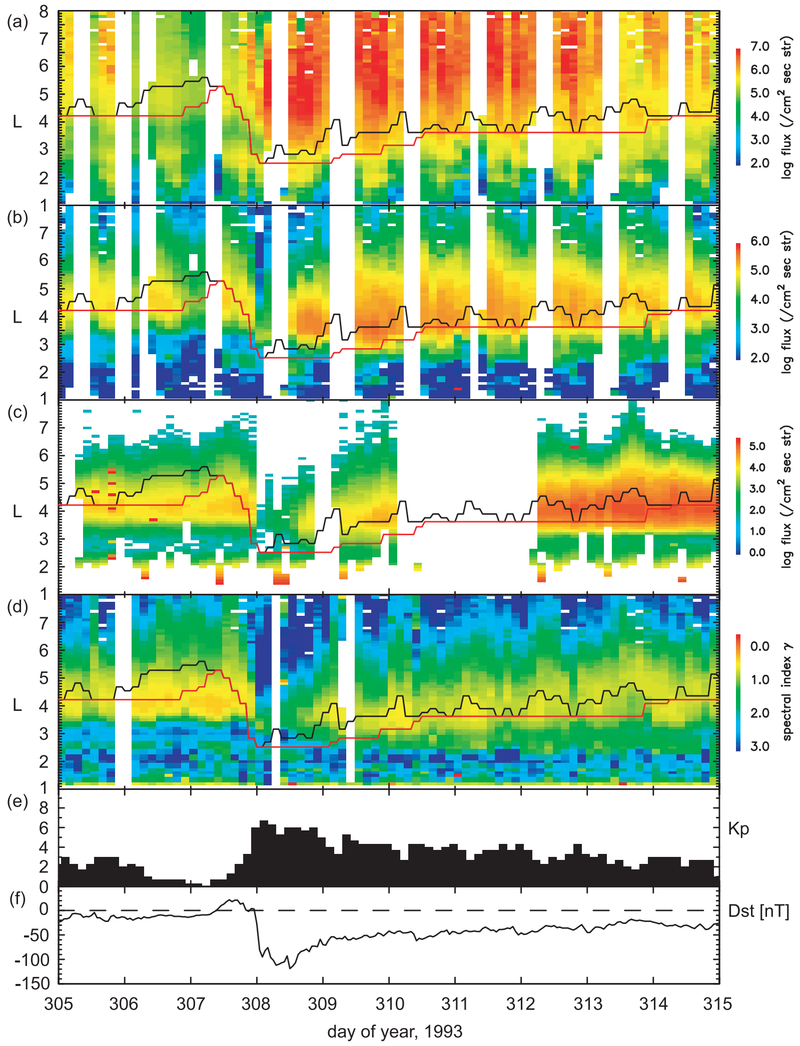

Figure 1.2: L–t diagram for electron flux, represented by color coded Kp and Dst indices during the 3 November 1993 storm [*Miyoshi et al.*, (2003)].

perturbed. Determining the mechanism of the disturbance of the energetic particles flux is a very significant issue in light of the recent increase in space activities. Countless studies have been conducted since the middle of the 20th century, including theoretical studies, *in-situ* and remote-sensing measurements, and computational simulations.

The objectives of space exploration have been not only to employ spacecraft for our welfare, but also to inquire into unreached regions of space and gather knowledge. During the coming decades, space exploration, development, and utilization are going to drastically expand, in developing countries as well as developed countries. The science revealing the physical phenomena in space, especially near Earth, should rapidly evolve as space activities increase. Thus, the observations of physical phenomena, including *in-situ* measurements using spacecraft, become increasingly important.

1.2 Space Electromagnetic Environment Sensors

Space plasmas are subject mainly to electromagnetic force, since the influence of gravity and collisions are negligible. The investigation of physical phenomena in space therefore involves determining the electromagnetic behavior of space plasmas, the so-called space electromagnetic environment. In this section, instruments for the measurement of the electromagnetic environment are briefly introduced.

Magnetic field measurement is the most basic probe of the electromagnetic environment. Magnetic fields universally exist in space. Since space plasma can be magnetized, magnetic field detection is essential. The fluxgate magnetometer, which precisely measures the magnetic field with zero-cross detection, is widely used in scientific exploration missions. Figure 1.3 shows an example of a fluxgate magnetometer designed for space exploration [4].

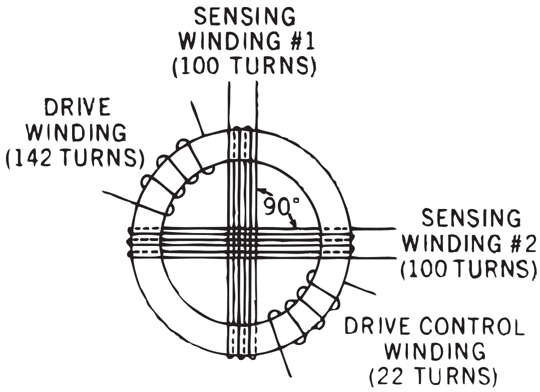

Figure 1.3: Design of a fluxgate magnetometer [*Acuna and Pellerin*, (1969)].

Plasma measurement is a direct way to probe space plasma. The energy of a plasma is distributed over a wide range. Typically, the energy of the electrons and ions in the terrestrial magnetosphere range from 1 eV to 10 MeV, and 1 eV to 10 keV, respectively. To analyze the energy, charge, and mass of the particles, an electrostatic analyzer and time-of-flight spectrometer are combined [5]. A basic electrostatic analyzer is presented in Fig. 1.4 [6]. The particles come from the left and enter the toroidal analyzer. The trajectories inside the analyzer depend on the voltage $-V_o$. By sweeping the voltage, the particles within a particular ranges of energy are directed to the imaging micro-channel plate (MCP). The time-of-flight spectrometer determines the velocity of a particle by measuring the flight time between a carbon foil and solid-state detectors (SSD). According to the target energy range, plasma measurement instruments with different energy ranges work concurrently to cover a wide energy range. The measured particle energy and detected direction are transformed into a velocity distribution function since the telemetry

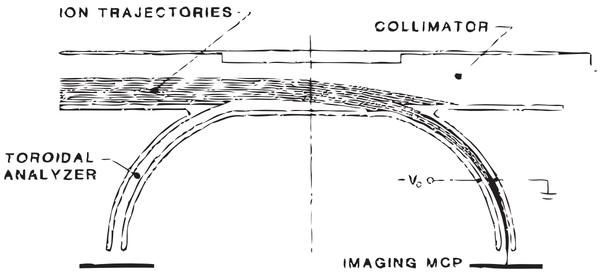

Figure 1.4: Cross section of a toroidal electrostatic analyzer [*Young et al.*, (1988)].

of spacecraft are not capable of collecting particle data.

The plasma wave is another physical quantity that reveals the behavior of space plasmas. The space plasmas are very subtle and can be treated as collisionless plasmas. Since the mean free path of plasma particles is typically around 1 A.U., the kinetic energies of the plasmas are not significantly altered through collisions. Therefore, interactions with electric and magnetic fields, so called plasma waves, is an important method of energy transport for space plasmas. The interaction between plasmas and plasma waves is called the wave particle interaction. Since a plasma is a dispersive medium, plasma waves have dispersion relations. A plasma wave is characterized by the plasma frequency and cyclotron frequency of the ions and electrons. Table 1.1 shows representative values of these frequencies, where $N, B_0, f_{\rm pe}, f_{\rm pi}, f_{\rm ce}$, and $f_{\rm ci}$ are, respectively, the plasma density, local static magnetic field, and plasma and cyclotron frequencies of electrons and protons, respectively.

Table 1.1: Typical plasma and cyclotron frequencies of protons and electrons at each region.

	Ionosphere	Plasmasphere	Magnetopause	Plasma Sheet	Solar Wind
$N[\mathrm{cm}^{-3}]$	10^6	10^2	10	1	10
B_0 [nT]	10^4	10^2	10	10	10
$f_{\rm pe}$ [kHz]	9×10^3	9×10^2	3×10^2	9	3×10^2
$f_{\rm pi}$ [kHz]	2×10^2	2	0.7	0.2	0.7
$f_{\rm ce}$ [kHz]	3×10^2	3	0.3	0.3	0.3
$f_{\rm ci}$ [Hz]	2×10^2	2	0.2	0.2	0.2

Plasma waves are classified into electrostatic and electromagnetic waves. Electrostatic waves have only an electric field component parallel to the propagation direction. The sensors that are used for detecting plasma waves are dipole antennas for the electric field component and loop antennas or search coils for the magnetic field component. Figure 1.5 shows the GEOTAIL satellite, which has wire and probe dipole antennas [7]. The length of both antennas are 100 m tip-to-tip. Since the wavelength of the plasma wave is much

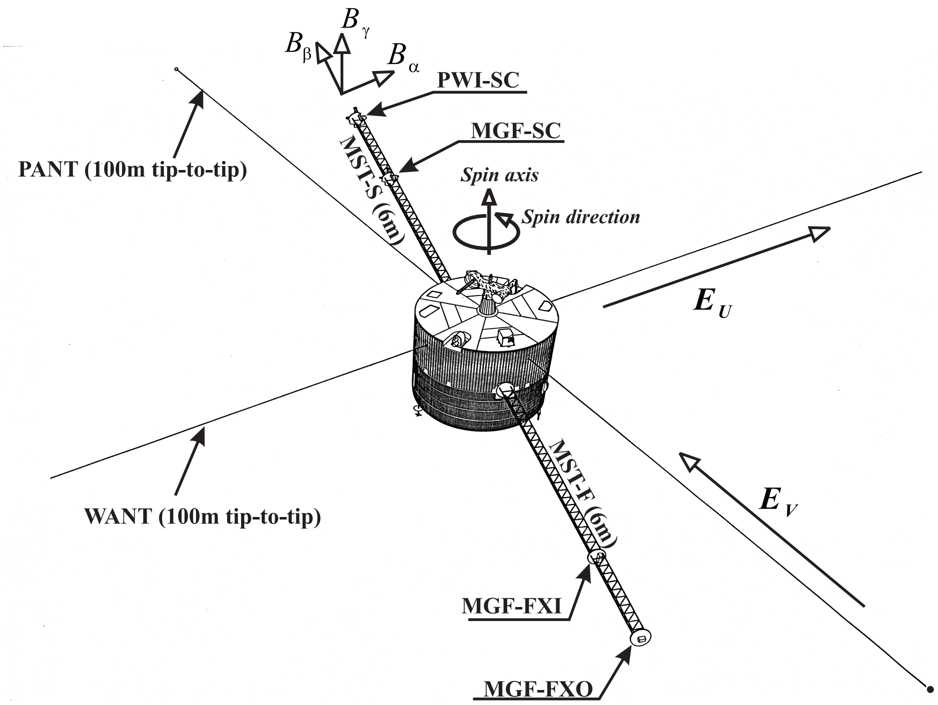

Figure 1.5: GEOTAIL satellite mounting electric and magnetic field sensors.

longer than the antenna length, the dipole antenna has capacitive impedance. A longer antenna allows for greater sensitivity for the dipole antenna sensor since the effective length (10 cm to 100 m) of the dipole antennas are typically smaller than the order of the wavelength of the plasma waves in the terrestrial magnetosphere. Loop antennas and search coils pick up the alternating-current component of the plasma waves. Although loop antennas have a low-frequency cutoff due to the use of a transformer, a loop antenna has a higher upper cutoff frequency than search coils [8]. Figure 1.6 shows the intensities and frequency band of the electric and magnetic field components. The sensitivities of a state-of-the-art plasma wave receiver are superposed. The plasma waves have a wide dynamic range over a wide frequency range, from the ELF to HF bands.

1.3 Scope and Contribution of the Present Study

Plasma waves have been observed using scientific spacecraft since the 1960s. The observed results have revealed curious phenomena in solar-terrestrial/planetary physics. Over the past decade, multiple satellite scientific missions, such as Cluster [9] by ESA and THEMIS [10] by NASA, have provided new insight into space plasma physics. The Scale Coupling in the Plasma Universe (SCOPE) mission has also been proposed in Japan by JAXA [11]. Since a spacecraft sailing in space usually has a relative velocity to the spatial

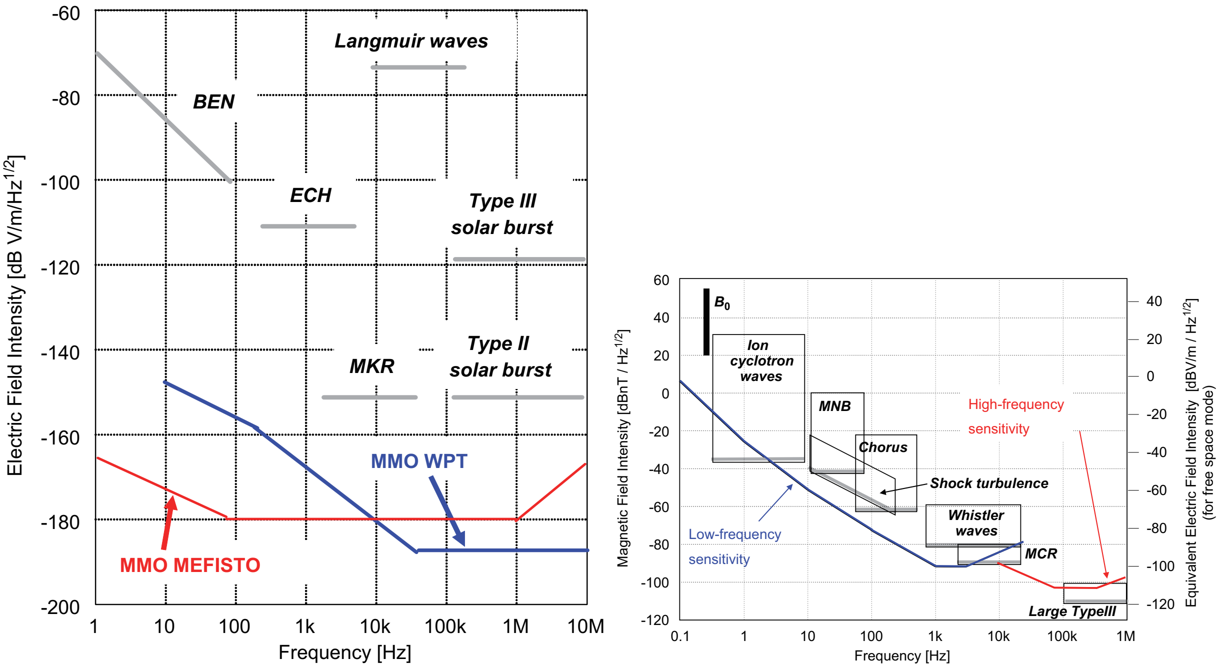

(a) Electric field components. (b) Magnetic field components.

Figure 1.6: Typical intensities and frequency band of plasma waves with the sensitivities of the sensors onboard BepiColombo/MMO [*Kasaba et al.*, 2010].

structures of plasmas and distribution of excited plasma waves, the observed waveforms involve not only temporal alterations but also convective derivative components. Studies involving multiple satellite missions have distinguished the temporal and spatial variations of physical processes. However, since multiple satellite missions have severe weight budget requirements, smaller onboard instruments are necessary. Reducing the weight and size of the instruments onboard satellite missions is important. Also, a breakthrough in observations for space plasma physics are desired that do not involve sizable increases in the weight and power budget.

The present thesis can be divided into two parts: the miniaturization of plasma wave receivers and the development of a new instrument which has the potential to bring about a breakthrough in study of space plasma physics.

In Chapter 2, miniaturization and integration approaches for measurement systems of space plasma physics are presented, including the plasma wave receiver. The plasma wave receiver is introduced with a few examples of previous scientific missions. The use of digital circuits and signal processing techniques are very advantageous. However, analog components continue to be used in instruments, preventing extreme miniaturization of the instruments, especially plasma wave receivers. Possible developments of integrated circuits for the purpose of plasma wave observations are demonstrated and circuits that can be miniaturized are introduced. The waveform receiver, which observes a plasma wave as a waveform, has become more important since the discovery of the electrostatic solitary wave (ESW) by GEOTAIL/WFC [12, 13]. A spectrum analyzer provides an overview of the time evolution of the intensity and frequency band of plasma waves. Both types of receiver are involved in the miniaturizing efforts.

In Chapter 3, designed circuits and their performances are demonstrated. Analog filters, an amplifier, a mixer, and a frequency synthesizer are introduced along with measurement results of manufacturing test trials. The waveform receiver has two kinds of low pass filter and differential amplifier. For the first block, a low-noise filter is adopted. The differential amplifier is located in the second stage. An anti-aliasing filter with steep attenuation characteristics is required. Sine the anti-aliasing filter needs to be realized with good accuracy, a switched capacitor technique is applied. Then, a noise eliminating filter is inserted before the anti-aliasing filter in order to turn down aliasing caused by the switched capacitor which operates in discrete-time. After the anti-aliasing filter, a second noise eliminating filter rejects the noise from the switching. A temperature compensation circuit is also integrated with these filters and the amplifier. A sweep frequency analyzer (SFA) – a double super heterodyne receiver – has filters, amplifiers, mixers and local oscillators. Frequency conversion in an SFA requires a frequency synthesizer and mixer. These circuits are also designed and evaluated. The performance and feasibility of the designed components introduced above are presented.

In Chapter 4, a miniaturized and integrated plasma wave receiver is presented. The developed circuits for the waveform receiver in Chapter 3 are integrated into an analog system-on-a-chip. The system chip has six observation channels for all the components of plasma wave observations. The physical layout design and overall performances of the system chip are introduced. The developed system chip is installed on a dedicated circuit board. The circuit board has power circuits, clock generator, divider, and analog-to-digital converters on the surface of both sides. The area per channel is reduced extremely compared to the instruments onboard previous planetary exploration missions.

In Chapter 5, two applications with miniaturized plasma receivers are introduced. One is a sensor network system for plasma wave measurement. Several sensor nodes are distributed in space and observe the local plasma waves. Each sensor node is palm-top sized and has electric and magnetic field sensors in three axes. The small sensor node demonstrates the performance of the available sensitivity for scientific missions. The second application is a constellation of very small satellites used to determine the position of the plasmapause. The constellation consists of two kinds of satellites: radio wave emitting satellites and receiving satellites. Radio waves lower than the HF band are strongly affected by the dispersion relations of plasmas in the plasmasphere. Faraday rotation can then be detected when a linear polarized radio wave in a particular frequency range travels in the plasmasphere. The constellation detects the Faraday rotation at multiple points and provides a spatial electron density distribution. A miniaturized plasma wave receiver is indispensable as the receiver for this system. The system design of the constellation is demonstrated.

In Chapter 6, the one-chip wave-particle interaction analyzer is demonstrated. To date, no method to detect the energy transfer between plasmas and plasma waves directly has been developed. The wave particle interactions have been studied by combining the measurement data of particles, waves, and magnetic fields visually. The time resolutions of plasma measurements and wave observations are not sufficient for the study of wave particle interactions because of the limitations of spacecraft telemetry. The wave-particle interaction analyzer (WPIA), which calculates the inner product of the electric field wave vector and individual velocity vector of the plasma particles, offers a method to overcome the limitation of spacecraft telemetry. The quantity of the inner product is proportional to the time derivative of the kinetic energies of the plasmas. Since the phase relation between these vectors is essential for this calculation, the amplitude and phase of the waveforms must be calibrated before the inner product calculation. The WPIA accumulates the inner products and provides the exchanged energies between the plasma waves and particles. To realize real-time observation of the wave-particle interaction, the WPIA is implemented in one chip with a field programmable gate array (FPGA). The performance and feasibility of the WPIA for future scientific missions are demonstrated.

In Chapter 7, the present thesis is summarized and concluded with several suggestions for future works.

Chapter 2

Miniaturization and Integration Techniques and Targets

2.1 Introduction

To measure space electromagnetic environments, plasma wave observations are very important as well as plasma and magnetic field measurements. The plasma wave observations make us to obtain the local density and temperature of plasmas, and disturbances of the electron/ion velocity distribution functions. Moreover, the waveforms of the plasma waves can provide phase information of the waves which is important to understand direction of energy transfer between plasmas and plasma waves. Onboard cooperation hardware with the plasma wave receiver, the particle (electrons/ions) detector, and the magnetic field sensor has very large significance to observe the time variation of the energy transfer directly and quantitatively. Since there in an only way for studying the physical process with qualitative discussion by visually comparing these kinds of data, this physical quantity has never been observed. The development of the novel cooperating instrument is the way to implement for the integration of the electromagnetic measurement system. The principle and detail design are discussed in Chapter 6. This extra instrument would compress the weight and power budgets of spacecraft even though its importance. Then, every onboard instrument should be miniaturized and integrated for the severe requirements of budgets. Especially, the analog electronics of plasma wave receiver remains which are not fully miniaturized. The approaches with techniques for miniaturization and integration are introduced. Subsequently, target circuits in the electronics and specifications to be miniaturized and integrated are described in this chapter.

2.2 Plasma Wave Receiver

2.2.1 Brief Summary of Instrument

The plasma wave is the important scientific target in the space plasma physics. The plasma wave is classified into electrostatic and electromagnetic waves according to the presence or absence of the magnetic field component. As sensors for the magnetic fields components, search coils and loop antennas are used. The dipole antennas are commonly used for the electric sensors. Generally, plasma wave instruments consist of the sensors, their pre-amps, and main electronics. The picked-up signal with the sensors are passed to the pre-amps for impedance transformation and amplification. The main electronics which consists of analog components which contain filters, and amplifiers, and etc., and digital components of memories, logic gates, and processors, for example. Then, the signal is converted into digital data and sent to the ground via telemetry of spacecraft.

Typical plasma wave instruments are of two types, namely, spectrum analyzers and waveform receivers. The spectrum analyzer is a classical instrument for plasma wave observation that provides an overview of space plasma physics. The waveform capture instrument onboard GEOTAIL is the first waveform receiver [12] and contributed the discovery of the existence of the electrostatic solitary wave (ESW) [13]. Waveform observation has a very important role to capture the phase information of plasma waves. Currently, waveform observation has become common in scientific missions [14, 15, 16, 17].

2.2.2 Typical Plasma Wave Receiver

Figure 2.1 shows an example of a block diagram of a typical plasma wave receiver [11]. This instrument is divided into four parts, HFA, WFC/OFA(E), EFD, and WFC/OFA(B). The WFC/OFA(B) is classified into the waveform receiver and connected three search coils (SC) through the pre-amps to obtain full magnetic field components of plasma waves. The HFA is one of the spectrum analyzer for the electric field components in the frequency band up to 30 MHz. The WFC/OFA(E) is the waveform receiver for full of the electric field components. The EFD also observes waveforms specialized in very low frequency band. The waveform receiver and spectrum receiver play complementary roles in plasma wave observations.

The analog components of these circuits have differential amplifiers, band-limiting or anti-aliasing filters in front of main amplifiers for sample-hold. The signals are filtered after amplifying After analog-to-digital (A/D) conversion, the digitized signals are stored in FIFO (First-In First-Out) memories. The digitized signals are usually processed in the field programmable gate array (FPGA) and other processors. The obtained data are then transmitted to the Earth through the onboard data handling unit.

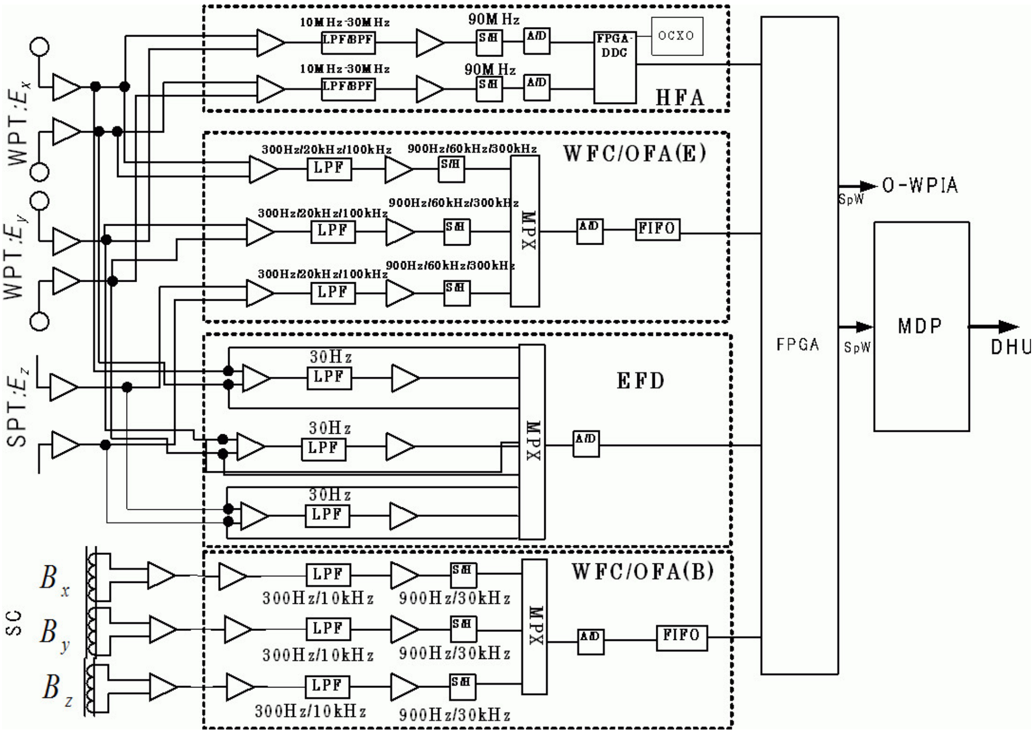

Figure 2.1: System block diagram of the plasma wave receiver of SCOPE [*SCOPE Working Group*, 2008].

2.3 Miniaturization and Integration Approach

2.3.1 Digital Components

From the point of view of miniaturization of the overall plasma wave receivers, the use of digital electronics such as a field programmable gate array (FPGA) is very effective in reducing the size of the digital components in the plasma wave instrument. Semiconductor processes have rapidly evolved since the 1960's according to Moore's law [18] as shown in Fig. 2.2 [19]. Thus, applying updated digital electronics can accelerate the miniaturization and integration of the space instruments.

The lunar radar sounder (LRS) is the instrument to investigate subsurface structure of the moon by using radar technique onboard KAGUYA (Selenological and Engineering Explorer: SELENE) launched on September 14th, 2007 [20]. As a subsystem, the LRS includes the waveform capture (WFC) expected to measure the plasma waves and radio emissions around the moon [17]. The WFC onboard KAGUYA was developed as a high performance software receiver implemented in digital signal processor (DSP). Both of the spectrum analyzer and the waveform receiver were realized with high time and frequency resolution by using a programmable down converter and sophisticated digital signal processing technique [21, 22].

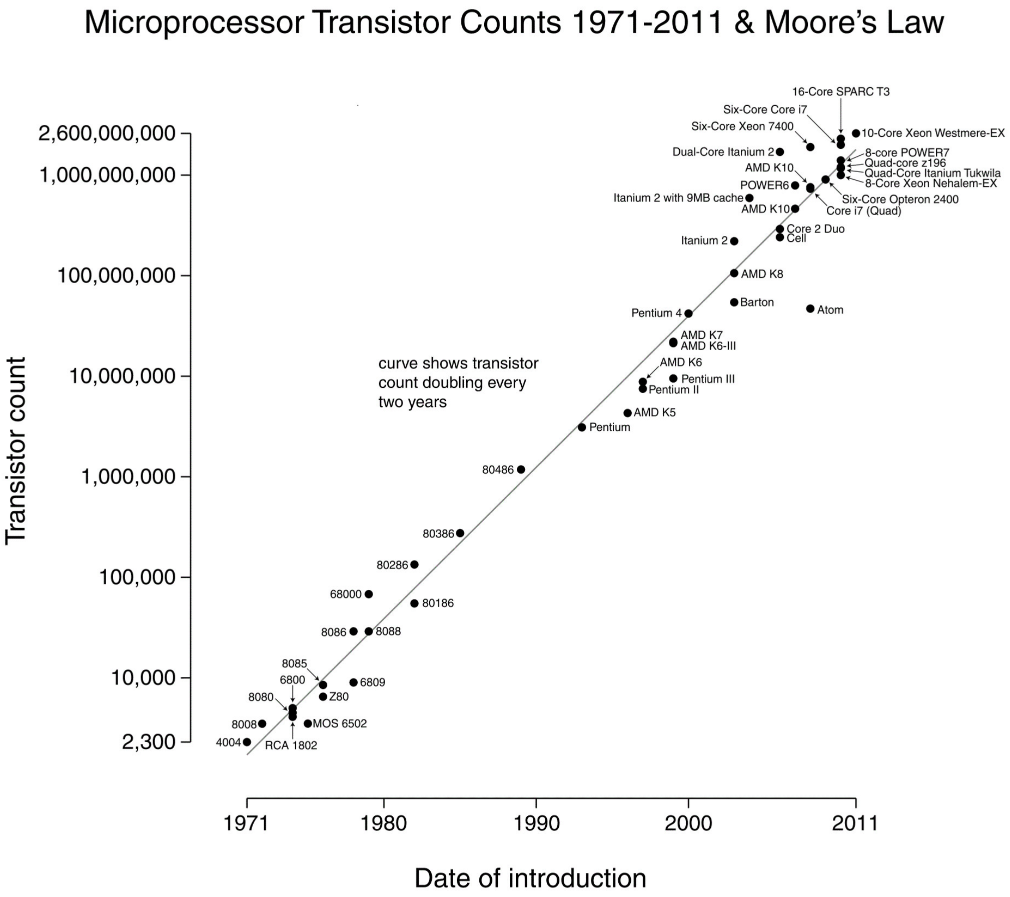

Figure 2.2: Number of transistors on a single processor.

Figure 2.3 shows the block diagram of the WFC onboard KAGUYA [17]. Even though the WFC on the KAGUYA was highly integrated by constructive adoption of the digital signal processing technology, the analog electronics could not be eliminated. Since the oversampling technique needs to amplify the received signals in the wide band frequency, the signal-to-noise ratio (SNR) was reduced and in relation of trade-off with degree of integration. In addition, the digital electronics was designed to operate at high speed, resulting in increase of the power consumption. This performance would be an inevitable problem in deep space exploration missions with more severe requirements than in terrestrial exploration missions.

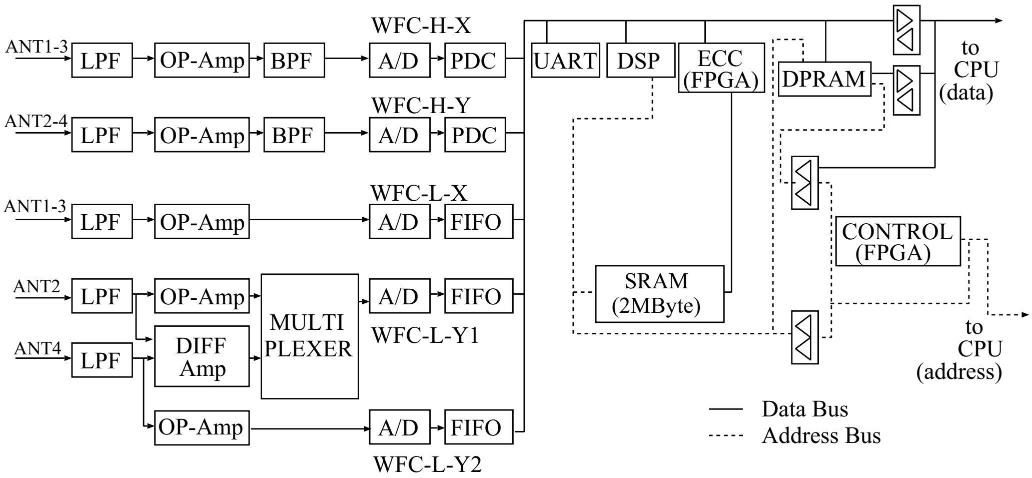

Figure 2.3: System block diagram of the WFC onboard KAGUYA [*Kasahara et al.*, 2008].

2.3.2 Analog Components

The analog components of the plasma wave receivers have not been made smaller. Since plasma waves exist with various intensities and frequencies as mentioned in Chapter 1, the receiver are required to have high sensitivity, low-noise characteristics, and a wide dynamic range. The analog components of both kinds of receivers (spectrum analyzer and waveform receiver) consist of a number of discrete electronics parts and ICs. In general the electronics devices must meet the military standard to enhance reliability of the instruments. The devices which have passed the tests specified by the standard can be used for the plasma wave receiver. As a result, the required performances leads increase of mass and size of the analog components. The evolution of the semiconductor technology have less contributed to the miniaturization of the analog components of the plasma wave receiver as contrasted with the digital components.

2.4 Analog ASIC Technology

In the present thesis, analog application specific integrated circuits (ASIC) technology is used. Generally, the ASIC technology has often meant integrated digital circuits for a specified purpose. In this decade, however, the ASIC which contains analog circuits for radio frequency (RF) transceivers and baseband processing becomes common. Currently, ASIC is commonly used in a number of kinds of consumer electronics products, for example, mobile phones, televisions, digital audio players, and etc. Representative purposes of the ASIC are to conduct efficient digital signal processing, and to downsize front-end of the RF receivers. The ASIC technology drastically reduces the mounted area of the circuits since little connection portions between the devices are needed.

2.4.1 Summary of ASIC

Complementary metal oxide semiconductor (CMOS) process is the most popular to manufacture ASIC since power consumption of the digital circuit becomes very low in comparison with bipolar and BiCMOS, combination of CMOS and bipolar, processes. The bipolar process provides higher operation speed and lower noise characteristics than the CMOS process though it needs large current to drive transistors. The BiCMOS process comprises the advantages of the CMOS and bipolar process. However, extra manufacturing procedure for the BiCMOS raises cost for manufacturing.

Silicon is widely used material for semiconductor manufacturing. Although GaAs, InP, GaN, and SiC have expanded operating frequency and mean output power of electronic devices, Si devices have still great advantages in abundance, ease for cleaning up, single crystallization, conditioning doping, and processability.

The ASIC has several advantages and disadvantages shown in Table 2.1 compared to conventional circuits. Obviously, a developed circuit for a specified purpose has less number of electronics parts and interfaces and individual area. The low power consumption is obtained because of low power-supply voltage. Sub-micron processes allow us to use 1.8-V or lower supply voltage. The high speed operation is possible because of small input capacitance of a gate node of transistors.

Table 2.1: Advantages and disadvantages of ASIC technology.

Advantages	Disadvantages
Reduction of area	High development cost
Low power consumption	Long development period
High speed operation	Difficulty of repair and remediation
Possibility of low unit price by mass production	

2.4.2 ASIC for Space Science

The low unit price by mass production is one of the important reasons why the ASIC is used in a number of consumer products. Private companies which release the products obtain profit by cutting down cost with mass production and the design to improve yield ratio. Before growth of ASIC market for consumer products, principal use of the ASIC was military applications of radar, communication equipments, onboard digital signal processors and so on. In other words, performances and compactness which the ASIC brings in are prioritized for the military use. Since space application partially includes the military use, thence ASIC began to be applied to space science.

The ASICs onboard spacecraft with science targets were initially developed for detection of high energy photons (X-ray and Gamma ray), ions, and electrons in NASA and ESA [23, 24, 25, 26, 27]. SUZAKU, the X-ray astronomy satellite launched in 2005, is the first Japanese scientific satellite to which the ASICs are applied [28, 29]. As the further progress, the performances such as timing resolution of the X-ray CCD have been improved using a CMOS process for the ASTOR-H mission to be launched in 2013 [30, 31, 32]. The development of ASICs for use in X-Ray CCDs and with feasible radiation tolerance was also achieved using a fully depleted silicon-on-insulator (SOI) device in a SOI-CMOS process [33]. The use of ASICs for X-ray astronomy in scientific spacecraft will increase and provide valuable perception.

Magnetic field sensors are scientific instrument traditionally onboard spacecraft. *Magnes et al.,* (2008) developed integrated flux-gate magnetic field sensor with the mixed-signal ASIC which contains the sigma-delta modulator and decimation filter [34]. Specifications of the developed sensor are indicated in Table 2.2 and feasible for space science missions in spite of success of extreme miniaturization.

A low-noise amplifier with programmable gain was developed as a dedicated chip, an application-specific integrated circuit (ASIC), for plasma wave observations [35]. The amplifier was designed to be radiation tolerant, in addition to having low noise of 100 $\text{nV}/\sqrt{\text{Hz}}$ @ 100 Hz, using the National Semiconductor SiGe 0.25-μm BiCMOS process. Robustness toward total ionizing dose and single event effects were confirmed. On the other hand, any suitable ASIC has not been developed or known as a system chip of the plasmsa wave receiver for any scientific missions so far. Then, we develop a system chip for the analog circuits of plasma wave instruments using ASICs and realize extreme miniaturization. The realization of on-chip instruments is very important for not only solar-terrestrial physics but also space science in general. Moreover, the realization of on-chip instruments will result in several new observation concepts which use extremely miniaturized instruments. In the following section, target circuits intended for development of ASIC in the present thesis.

Table 2.2: Specifications of the integrated magnetic field sensor with ASIC [*Magnes et al.*, (2008)].

Total dose hardness	Full specs: < 170 Rad Functional: > 300 krad
Single event latch-ups	>14 MeV cm^2 mg^{-1}
Field mode	
Dynamic range (128/2 Hz)	92/>103 dB (< ±60,000 nT)
SNR (128/2 Hz)	89/>99 dB
Internal voltage mode	
Dynamic range (128/2 Hz)	98/114 dB (±1.25 V differential) 92/108 dB (±0.625 V single-ended)
SNR (128/2 Hz)	91/107 dB (±1.25 V differential)
Digital resolution	23 significant bits
Offset stability.field mode	<5 pT $°\mathrm{C}^{-1}$ MFA temperature < ±0.2 nT within 250 h
Gain stability.field mode	60 ppm $°\mathrm{C}^{-1}$ (± 1,000 nT dynamic range)

2.5 Target of Miniaturization

Development of analog circuits using ASICs is very effective for the miniaturization plasma wave receiver. The waveform receiver and spectrum analyzer are integrated into different chips independently though overall integration is to be the final goal.

The scope of integration and functions of subcomponents for each type of the receiver are described in this section.

2.5.1 Waveform Receiver

As the name suggest, the waveform receiver observes waveforms, temporal alterations of a certain physical quantity (i.e., electric and magnetic fields for plasma wave receiver) at a point. Thus, the waveform receiver should accommodate maintaining noise level without narrowing down of the frequency band in amplification. The upper limit frequency of the waveform receiver is typically a few hundred kilohertz, and is decided by considering target phenomena as well as the power budget and telemetry capacity. A waveform receiver with an upper frequency of a few hundred kilohertz covers the local electron plasma frequency in the outer magnetosphere and the local ion plasma frequency in the ionosphere. We set the upper limit to 100 kHz to prevent rising up the sampling frequency.

The block diagram shown in Fig. 2.4 is the waveform receiver and indication of the target for the miniaturization. The dotted line means the scope where we design and develop in the following chapters. The broken line inside the dotted line region is the target circuits realized with the ASIC. The analog circuits, except for the pre-amps and A/D converters are objectives for development inside the ASIC. Simultaneous observation

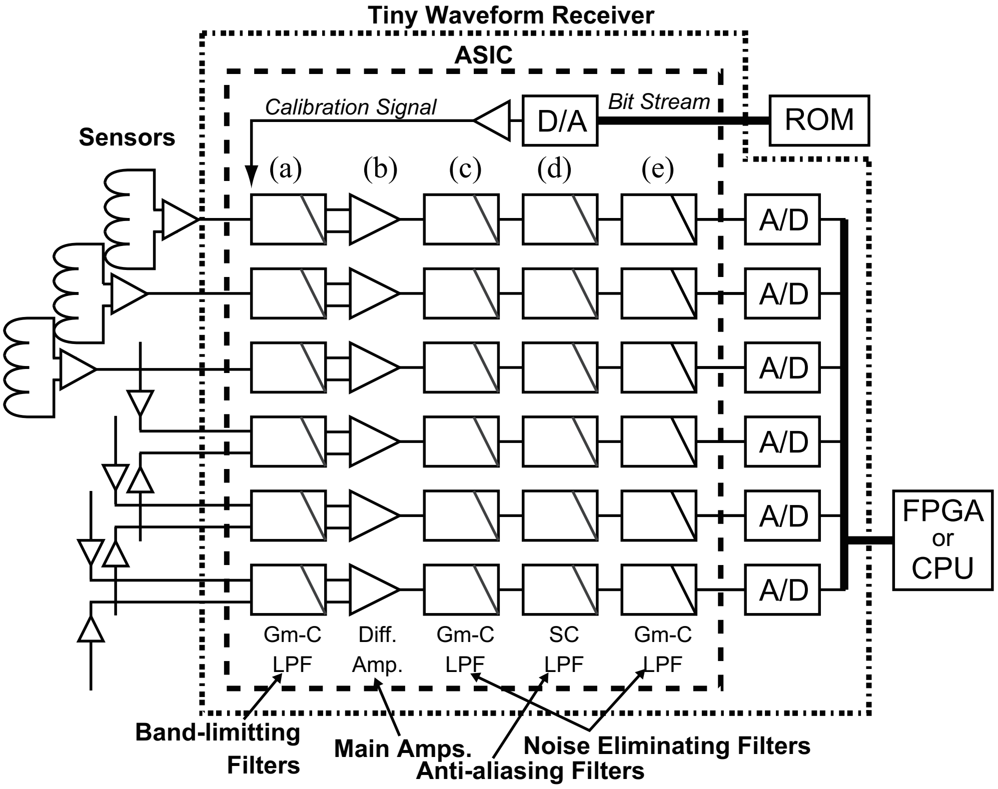

Figure 2.4: Block diagram of the system chip for the waveform receiver.

using six channels (all components of electromagnetic fields) is appropriate for complete plasma wave observations which can determine direction of the Poyinting vector of the observed electromagnetic waves. The pre-amps are needed to be located very close to the sensors not to drop the signal level. Thus, including the pre-amps for six channels are insufficient. The A/D converters are required to have the dynamic range of 14 bits or more for productive scientific investigation. Since the adequate A/D converter to the waveform receiver can be realized with the CMOS process [36], integrating the A/D converters into the ASIC could be involved. However, we address the integration of the filters and the amplifiers rather than the A/D converters in view of the priority issue to down size the overall waveform receiver.

There are two options when an analog filter is designed in an integrated circuits; continuous-time filter and discrete-time filter. Representatives of both kinds of filters are a G_m–C filter and a switched capacitor filter. The G_m–C filters are classified into a continuous-time filter. The filter response of the Gm-C filter is determined by capacitance and transconductance of a operational transconductance amplifier (OTA). The transconductance of the OTA can be adjusted with bias current inside the OTA. The G_m–C filter has relatively low-noise characteristics and does not need an external signal or a local oscillator for the filter itself. On the other hand, the G_m–C filters have large temperature drift and considerable variation and usually need compensation circuits. The switched capacitor (SC) filter is a kind of discrete-time filter, in which a clock signal switches connections between capacitors and OP-amps. Since periodical switching of the capacitors flows the charge during the period, we can recognize the switched capacitor as a resistor when the frequency of a signal is much lower than the switching frequency. The characteristics of the SC filter is denoted with capacitance ratios, resulting in acceptable accuracy of manufacturing. Then, the SC filter is suitable for filters which need to be accurately manufactured. However, the external signal or the local oscillator is necessary for switching. Switching of the SC filter results in switching noise and aliasing because of spurious in higher frequency band than the interested frequency band. Then, noise eliminating filters are combined with the SC filter.

The essential components in the waveform receiver are the band-limiting filter, the main amplifier, and the anti-aliasing filter. The band-limiting filter ((a) in Fig. 2.4) is a G_m–C filter because of the noise requirement. The SC filter is suitable for use as an anti-aliasing filter ((d) in Fig. 2.4) because the cutoff frequency of the anti-aliasing filter should be obtained accurately. The amplifier ((b) in Fig. 2.4) has several gain steps to ensure the requirement dynamic range. Two G_m–C filters ((c) and (e) in Fig. 2.4) are inserted into the front and rear of the SC filter to eliminate noises. The digital-to-analogue (D/A) converter in Fig. 2.4 is included for onboard calibration, An antenna in plasma shows different characteristics from that in vacuum. Besides, the antenna impedance strongly depends on the plasma density and temperature. Hence, onboard calibration is indispensable in order to obtain absolute quantity of the electric field components of the plasma wave. Commonly, the calibration system is implemented closed to waveform receiver. Setting the input of the D/A converter appropriately, an analog calibration signal is obtained. It is assumed that the calibration signal is a set of several monolithic sinusoidal waves or a chirp signal from several hundred hertz to 100 kHz. These waveform data of the calibration signal are digitally stored in a flash memory and periodically read out for D/A conversion. The calibration signal is fed to the waveform receiver after the D/A conversion. The intended operation of the D/A converter has been confirmed. Although development of the small calibration system with the waveform receiver is also an important issue, it is beyond the scope of the present thesis.

Table 2.3 compares the target specifications of the waveform receiver using ASIC with those of the previous waveform receivers. The low frequency plasma wave analyzer (LFA) is the waveform receiver onboard the Japanese NOZOMI spacecraft [37]. The NOZOMI (Planet-B) was the Mars explorer launched on 4 July, 1998. The operation was terminated because of communication black out before starting observation in 2003. The Mars is different from the Earth since the Mars does not have global inherent magnetic field and directly interacts with the solar wind. In general, the instruments for observing electromagnetic environment are designed to accommodate the conditions inside and out of the magnetosphere in terrestrial exploration missions. Then, the instruments for mars exploration was designed in the condition close to the terrestrial exploration missions. The analog component of the LFA was one third the A4-sized substrate. The WFC-L performed observations of lower frequency band in the WFC shown in Fig. 2.3. Only two components of the electric fields were observed by the LFA and WFC-L.

Table 2.3: Specifications of the waveform receivers.

	with ASIC	LFA [37]	WFC-L [17]
Sampling Frequency	400 kHz	100 kHz	1 / 2 MHz
Observation Bandwidth	100 kHz	32 kHz	50/100 kHz
Gain	0/20/40 dB	0/20 dB	0/20/40 dB
Resolution of A/D	14-bit	16-bit	16-bit
Dynamic Range	78 dB	90 dB	70 dB
Target Component	All components of EM fields	2 components of Electric fields	
Size of the analog part	50 × 45 mm^2	1/3 of 210 × 297 mm^2	N/A

2.5.2 Spectrum Analyzer

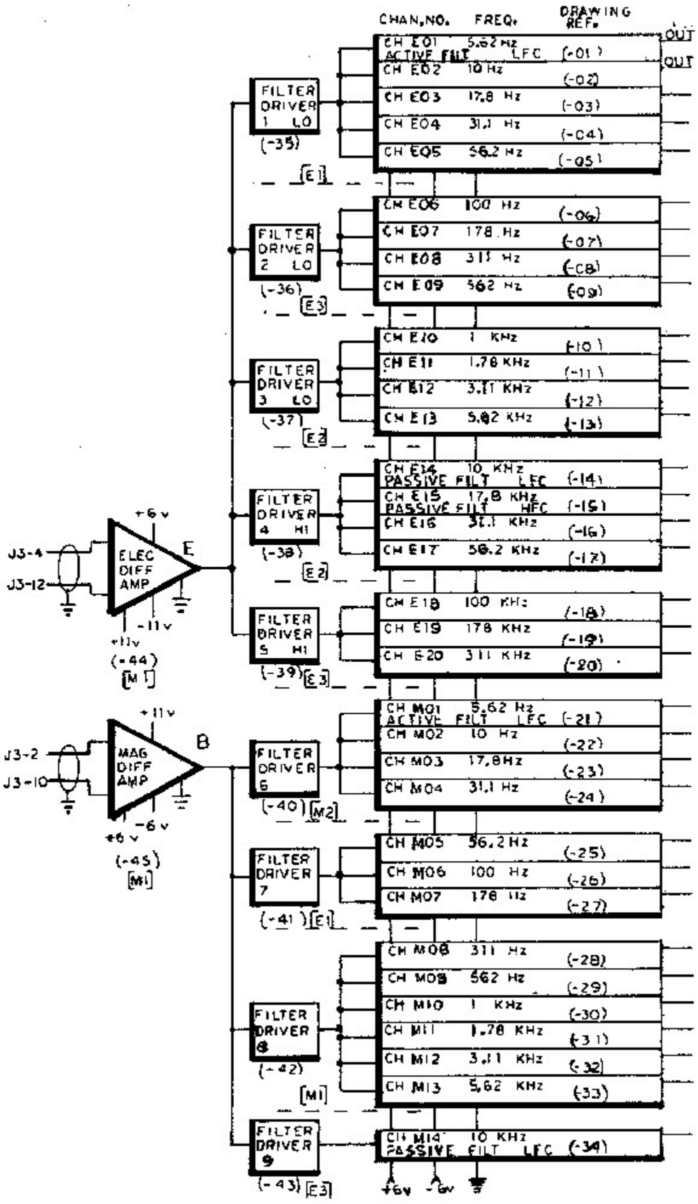

Figure 2.5: Block diagram of the MCA onboard GEOTAIL [*Matsumoto et al.*, (1994)].

The spectrum analyzer is divided into the multi-channel analyzer (MCA) and sweep frequency analyzer (SFA). The MCA is the analog filter bank which passes signal in different frequency bands as shown in Fig. 2.5 [12]. The observed signals which pass through differential amplifiers are simply fed to the band pass filter (BPF). The filtered signal are the output of the MCA. The SFA is the double super heterodyne receiver, which sweeps frequency band to observe by changing the 1st local frequency in Fig. 2.6 [12]. The observed signals are mixed with the local oscillating signal (1st Local) and converted into

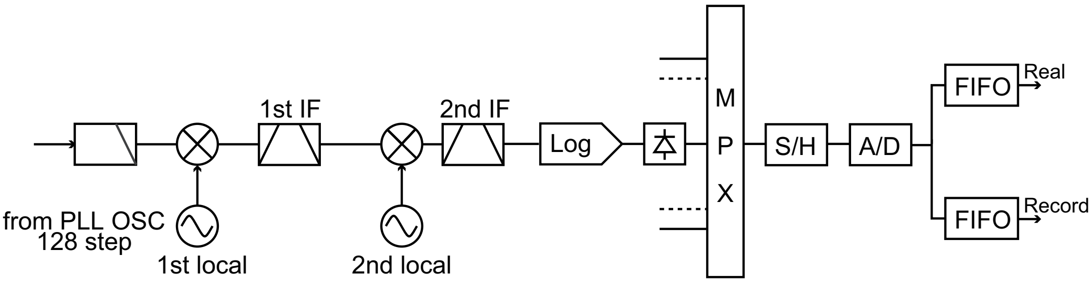

Figure 2.6: Block diagram of the SFA onboard GEOTAIL [*after Matsumoto et al.*, (1994)].

upper and lower frequency which equals to either of the sum and difference. By conducting down conversion at 1st or 2nd IF, the frequency becomes low enough to detect the peak level. The different 1st local frequency brings the different frequency to be observed into the fixed frequencies of the 1st and 2nd IF. The output of the BPF in 2nd IF is logarithmically amplified to obtain wide dynamic range. Then, detected peak levels are multiplexed and digitized in sequence.

The MCA and SFA complement time and frequency resolutions with each other. For overcoming the weakness of the MCA, the number of filters is to be increased resulting in large circuit size. The SFA should be swept in short time in order to improve the time resolution. To maintain the fine frequency resolution of the SFA, we propose a new composition which combines the SFA with digital signal processing.

Figure 2.7 shows the SFA we improve the time resolution without degradation of the frequency resolution. Compared to Fig. 2.6, crucial differences are eliminating the log amplifier and detector. An illustration of the proposal for the improvement is shown in Fig. 2.8. Sweeping frequency from the lower to the upper range causes the long time resolution, e.g., 64/8 second of the SFA onboard GEOTAIL [12]. The proposed method reduces the number of sweep steps and expands the bandwidth. The sweep time becomes short, at the same time, the frequency resolution is forced to be coarse as it is. Eliminating the log amplifier and the detector enables the signal to be digitized as a waveform since the both circuits make the signal to lose phase information. The digitized waveform can be applied the fast Fourier transform (FFT) on the signal processing unit such as the FPGA. The spectrum obtained by the FFT has magnitudes of the frequencies, which are equal to the integral multiple of the sampling frequency divided by the number of FFT. Hence, the frequency resolution becomes as fine as the sampling frequency divided by the number of FFT. This proposed SFA is similar to the WFC onboard KAGUYA which provide the spectrum by applying FFT to the digitized waveform. However, the high speed operation is not needed in the digital electronics since the sampling frequency can be set to lower than the upper limit frequency by using analog down conversion before the sampling. The proposed SFA is very effective for the power budget of the digital electronics when the upper limit frequency of the observation range is high.

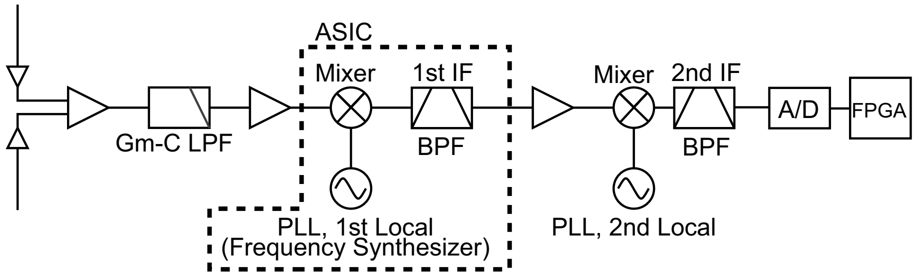

Figure 2.7: Block diagram of the SFA with improvement of time resolution.

The circuits inside the dotted line in Fig. 2.7 are the objective of the miniaturization by using the ASIC. The PLL stands for phase-locked loop, which is a coherent oscillator realized by forming the negative feed back loop for phase of the signal. The frequency synthesizer is the most important component in the SFA. The mixer and the BPF of 1st IF are also important for frequency conversion and rejection of image caused by mixing. The 1st BPF needs to have a steep reduction characteristics in the frequency response gain to lower 2nd IF frequency without losing SNR. In the present thesis, we design these circuits and evaluate the performances related to the frequency conversion with the ASIC before undertaking overall design of the proposed SFA.

The frequency configuration of the SFA in Table 2.4. The SFA consists of four independent frequency band. Although the lowest frequency range of all band number is zero, actual lowest limit is determined by configuration of pre-amps to avoid saturation caused by very low frequency signals. The circuits to be described in this thesis is dedicated to the band number 2. For the other frequency bands, extra designs are necessary though the basic principle for design is mostly common.

Table 2.4: Frequency configuration of the SFA.

Band No.	Frequency Range	1st Local	1st IF	2nd Local	2nd IF
1	0 Hz ∼ 10 kHz	20.0 kHz ∼ 29.0 kHz	19.5 kHz	18.5 kHz	1 kHz
2	0 Hz ∼ 100 kHz	200 kHz ∼ 290 kHz	195 kHz	185 kHz	10 kHz
3	0 Hz ∼ 1 MHz	2.00 MHz ∼ 2.90 MHz	1.95 MHz	1.85 MHz	100 kHz
4	0 Hz ∼ 10 MHz	20.0 MHz ∼ 29.0 MHz	19.5 MHz	18.5 MHz	1 MHz

The target time resolution requirement is set to less than 1 s. The total number of sweep steps needs to be 10 or more to cover all the frequency range. Then, it should take less than 100 ms for one sweep step to lock the PLL of the 1st local frequency, sample

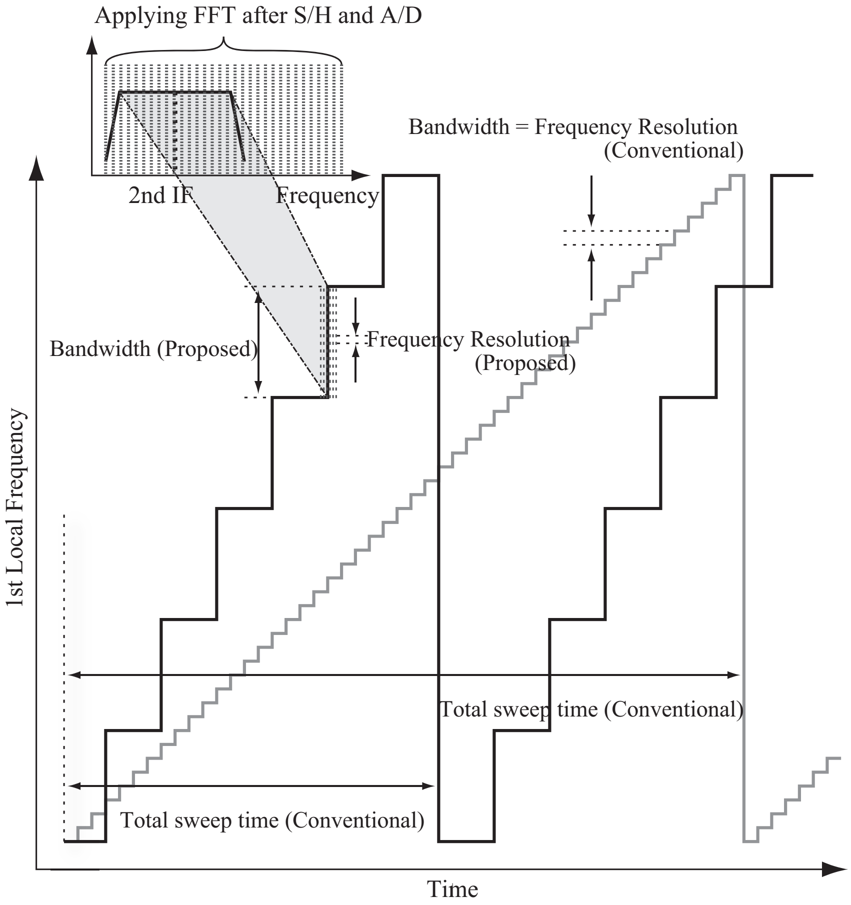

Figure 2.8: Proposal to maintain frequency resolution with the short sweep time.

and convert the signals after stabilizing the frequency, read the stored signals in memory in the FPGA, apply FFT, and write the obtained spectrum. The allocation of time for the one sweep step is represented in Fig. 2.9, where the sampling frequency, the number of FFT, and total memory access time to read or write data of length of the number of FFT are 40 kHz, 1024 points, and 10 ms respectively. The processing time for FFT is negligible. If PLL can be locked and stabilized within 53 ms, the time requirement of the one step is satisfied. The PLL design is described with considering the lock time requirement in Chapter 3.

2.6 Summary

Integration of the space electromagnetic environment, for which the the cooperating instrument which coordinates the plasma wave receiver, the plasma detector, and the magnetic field sensors is developed, would provides scientific outcome. The plasma wave receiver has an important role to obtain information of the local plasma environment. Progress of the semiconductor technology and digital signal processing has allowed the

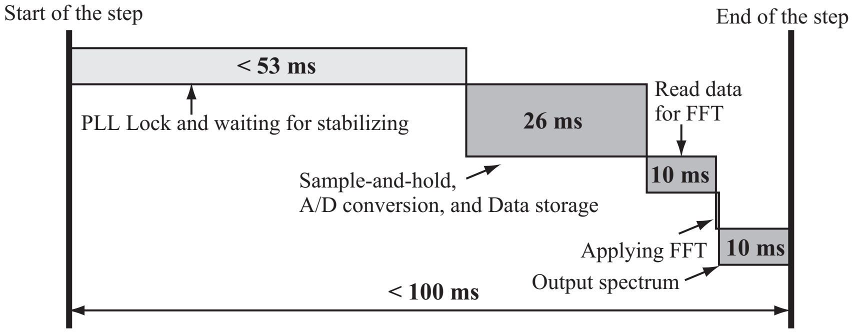

Figure 2.9: Allocation of time.

evolution of the plasma wave receiver, resulting in the WFC onboard KAGUYA. On the other hand, the analog electronics remains without notable miniaturization. For particle detectors, and the flux-gate magnetic field sensor, the ASIC technology downsized the analog circuit in the instrument. The ASIC is very suitable to realize extremely miniaturized instruments. We apply the plasma wave receiver, classified into the waveform receiver and the sweep frequency analyzer (SFA) that have complementary roles in plasma wave observations. The waveform receiver to be designed includes six-channel circuits of analog filters and amplifiers. The band-limiting, differential amplifier, and anti-aliasing filters are essential components for the waveform receiver. In order to realize accurate characteristics of the anti-aliasing filter, the switched capacitor filter with noise eliminating filters is applied. The band-limiting filter and the noise eliminating filters are implemented with G_m–C filter which has low-noise characteristics. The novel SFA was proposed in order to improve time resolution with keeping fine frequency resolution by combining FFT. The SFA contains phase-locked loop (frequency synthesizer), mixer, low pass filter, band pass filter (BPF), and amplifiers. We are to design the frequency synthesizer, mixer, and the BPF, that are key components for the SFA. The development of the ASIC for the waveform receiver and spectrum analyzer plays a huge role for the miniaturization. The instrument and the miniaturization technique presented in this chapter are surely to be indispensable in coming scientific missions.

Chapter 3

Component Designs and Evaluations of the Plasma Wave Receiver

3.1 Introduction

For miniaturization of the plasma wave receiver, we design and evaluate the circuits indicated in Chapter 2 with the ASIC technology. According to the objectives, the target circuits are listed as follows:

- $\mathrm{G_m}$–C LPF (Waveform Receiver)
- Temperature compensation circuit (Waveform Receiver)
- Differential amplifier (Waveform Receiver)
- Switched capacitor LPF (Waveform Receiver)
- Switched capacitor BPF (SFA)
- Mixer (SFA)
- PLL (SFA)

The applied circuits (Waveform Receiver / Sweep Frequency Analyzer: SFA) are also indicated in brackets. Since the $\mathrm{G_m}$–C filter has non-negligible temperature drift on the characteristics, we design the temperature compensation circuit for the $\mathrm{G_m}$–C filter. The switched capacitor (SC) LPF and BPF are based on the same principle of the switched capacitor technique. The mixer is the double-balanced-type multiplier to clarify problems in the practical usage for the plasma wave receiver. The PLL consists of the voltage controlled oscillator, the divider, the phase comparator, and the loop filter. We introduce the respective designs by showing operations and performances obtained by simulations and measurement after manufacturing.

The CMOS 0.25-μm mixed-signal process with one-poly and five-metal layers (1P5M) provided by Taiwan Semiconductor Manufacturing Company (TSMC) is used in the present thesis. We use S-Edit, and T-SPICE by Tanner EDA, and Layout Editor by Cadence as the design tools. Calibre is also used for design rule check (DRC), layout versus schematic (LVS), and parasitic extraction (PEX). In the CMOS 0.25-μm process by TSMC, two kinds of MOSFETs which have 2.5 V and 3.3 V of the maximum voltage are employable. The 3.3-V devices are selected in principle since available voltage range for signals are wide. The 3.3-V single supply and 1.6 V are adopted to the power supply (V_{DD}) and the common-mode DC voltage (V_{CM}), respectively. The manufactured chip is enclosed the 80-pin quad flat package (QFP). A photograph of the chip packages is shown in Fig. 3.1. The sizes of the bare chip and the chip package are 5 × 5 mm^2 and 15 × 15 mm^2, respectively.

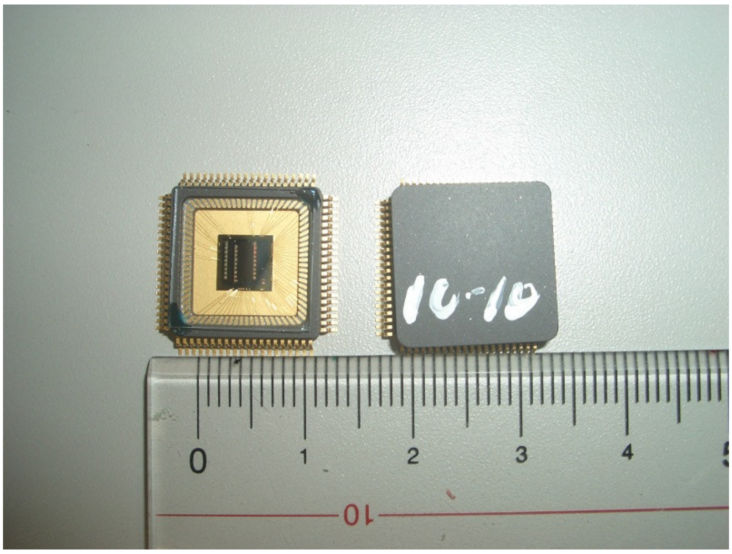

Figure 3.1: Photograph of packages including an ASIC.

3.2 Attention to Radiation Tolerance

For space application, radiation tolerance is a very important property of the integrated circuits including the ASIC, and FPGA. Performance degradation, and unintended operations are caused by incident radiation on the semiconductor. Single event upset, which brings on soft error in processors and memories, can be excluded in the analog component. On the other hand, total ionization doze and single event latch up should be attended. The total ionization dose means that total amount of the incident radiation increases the interstitial deficit of SiO_2 and affects interface state between the SiO_2 and Si bulk layer by generated electron-hole pairs. As a result, variation of characteristic of the semiconductor, and increase of leak current at the gate node of MOSFET are raised. The total ionizing dose of the ASIC using the TSMC CMOS process has been confirmed to be over 10 krads for space applications [31]. The single event latch up is a critical failure which does not recover until reset of the device or for eternity. The PNPN junction which inherently exists in CMOS process forms a thyristor as shown in Fig. 3.2. When the NPN transistor connected to the V_{SS} turns on, the avalanche current flows out through the emitter and gate of the PNP transistor to the NPN transistor. Then, the current cannot stop until shutting the current out.

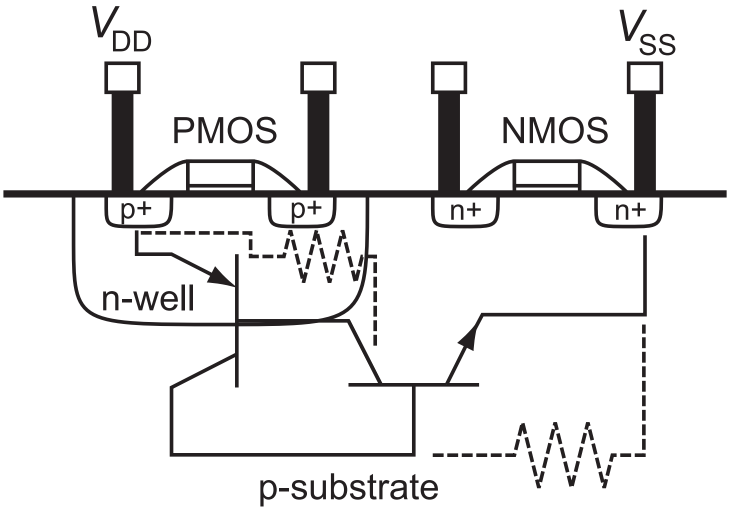

Figure 3.2: Unintended PNPN junction in the CMOS circuit.

To avoid the latch-up, the PN junctions of the transistors should be zero-biased. N-channel MOSFET (NMOS), and P-channel MOSFET(PMOS) are formed on the P-substrate (PSUB) and N-well (NWELL) layers, respectively. Reducing resistances of the PSUB and NWELL is important for the zero-bias. The ring of a number of via holes are placed around MOSFETs as shown in Fig. 3.3 in order to reduce the resistances in layout design stage.

The objective of the present thesis is focused on achieving miniaturized plasma wave receiver with the ASIC. The realizing the ASIC as the system for the receiver is most emphasized than investigating radiation tolerance. Thus, we take the measure of the placing via holes to decrease fear of the latch up, and recognize evaluation of the effectiveness is beyond the scope of this thesis.

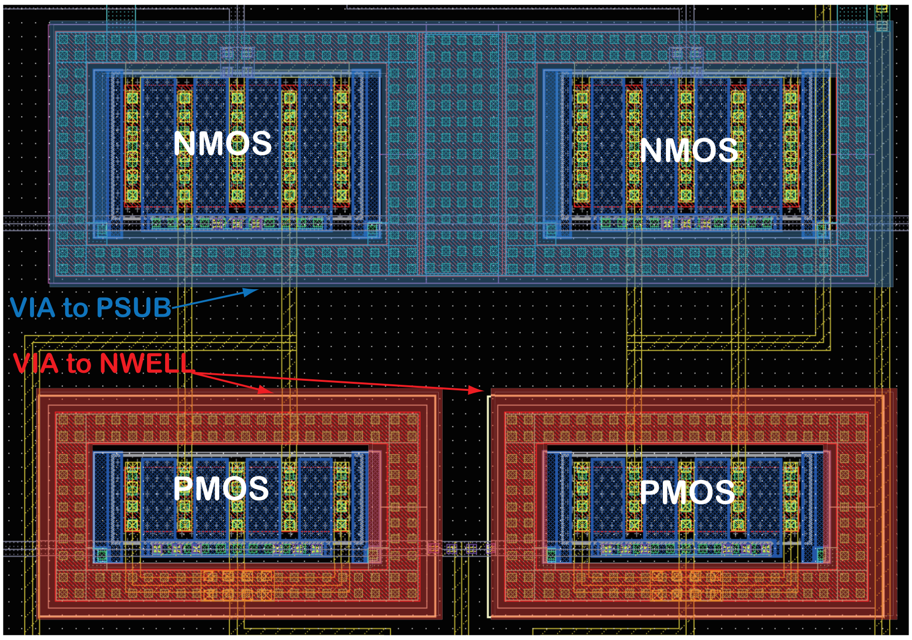

Figure 3.3: Via holes between the bottom metal layer and p-substrate/n-well layer exist in blue/red color areas.

3.3 $\mathrm{G_m}$–C Filters

3.3.1 Fully Differential Band-limiting $\mathrm{G_m}$–C Filter

Since the band-limiting filter ((a) in Fig. 2.4) is the front-end of the waveform receiver, its equivalent input noise should be low enough to observe the output noise at the preamplifier at minimum. We use a $\mathrm{G_m}$–C filter instead of a switched capacitor filter, which is likely to emit switching noise at output. The circuit of the fully differential first-order $\mathrm{G_m}$–C filter is shown in Figure 3.4. The first-order attenuation characteristic is enough for the band-limiting.

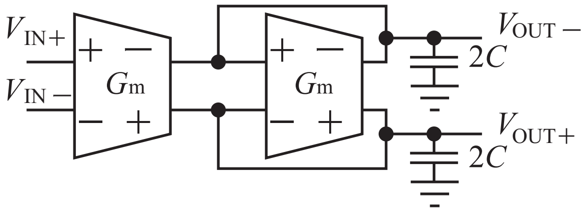

Figure 3.4: Circuit diagram of the first block, fully differential $\mathrm{G_m}$–C low pass filter.

The transfer function $H_{\mathrm{GmC,FD}}(s)$ and cutoff frequency f_{cutoff} of the $\mathrm{G_m}$–C filter are expressed as follows:

$$H_{\mathrm{GmC,FD}}(s) = \frac{V_{\mathrm{OUT+}} - V_{\mathrm{OUT-}}}{V_{\mathrm{IN+}} - V_{\mathrm{IN-}}} \tag{3.1}$$

$$= \frac{\frac{G_{\mathrm{m}}}{C}}{s + \frac{G_{\mathrm{m}}}{C}}, \tag{3.2}$$

$$f_{\mathrm{cutoff}} = \frac{G_{\mathrm{m}}}{2\pi C}, \tag{3.3}$$

where G_{m} is transconductance of the OTA.

The specifications of the first-order $\mathrm{G_m}$–C filter are listed in Table 3.1. The input equivalent noise is should be comparable to the output noise of the preamps, which is approximately 100 nV/$\sqrt{\text{Hz}}$.

Table 3.1: Specifications of the designed first block, fully differential Gm-C low-pass filter.

Order	1st-order
Cutoff Frequency	200 kHz
Input Equivalent Noise	200 nV/$\sqrt{\text{Hz}}$ @100 kHz

The circuit schematic of the OTA is shown in Fig. 3.5. The grounded-source differential-pair with the cascode amplifier and current sources is the main part of the OTA ($\mathrm{M_1}$–$\mathrm{M_{10}}$). The linearized transconductance technique [38] is applied ($\mathrm{M_{11}}$, $\mathrm{M_{12}}$). The other MOSFETs are the biasing circuit. Fully-differential-type circuit should have a common-mode feed back (CMFB) circuit in order to peg the common-mode voltage to the reference voltage V_{CM} of 1.6 V. The circuit schematic of the CMFB is shown in Fig. 3.6. The CMFB circuit is cross-coupled grounded-source differential amplifier. When the average of the $V_{\mathrm{OUT+}}$ and $V_{\mathrm{OUT-}}$ becomes larger than V_{CM}, the currents of $\mathrm{M_9}$ and $\mathrm{M_{10}}$ rise up. These currents flow MOSFET stacks including $\mathrm{M_1}$ and $\mathrm{M_2}$ in Fig. 3.5. Since $\mathrm{M_{7(8)}}$ and $\mathrm{M_{5(6)}}$ compose high-impedance current sources, the currents flowing along $\mathrm{M_{1(2)}}$ are regulated. Then, to cancel the increased currents, voltage at nodes of $V_{\mathrm{OUT+}}$ and $V_{\mathrm{OUT-}}$ decreases as well as at drain node of $\mathrm{M_1}$ and $\mathrm{M_2}$.

The G_{m} of the OTA is indicated by the following equation.

$$G_{\mathrm{m}} = g_{\mathrm{m1}} \frac{2(W/L)_{11}}{(W/L)_1 + 4(W/L)_{11}} \tag{3.4}$$

$$= A\ g_{\mathrm{m1}} \tag{3.5}$$

$$= A\sqrt{2\mu_n C_{\mathrm{ox}} \left(\frac{W}{L}\right)_1 I_{\mathrm{D1}}}, . \tag{3.6}$$

where

$$A = \frac{2(W/L)_{11}}{(W/L)_1 + 4(W/L)_{11}}. \tag{3.7}$$

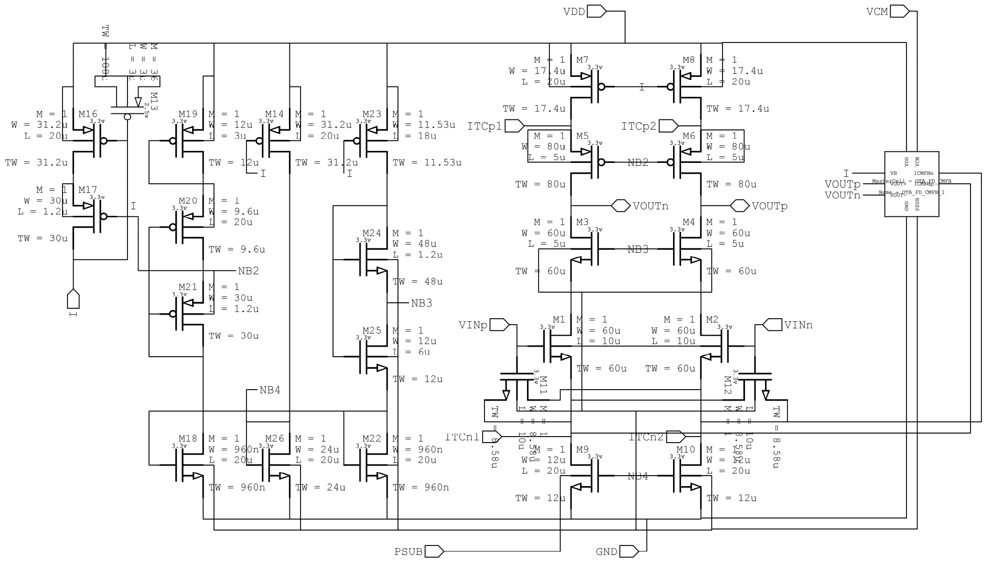

Figure 3.5: Circuit schematic of OTA for the fully differential G_m–C LPF.

μ_n, and $C_{\rm ox}$ are the mobility of electron in n-channel MOSFET, and capacitance per unit area of the oxide film. $(W/L)_1$, and $(W/L)_{11}$ are aspect ratios of M_1, and M_{11} and equal to 60μm/10μm, and 8.58μm/10μm, respectively. $g_{\rm m1}$ (185 μS), and $I_{\rm D1}$ (20μA) are the mutual conductance and drain current of M_1. The values of $G_{\rm m}$ and C are 26 μS and 24 pF, respectively.

Figure 3.7 shows the measurement and simulation results of the differential gain of frequency response of the fully differential G_m–C filter. The gain in pass-band was 0 dB. The cutoff frequency in the measurement results was approximately equal to 181 kHz, 7 kHz lower than the simulation results. The cutoff frequency had variation of 5%. The gradient of the −6 dB/octave was obtained above the cutoff frequency.

The equivalent input noise voltage density is calculated from the gain and output noise of the G_m–C filter. Figure 3.8 shows the measured and simulation results for the equivalent input noise voltage density. The measured result is approximately equal to the simulation result. The noise voltage densities of 600 nV/$\sqrt{\rm Hz}$ at 10 kHz and 200 nV/$\sqrt{\rm Hz}$ at 100 kHz were comparable with the output noise of the preamplifier, i.e., 100 nV/$\sqrt{\rm Hz}$. Spike noises in hundreds of kilohertz did not originate from the G_m–C filter.

The simulated results of the equivalent input noise voltage density at temperature of −30, 25 and 60 °C are shown in Fig. 3.9. There is little variation (< 1 dB) of the equivalent input noise at the temperature range of −30 to 60 °C. From these obtained results, the G_m–C filter is acceptable for the first stage filter of the plasma wave receiver. However, the temperature drift of the cutoff frequency cannot be ignored. The temperature drift and its compensation are described in section 3.4.

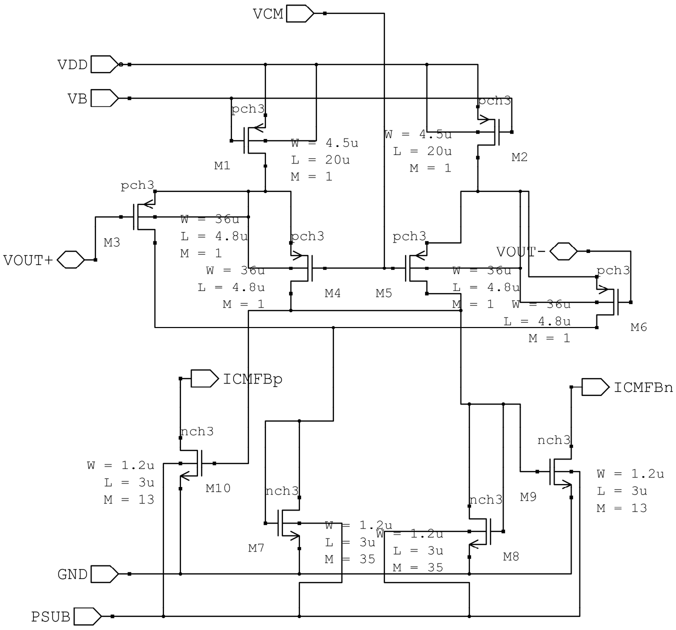

Figure 3.6: Circuit schematic of CMFB of OTA shown in Fig. 3.5.

3.3.2 Single-ended Noise Rejection G_m–C Filters

The single-ended G_m–C LPFs are placed at the third and fifth blocks ((c) and (e) in Fig. 2.4). These G_m–C filters are necessary for noise rejection in relation to the switched capacitor filter. The essence of the switched capacitor technique is charge transfer in discrete time. This means that the switched capacitor circuits sample the continually-changing voltage and the aliasing is caused if input signal exists at higher frequency than half the switching frequency. Saturation in the circuit block placed in front of the switched capacitor could be the one of this reason. Accordingly, anti-aliasing filters for the switched capacitor circuits are needed to be placed before them. The Switched capacitor circuits generate not only aliasing noise but also switching noise. The frequency of the switching noise is equal to the clock frequency multiplied by an integer and is higher than the cutoff frequency of the switched capacitor filter. Without eliminating this switching noise, aliasing could occur in sample-hold and A/D conversion. For eliminating these two noises, the low-pass filter which has sufficient attenuation at half the frequency of the switching frequency is suitable.

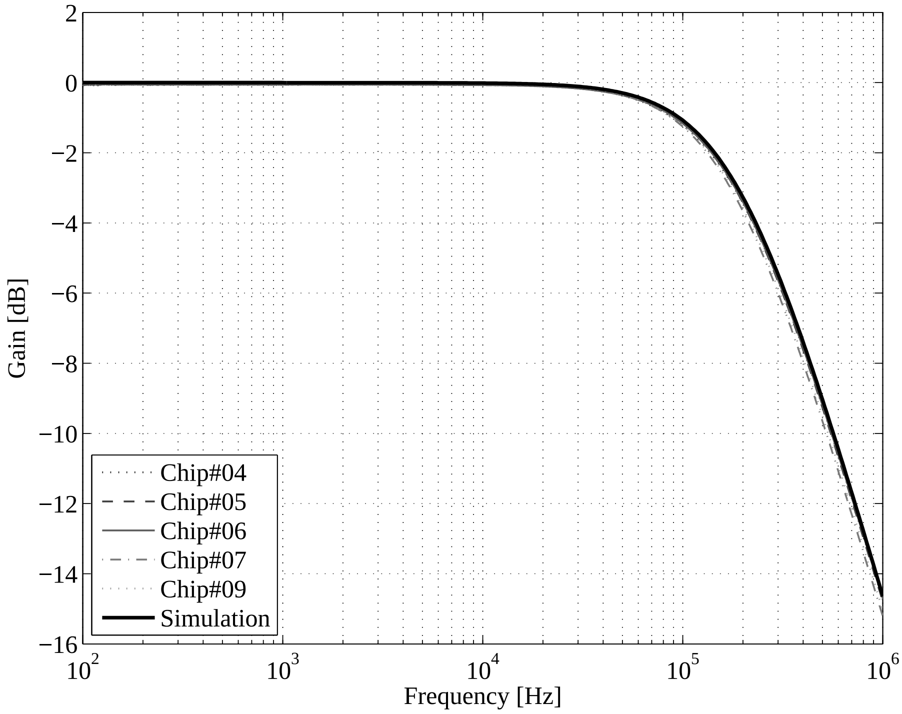

Figure 3.7: Measurement and simulation results of frequency response of differential gain of the fully differential $\mathrm{G_m}$–C filter.

$$H_{\mathrm{GmC,SE}}(s) = \frac{\dfrac{G_{\mathrm{m1}}G_{\mathrm{m2}}}{C_1C_2}}{s^2 + \dfrac{G_{\mathrm{m4}}}{C_2}s + \dfrac{G_{\mathrm{m2}}G_{\mathrm{m3}}}{C_1C_2}}, \tag{3.8}$$

$$f_{\mathrm{cutoff}} = \frac{1}{2\pi}\sqrt{\frac{G_{\mathrm{m2}}G_{\mathrm{m3}}}{C_1C_2}}, \tag{3.9}$$

The circuit diagram and specifications of the single-end second-order $\mathrm{G_m}$–C low-pass filter are shown in Fig. 3.10. The transfer function $H_{\mathrm{GmC,SE}}(s)$ is expressed in Eq. (3.8). All the G_{m} are set to 12 μS. C_1 and C_2 are 8.2, and 3.8 pF, respectively. The cutoff frequency becomes 380 kHz, hence second-order attenuation is suitable for reduction of noises and unwanted signals in the higher frequency band than 5 MHz.

The circuit schematic of the OTA for the single-ended $\mathrm{G_m}$–C filter is shown in Fig. 3.11. This OTA also has the differential pair with cascode amplifier with the biasing circuit. The CMFB circuit is not necessary.

Figure 3.12 shows the measurement and simulation results of frequency response gain of the single-ended $\mathrm{G_m}$–C filter. The -12dB/octave gradient was correctly obtained. The cutoff frequency of the measured responses was around 361 kHz with approximately 5% variations. The simulation results provided 370 kHz cutoff frequency. This error might

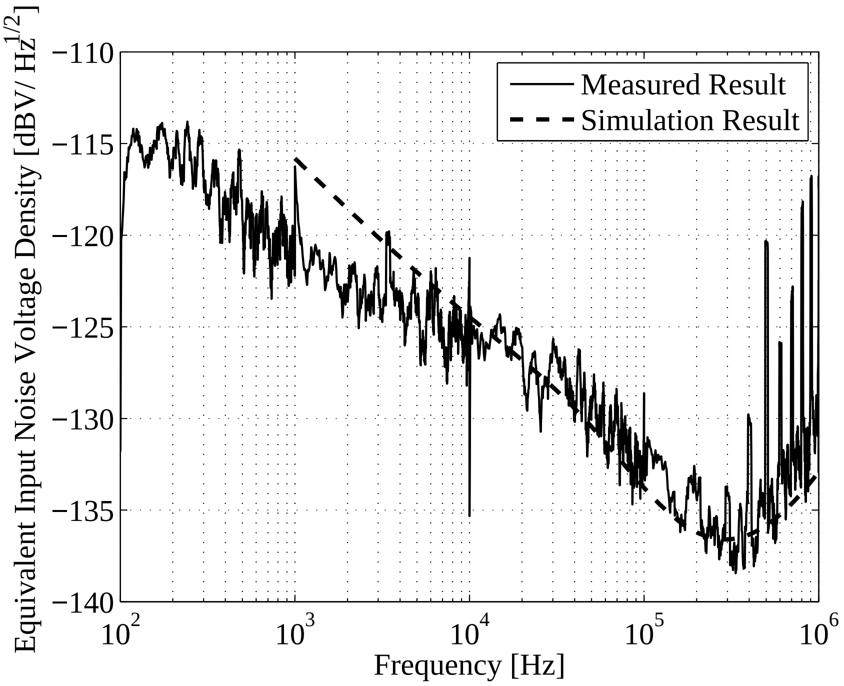

Figure 3.8: Equivalent input noise voltage densities of the fully differential $\mathrm{G_m}$–C filter, obtained from the measurement and simulation.

caused by stray capacitance at connection nodes of the C_1 and C_2.

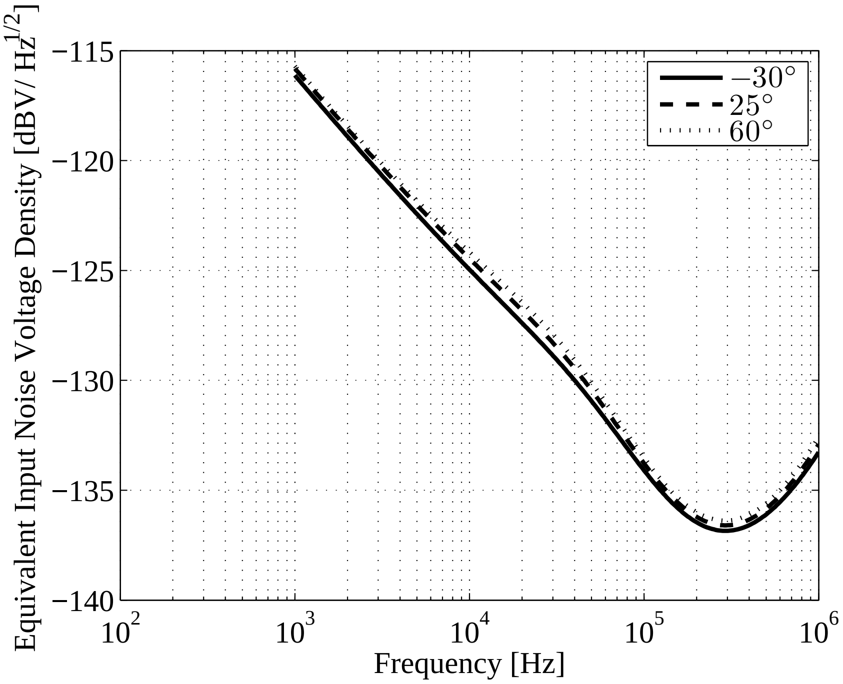

Figure 3.9: Simulation results of the equivalent input noise voltage densities of the fully differential G_m–C filter at the temperature of $-30, 25$, and 60 °C.

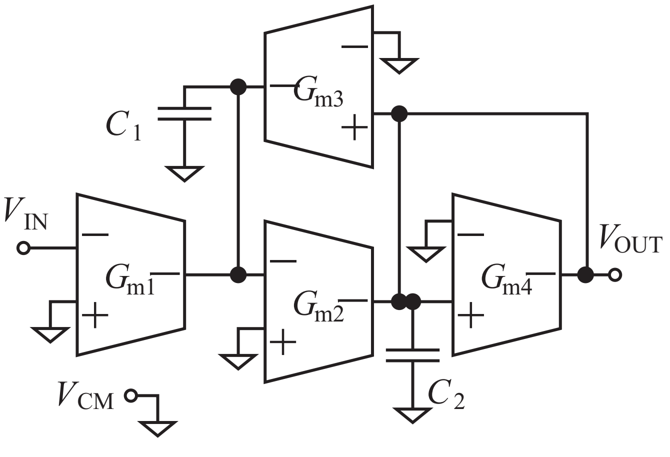

Figure 3.10: Circuit diagram of the single-end second-order G_m–C filter.

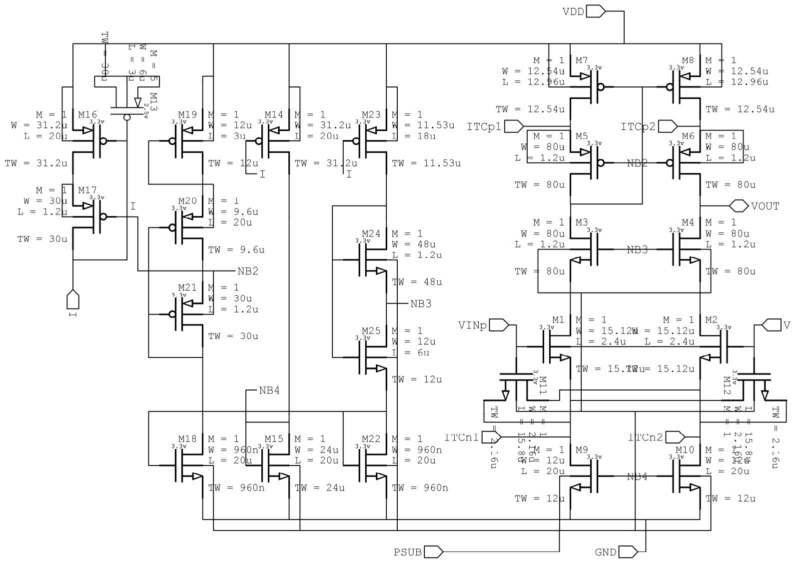

Figure 3.11: Circuit schematic of OTA for the single-ended G_m–C filter.

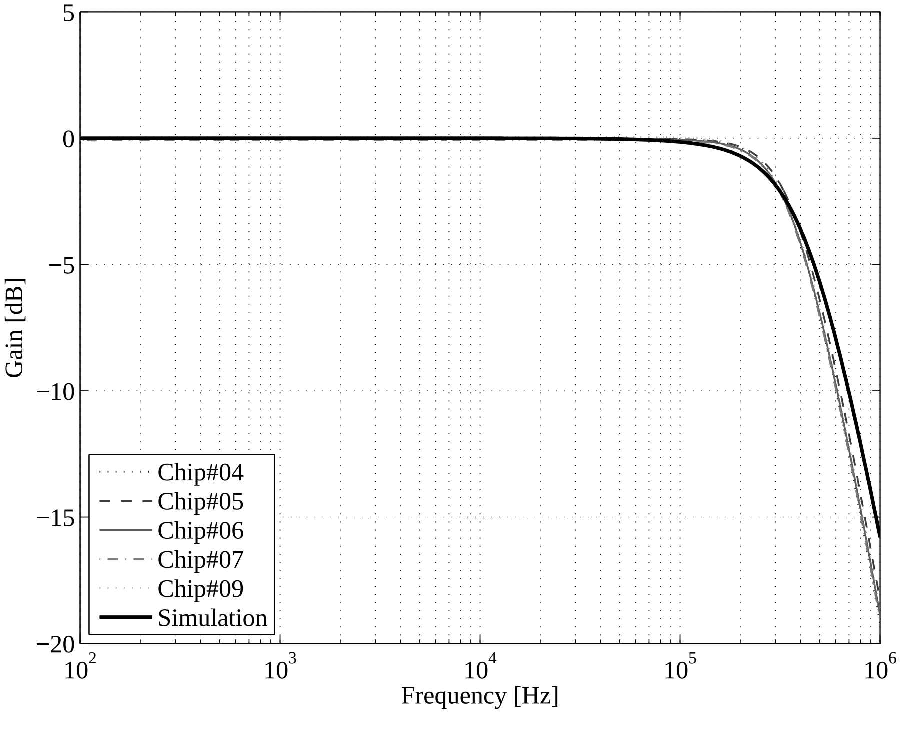

Figure 3.12: Measurement and simulation results of frequency response gain of the single-ended Gm-C filter.

3.4 Temperature Compensation for the $\mathrm{G_m}$–C filters

Circuits described in the present chapter are to be integrated into system chips with the ASIC technology for onboard plasma wave receivers. Each scientific mission requires specified design of the system chip. There has been no report which shows the system chip is employed for plasma wave observation in the space scientific mission.

Temperature on the surface of spacecraft varies greatly according to the presence or absence of sunshine. Thermal design of spacecraft regulates the internal temperature of the spacecraft within a certain range according to its orbit and attitude. The onboard instruments are generally proved to operate in the temperature. The most sensitive circuit against temperature variation in Fig. 2.4 is the $\mathrm{G_m}$–C filters. The characteristic frequency of the $\mathrm{G_m}$–C filter depends on the g_m of the MOSFET which consists $\mathrm{G_m}$–C filter. The g_m has the temperature characteristics because of both temperature characteristics of mobilities of careers (~ -0.5 %/°C), and threshold voltage (~ -1 mV/°C) [39]. Assuming that either of the mobility or threshold voltage dominates the temperature characteristics of the $\mathrm{G_m}$–C filter, the characteristic frequency drift is expected to be more than 10% when temperature of the chip changes several tens of degrees. In the latter part of this section, we focus on the cutoff frequency of the first stage $\mathrm{G_m}$–C filter and describe the temperature compensation circuit with the target range of the cutoff frequency of ±3%, when temperature may change from -30 to 60 °C.

3.4.1 Design Policy

System chip design for scientific spacecraft needs following attention. The trade-off from the attention determines the final design.

1. Stability on radiation and temperature variation in space
2. Power consumption, weight, and size
3. Failure rate
4. Ease of problem recognition in development
5. Ease of multi-production for the same performance (for multi-spacecraft mission)

Although in usage of special purpose system chip on Earth, the stability mentioned above may set up, the stability in space relates closely with the requirement 2. For radiation, it is possible to care the layout in the system chip and to shield the chip partially. On the other hand, stability on temperature variation is difficult to be controlled completely though thermal design and temperature control by a heater can contribute to the stability. In fact, guaranteed operating temperature range for instruments onboard scientific spacecraft is generally set from −30 to +60 °C. to obtain data with stable accuracy, the $\mathrm{G_m}$–C filter described in this thesis needs temperature compensation.

The requirements 3 and 4 are especially important for space missions. After launching, the failure of the space system is impossible to be fixed by direct handling. Thus, the system chips which passed screening should work with very high reliability. For consumer devices, yield ratio for mass-production is also essential. In other words, uniform performance of a number of chips needs to be considered. On the other hand, the system chip does not uniform performance for space applications. Then, we choose a suitable circuit topology for space applications without consideration of uniform performance.

Besides, the requirement 4 is the extra important point of view. Unlike the consumer chip which is upgraded frequently for improvement, the system chip for space applications has very few chances to develop or upgrade. Thus, the circuit topology which makes clear many problem in developing and enhances the final performances should be preferred.

In case of multi-spacecraft with formation flight mission, the requirement 5 is significant since identical instruments are installed on the spacecraft. The process flow increases when the multiple instruments are concurrently developed, then the scheme which facilitate the concurrent development of multiple instruments needs to be established.

In brief, the circuit topology should be simple and provide good quality of data for science target ignoring the yield ratio.

With this point, we designed and developed the temperature compensated $\mathrm{G_m}$–C filter for the scientific instrument onboard satellite, then evaluated the temperature characteristics. Generally, $\mathrm{G_m}$–C filters exhibit temperature drift and distributed characteristics frequency. There are several ways to compensate for these variations [40]. Complex circuits increase the circuit scale and the probability of failures. We herein choose a simple method by which to compensate for temperature drift, ignoring the improvement in the accuracy of manufacturing. For example, G_{m} which is equal to the inverse of the external register is realized for the temperature compensation. Alternatively, clock signal can accurately maintain the characteristic frequency of the $\mathrm{G_m}$–C filter [38, 41]. These methods enable to compensate not only the temperature characteristics but also the process variation. However, temperature of the external resistor is not always the same as the that in the system chip, or the clock signal could contaminate the output of the $\mathrm{G_m}$–C filter. In addition, although the latter method could accurately compensate the characteristics in the wide temperature range, the circuit could become complex. We adopted another method for these reasons.

3.4.2 Compensation Scheme

Band-gap reference technique and proportional to absolute temperature (PTAT) current source are commonly known as techniques to produce reference voltage and current which

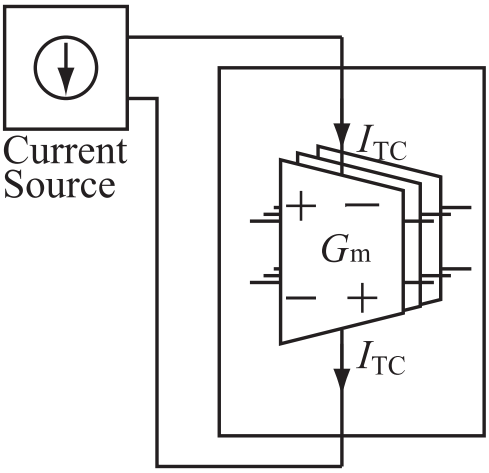

Figure 3.13: The temperature compensation current source I_{TC} is fed to OTAs which consist of the G$_{\mathrm{m}}$–C filter.

have less sensitivity for temperature [42]. *Agawa et al.* proposed the compensation method for sensitivity of the CMOS Bluetooth receiver by using the current source with piecewise-linear temperature characteristics [43]. This method is simpler than other methods with reference signals. Besides, since the first G$_{\mathrm{m}}$–C filter is placed as a front-end of the plasma wave receiver, the G$_{\mathrm{m}}$–C filter should be low noise. We apply the current source with the piecewise-linear temperature characteristics for compensation of the cutoff frequency of the G$_{\mathrm{m}}$–C filters. The transconductance of the OTA depends on the current which flows in the differential pair. The compensation currents I_{TC} are fed to the OTAs, as shown in Figure 3.13. Then, the temperature dependence of the G_{m} , and characteristics of the G$_{\mathrm{m}}$–C filter are compensated.

3.4.3 Temperature Compensation Current Source

Figure 3.14 shows the circuit of the PTAT current source. The PTAT current I_{PTAT} is expressed as follows:

$$I_{\mathrm{PTAT}} = \frac{1}{R}\frac{k_B T}{q}\ln n = \alpha T \qquad (3.10)$$

$$\alpha = \frac{1}{R}\frac{k_B}{q}\ln n \qquad (3.11)$$

k_B, q, T, and n are the Boltzmann constant (1.3802×10^{-23} J/K), charge of an electron (1.602×10^{-19} C), absolute temperature, and ratio of the number of PNP transistor in Fig. 3.14, respectively. R is resistor of paralleled the poly-silicon resistor inside the chip R_{poly} and the external resistor to adjust α described in the following paragraph.

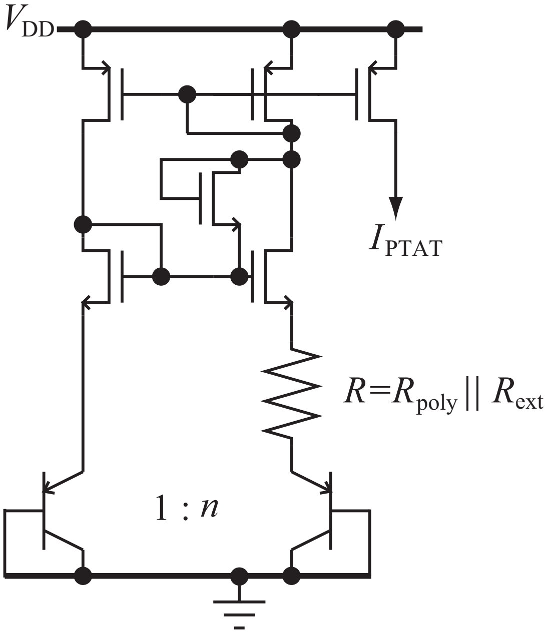

Figure 3.14: Circuit schematic of PTAT current source.

The current source with the piecewise-linear temperature characteristics consists of two constant and two PTAT current sources. Figure 3.15 shows the combined circuit of the PTAT current source with a constant current source to obtain the current I_{pl}. The current has the temperature characteristics shown in Eq. (3.12).

$$I_{\mathrm{pl}} = \begin{cases} 0 & (T \leq T_{\mathrm{b}}) \\ \alpha(T - T_{\mathrm{b}}) & (T > T_{\mathrm{b}}), \end{cases} \tag{3.12}$$

where T_{b} is equal to $I_{\mathrm{const}}/\alpha$, and R_{bias} is the resister to feed the bias current to the system chip.

Figure 3.16 shows the circuit diagram of the temperature compensation circuit. The currents I_{pl1} and I_{pl2} are generated by subtracting the constant currents I_{const1} and I_{const2} from I_{PTAT}, respectively. Then, I_{TC} is obtained and expressed in the following equation.

$$I_{\mathrm{TC}} = K_0(K_1 I_{\mathrm{pl1}} + K_2 I_{\mathrm{pl2}}) = \begin{cases} 0 & (T \leq T_{\mathrm{b1}}) \\ K_0 K_1 \alpha_1 (T - T_{\mathrm{b1}}) & (T_{\mathrm{b1}} < T \leq T_{\mathrm{b2}}) \\ K_0 K_1 \alpha_1 (T - T_{\mathrm{b1}}) + K_0 K_2 \alpha_2 (T - T_{\mathrm{b2}}) & (T > T_{\mathrm{b2}}), \end{cases} \tag{3.13}$$

where, $K_{0,1,2}$ are constant, $\alpha_{1,2}$ are temperature coefficients of the PTAT currents corresponding to $I_{\mathrm{const1,2}}$. $T_{\mathrm{b1,2}}$ are equal to $I_{\mathrm{const1,2}}/\alpha_{1,2}$, respectively. $\alpha_{1,2}$ can be adjusted by the external resistors $R_{\mathrm{ext1,2}}$. Temperature compensation current I_{TC} has the temperature characteristics as shown in Fig. 3.17. The couple of resistances in the graph legend

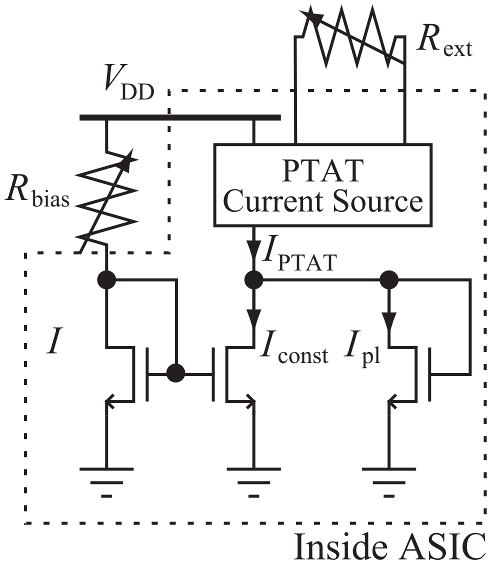

Figure 3.15: Circuit to generate I_{pl} which has piecewise-linear temperature characteristics.

correspond to R_{ext1}, and R_{ext2}. Metal coating resistor of 100 kΩ are used for R_{ext1}, and R_{ext2}. R_{poly1} and R_{poly2} are 2.33 kΩ. T_{b1}, T_{b2}, I_{const1}, and I_{const2} are set to −75°C, 50°C, 8.8 μA, 13.5 μA. K_0, K_1, and K_2 are 0.59, 3.3, and 0.30, respectively.

3.4.4 Implementation

Design for Compensation

The target compensation result is less than 3 % of the average cutoff frequency. Although we chose 1st-order G_m–C filter as the compensated target for simplicity as shown in Fig. 3.18, the method presented here can be applied in case of the higher-order filters. I_{TC} is the current from the temperature compensation circuit. I_{D1} is equal to sum of I_{TC} and I_{bias}.

The G_{m} of the OTA is expressed in Eq. (3.6). Differentiating G_{m} with respect to absolute temperature T, we can obtain following equations.

$$\frac{dG_{\text{m}}}{dT} = \frac{\partial G_{\text{m}}}{\partial \mu_n}\frac{\partial \mu_n}{\partial T} + \frac{\partial G_{\text{m}}}{\partial I_{\text{D1}}}\frac{\partial I_{\text{D1}}}{\partial T} \tag{3.14}$$

$$= \frac{G_{\text{m}}}{2\mu_n}\frac{\partial \mu_n}{\partial T} + \frac{G_{\text{m}}}{2I_{\text{D1}}}\frac{\partial I_{\text{D1}}}{\partial T} \tag{3.15}$$

$$= \frac{G_{\text{m}}}{2}\left\{\frac{1}{\mu_n}\frac{\partial \mu_n}{\partial T} + \frac{1}{I_{\text{D1}}}\left(\frac{\partial I_{\text{TC}}}{\partial T} + \frac{\partial I_{\text{bias}}}{\partial T}\right)\right\}. \tag{3.16}$$

In general, $(\partial \mu_n/\partial T)/\mu_n < 0$, I_{TC}, which has appropriate $\partial I_{\text{TC}}/\partial T$ to cancel the temperature characteristics of μ_n and I_{bias}, decreases the temperature coefficient of $G_{\text{m}} \propto$

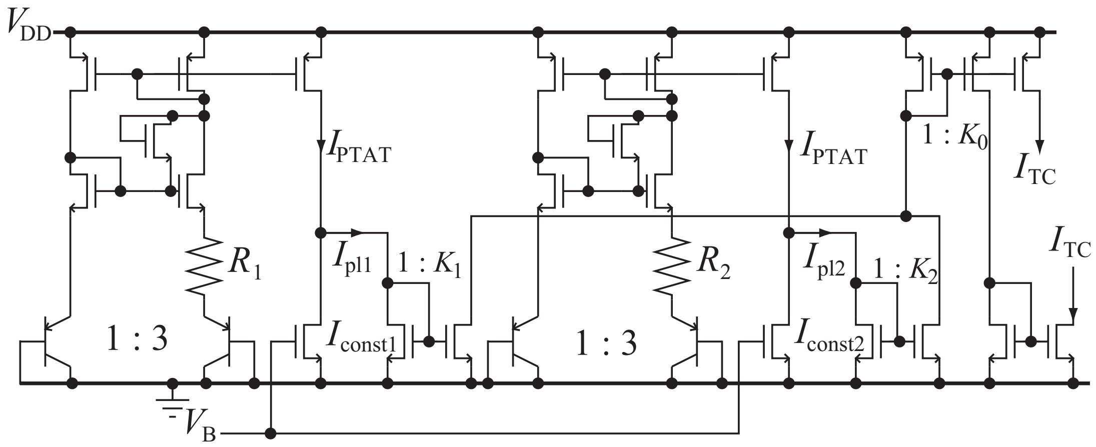

Figure 3.16: Circuit schematic to generate current I_{TC}.

f_{cutoff}.

Experimental Results

Here, the temperature dependence of the cutoff frequency with or without the compensation. After manufacturing, the frequency response gain of the first-order G_m–C LPF was measured as shown in Fig. 3.7. We tested the temperature dependence of the G_m–C filter by placing the packaged ASIC and the measuring board which has a socket for the package in the constant temperature reservoir. We defined the surface of the package as the temperature of the chip. The temperature is set from −30 to 60 °C. To decouple parasitic capacitors caused by the measurement system and bonding wires from the G_m–C LPF, the low-impedance buffer amplifier is dedicated to the output of the G_m–C LPF. We confirmed the temperature dependence of the frequency response of the buffer amplifier can be ignored.

We compare the temperature characteristics of the cutoff frequency with the compensation circuit to the result without the circuit ($I_{TC} = 0$). In Fig. 3.19, the vertical axis indicates relative value with respect to the cutoff frequency measured in room temperature (25 °C). In the case of $I_{TC} = 0$, the drain current I_{D1} equals to the bias current I_{bias} which has the negative temperature coefficient. Hence, the cutoff frequency also showed the negative temperature coefficient. On the other hand, the compensated result showed that the positive temperature coefficient and narrow variation range can be confirmed. This results means the designed temperature compensation circuit operates in the chip.

Figures 3.20 and 3.21 are the comparisons of the relative and absolute cutoff frequencies of measurement and simulation results for each process corner (Slow, Fast, and Typical). The corners of the Slow means all the MOSFETs in the circuits operate with the largest

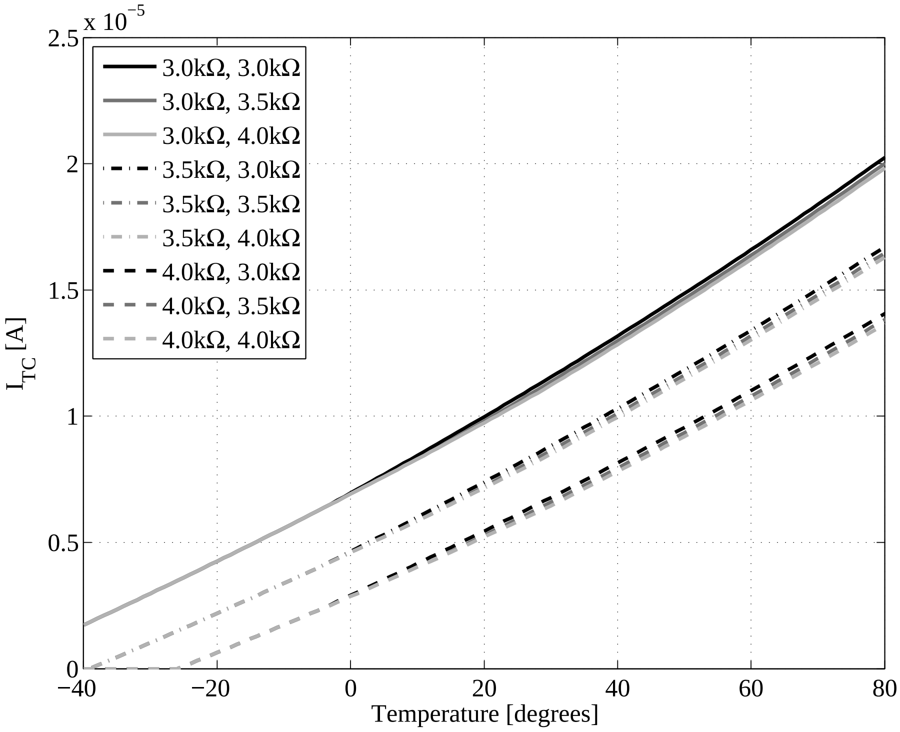

Figure 3.17: Characteristics of I_{TC} versus temperature with combinations of R_{ext1} and R_{ext2}.

threshold voltage and the smallest mobility that the fabrication process might provide. The Fast corner is the opposite case of the Slow.

Discussion

In Fig. 3.20, the cutoff frequency of simulated result is controlled within ±1% in the Fast and Typical cases. In the worst case (Slow), the cutoff frequency changes from −2 to +4 % in respect to the room temperature (25°c) cutoff frequency. By contrast, the

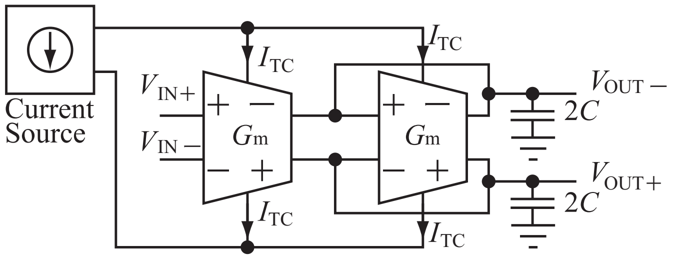

Figure 3.18: Fully differential first-order G_m–C LPF with current source for temperature compensation.

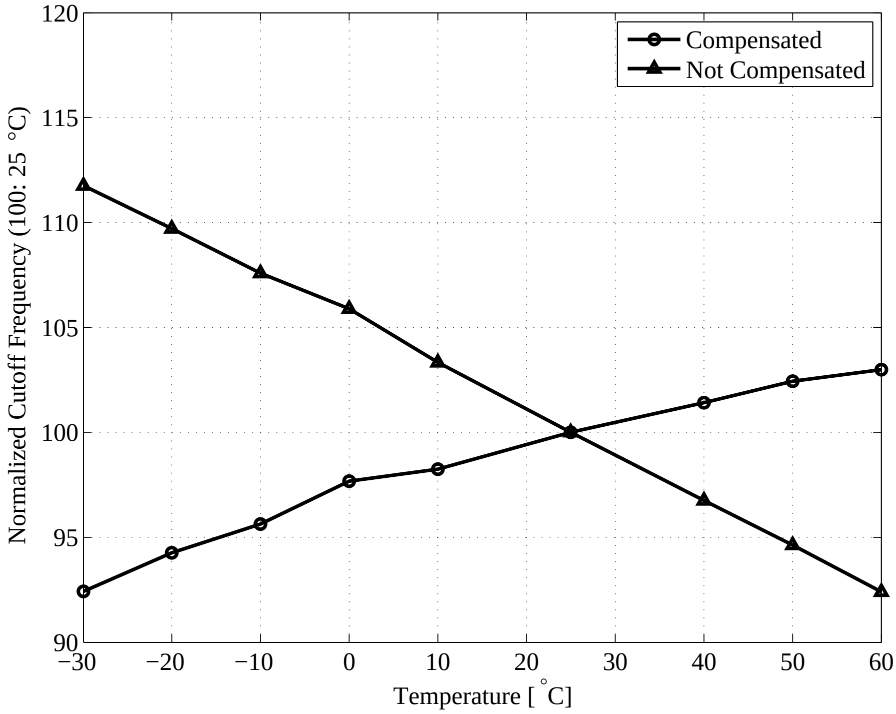

Figure 3.19: Measured temperature dependence of the cutoff frequency of $\mathrm{G_m}$–C LPF with the compensation circuits compared with that of the $\mathrm{G_m}$–C LPF without the compensation circuit.

measured result showed the variation becomes larger than any simulation results in the lower temperature range; −6 % at −30°C. In the higher temperature range, the measured cutoff frequency also larger than the Typical and Fast cases; +3% at 60°C.

The measured absolute values of the cutoff frequency exist between simulated results of the Slow and Typical cases. The Fast case result is higher than others. The measured cutoff frequency is different from the any simulation results. When the T_{b1} becomes low, the larger I_{TC} is obtained with increase of the temperature dependence. This could lead transition of the operating point of the MOSFET $\mathrm{M_1}$ into the triode region. Thus, the cutoff frequency is low because g_{m1} is less than $\sqrt{2\mu_n C_{\mathrm{ox}}(W/L)_1 I_{\mathrm{D1}}}$ in the triode region. In brief, increase of compensation current I_{TC}, caused by mismatching in layout design, displaces the operation point of $\mathrm{M_1}$. The temperature characteristics of the cutoff frequency deteriorates as well as reduction of the G_{m} . Although the accuracy of the compensation has to be improved, the compensation method itself is effective for $\mathrm{G_m}$–C LPF of the plasma wave receiver. The temperature dependence of the cutoff frequency was compensated within the target range of ±3% in the temperature range of −10 to 60 °C. Compensation in the temperature range less than −10°C is possible by applying high-accuracy current mirror to the circuit to generate I_{TC}.

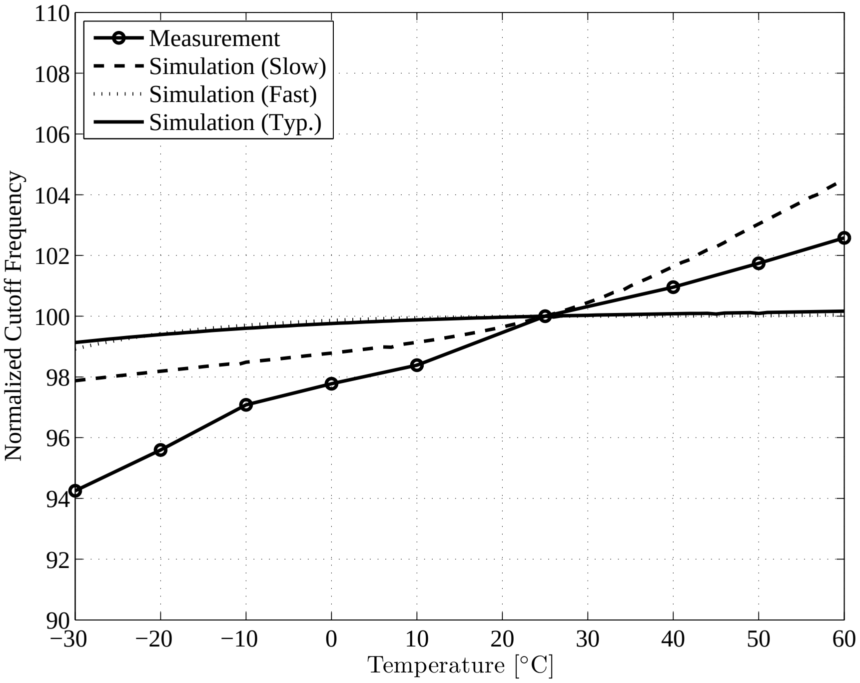

Figure 3.20: Relative temperature dependence of cutoff frequencies of the measurement and simulation results.

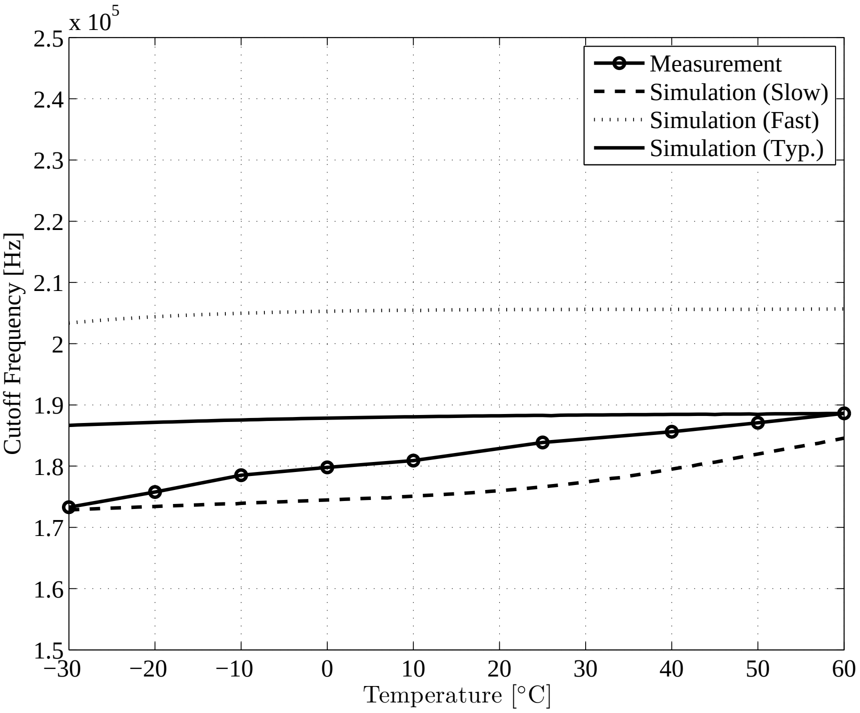

Figure 3.21: Temperature dependence of cutoff frequencies of the measurement and simulation results.

3.5 Differential Amplifier

The required gain of the receiver depends on the antenna sensitivity as well as the intensities of target plasma waves. However, a maximum gain of 40 dB is typically sufficient for use in space missions. Furthermore, the changeable gain function is necessary in order to cover the wide dynamic range of plasma waves. The differential amplifier ((b) shown in Fig. 2.4) takes the role of not only differential but also large gain amplification in the waveform receiver.

In the present thesis, we combine the differential amplifier circuit of 0 dB gain and the non-inverting amplifier circuit with three steps of gain: 0, 20, and 40 dB. Figure 3.22 shows the circuit diagram of the overall differential amplifier. The circuit of OP1 and the resistors R_1 and R_2 composes the differential amplifier. The OP2 and the resistors R_3 and R_4 are the non-inverting amplifier.

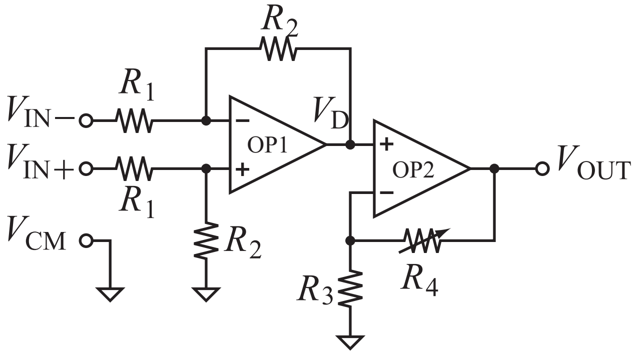

Figure 3.22: Circuit diagram of the main amplifier.

Assuming the OP1 and OP2 are ideal Op-Amp, the relations of the node are expressed in following equations.

$$\frac{V_{\mathrm{D}}}{V_{\mathrm{IN+}} - V_{\mathrm{IN-}}} = \frac{R_2}{R_1} \tag{3.17}$$

$$\frac{V_{\mathrm{OUT}}}{V_{\mathrm{D}}} = 1 + \frac{R_4}{R_3} \tag{3.18}$$

The resistance ratio should be approximately equal to 10^2 to realize the gain of 40 dB. In the differential amplifier circuit, a couple of the same resistance is needed to obtain good common-mode rejection ratio, so-called CMRR. If the differential amplifier circuit has gain of 40 dB, the double large resistances are to be applied. Combining the non-inverting amplifier circuit with the high gain enables the couple of resistances of the differential amplifier circuit to be as small as the other resistances.

We designed two Op-Amps, OP1 and OP2, for the overall differential amplifier. Figure 3.23 is the circuit schematic of the Op-Amp of used in the differential amplifier circuit.

The Op-Amp consists of the differential pair, biasing circuit, the folded-cascode structure, and two stage amplifier with phase compensation. The capacitance for the phase compensation is 2.5 pF by metal-insulator-metal capacitor (MIMCAP). The current which flows the MOSFETs for secondary amplifying is 305 μA in order to obtain low output impedance.

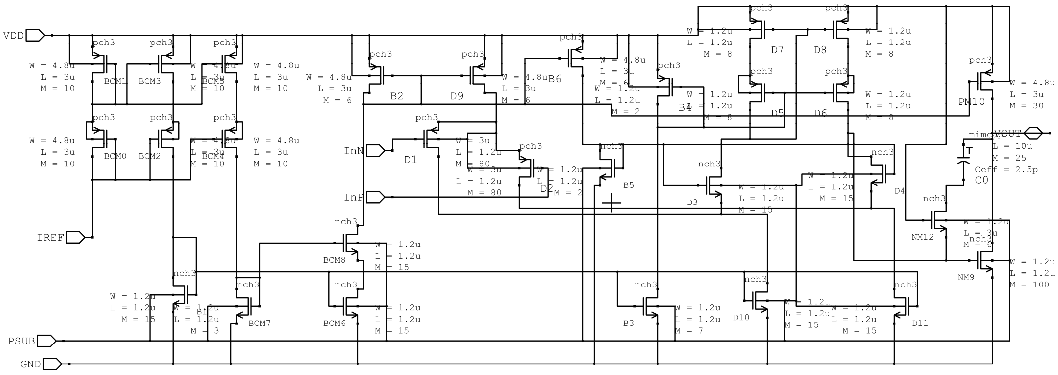

Figure 3.23: Circuit schematic of the OP1.

The gain of the Op-Amp is simulated and shown in Fig. 3.25. The DC gain is approximately equal to 118 dB because of the high impedance of the cascode and the secondary amplifying. The gain bandwidth (GBW) is 28 MHz.

In order to realize the gain of 40 dB in the frequency range up to 100 kHz, the larger GBW is necessary than the Op-Amp shown in Fig. 3.23. The GBW of 28 MHz was caused by the secondary amplifying. The large GBW Op-Amp was designed by *Okada* for the high gain amplifier without gain switching [44]. The circuit schematic of the large GBW Op-Amp is shown in Fig. 3.25. Only the folded-cascode structure is applied in order to obtain both of high DC gain and large GBW. The folded-cascode brings about the high gain and GBW by multiplying the output impedance by $g_{\mathrm{m}} r_{\mathrm{o}} (\sim 30)$, where r_{o} is the output impedance of a MOSFET. Thus, the output impedance of this Op-Amp becomes as high as 37 MΩ. The gain of the frequency response is shown in Fig. 3.26. The DC gain and GBW are 79 dB and 600 MHz, respectively. Equation (3.18) is needed to be modified because of the non-ideality of the Op-Amp.

$$\frac{V_{\mathrm{OUT}}}{V_{\mathrm{D}}} = \frac{1}{\dfrac{1}{A_{\mathrm{DC,OP2}}} + \dfrac{\dfrac{R_{\mathrm{O}}}{A_{\mathrm{DC,OP2}}} + R_3}{R_3 + R_4}} \quad , \tag{3.19}$$

where the $R_{\mathrm{O}} = 37$ MΩ and $A_{\mathrm{DC,OP2}} = 79$ dB are the output impedance and gain of the OP2 on DC operation, respectively.

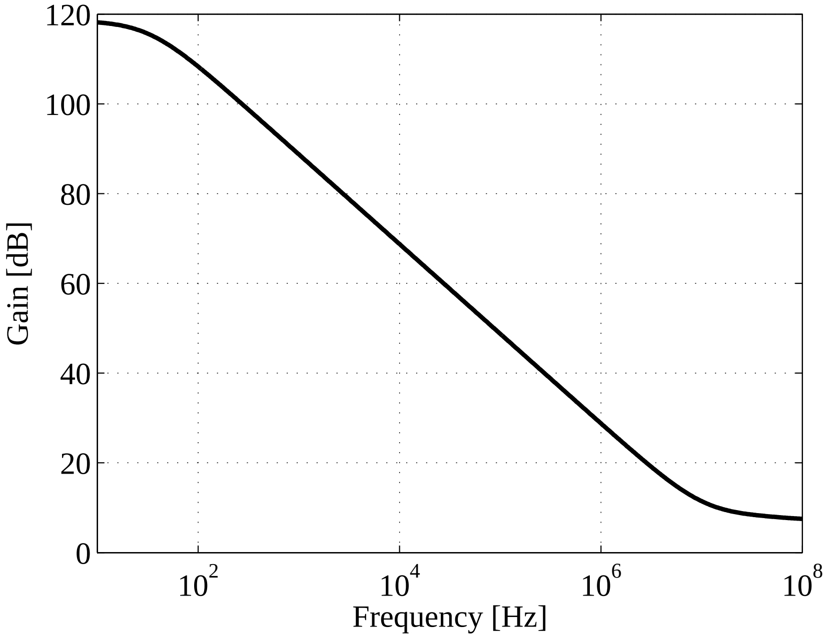

Figure 3.24: Simulated gain of the frequency response of the Op-amp for the differential amplifier circuit.

All the resistances of the R_1 and R_2 are set to 25 kΩ for the 0 dB differential gain. R_3 is 0.63 kΩ. The variable resistor R_4 is realized series resistors and two switches as shown in Fig. 3.27. The resistances of R_{41} to R_{43} are decided according to Eq. (3.19) and become 4×10^2, 42, and 1.3 kΩ, respectively. CMOS switches, paralleled PMOS and NMOS, are used for the switches to assure the triode region operation for either of the MOSFET in wide voltage range. The switch turns on when gate voltages of NMOS and PMOS become V_{DD} and ground level though the not negligible on-resistance of the switch exists and is approximately equal to 3 kΩ. The low on-resistance MOS switch increases the capacitances in related to the gate node, which could affect the bandwidth of the amplifier circuit. Then, we reduce the capacitance with considering not negligible of the on-resistance. The gain setting is correspond to the switch configuration as shown in Table 3.2.

A number of polycrystal silicon (polysilicon) resistors connected in series are used for the resistors in the differential and the non-inverting amplifier circuits. The highest sheet resistance and least sensitivity for the temperature and voltage are available by applying n-diffusion polysilicon without self-aligned silicide (salicide). This type of resistance, width, length, and number of series element of the resistances are shown in Table 3.3, where W and L are width and length of the resistor element inside the ASIC, respectively.

Figure 3.28 shows the measurement results of the overall differential amplifier. The

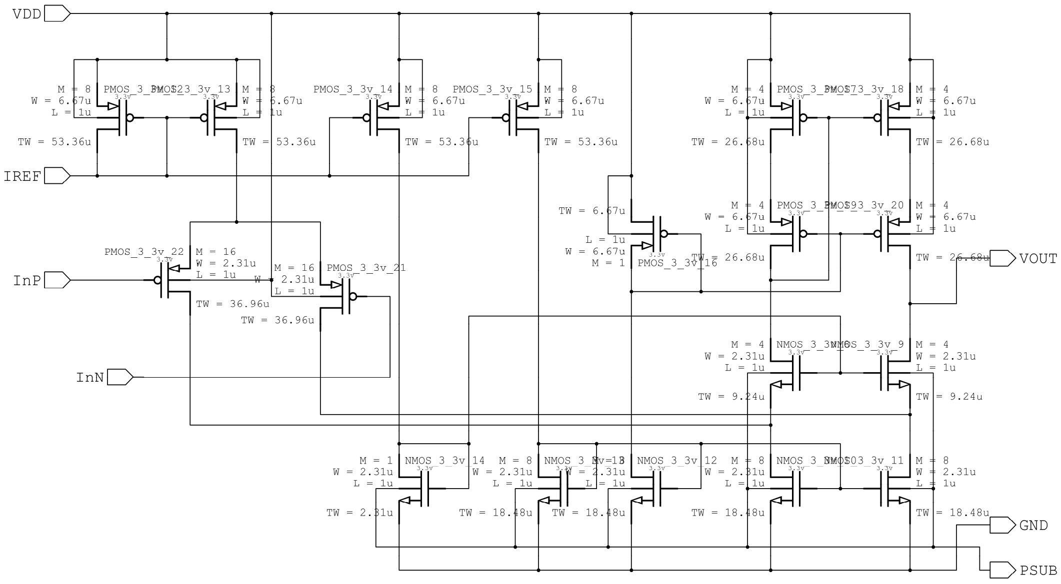

Figure 3.25: Circuit schematic of the OP2.

Table 3.2: Correspondence of the gain to switch configuration.

S_1	S_2	Gain [dB]
OFF	OFF	40
ON	OFF	20
OFF	ON	(0, Not in use)
ON	ON	0

dotted, broken and solid lines are the gain of frequency response for the settings of 0, 20, and 40 dB, respectively. The each passband gain has the error of around −3 dB. The bandwidth for the 40 dB setting is equal to 100 kHz. Local maximal of the gain appears in the response at 4 to 5 MHz.

We assume that the gain of the differential amplifier A_v has the relative error of ΔA_v. From Eq. (3.19), the ΔA_v can be expressed in the following equation.

$$\begin{aligned} \Delta A_v &= \frac{\Delta A_{\mathrm{DC,OP2}}}{A_v}\frac{\partial A_v}{\partial A_{\mathrm{DC,OP2}}} + \frac{\Delta R_{\mathrm{O}}}{A_v}\frac{\partial A_v}{\partial R_{\mathrm{O}}} + \frac{\Delta R_3}{A_v}\frac{\partial A_v}{\partial R_3} + \frac{\Delta R_4}{A_v}\frac{\partial A_v}{\partial R_4} \qquad (3.20) \\ &= \Delta A_{v,A_{\mathrm{DC,OP2}}} + \Delta A_{v,R_{\mathrm{O}}} + \Delta A_{v,R_3} + \Delta A_{v,R_4}. \qquad (3.21) \end{aligned}$$

Each term in Eq. (3.21) is calculated as follows:

$$\frac{\Delta A_{v,A_{\mathrm{DC,OP2}}}}{\Delta A_{\mathrm{DC,OP2}}} = \frac{-1}{A_{\mathrm{DC,OP2}} + \dfrac{R_3}{R_{\mathrm{O}} + R_3 + R_4}}, \qquad (3.22)$$

$$\frac{\Delta A_{v,R_{\mathrm{O}}}}{\Delta R_{\mathrm{O}}} = \frac{1}{R_{\mathrm{O}} + (A_{\mathrm{DC,OP2}} + 1)R_3 + R_4}, \qquad (3.23)$$

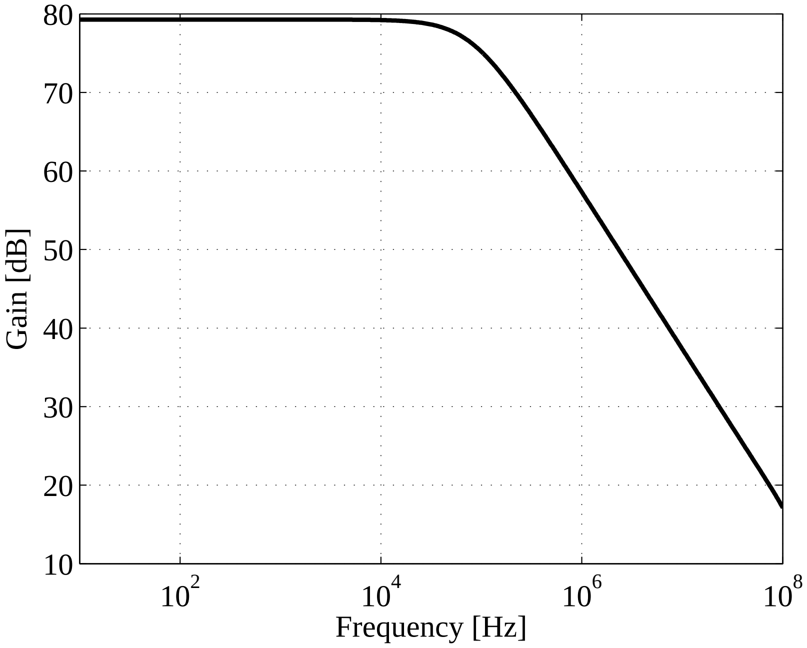

Figure 3.26: Simulated gain of the frequency response of the Op-amp for the non-inverting amplifier for high gain.

$$\frac{\Delta A_{v,R_3}}{\Delta R_3} = \frac{1}{R_3+R_4}\frac{\dfrac{R_\mathrm{O}}{A_\mathrm{DC,OP2}} - R_4}{R_3 + \dfrac{R_\mathrm{O}+R_3+R_4}{A_\mathrm{DC,OP2}}}, \tag{3.24}$$

$$\frac{\Delta A_{v,R_4}}{\Delta R_4} = \frac{-1}{R_3+R_4}\frac{\dfrac{R_\mathrm{O}}{A_\mathrm{DC,OP2}} + R_3}{R_3 + \dfrac{R_\mathrm{O}+R_3+R_4}{A_\mathrm{DC,OP2}}}. \tag{3.25}$$

The R_3 is negligibly-small compared with R_O. For all the gain settings, R_4 is much smaller

Table 3.3: Type of the resistance, width, length, number of series element of the resistors for the differential amplifier.

Resistor	Type	W [μm]	L [μm]	Number of series element	Total Resistance [kΩ]
R_1 R_2	N+ Poly. w/o Salicide	2.00	17.36	16	25
R_3	N+ Poly. w/o Salicide	3.00	10.71	10	0.63
R_{41}		3.00	10.60	632	4.0 $\times 10^2$
R_{42}		3.00	10.60	66	42
R_{43}		3.00	10.60	2	1.3

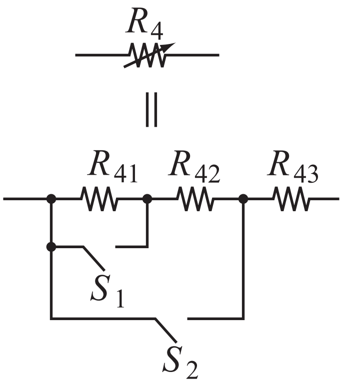

Figure 3.27: Resistors for gain switching of the main amplifiers.

than R_O, and $(A_{DC,OP2} + 1)R_3$. Then, the values of Eqs. (3.22) and (3.23) are constant with R_4. In contrast, the values in Eqs. (3.24) and (3.25) obviously depend on R_4. Thus, the passband gain obtained in all the gain setting could be caused by the error of the DC gain and output impedance of Op-Amp. Table 3.4 shows the calculated gain of the differential amplifier according to Eq. (3.19). When either of $A_{DC,OP2}$ or R_O has an error from the simulation result, the gain of the measured result can be obtained.

Table 3.4: Gains of the differential amplifier under different conditions of the internal Op-Amp.

$A_{DC,OP2}$ [dB]	R_O [MΩ]	Low Gain [dB]	Medium Gain [dB]	High Gain [dB]
78	37	−0.61	19.0	38.4
76	37	−2.39	17.2	36.6
78	47	−2.46	17.1	36.6

Okada reported the bandwidth for the 40 dB gain narrows down to around 100 kHz because of parasitic capacitances at each node of the non-inverting amplifier circuit [44]. As a result, the total passband gain of the waveform receiver would slightly be decreased for the high gain setting. The local maximum gain is caused by the zero and second pole of the OP1. This emphasis is to be suppressed in the next filters. Since these problems cannot be critical problems, the performances of the differential amplifier is acceptable.

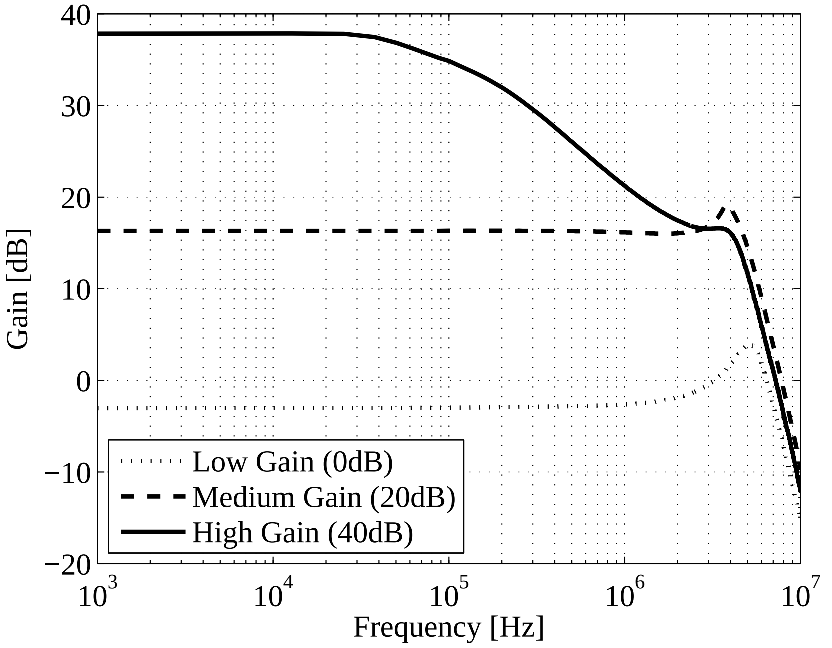

Figure 3.28: Measured results of the frequency response gains of the overall differential amplifier.

3.6 Switched Capacitor LPF

Anti-aliasing filter ((d) in Fig. 2.4) is the very critical component for the waveform receiver because of the requirement for the dynamic range. The observation bandwidth, sampling frequency and the dynamic range of the A/D converter determine the required frequency response for the anti-aliasing filter. As described in the previous section, the observation bandwidth, sampling frequency and the dynamic range are 100 kHz, 400 kHz, and 78 dB, respectively. Then, the lowest frequency which engages with aliasing is 300 kHz. In brief, flat passband response up to 100kHz and 78 dB attenuation at 300 kHz must be realized in the anti-aliasing filter.

The sixth-order Chebyshev filter yields an attenuation of 79 dB at 300 kHz. The effective bit of the resolution satisfies the requirement. Thus, we apply a sixth-order Chebyshev-type filter for the anti-aliasing filter.

The switched capacitor technique deals with continuous physical quantity in discrete-time. The first switched capacitor filter was implemented with FET gates, capacitors, and timing signals [45]. Combinations of amplifiers, such as a current multiplier and Op-Amp, widely extended potential applications of the switched capacitor technique [46, 47, 48, 49]. Since the relative accuracy between adjacent two capacitances in ICs is better than the absolute accuracy of each capacitance, the switched capacitor filter can have the accurate frequency response. Stability to temperature variation and accuracy of manufacturing are much more important in the anti-aliasing filter than in the filters of other blocks. Thus, a switched capacitor type filter is optimal.

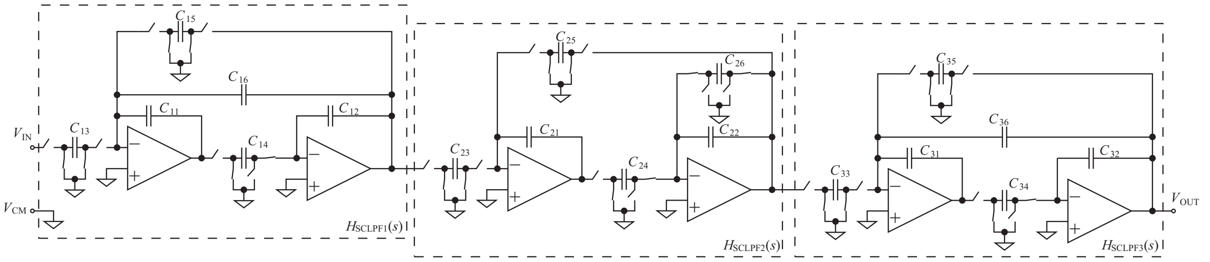

Figure 3.29: Circuit diagram of the sixth-order switched capacitor filter. The clock generating circuit is not shown.

The circuit diagram of the six-order Chebyshev-type switched capacitor filter is shown in Fig. 3.29. The switching clock is externally fed to the chip, and the clock frequency is 10 MHz. The external clock generates a set of non-overlapping complementary clocks in the chip. The Op-Amps and switches are the same as the OP2 and the CMOS switches described in the previous section. The unity gain frequency of the OP2 is high enough in compared with the clock frequency. The MIMCAP is used for the capacitors. The sixth-order filter consists of three cascaded biquad low pass filters. The transfer functions

$H_{\mathrm{SCLPF},1(2,3)}(s)$ are expressed in the Eq. 3.27.

$$H_{\mathrm{SCLPF},i}(s) = \frac{A_v {\omega_0}^2}{s^2 + \frac{\omega_0}{Q}s + {\omega_0}^2} \tag{3.26}$$

$$= \begin{cases} \dfrac{-{f_{\mathrm{CK}}}^2 \dfrac{C_3 C_4}{C_1 C_2}}{s^2 + f_{\mathrm{CK}}\dfrac{C_4 C_6}{C_1 C_2}s + {f_{\mathrm{CK}}}^2 \dfrac{C_4 C_5}{C_1 C_2}} & (i = 1, 3), \\ \dfrac{-{f_{\mathrm{CK}}}^2 \dfrac{C_3 C_4}{C_1 C_2}}{s^2 + f_{\mathrm{CK}}\dfrac{C_6}{C_2}s + {f_{\mathrm{CK}}}^2 \dfrac{C_4 C_5}{C_1 C_2}} & (i = 2), \end{cases} \tag{3.27}$$

where f_{CK} and C_1 to C_6 are the clock frequency for switching and the capacitors in the each biquad filter, respectively. Since the clock frequency (10 MHz) is a hundred times larger than the cutoff frequency of the anti-aliasing filter, we can recognize the switched capacitor as a continuous time filter in the notable frequency range for simplicity.

The feedback circuit is in the second biquad filter is different from those of the first and third filter. We chose the suitable one for obtaining integer ratio of the capacitances based on the unit capacitance. The capacitance used in this switched capacitor filter are shown in Table 3.5. The unit capacitance is set to 25 fF, the minimum value in available, in order to minimize capacitance area in the filters.

Table 3.5: Capacitance ratios based on the unit capacitance (25 fF) of the switched capacitor LPF.

×25 fF	$H_{\mathrm{SCLPF},1}$	$H_{\mathrm{SCLPF},2}$	$H_{\mathrm{SCLPF},3}$
C_1	45	47	16
C_2	45	47	16
C_3	1	1	1
C_4	1	5	1
C_5	1	1	1
C_6	59	1	2
$\omega_0/2\pi$ [kHz]	35.4	75.7	99.5
Q	0.76	2.24	8.00
A_v [dB]	0	0	0

The frequency response gains of the switched capacitor are shown in Fig. 3.30. The measurement result and the theoretically obtained transfer function expressed with the solid line and the broken line, respectively. Although the attenuation characteristics above the cutoff frequency are slightly shifted toward the higher frequency from each other, the two lines almost agree with each other. The passband ripple in frequency range of over 80

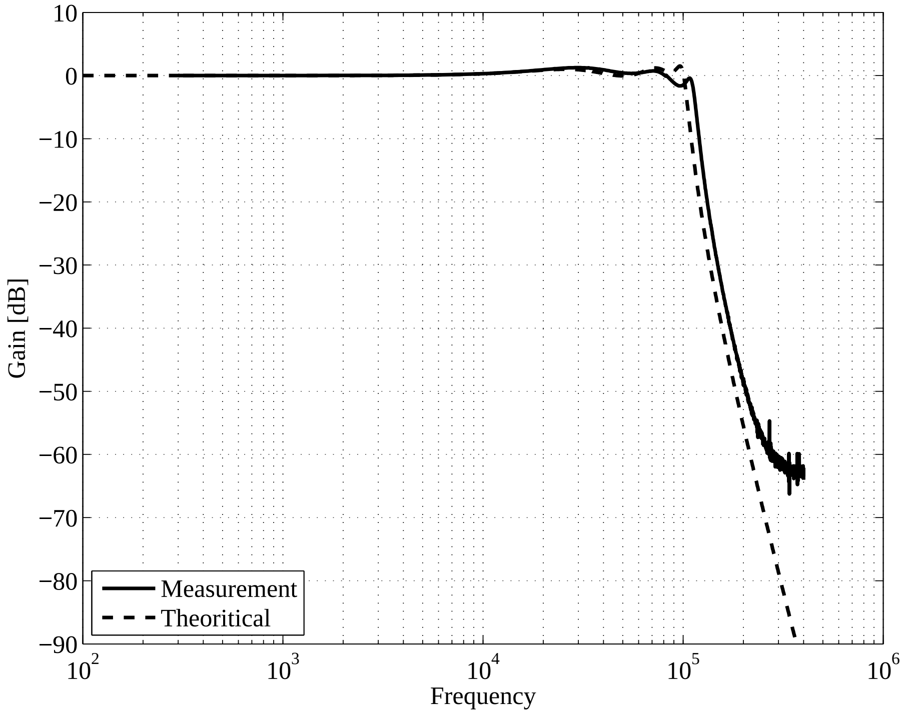

Figure 3.30: Frequency response gains for the measured result (solid line), and the theoretical transfer function calculated from the capacitance ratios (broken line).

kHz is increased because of this frequency shift. Parasitic capacitances of the MIMCAPs shifted the capacitance ratios and the poles. The high-Q circuit, the third biquad filter, is sensitive to the parasitic capacitances than low-Q circuit. Although the attenuation level does not satisfy the requirement, the gradients of the attenuation fit closely with each other. Table 3.6 shows the summary of the anti-aliasing filter with comparison of the performances between the design and measurement result. The feasibility of the performances are discussed in Chapter 4.

Table 3.6: Specifications of the anti-aliasing filter.

Type & Order	6th-order Chebyshev	
Architecture	Switched Capacitor	
Clock frequency	10 MHz	
	Design	Result
Cutoff frequency	100 kHz	110 kHz
Pass-band ripple	< 1 dB	< 1 dB (< 80 kHz), < 3 dB (> 80 kHz)
Attenuation at 300 kHz	79 dB	61 dB

3.7 Switching Capacitor BPF

Two band pass filters (BPF) exist in the sweep frequency analyzer (SFA), shown in Fig. 2.7. The BPFs in the SFA have a crucial role to reject an interfering image which appear in frequency conversion. In the present section, the BPF for first IF band is described. The second local oscillator should have oscillation frequency close to the first IF in order to bring down second IF and sampling frequency. Hence, the frequency response of the first BPF is needed to have steep attenuation characteristics. According to Table 2.4, difference between the first IF and the second local is 10 kHz and for the Band number 2. When the IF band width is 10 kHz, the highest frequency of the image in the second frequency conversion is equal to 180 kHz ($= 195 - 2 \times 10 + 10/5\,\text{kHz}$). This is the frequency where the first BPF should have enough attenuation. Since the frequencies where signals appear as image in the first frequency conversion exist in the observation range (0 to 100 kHz), there is no filter to reject this image without the first BPF. The attenuation of the first BPF strongly affects the signal-to-noise ratio of the SFA. Thus, the requirement is very exacting.

Since the accuracy of manufacturing is strongly desired, the switched capacitor is suitable. In order to realize the requirement, very high-order and high-Q filter are in options. This means the trade-off between accuracy and occupied area of the BPF. We chose three cascaded sixth-order Chebyshev BPF of which eighteenth-order term exist in denominator of the total transfer function. The circuit diagram of the unit switched capacitor biquad filter is shown in Fig. 3.31.

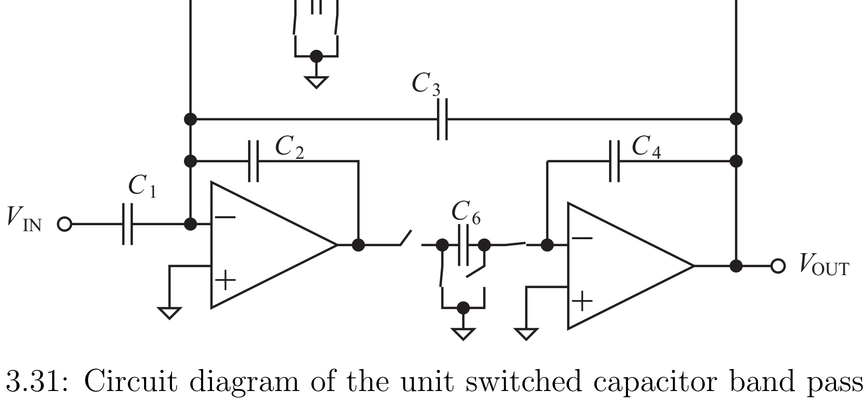

Figure 3.31: Circuit diagram of the unit switched capacitor band pass filter.

The transfer function of the unit BPF is expressed as follows:

$$\frac{V_{\mathrm{OUT}}}{V_{\mathrm{IN}}} = \frac{A_v \frac{\omega_0}{Q} s}{s^2 + \frac{\omega_0}{Q} s + {\omega_0}^2} \tag{3.28}$$

$$= \frac{f_{\mathrm{CK}} \frac{C_1 C_6}{C_2 C_4} s}{s^2 + f_{\mathrm{CK}} \frac{C_3 C_6}{C_2 C_4} s + {f_{\mathrm{CK}}}^2 \frac{C_5 C_6}{C_2 C_4}}. \tag{3.29}$$

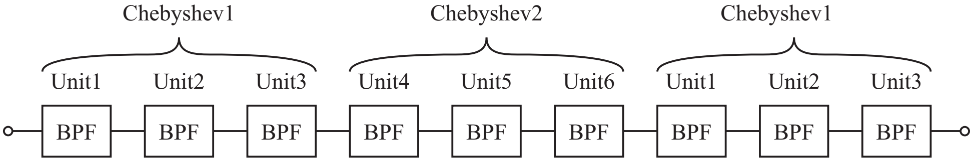

Figure 3.32: Circuit diagram of the total switched capacitor band pass filter.

The eighteenth-order BPF consists of the three cascaded sixth-order Chebyshev BPF as shown in Fig. 3.32. The Chebyshev BPF is composed of three second-order BPF units (Unit 1 to 3 or 4 to 6) which have different the center frequencies and the maximum gains in the frequency responses. The Chebyshev filter with number 2 is different from the others to adjust the passband gain though ripple of the gain can be compensated in signal processing in the digital components. The capacitance ratios used in the switched capacitor BPF units are listed in Table 3.7.

Table 3.7: Ratios of each capacitance to the unit capacitance of 25 fF, and characteristic values in the each unit switched capacitor BPF.

× 25 fF	Unit1	Unit2	Unit3	Unit4	Unit5	Unit6
C_1	3	4	11	2	3	6
C_2	13	14	40	13	14	40
C_3	3	3	4	2	3	3
C_4	41	70	59	41	70	59
C_5	4	8	11	4	8	11
C_6	2	2	3	2	2	3
$\omega_0/2\pi$ [kHz]	195	203	188	195	203	188
Q	11	21	23	16	21	31
A_v [dB]	0.0	2.5	8.8	0.0	0.0	6.0

Sensitivity of the frequency response to the parasitic capacitance becomes large when the filter contains high-Q circuits. The center frequency of the BPF is obtained with the same accuracy as the relative accuracy of the capacitance. Then, the error of the center frequency of the high-Q BPF largely affects the total frequency response. However, even though the capacitance in itself is completely realized, the parasitic capacitance must be considered in the high-Q BPF. Here, parasitic capacitance is additional capacitance because of the fringes of the metals. Assuming that capacitances C_1 and C_2 are sum of capacitances from aspect and periphery of the capacitors, the ratio of C_2 to C_1 is expressed as following equations.

$$C_1 = C_{1\mathrm{A}} + C_{1\mathrm{P}}, \tag{3.30}$$

$$C_2 = C_{2\mathrm{A}} + C_{2\mathrm{P}}, \tag{3.31}$$

$$\frac{C_2}{C_1} = \frac{C_{2\mathrm{A}} + C_{2\mathrm{P}}}{C_{1\mathrm{A}} + C_{1\mathrm{P}}} = \frac{C_{2\mathrm{A}}}{C_{1\mathrm{A}}} \left(\frac{1 + \dfrac{C_{2\mathrm{P}}}{C_{2\mathrm{A}}}}{1 + \dfrac{C_{1\mathrm{P}}}{C_{1\mathrm{A}}}} \right), \tag{3.32}$$

where $C_{1\mathrm{A}}$ and $C_{2\mathrm{A}}$ are capacitances which is proportional to the area of the capacitors, and $C_{1\mathrm{P}}$ and $C_{2\mathrm{P}}$ are proportional to the perimeter, respectively. Equation (3.32) suggests that keeping $C_{1\mathrm{P}}/C_{1\mathrm{A}}$ and $C_{2\mathrm{P}}/C_{2\mathrm{A}}$ equal is very important for avoidance of parasitic capacitance problems.

To maintain this equality for any ratio of capacitances, Yiannoulos path is introduced by *Allen and Holberg* [50]. As shown in Fig. 3.33, the Yiannoulos path enables the ratio of two capacitances to be equal when both of the capacitances are larger than or equal to eight units. The total unit lengths are 26 and 34 for the total unit areas are 13 and 17, respectively. We can have the total unit length l,

$$l = 2a \quad (a \geq 8), \tag{3.33}$$

where a is the total unit area. The ratio of l to a becomes constant. This technique is suitable for the switched capacitor circuits where all capacitance ratios to the unit capacitance are eight or more.

When the Yiannoulos path is applied to the present switched capacitor BPF, all the capacitors have to be fourfold to substitute capacitors less than eight units. In fact, the Yiannoulos path could result in the fourfold area of the capacitance inside the chip at least. Then, we chose the checkered layout design to keep the capacitance ratios [44]. Figure 3.34 shows the layout design of the BPF of Unit 6. The total unit length l is equal to

$$l = 4a \tag{3.34}$$

without any limitation of the unit area. The checkered layout doubles the capacitance area at least, even if the increased amount is smaller than that with the Yiannoulos path method. In design of another switched capacitor filter, the Yiannoulos path method would effectively perform without increment of capacitance area.

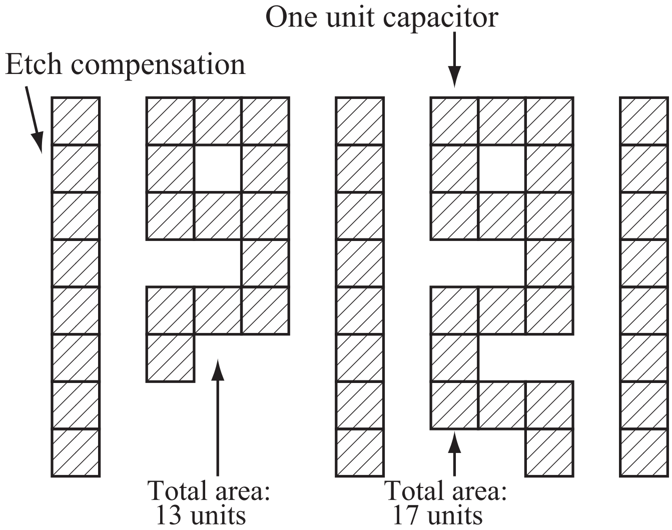

Figure 3.33: Capacitances of thirteen and seventeen units realized with the Yiannoulos path.

As a result, the measured frequency responses shown in Fig. 3.35 are obtained with good accuracy. Although the passband gain has ripple in every measurement result, the center frequencies of the BPF fit closely with the theoretical and simulated results. On the other hand, the measured attenuation level at 180 kHz is around 50 dB. The attenuation in the higher range is also not obtained enough. These are caused by zeros points which involuntarily appeared in the transfer function of the BPF.

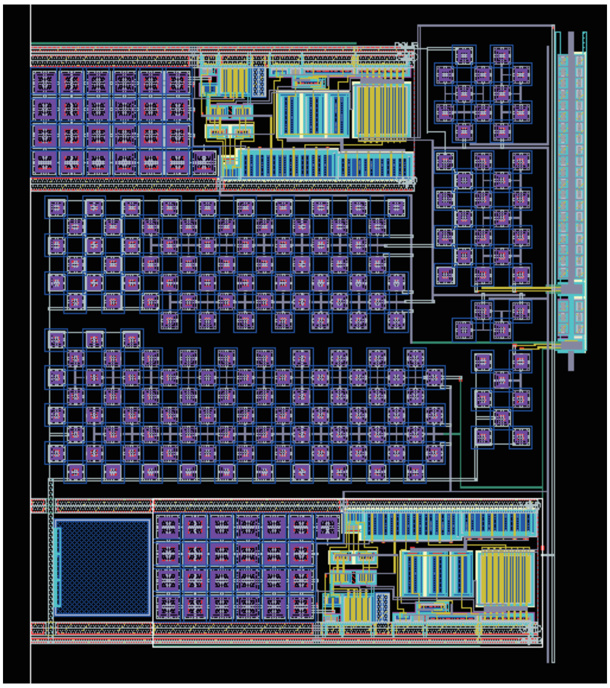

Figure 3.34: Layout design of the BPF of Unit 6 with checkered capacitances.

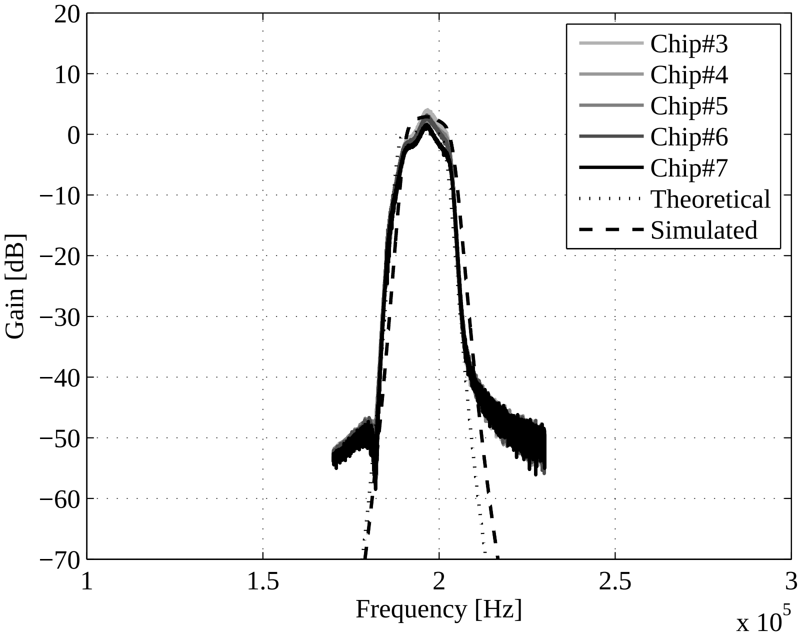

Figure 3.35: Frequency response gains for the measured results of individual chips (solid lines), the theoretical transfer function calculated from the capacitance ratios (dotted line), and interpolated simulation results with transient analysis (broken line).

3.8 Mixer

Mixer is widely used for frequency conversion by multiplying input signals in radio frequency (RF) with local oscillating (LO) signals. The frequency of output is called intermediate frequency (IF) when the signal is further to be mixed in another frequency conversion. The mixer, shown in Fig. 2.7, is required to have good linearity and inter modulation (IM) for the SFA. Here, we design and investigate the elemental mixer to clarify problems of usage of the mixer for the SFA.

Principle of the mixer is based on an analog multiplier. When signals of RF and LO are expressed in Eqs. (3.35) and (3.36), the products of these signals are obtained in Eq. ((3.37).

$$\begin{aligned} s_{\mathrm{RF}}(t) &= V_{\mathrm{RF}} \cos \omega_{\mathrm{RF}} t, && (3.35) \\ s_{\mathrm{LO}}(t) &= V_{\mathrm{LO}} \cos \omega_{\mathrm{LO}} t, && (3.36) \\ s_{\mathrm{IF}}(t) &= s_{\mathrm{RF}}(t)\ s_{\mathrm{LO}}(t) \\ &= \frac{V_{\mathrm{RF}} V_{\mathrm{LO}}}{2} \cos(\omega_{\mathrm{RF}} + \omega_{\mathrm{LO}})t + \frac{V_{\mathrm{RF}} V_{\mathrm{LO}}}{2} \cos(\omega_{\mathrm{RF}} - \omega_{\mathrm{LO}})t\ , && (3.37) \end{aligned}$$

where V_{RF}, V_{LO}, ω_{RF} and ω_{LO} are amplitudes RF and LO signals, and frequencies of those, respectively.

Figure 3.36 shows the circuit diagram of the Gilbert cell mixer [51], which has differential RF and LO input nodes and IF output nodes. The gilbert cell mixer consists of three differential MOSFET pairs with common current source. The differential switching signals are fed to LO+ and LO− nodes in order to change over the current path to the current source. Then, the one-sided signals of LO and IF are shown in Eqs. (3.38) and (3.39) by Fourier series expansion.

$$\begin{aligned} s_{\mathrm{LO}}(t) &= \frac{V_{\mathrm{DD}}}{2} + V_{\mathrm{DD}} \frac{2}{\pi} \sum_{n=1}^{\infty} \left(\frac{1}{2n-1} \cos\{(2n-1)\ \omega_{\mathrm{LO}} t\} \right) && (3.38) \\ s_{\mathrm{IF}}(t) &= \frac{V_{\mathrm{DD}} V_{\mathrm{RF}}}{2} \cos \omega_{\mathrm{RF}} t \\ &\quad + \frac{2 V_{\mathrm{DD}} V_{\mathrm{RF}}}{\pi} \sum_{n=1}^{\infty} \left(\frac{1}{2n-1} \cos\{\omega_{\mathrm{RF}} + (2n-1)\ \omega_{\mathrm{LO}}\} t \right) \\ &\quad + \frac{2 V_{\mathrm{DD}} V_{\mathrm{RF}}}{\pi} \sum_{n=1}^{\infty} \left(\frac{1}{2n-1} \cos\{\omega_{\mathrm{RF}} - (2n-1)\ \omega_{\mathrm{LO}}\} t \right). && (3.39) \end{aligned}$$

In the present thesis, the SFA needs up-conversion from the baseband frequency into the first IF. The intended IF signal is the second term in Eq. (3.39) for the case of $n = 1$. The band pass filter described in the previous section is aimed to reject every other component.

The common-mode voltage at the output nodes of mixer $V_{\mathrm{MX,DC}}$ is determined by load

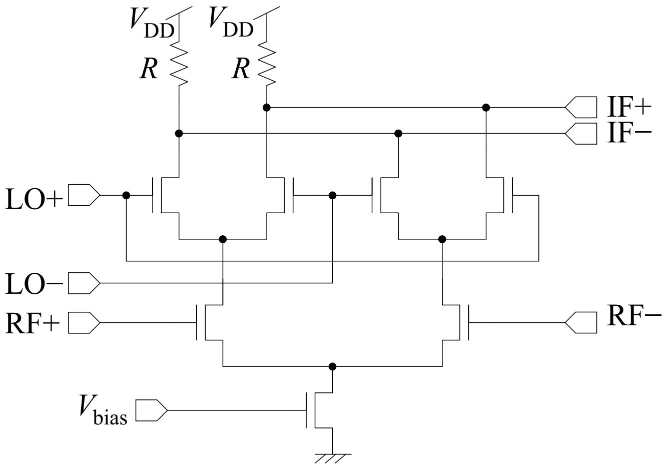

Figure 3.36: Circuit diagram of the Gilbert cell mixer.

resistance R and the bias current I_{bias} as follows:

$$V_{\mathrm{MX,DC}} = V_{\mathrm{DD}} - R\frac{I_{\mathrm{bias}}}{2}. \tag{3.40}$$

R and I_{bias} are set to 32 kΩ and 128 μA, respectively [44].

Figure 3.37 shows the measurement and simulation results of spectra of the one-sided output mixer. Differential clock signals are supplied to LO+ and LO− nodes. Sinusoidal RF signal is fed to RF+, and RF− is shorted to V_{CM}. Setting the frequencies of RF and LO to 55 kHz and 250 kHz, the IF signal appeared at 195 kHz with both even and odd harmonics. The frequencies of intermodulated harmonics of spurious are tabulated in Table 3.8. The harmonics of f_{RF} are caused by non-linear operation of the MOSFETs. The third intermodulation of −70 dB appears at 360 and 445 kHz for $V_{\mathrm{RF}} = 20$ mV. The common-mode spurious can be eliminated by obtaining difference between IF+ and IF− [44]. Hence, fully-differential mixers, BPFs, and amplifiers are appropriate in order to ensure the noise level requirement. Although this coping also leads increase of circuit size, the ASIC can minimize the enlargement.

Measurement and simulation results of linearity of the mixer is shown in Fig. 3.38. The mixer in linearity is kept up to −15 dBVrms of the input and output magnitude. The simulation result shows better linearity than the experimental result because of ideal matching of differential pairs in the mixers. However, since the difference is a few dB, the linearity should be improved by redesigning the circuit. The limitation of the range which is related to gain of the mixer is determined by the output resistance R and r_{o}. Since the output common-mode voltage also depends on R, the mixer should be modified in order to separate the linearity from the output common-mode voltage. One of the solutions is shown in Fig. 3.39. Sum of the R_1 and R_2 is replaced with R in Eq. (3.40) though the gain is governed by only R_2. The improved linearity was confirmed by simulation [44].

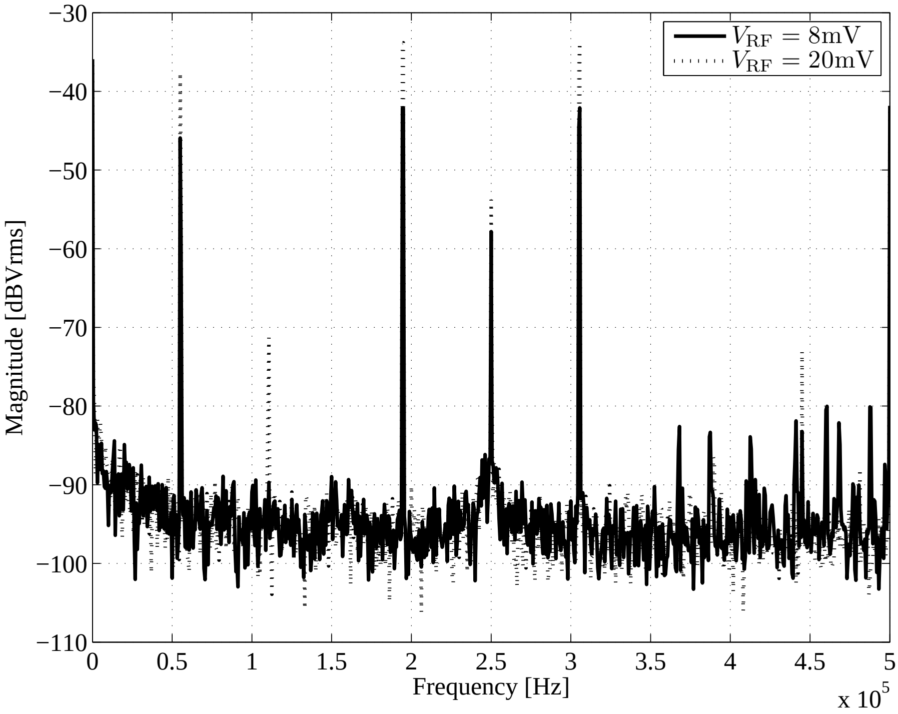

Figure 3.37: Measured spectra of the IF signals for $V_{\mathrm{RF}} = 8$ mV (solid line), and $V_{\mathrm{RF}} = 20$ mV (dotted line). $f_{\mathrm{RF}} = 55$ kHz, $f_{\mathrm{LO}} = 250$ and kHz.

Table 3.8: Frequencies and their expression of the output of the mixer.

Frequency [kHz]	Expression	Order
55	f_{RF}	1
250	f_{LO}	1
110	$2f_{\mathrm{RF}}$	2
500	$2f_{\mathrm{LO}}$	2
195	$f_{\mathrm{LO}} - f_{\mathrm{RF}}$	2
305	$f_{\mathrm{LO}} + f_{\mathrm{RF}}$	2
360	$f_{\mathrm{LO}} + 2f_{\mathrm{RF}}$	3
445	$2f_{\mathrm{LO}} - f_{\mathrm{RF}}$	3
390	$2f_{\mathrm{LO}} - 2f_{\mathrm{RF}}$	4
415	$f_{\mathrm{LO}} + 3f_{\mathrm{RF}}$	4
470	$f_{\mathrm{LO}} + 4f_{\mathrm{RF}}$	5

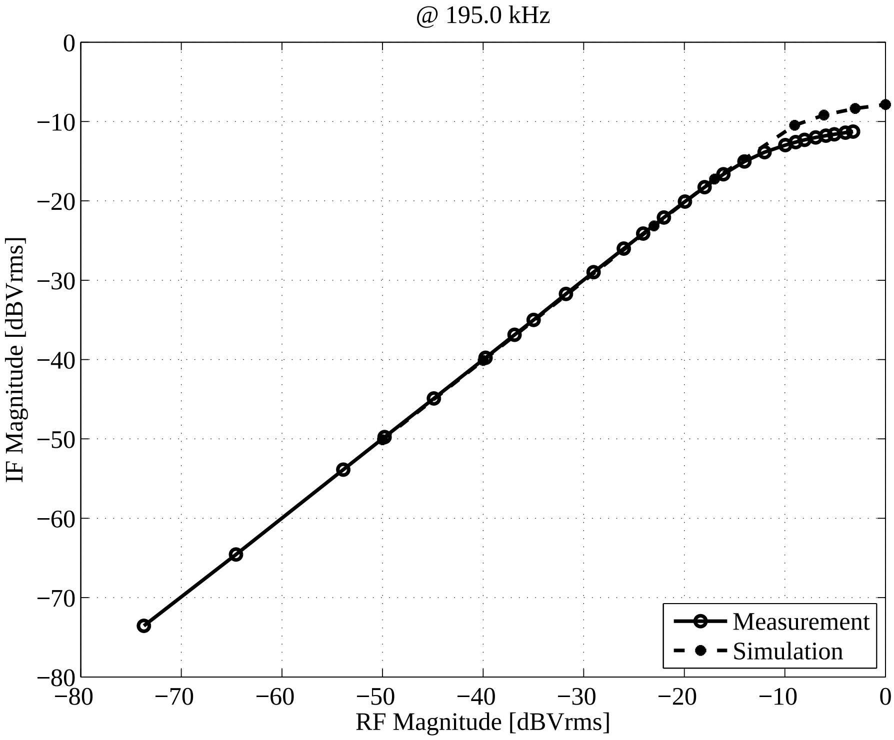

Figure 3.38: Input versus output amplitude characteristics.

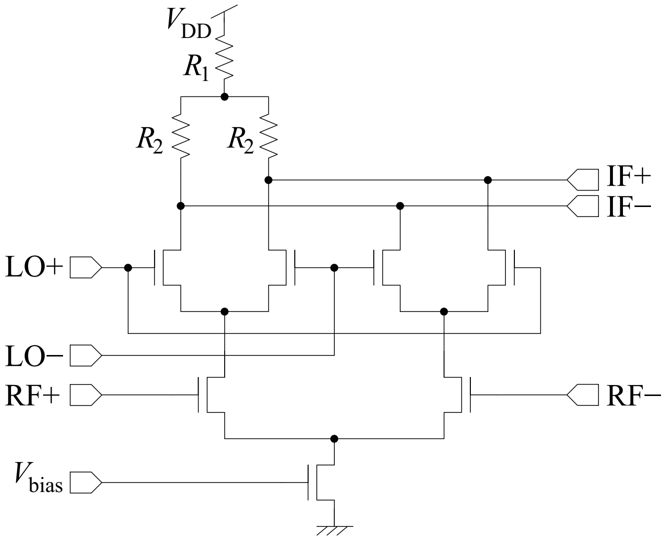

Figure 3.39: Circuit diagram of the Gilbert cell mixer which has independent the gain and the output common-mode voltage to improve the linearity.

3.9 Phase-Locked Loop

The frequency synthesizer, shown in Fig. 2.7, has more important role than any components of the SFA since its specifications critical for the time and frequency resolutions. The frequency synthesizer is a phase-locked loop (PLL) which has a programmable divider to change the output frequency. Since the PLL accounts for a substantial fraction of the circuit size in the SFA, development of the frequency synthesizer and integration into ASIC are inevitable for miniaturization of the SFA.

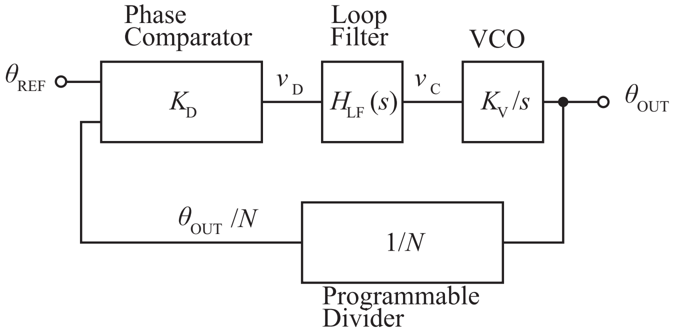

Figure 3.40: Block diagram of the PLL.

Figure 3.40 shows the block diagram of a typical PLL, where $\theta_{\rm REF}, \theta_{\rm OUT}, N$, and $V_{\rm C}$ are reference phase, output phase, division ratio, and voltage for the voltage controlled oscillator (VCO), respectively. The frequencies of the reference and output are obtained by differentiating $\theta_{\rm REF}$ and $\theta_{\rm OUT}$ with respect to time. In frequency domain, these relations are expressed as follows:

$$f_{\rm REF} = s\theta_{\rm REF}, \tag{3.41}$$

$$f_{\rm OUT} = s\theta_{\rm OUT}. \tag{3.42}$$

Phase difference between the reference and divided output signals is detected at the phase comparator. The loop filter rejects high frequency component with keeping the stability of the loop and lock time. The filtered voltage signal $V_{\rm C}$ is provided to the VCO. The VCO oscillates at frequency which depends on $V_{\rm C}$. Since the divider feeds the signal at the frequency divided by N, the output frequency of the VCO, the time derivative of $\theta_{\rm OUT}$ is equal to $Nf_{\rm REF}$ when the loop is completely locked. Equations (3.43) to (3.45) indicate relations between $v_{\rm D}, v_{\rm C}$, and $\theta_{\rm OUT}$.

$$v_{\rm D} = K_{\rm D}(\theta_{\rm REF} - \frac{\theta_{\rm OUT}}{N}), \tag{3.43}$$

$$v_{\rm C} = H_{\rm LF}(s)v_{\rm D}, \tag{3.44}$$

$$\theta_{\rm OUT} = \frac{K_{\rm V}}{s}v_{\rm C}. \tag{3.45}$$

From these equations, the transfer function from v_{C} to v_{D} without the loop filter is obtained.

$$\begin{aligned} H_{\mathrm{VCO-PC}}(s) &= \frac{v_{\mathrm{D}}}{v_{\mathrm{C}}} \\ &= \frac{K_{\mathrm{D}}K_{\mathrm{V}}}{N}\frac{1}{s}. \qquad (3.46) \\ |H_{\mathrm{VCO-PC}}(j\omega)| &= \frac{K_{\mathrm{D}}K_{\mathrm{V}}}{N\omega} \qquad (3.47) \\ \angle H_{\mathrm{VCO-PC}}(j\omega) &= -90^{\circ} \qquad (3.48) \end{aligned}$$

The unity gain frequency of $H_{\mathrm{VCO-PC}}(s)$ becomes $K_{\mathrm{D}}K_{\mathrm{V}}/N$. $H_{\mathrm{VCO-PC}}(s)$ is constant in phase of -90°. The total transfer function of the loop filter and $H_{\mathrm{VCO-PC}}(s)$ becomes the open-loop transfer function. Thus, the loop filter must have enough phase margin at the unity gain frequency of the open-loop transfer function.

Table 3.9: Specifications of the PLL.

	SFA	Proto-type
Frequency Range	200 to 290 kHz	192 / 320 kHz
Number of sweep steps	10	2
Reference frequency	5 kHz	6 kHz / 5 kHz
Division Ratio (Min/Max/Step)	40/58/2	32/64/32
Lock Time	< 53 ms	40 ms

Target specifications of the PLL for the SFA is shown in Table 3.9. The output frequency of the PLL is need to change from 200 kHz to 290 kHz every the 10 kHz in 53 ms. The reference frequency is set to 5 kHz. Changing the division ratio from 40 to 58 in steps of 2, the output frequency is obtained. Here, the lock time is defined as time taken to converge the output frequency within 0.1 % of the convergent value.

In the present thesis, we simplify the division ratio to confirm the lock operation of the PLL. A six-bit binary counter is applied to the divider. Since the each bit of the divider is multiplexed, we can obtain $N = 2^m$ $(m = 1, 2, \cdots, 6)$. Here, we choose the reference frequency 6 kHz for $N = 32$, and 5 kHz for $N = 64$ to cover the f_{OUT} range of 200 to 290 kHz.

The objective of this section is to demonstrate the components for the PLL and confirm the lock operation from an unlocked state in these two conditions. From here, we describe designs of the VCO, phase comparator, divider, and loop filter. The closed-loop operation of the PLL is finally demonstrated.

3.9.1 Voltage Controlled Oscillator

Circuit Design

The VCO ideally has linear voltage to oscillation frequency characteristics. The VCO has been realized in monolithic circuits for a local oscillator in wireless communication application, e.g., cell-phone, bluetooth device, and etc. The LC VCO with on-chip inductors are commonly used for such the VCOs. However, available frequency for the inductor is much higher than the target range of the plasma wave receiver.

Here, the oscillator is realized with $\mathrm{G_m}$–C band pass filter with positive feedback. The transconductance of the OTA (G_m) can be varied with combining MOSFET in triode region and cascode current mirror [52].

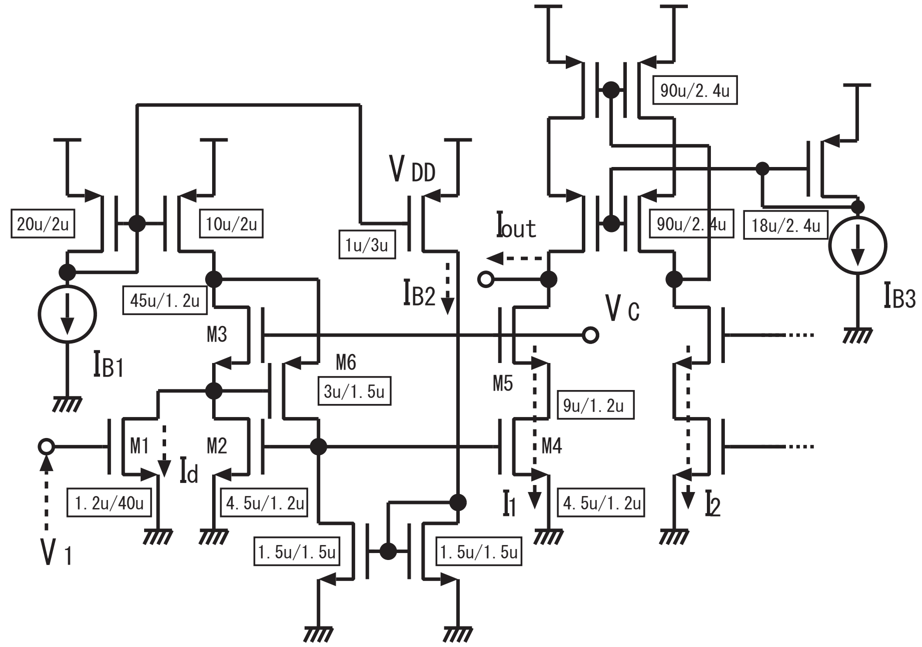

Figure 3.41: Half circuit schematics of variable G_m OTA [*after Sato et al.*, (2005)].

The circuit to vary G_m with voltage is shown in Fig. 3.41. The $\mathrm{M_1}$ is operating in triode region for a certain V_C range. The current flowing in $\mathrm{M_3}$ is indicated equal to $I_\mathrm{B1} - I_\mathrm{B2}$. Then the voltages at source and source nodes of $\mathrm{M_3}$, $V_{\mathrm{s_{M3}}}$ and $V_{\mathrm{d_{M3}}}$, are shown as follow:

$$V_{\mathrm{s_{M3}}} = V_\mathrm{C} - \sqrt{\frac{2(I_\mathrm{B1} - I_\mathrm{B2})}{\mu_n C_\mathrm{ox} \frac{W_{\mathrm{M_3}}}{L_{\mathrm{M_3}}}}} - V_\mathrm{tn}, \tag{3.49}$$

$$V_{\mathrm{d_{M3}}} = V_{\mathrm{s_{M3}}} + \sqrt{\frac{2I_\mathrm{B2}}{\mu_p C_\mathrm{ox} \frac{W_{\mathrm{M_6}}}{L_{\mathrm{M_6}}}}} + |V_\mathrm{tp}|, \tag{3.50}$$

where $\mu_n, \mu_p, V_{\text{tn}}$, and V_{tp} are mobilities of N and P type semiconductors and threshold voltages of the MOSFETs, respectively. The condition where M_3 operates in saturation region is expressed with Eq. (3.51).

$$\sqrt{\frac{2I_{\text{B2}}}{\mu_p C_{\text{ox}}\frac{W_{\text{M}_6}}{L_{\text{M}_6}}}} + |V_{\text{tp}}| \;>\; \sqrt{\frac{2(I_{\text{B1}}-I_{\text{B2}})}{\mu_n C_{\text{ox}}\frac{W_{\text{M}_3}}{L_{\text{M}_3}}}} \tag{3.51}$$

When the above condition is satisfied and $V_{\text{C}} > V_{\text{tn}}$, the $I_{\text{d}_{\text{M1}}}$ is provided in Eq. (3.52).

$$I_{\text{d}_{\text{M1}}} \;=\; \mu_n C_{\text{ox}}\frac{W_{\text{M}_1}}{L_{\text{M}_1}}\left\{(V_1 - V_{\text{tn}})\,V_{\text{s}_{\text{M3}}} - \frac{{V_{\text{s}_{\text{M3}}}}^2}{2}\right\}, \tag{3.52}$$

where $I_{\text{d}_{\text{M1}}}$ and $V_{\text{s}_{\text{M3}}}$ are the drain current of M_1 and source voltage of M_3, respectively. The currents I_1, I_{OUT}, and G_{m} are expressed as follows:

$$I_1 \;=\; I_{\text{B1}} - I_{\text{B2}} - I_{\text{d}_{\text{M1}}}, \tag{3.53}$$

$$\begin{aligned} I_{\text{OUT}} &= I_2 - I_1 \\ &= \mu_n C_{\text{ox}}\frac{W_{\text{M}_1}}{L_{\text{M}_1}}(V_1 - V_2)V_{\text{s}_{\text{M3}}} \\ &= \mu_n C_{\text{ox}}\frac{W_{\text{M}_1}}{L_{\text{M}_1}}(V_1 - V_2)\left(V_{\text{C}} - \sqrt{\frac{2(I_{\text{B1}}-I_{\text{B2}})}{\mu_n C_{\text{ox}}\frac{W_{\text{M}_3}}{L_{\text{M}_3}}}} - V_{\text{tn}}\right), \end{aligned} \tag{3.54}$$

$$\begin{aligned} G_{\text{m}} &= \frac{I_{\text{OUT}}}{V_1 - V_2} \\ &= \mu_n C_{\text{ox}}\frac{W_{\text{M}_1}}{L_{\text{M}_1}}\left(V_{\text{C}} - \sqrt{\frac{2(I_{\text{B1}}-I_{\text{B2}})}{\mu_n C_{\text{ox}}\frac{W_{\text{M}_3}}{L_{\text{M}_3}}}} - V_{\text{tn}}\right). \end{aligned} \tag{3.55}$$

The G_{m} which depends on V_{C} are applied for the G_m–C bandpass filter with positive feedback. In fact, the cascode current mirror is adopted in order to generate I_{OUT}. I_{B1}, I_{B2}, $W_{\text{M}_1}/L_{\text{M}_1}$, and $W_{\text{M}_3}/L_{\text{M}_3}$ are 32 μA, 2.3 μA, 12 μm / 40 μm, and, 45 μm / 1.2 μm respectively. In Fig. 3.42, G_{m} is changed by controlling V_{C}.

The G_{m} in Eq. (3.55) contains V_{tn}. This means that G_{m} in Eq. (3.55) has sensitivity for not only μ_n but also V_{tn}. The cancelling circuit in front of the gate node of V_{C} are adopted as shown in Fig. 3.43. The V_{C} is provided by the source follower with the current source I_{SF}. Then, the $V_{\text{SF}} = V_{\text{C}} - \sqrt{2I_{\text{SF}}/\beta_{\text{M}_{\text{SF}}}} - V_{\text{tn}}$ brings $V_{\text{C}}{}'$ as shown in Eq. (3.56), where $\beta_{\text{M}_{\text{SF}}} = \mu_n C_{\text{ox}} W_{\text{M}_{\text{SF}}}/L_{\text{M}_{\text{SF}}}$ in Fig. 3.43.

$$V_{\text{C}}{}' \;=\; -\frac{R_4}{R_1}V_{\text{SF}} + \frac{(R_1+R_4)R_3}{R_1(R_2+R_3)}V_{\text{CM}}. \tag{3.56}$$

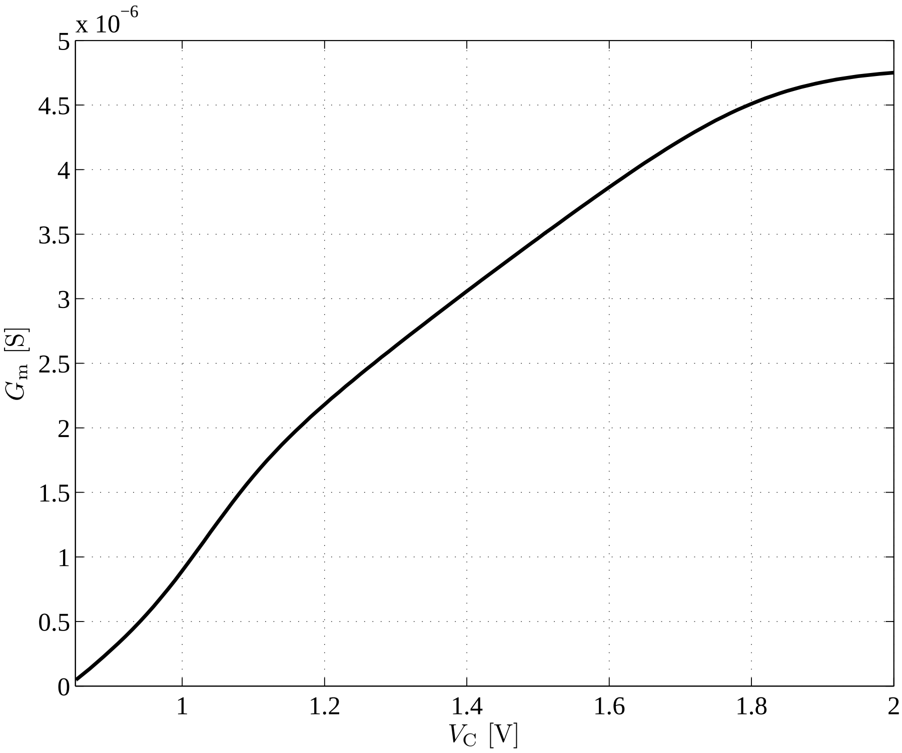

Figure 3.42: Controlled G_{m} by the control voltage V_{C} of the OTA.

V_{C} in Eq. (3.55) is replaced with $V_{\mathrm{C}}{}'$ and the G_{m} expression is modified as follows:

$$\begin{aligned} G_{\mathrm{m}} &= \mu_n C_{\mathrm{ox}} \frac{W_{\mathrm{M_1}}}{L_{\mathrm{M_1}}} \left\{ -\frac{R_4}{R_1} \left(V_{\mathrm{C}} - \sqrt{\frac{2I_{\mathrm{SF}}}{\beta_{\mathrm{M_{SF}}}}} \right) + \frac{(R_1+R_4)R_3}{R_1(R_2+R_3)} V_{\mathrm{CM}} \right. \\ & \left. - \sqrt{\frac{2(I_{\mathrm{B1}} - I_{\mathrm{B2}})}{\mu_n C_{\mathrm{ox}} W_{\mathrm{M_3}}/L_{\mathrm{M_3}}}} + \left(\frac{R_4}{R_1} - 1 \right) V_{\mathrm{tn}} \right\}. \qquad (3.57) \end{aligned}$$

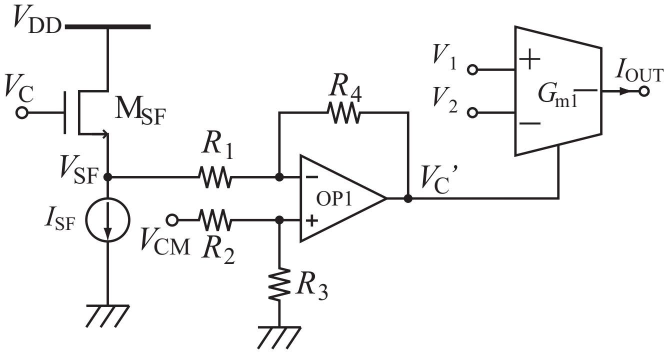

Figure 3.43: Variable G_{m} OTA with cancelling V_{tn} variation circuit.

In practice, R_4/R_1 is equal to 1 since V_{tn} of M_{SF} and M_3 in Fig. 3.41 are different from each other because of body effect in NMOS. The resistors R_1 to R_4, I_{SF}, and $W_{\mathrm{M_{SF}}}/L_{\mathrm{M_{SF}}}$

are set to 20 kΩ, 5.0 kΩ, 14 kΩ, 20 kΩ, 64μA, and 240μm/1.2μm, respectively.

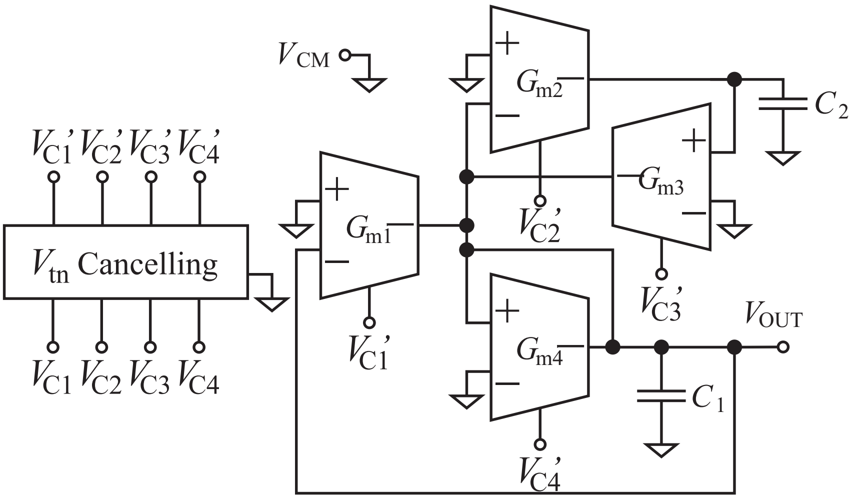

Figure 3.44: Circuit diagram of the VCO with $V_{\rm tn}$ cancelling circuit.

The circuit diagram of the VCO is shown in Fig. 3.44. The VCO consists the of positive feedback $\rm G_m$–C bandpass filter and the $V_{\rm tn}$ cancelling circuit. The open-loop transfer function $H_{\rm VCO,Open}$ is indicated in Eq. (3.58).

$$H_{\rm VCO,Open} = \frac{\frac{G_{\rm m1}}{C_1}s}{s^2+\frac{G_{\rm m4}}{C_1}s+\frac{G_{\rm m2}G_{\rm m3}}{C_1C_2}} \tag{3.58}$$

The oscillating frequency $f_{\rm OUT}$ of VCO is determined by $G_{\rm m2}$, $G_{\rm m3}$, C_1, and C_2.

$$f_{\rm OUT} = \frac{1}{2\pi}\sqrt{\frac{G_{\rm m2}G_{\rm m3}}{C_1C_2}} \tag{3.59}$$

When $G_{\rm m2}$ and $G_{\rm m3}$ are controlled by the same voltage, $V_{\rm C}$, the oscillating frequency $f_{\rm OUT}$ is proportional to $V_{\rm C}$. The capacitances of C_1 and C_2 0.4 and 0.1 pF, respectively.

The gain and phase are constant, -5.1 dB and 180°, respectively. The gain of this circuit is included in the gain of the VCO, $K_{\rm V}$.

Characteristics of the VCO

First, we had a trial production of the VCO using the $\rm G_m$–C filter. Comparison of the measurement results with the simulation is indicated in Fig. 3.45. $V_{\rm C1}$ to $V_{\rm C4}$ are all in the same voltage $V_{\rm C}$. The output frequency in the measurement results are largely different from the simulation result. The gradients of the measurement also becomes different. The result from the chip #1 is the closest trace to the simulation result. The gain of the VCO is estimated from the simulation and measurement results. At 200, and 290 kHz, the gain is approximately equal to $2\pi\times$ 1.6 $\times 10^5$, and $2\pi\times$ 6.5 $\times 10^4$ rad/s/V, respectively.

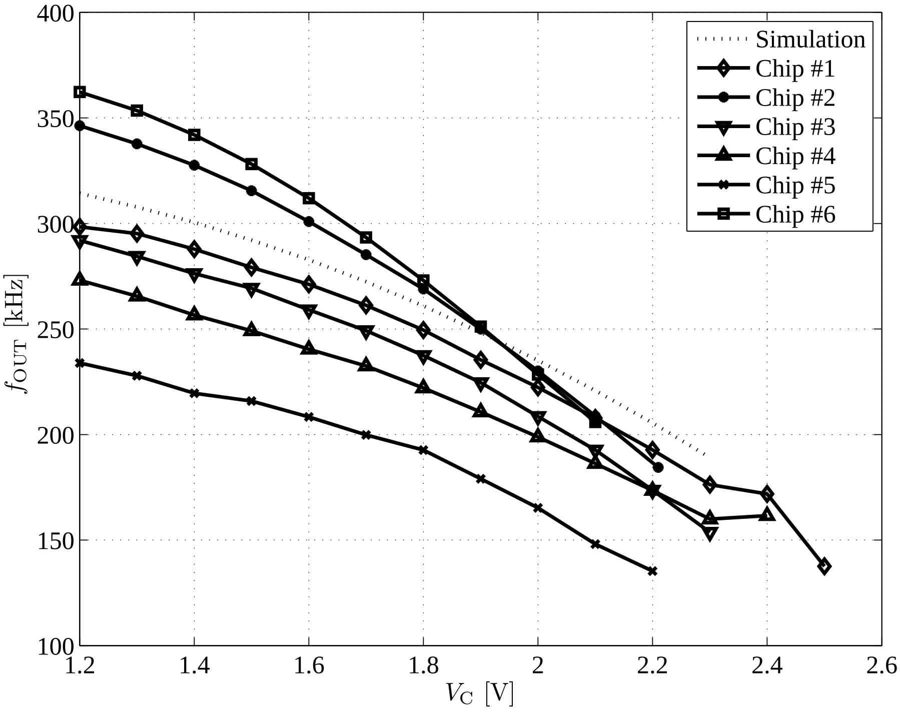

Figure 3.45: Output frequency versus input voltage characteristics of the VCO.

Obviously, the variations of output frequency are large and to be improved. The large variations are thought to be due to the small capacitances ($\sim$ 100 fF) of the VCO which are comparable to the input and output capacitance of the OTA. We increase the capacitances of the C_1 and C_2 to 28.6 and 20 pF for the integration into the PLL. To maintain frequency range of the VCO, the G_{m} are increased ten-fold. The resistors R_1 to R_4 are 32 kΩ, 13 kΩ, 22 kΩ, 22 kΩ, respectively.

Two OTAs which have different G_{m} are applied to the modified VCO in order to ensure the larger gain than 0 dB. Figure 3.46 shows the controlled G_{m} of the OTAs. G_{m1} is approximately twice as much as $G_{\mathrm{m2,3,4}}$ at the same V_{C}'. G_{m} of the both OTAs linearly rises at higher voltage at 0.95 V. G_{m1} changes its behavior at higher V_{C}' than 1.3 V. Since the current in M_1 is increased to be equal to the current in M_3 at the voltage, the incremental voltages decreases the current in M_6 and the gate voltage of M_4. However, the linear voltage region can applicable to the VCO with the larger G_{m} than the former one. I_{B1}, I_{B2}, and $W_{\mathrm{M_3}}/L_{\mathrm{M_3}}$ are 320 μA, 24 μA, and 90 μm / 1.2 μm, respectively. $W_{\mathrm{M_1}}/L_{\mathrm{M_1}}$ is 24 μm / 6 μm for G_{m1} and 24 μm / 6 μm for $G_{\mathrm{m2,3,4}}$. Figure 3.47 indicates the simulation results of the control voltage and oscillation frequency characteristics. The gain of the modified VCO, K_V is $2\pi\times$ 1.6 $\times 10^5$ and $2\pi\times$ 3.2 $\times 10^5$ rad/s/V at 192 kHz (N = 32), and 320 kHz (N = 64), respectively. The phase of the transfer function of the VCO is inverted due to the V_{tn} cancelling circuit.

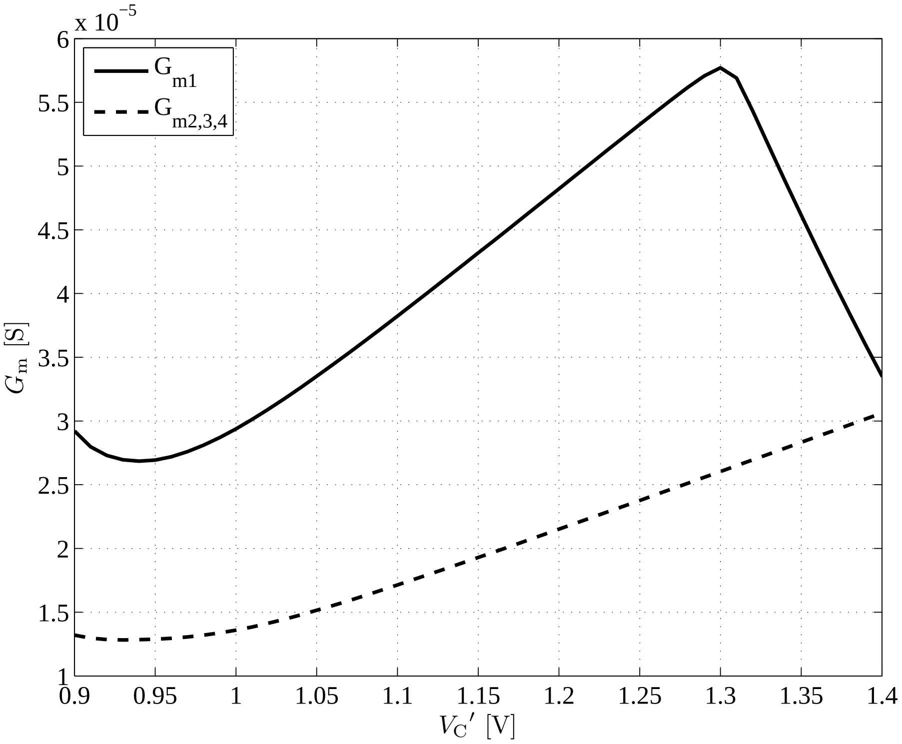

Figure 3.46: Controlled G_m by the control voltage V_C' of the OTAs for the modified VCO.

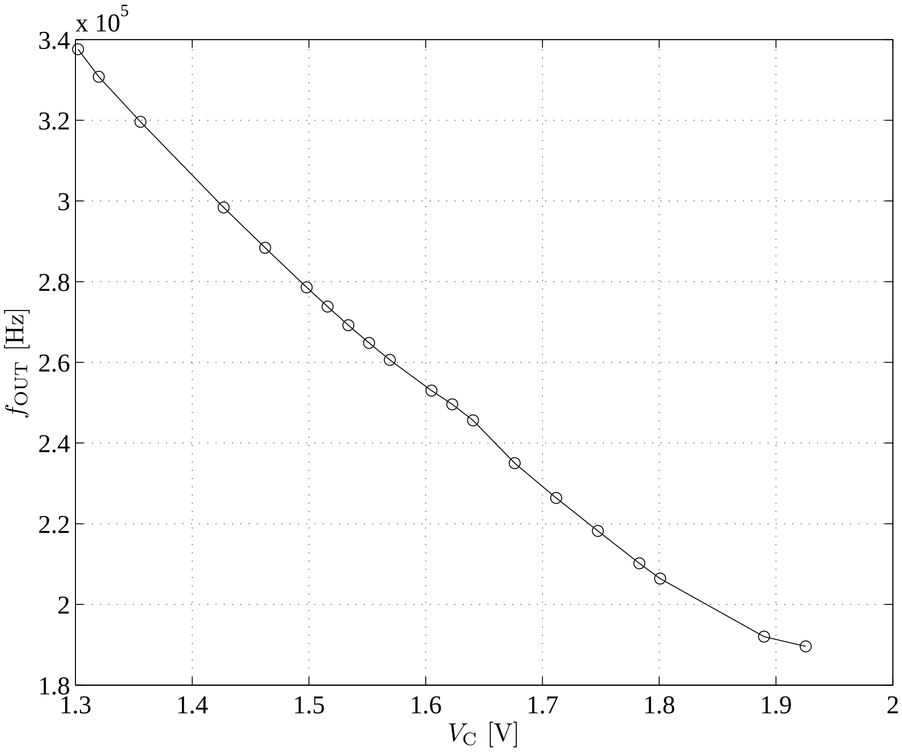

Figure 3.47: Output frequency versus input voltage characteristics of the modified VCO.

3.9.2 Phase Frequency Comparator and Divider

The phase frequency comparator shown in Fig. 3.48 is applied to the phase comparator. The reference and divided signals of θ_{REF} and θ_{OUT}/N are input to $\mathrm{IN}_{\mathrm{REF}}$ and $\mathrm{IN}_{\mathrm{SIG}}$. The outputs of two D flip-flops $\mathrm{OUT}_{\mathrm{U}}$ and $\mathrm{OUT}_{\mathrm{D}}$ changes from the low level (ground) to high level (V_{DD}) at the negative edge of $\mathrm{IN}_{\mathrm{REF}}$ and $\mathrm{IN}_{\mathrm{SIG}}$, respectively. The flip-flops are reset when both $\mathrm{OUT}_{\mathrm{U}}$ and $\mathrm{OUT}_{\mathrm{D}}$ becomes high level. Then, the period in which $\mathrm{OUT}_{\mathrm{U}}$ or $\mathrm{OUT}_{\mathrm{D}}$ is the high level is proportional to the delay between $\mathrm{IN}_{\mathrm{REF}}$ and $\mathrm{IN}_{\mathrm{SIG}}$. The advantage of this circuit is possible to compare frequency of the $\mathrm{IN}_{\mathrm{SIG}}$ with that of $\mathrm{IN}_{\mathrm{REF}}$. When the $\mathrm{IN}_{\mathrm{SIG}}$ has higher frequency than $\mathrm{IN}_{\mathrm{REF}}$, pulses appear more frequently at $\mathrm{OUT}_{\mathrm{U}}$ than $\mathrm{OUT}_{\mathrm{D}}$.

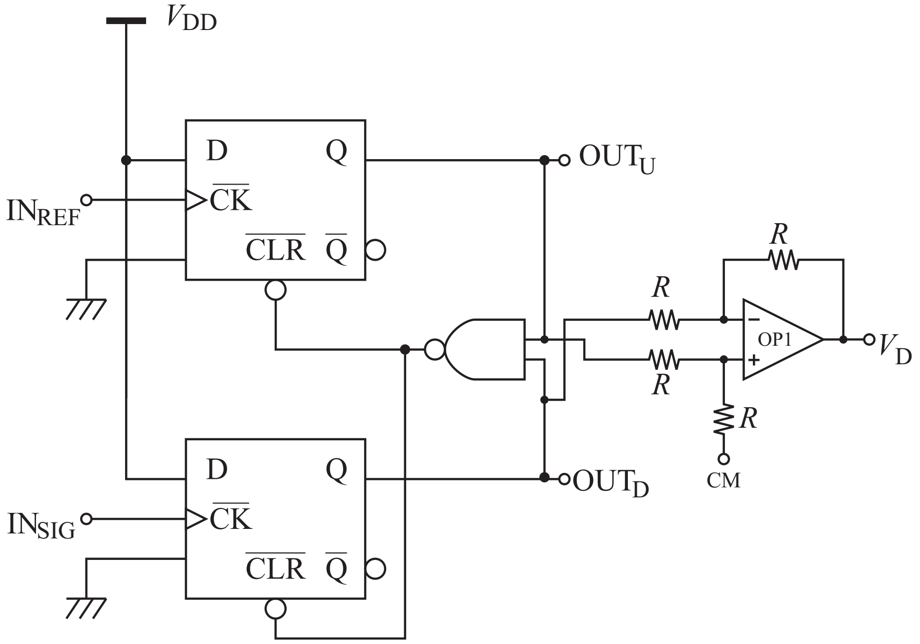

Figure 3.48: Circuit diagram of the phase frequency comparator.

Figure 3.49 shows the simulated pulse widths of the detection pulse signals of the phase comparator. When the delay of the input signals of the phase comparator is positive, only the $\mathrm{OUT}_{\mathrm{U}}$ has non-zero pulse width. On the contrary, the pulse width of only $\mathrm{OUT}_{\mathrm{D}}$ is proportional to the delay when the delay is negative.

The unity gain differential amplifier placed behind the D flip-flops converts the two output pulses into the input voltage to the loop filter. The mean voltage of V_{D} changes linearly as shown in Fig. 3.50, where the frequency of the reference and compared signals are 5 kHz. The horizontal axis means the phase delay of the $\mathrm{IN}_{\mathrm{SIG}}$ to $\mathrm{IN}_{\mathrm{REF}}$. According to this result, the gain of the phase comparator K_{D} is determined to be $V_{\mathrm{DD}}/4\pi \simeq 0.263$.

For the divider, the six-bit binary counter is designed for simplicity and implemented by sequentially connected six flip-flops. The divider count value N is can be set to 2^m,

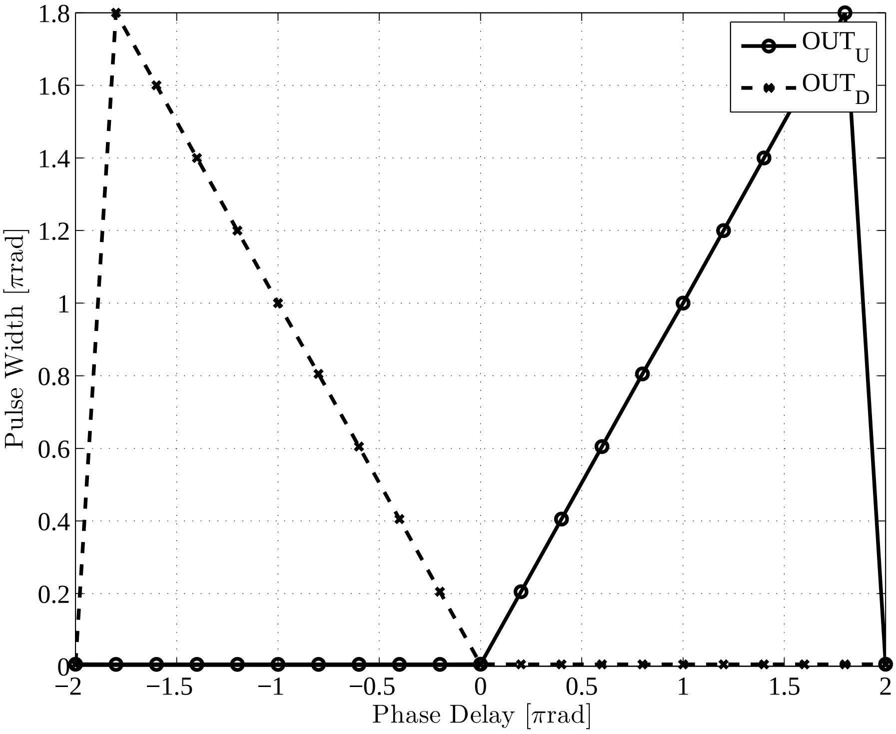

Figure 3.49: Simulation result of the pulse width of the detection pulse signals to phase delay of the input signal.

where m is an integer from 1 to 6, by multiplexing the each bit.

3.9.3 Loop Filter

The purposes of the loop filter are to pass the DC and low frequency component for the VCO and reject high frequency components of the reference and harmonics. Figure 3.51 shows the circuit diagrams of the filters to be options for the loop filter: lag, lag-lead, and lag-lead-lag filters composed of R and C. The lag filter is simply the first-order RC filter. Since the $H_{\mathrm{VCO-PC}}(s)$ has the phase of $-90°$, the open-loop characteristics with the lag filter could have phase of nearly $-180°$ over the cutoff frequency of the filter. Then, the lag-lead or lag-lead-lag filters are used for the loop filter in order to produce phase-lead. The lag-lead filter is simpler and has less enough attenuation in high frequency band than the lag-lead-lag filter.

We chose the lag-lead-lag filter to obtain the good spurious rejection performance. The lag-lead-lag filter has the transfer function indicated in Eq. (3.60).

$$H_{\mathrm{LF}}(s) = \frac{1+\dfrac{s}{\omega_{\mathrm{z}}}}{\left(1+\dfrac{s}{\omega_{\mathrm{p1}}}\right)\left(1+\dfrac{s}{\omega_{\mathrm{p2}}}\right)}, \tag{3.60}$$

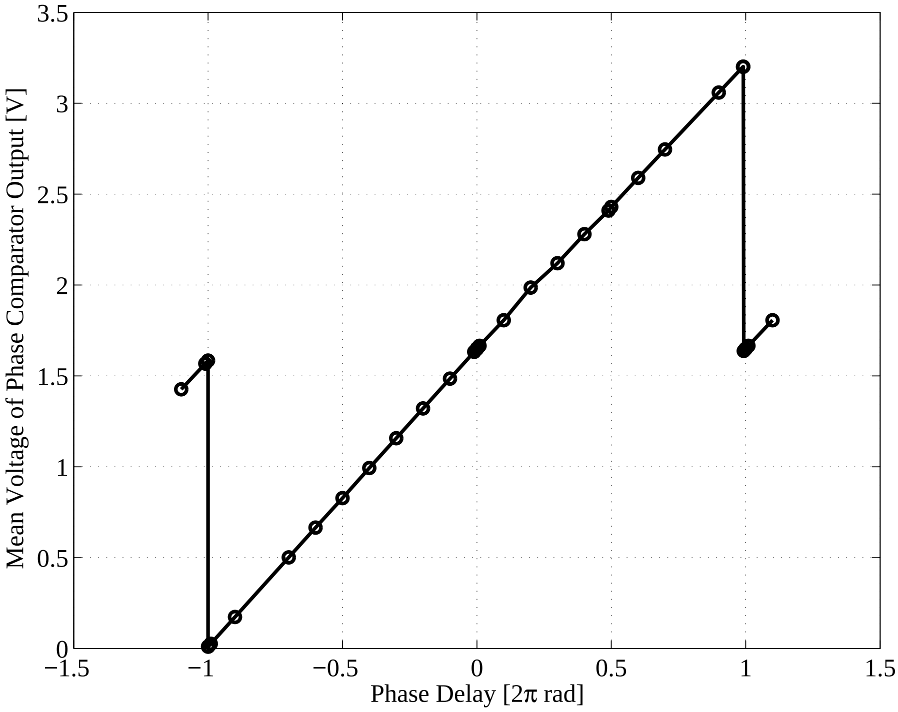

Figure 3.50: Simulation result of the phase delay versus the mean voltage of the phase comparator output.

where ω_{z}, ω_{p1}, and ω_{p2} are zero, the first and second poles, respectively. Assuming that $\omega_{\mathrm{p1}} < \omega_{\mathrm{z}} < \omega_{\mathrm{p2}}$, $H_{\mathrm{LF}}(j\omega)$ shows the frequency response in Fig. 3.52, where $\omega_{\mathrm{z}}/\omega_{\mathrm{p1}} = 10$, and $\omega_{\mathrm{p2}}/\omega_{\mathrm{p1}} = 500$, respectively. The flat gain response appears in higher frequency than ω_{p1}. The maximum phase return is obtained at $\sqrt{\omega_{\mathrm{z}}\omega_{\mathrm{p2}}}/\omega_{\mathrm{p1}} = \omega_{\mathrm{m}}/\omega_{\mathrm{p1}} = 70.7$. The attenuation at ω_{m} is -20 dB. These parameters are determined by considering requirements for the PLL and characteristics of the VCO, phase comparator, and divider.

Parameters shown in Table 3.10 have been obtained from the design of the other components in order to design the loop filter. Figure 3.53 shows frequency response of

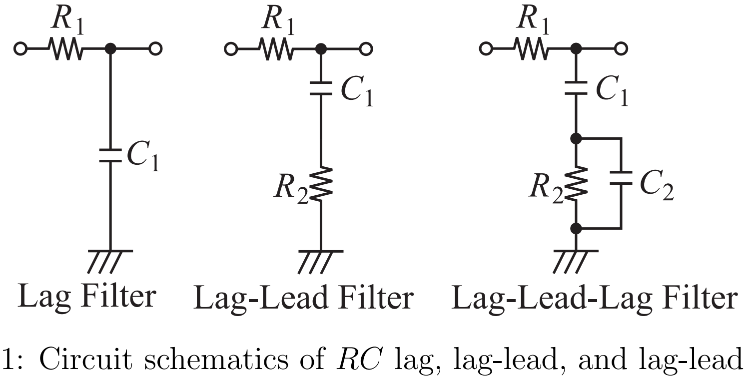

Figure 3.51: Circuit schematics of *RC* lag, lag-lead, and lag-lead-lag filters.

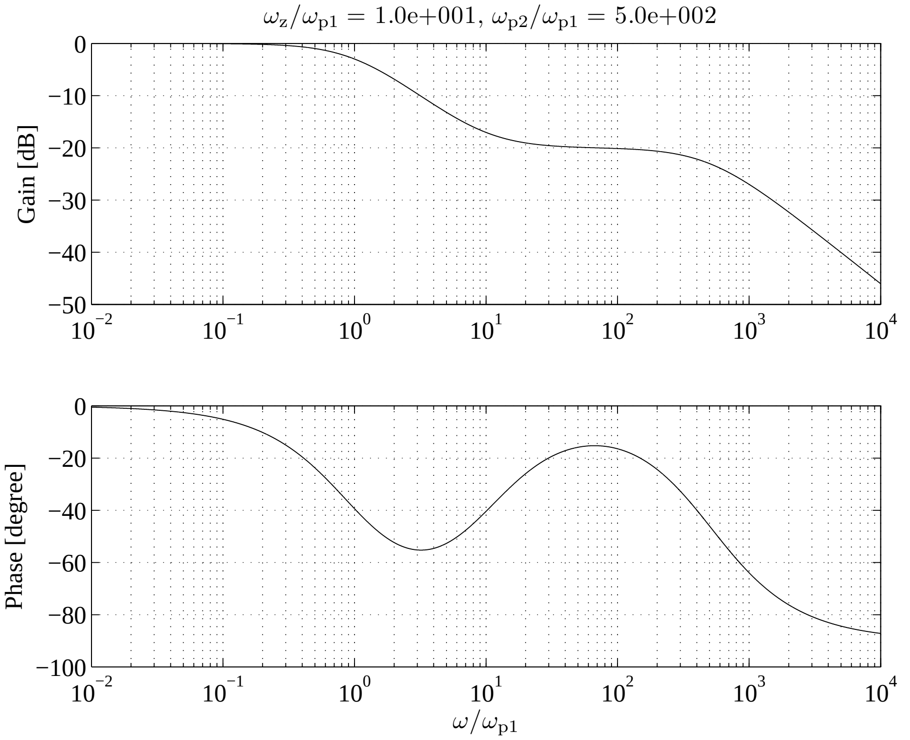

Figure 3.52: Frequency response of the lag-lead-lag-filter. Upper panel: Gain, and lower panel: phase.

the $-H_{\mathrm{VCO-PC}}(s)$ with the parameters in Table 3.10. The minus sign of $-H_{\mathrm{VCO-PC}}(s)$ means the phase of 180° of the VCO. The unity gain frequency of the $-H_{\mathrm{VCO-PC}}(s)$ is 1.31 kHz.

Table 3.10: Parameters for design of the loop filter.

f_{OUT}	192 kHz	320 kHz
N	32	64
K_{D}	$3.3/4\pi$	
K_{V}	$2\pi\times$ 1.6 $\times 10^5$	$2\pi\times$ 3.2 $\times 10^5$

In the present thesis, the lock time of the PLL is needed less than 40 ms. This leads the open-loop response to have unity gain frequency of higher than 25 Hz. The phase margin of the open-loop characteristics is at least required to be more than 30° for stability.

Figure 3.54 shows the circuit diagram of the loop filter. The G$_{\mathrm{m}}$–C filter is applied to the loop filter with the variable characteristics of G_{m} OTA shown in Fig. 3.42 in order to have capability for fine adjustment of G_{m} . Since the G_{m} is low on accuracy, the fine adjustment is desirable. Controlling each V_{C} of the OTAs enables the G$_{\mathrm{m}}$–C filter to change its gain, and frequencies of pole and zero. Since the capacitor C_1 and C_2 used in the loop filter are need to be more than 1 nF, the external ceramic capacitors are used in

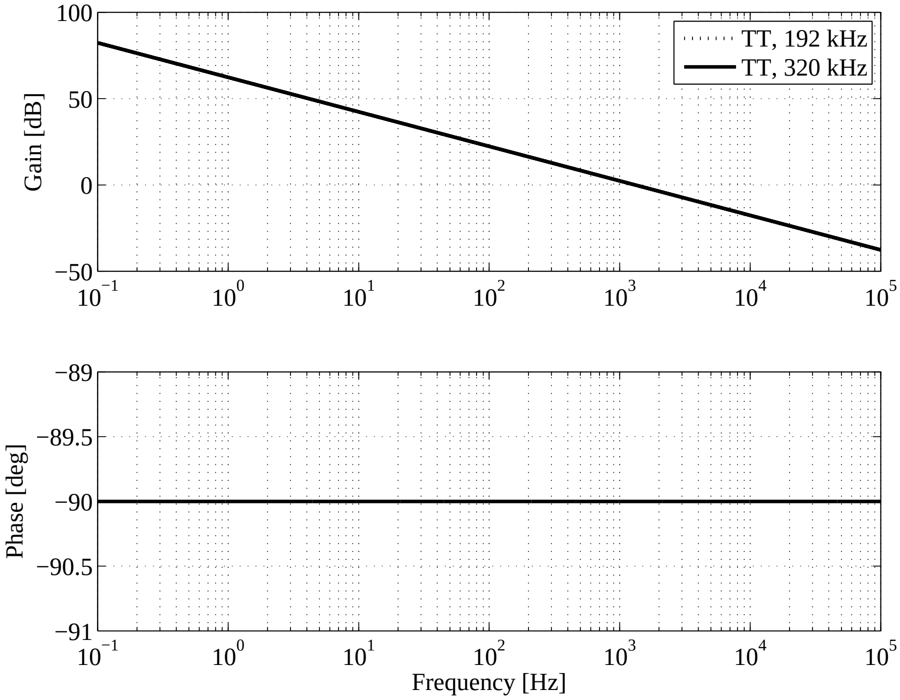

Figure 3.53: Frequency response of the $H_{\mathrm{VCO-PC}}(s)$. Upper panel: Gain, and lower panel: phase.

order to eliminate vast internal capacitance area.

The transfer function of the loop filter is expressed in Eq. (3.61).

$$H_{\mathrm{LF}}(s) = \frac{-\dfrac{G_{\mathrm{m1}}}{G_{\mathrm{m2}}}\left(1+s\dfrac{C_1+C_2}{G_{\mathrm{m3}}}\right)}{1+s\left(\dfrac{C_1}{G_{\mathrm{m2}}}+\dfrac{C_1+C_2}{G_{\mathrm{m3}}}\right)+s^2\dfrac{C_1C_2}{G_{\mathrm{m2}}G_{\mathrm{m3}}}}. \tag{3.61}$$

The poles, zero and gain are shown in following equations.

$$\left.\begin{aligned} \omega_{\mathrm{p1}} &= \frac{G_{\mathrm{m2}}G_{\mathrm{m3}}}{(G_{\mathrm{m2}}+G_{\mathrm{m3}})C_1}, & \omega_{\mathrm{p2}} &= \frac{G_{\mathrm{m3}}}{C_2} \\ \omega_{\mathrm{z}} &= \frac{G_{\mathrm{m3}}}{C_1+C_2}, & \omega_{\mathrm{m}} &= \frac{G_{\mathrm{m3}}}{\sqrt{C_2(C_1+C_2)}} \\ |H_{\mathrm{LF}}(0)| &= \frac{G_{\mathrm{m1}}}{G_{\mathrm{m2}}}, & |H_{\mathrm{LF}}(j\omega_{\mathrm{m}})| &= \frac{G_{\mathrm{m1}}}{G_{\mathrm{m2}}+G_{\mathrm{m3}}} \end{aligned}\right\} \tag{3.62}$$

The frequency response of the loop filter obtained by simulation is indicated in Fig. 3.55, where G_{m1}, G_{m2}, G_{m3}, C_1, and C_2 are 0.89 μS, 0.28 μS, 4.8 μS, 100 nF, and 10 nF, respectively. Figure 3.56 shows the frequency response of the open-loop in the PLL, which is obtained for the product of $H_{\mathrm{LF}}(s)$ and $H_{\mathrm{VCO-PC}}(s)$. The phase margin of 30° is ensured at the unity gain frequency of 140 Hz.

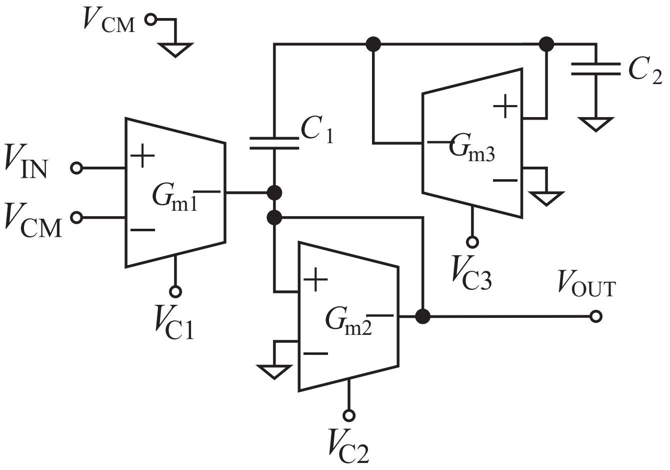

Figure 3.54: Circuit diagram of the loop filter.

3.9.4 Closed-Loop Operation

Lock in operation of the PLL is confirmed for the two conditions of (a): $f_{\mathrm{REF}} = 5$ kHz, $N = 64$, and (b): $f_{\mathrm{REF}} = 6$ kHz, $N = 32$. The initial condition is free-running operation where f_{OUT} is 250 kHz.

Figures 3.57 and 3.58 indicate time evolution of f_{OUT} and voltage output of the loop filter. Both figures are similar to the mirror symmetry of each other because of inversion by the V_{tn} cancelling circuit in the VCO. The non-smoothed traces in Fig. 3.57 are inverse numbers of each cycle of oscillation waveforms. The lock time criterion ($<$ 0.1 % of the convergent value) is applied to the smoothed traces, obtained by calculating moving average the non-smoothed traces with duration 0.1 ms. The removed components are considered to be spurious, phase noise, and error caused by finite time resolution. The calculated lock time is 32 and 17 ms for the conditions (a) and (b), respectively. The requirement for the lock time in the present thesis is satisfied. The longer lock time of the condition (a) is caused by smaller gain of the VCO K_{V} at the free-running frequency than that at the lock frequency for the condition (a). Considering sweeping f_{OUT} from end to end at one time, the decremental sweeping from 290 to 200 kHz is the better choice because of the lock time difference between the conditions (a) and (b). Assuming it takes as 2.5 times longer as the lock time (b) to change f_{OUT} from 290 to 200 kHz, the lock time for end-to-end sweeping becomes 51 ms. Thus, the lock time requirement for the SFA would be satisfied in the most severe case.

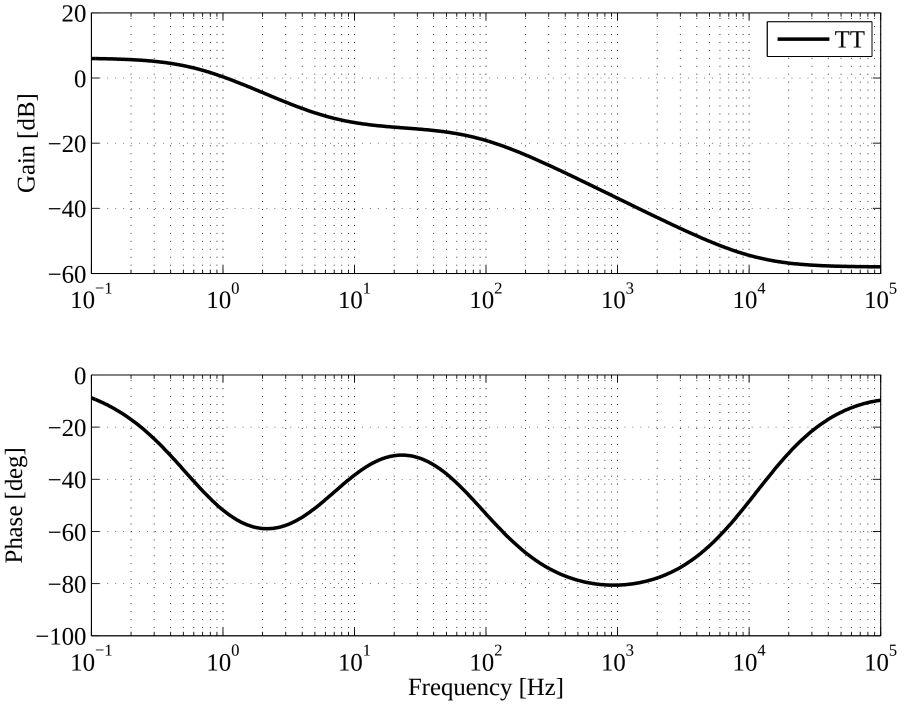

Figure 3.55: Simulation result of the frequency response gain (upper panel) and phase (lower panel) of the loop filter under the each corner condition.

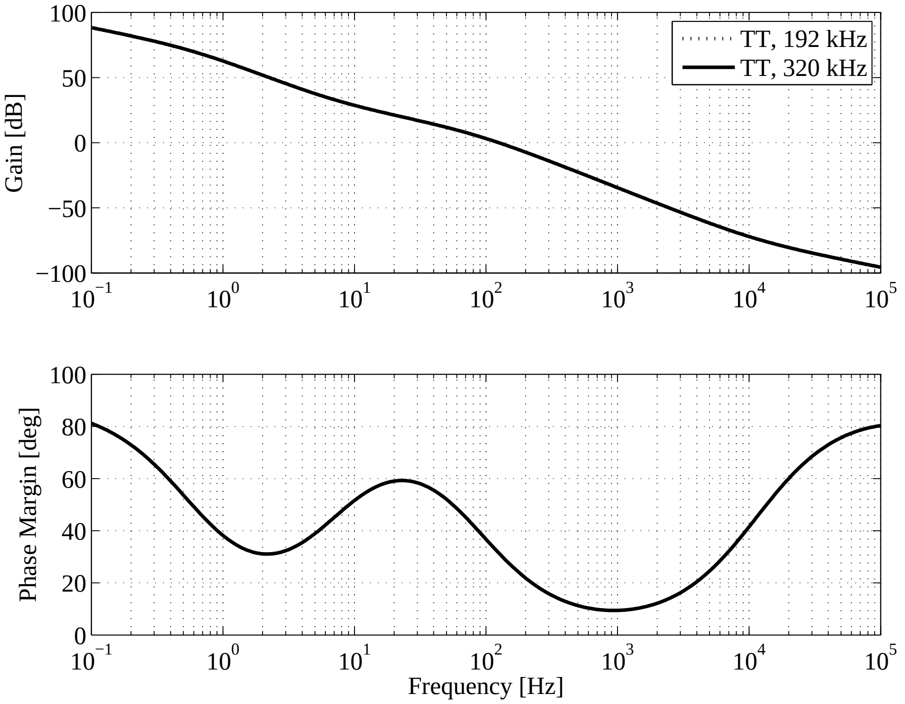

Figure 3.56: Simulation result of the frequency response gain (upper panel) and phase (lower panel) of the open-loop in the PLL under the each corner condition.

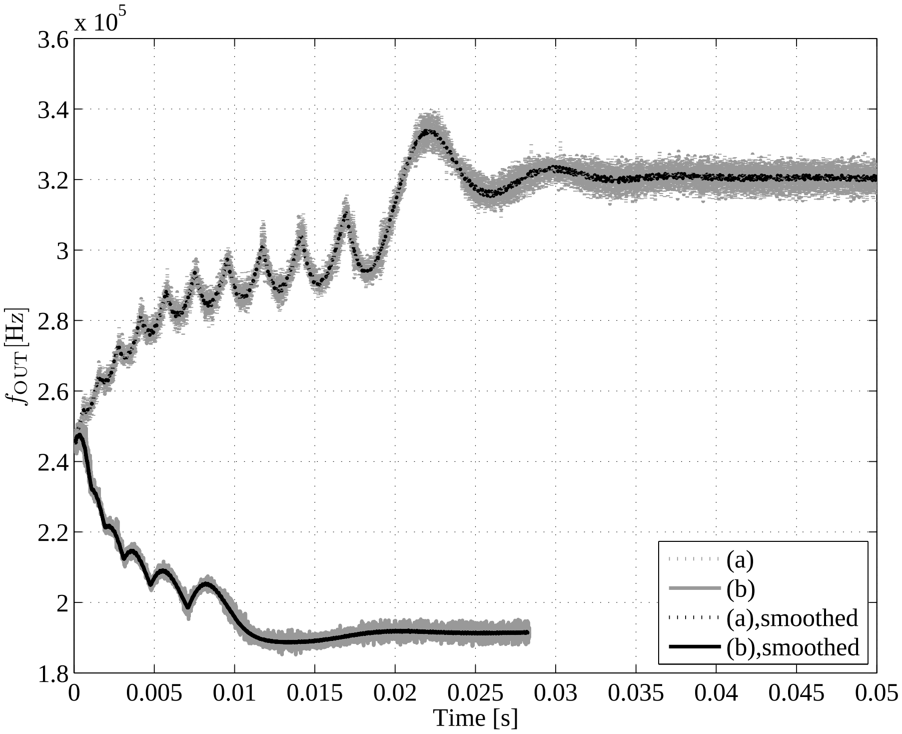

Figure 3.57: Time evolution of f_{OUT} for two conditions of $f_{\mathrm{REF}} \times N$: (a) 5kHz × 64, and (b) 6kHz × 32.

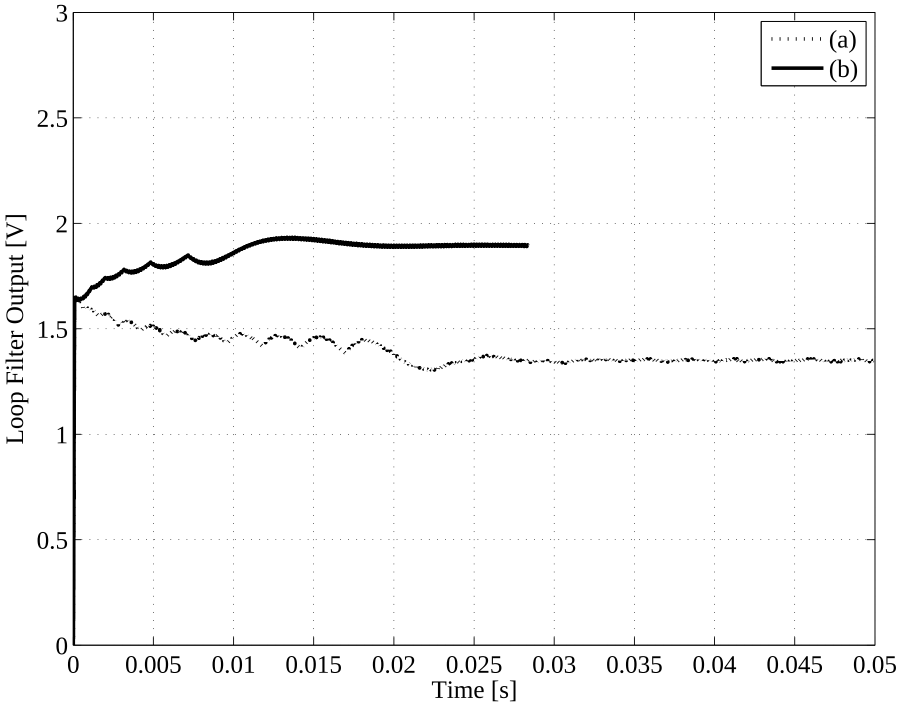

Figure 3.58: Time evolution of the loop filter output for the conditions of (a) and (b).

3.10 Conclusions

In this chapter, we demonstrated components circuits of the waveform receiver and spectrum analyzer for plasma wave observations. The G_m–C low pass filters with temperature compensation, gain switching differential amplifier, and the switched capacitor low pass filter for anti-aliasing were developed with the ASIC for the waveform receiver. The performances and several existing errors from the simulation results of these components were shown and discussed. As a result, all the target components are accepted to be integrated into a system chip of the waveform receiver. The integrated system chip and the miniaturized waveform receiver are to be introduced in the next chapter.

The spectrum receiver of the sweep frequency analyzer (SFA) is a double super heterodyne receiver. The band pass filter for image rejection, which is three cascaded sixth-order Chebyshev band pass filter, was realized inside the ASIC. The double-balanced type mixer was also developed and showed mixing operation with acceptable linearity. The phase-locked loop (PLL) for frequency synthesizer is the most significant component in the SFA. The voltage controlled oscillator, the loop filter, phase comparator, and divider were designed for the PLL. In order to confirm locking in of the output frequency, closed-loop operations of the PLL were simulated. The lock time requirements were satisfied in the conditions which cover the requirements for the SFA.

Chapter 4

Miniaturized Plasma Wave Receivers

4.1 Introduction

The objective of the present paper is to demonstrate the overall performance of the developed system chip and to introduce a tiny circuit board for a waveform receiver. The ASIC is fabricated using the TSMC 0.25-μm CMOS process. The size of the waveform receiver was successfully reduced to 45$\times$50 mm^2, which is approximately half the size of a business card. The sensitivity and dynamic range are acceptable for scientific observation missions

4.2 Specifications

The specifications of the tiny waveform receiver are summarized herein and compared with the NOZOMI (previous Japanese Mars explorer mission) low-frequency analyzer (LFA) in Table 4.1. NOZOMI was spacecraft for the previous Japanese Mars explorer mission [37].

Table 4.1: Specifications of the waveform receiver.

	Present Design	NOZOMI LFA
Electric Field	Three components	Two components
Magnetic Field	Three components	None
Upper Limit Freq.	100 kHz	32 kHz
Sampling Frequency	400 kHz	100 kHz
Gain	0,20,40 dB	0,20 dB
Dynamic Range	78 dB (14 bit)	90 dB (16 bit)
Sensitivity	-120 dBV/$\sqrt{\text{Hz}}$ @ 1 kHz -140 dBV/$\sqrt{\text{Hz}}$ @ 100 kHz	-117 dBV @ 1 kHz -111 dBV @ 32 kHz
Size of Analog Part	45 × 50 mm^2	1/3 of A4-size
Power Consumption	$<$ 800 mW	- [1]

The specifications of the tiny waveform receiver are generally superior to those of the LFA in most respects. The details of the system chip and peripheral circuitries that satisfy these the specifications are described in following sections.

4.3 Integrated Waveform Receiver

In Chapter 3, the component circuits of the waveform receiver were developed and evaluated. A block diagram of the system chip is shown in Fig. 4.1. The system chip includes the analog circuitry, except for the preamplifiers and A/D converters. The layout of the system chip is shown in Fig. 4.2, in which the six channels appear stacked horizontally, and the dimensions are 3.77×3.01 mm^2. The indications (a) through (e) are correspond to those in Fig. 4.1. A photograph of the system chip is shown in Fig. 4.3. The manufactured chip is contained in an 80-pin quad flat package. The bonding wires connect to the pins through electrostatic discharge protection pads inside the chip. The dimensions of the die and the package are 5×5 mm^2 and 15×15 mm^2, respectively.

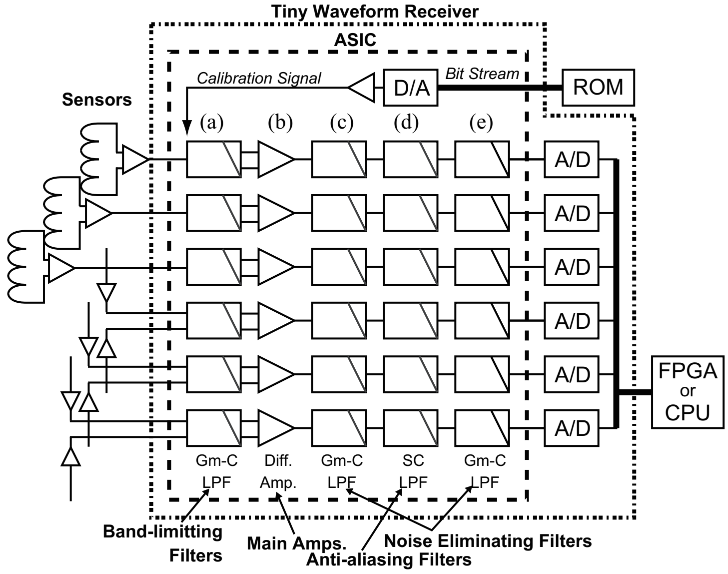

Figure 4.1: Block diagram of the system chip for the waveform receiver (Reprint of Fig. 2.4).

Figure 4.4 shows the typical gain and phase frequency response performance of the system chip for each gain-setting. Within the pass band, gains of −2.38, 17.1, and 36.1 dB are observed for the each gain-setting. The differences in these gains from the designed gains are due to the output conductance error of the internal OP-amps as described in Chapter 3.

---

[1] Exclusive power consumption of the NOZOMI LFA is unstated.

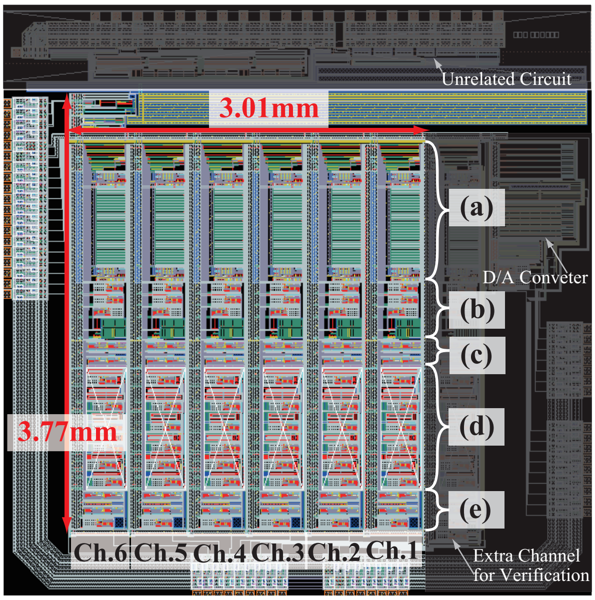

Figure 4.2: Layout design of the system chip.

The pass-band gain and dynamic range at 1 kHz and 100 kHz are shown in Table 4.2 with the correspond gain in attenuation band which causes aliasing. The effective bits of the A/D converter decreases to 10-bit for the low gain setting. The medium and high gain setting ensure the dynamic range implied by 14-bit resolution of the A/D converter.

Table 4.2: Gain and dynamic range at 1 and 100 kHz with correspond gain that causes aliasing.

Gain Setting	Low	Medium	High
Gain @ 1 kHz [dB]	−2.38	17.1	36.1
Gain @ 399–401 kHz [dB]	−60	−62	−39
Dynamic Range @ 1 kHz [dB]	62	79	75
Gain @ 100 kHz [dB]	−4.16	14.9	33.7
Gain @ 300/500 kHz [dB]	−64/−58	−62/−62	−36/−47
Dynamic Range @ 100 kHz [dB]	54	75	70

A block diagram of the overall waveform receiver is shown in Fig. 4.5. A +5 V power supply, the ground level, and six differential pairs of input signals are fed to the waveform receiver. Common-mode noise on the power line is rejected in the common-mode choke coil. The 3.3 and 1.6 V power supplies for the system chip are supplied from the two regulators. The other devices also operate with the regulated 3.3 V power supply. The reference current can be determined using an external variable resistor, so that the reference current may be changed. The crystal oscillator generates a 10 MHz clock

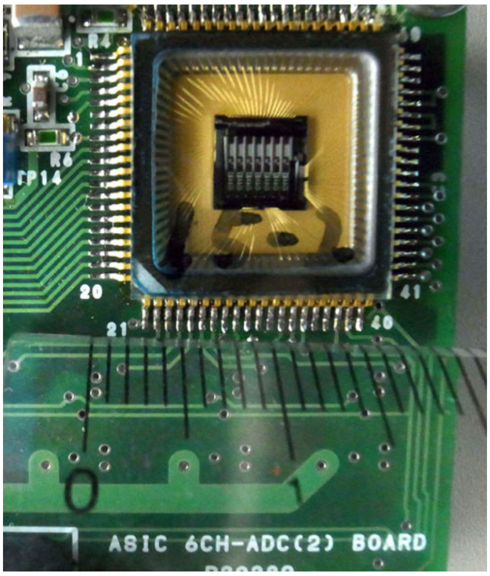

Figure 4.3: Photograph of the system chip enclosed in the package.

signal, which is fed to the ASIC, the A/D converters, and the divider through two series inverters. The divider produces a sampling frequency of 400 kHz. Six A/D converters operate synchronously with the sampling frequency and output digitized signals of the waveforms. Each bit of the A/D converter output is serial.

Table 4.3 presents the model number, current, and power loss of all the devices in the waveform receiver. The percentages of the power loss are presented in Fig. 4.6 The regulator for 3.3 V and the ASIC account for a large portion of the power consumption. Therefore, these two devices should have specified heat radiators for a flight module.

Table 4.3: Device model, current and power consumption of peripheral circuitries.

Device	Model Number	Current [mA]	Power [mW]
Common-mode Choke Coil	ACM4532-801-2P		
Regulator (3.3 V)	LM1117	94	197
Regulator (1.6 V)		10	52
Crystal Oscillator	KC7050B10.0000C31A00		
Inverter	TC7PA05FU		0.09
Divider	TC74HC40102		0.01
A/D Converters	LTC2355I-14	5.5 × 6	18 × 6
ASIC		50	165
Total		105	525

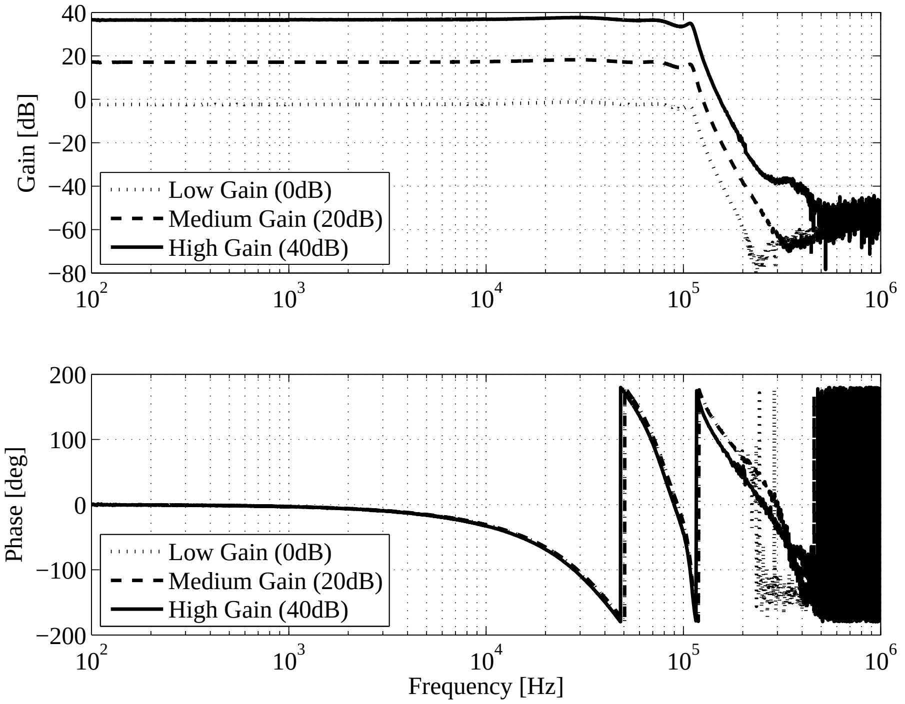

Figure 4.4: Gains and phases for the frequency response of the chip on the waveform receiver module. The pass band gain can be set to three different values: low (0 dB), medium (20 dB), and high (40 dB) gain.

4.4 Overall Evaluation

Figure 4.7 shows photographs of the fabricated waveform receiver. The panels (a) and (b) in Fig. 4.7 show the top and back of the printed circuit board, respectively. The system chip is installed on the upper-right corner of the top side. Two 15-pin MDM connectors are used: one for the power lines and input signals, and the other for the output signals. The A/D converters, oscillator, and the divider on the back are separated from the analog ground plane by the digital ground plane inside the board.

The dimensions of the waveform receiver board are 45×50 mm^2. Compared to the LFA presented in Table 4.1, the area per observation channel of the present device is reduced to less than 1/20. The weight and power consumption of the receiver are 24.9 g and 525 mW, respectively.

Figure 4.8 shows the measurement results for crosstalk of the circuit board and system chip. The crosstalk of the system chip is larger than that of the circuit board, because of the coupling in the chip-testing board. Crosstalk is typically required to be less than -50 dB. In Fig. 4.8, the crosstalk requirement is fulfilled at frequencies lower than 20 kHz. Although the crosstalk becomes larger than the typical requirements in the frequency

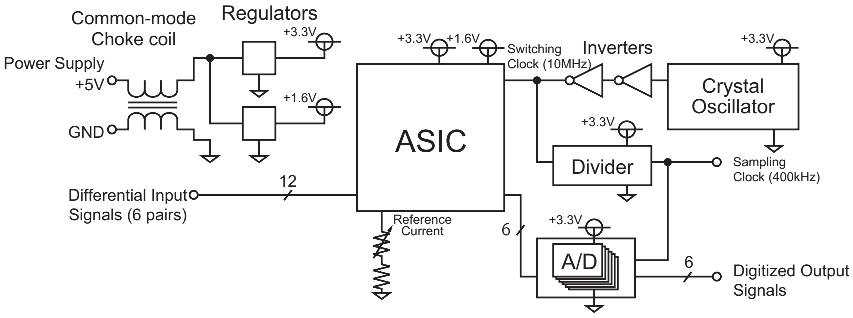

Figure 4.5: Block diagram of the waveform receiver.

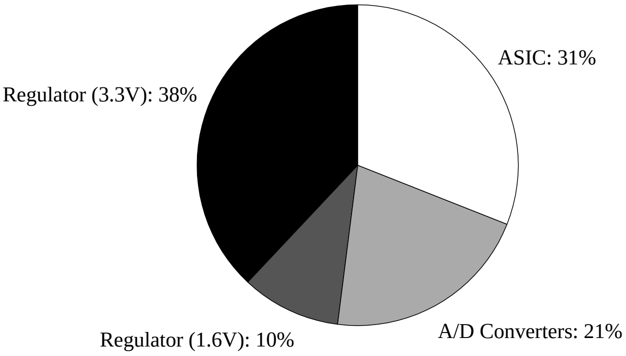

Figure 4.6: Percentages for power loss of the devices on the waveform receiver module.

band higher than 20 kHz, the crosstalk is acceptable up to −40 dB, compared to that for the search coil of the on-board BepiColombo/MMO [53].

The sensitivity of the circuit board shown in Fig. 4.9 is calculated from the measured output noise voltage densities at the input of the A/D converter and the frequency responses. The sensitivities for the medium- and high-gain configurations are better than that for low gain. The noise is amplified as much as the pass-band gain for the high-gain configuration, so that the sensitivity at high gain is approximately equal to that at medium gain. The sensitivity results indicate that the developed circuit board is suitable for use on scientific missions. However, the $1/f$ noise in the low frequency band raises considerable concern regarding the sensitivity. To reduce the $1/f$ noise, a chopper amplifier and correlated double sampling may be suitable.

It is assumed that the waveform receiver will operate in the temperature range from −30 to 60 °C. The correct operation of all components has been confirmed in this range by temperature testing. When the temperature changes from −30 to 60 °C, the change

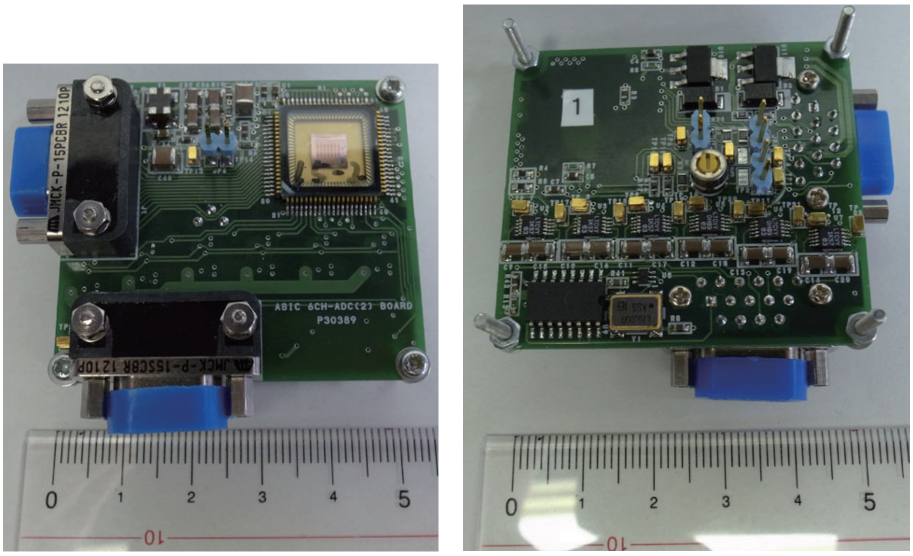

(a) Top side (b) Back side

Figure 4.7: Photographs of both surfaces of the fabricated waveform receiver.

in the gain at 10 kHz is −0.6, −2.1, and −1.8 dB for the low, medium, and high gain settings, respectively. The change in sensitivity at 10 kHz is −3.4, +0.7, and +0.8 dB for the respective gain settings. The cut-off frequency changes within +2 kHz. Thus, the developed waveform receiver is compatible with the thermal environment inside a spacecraft.

4.5 Conclusions

Plasma wave observations are very important in the understanding of space electromagnetic phenomena. The waveforms can provide not only amplitude but also phase information of the plasma waves. We have introduced a waveform receiver miniaturized to dimensions of 45×50 mm^2, which is half the size of a business card. The design and performance of the developed waveform receiver were described. A system chip that includes the analog components (six channels of filters and amplifiers) of the waveform receiver was developed. The frequency response, dynamic range, sensitivity, and temperature dependence were discussed. Downsizing with the system chip was demonstrated to be effective to realize an instrument that satisfies the requirements for miniaturization and plasma wave observation. Consequently, a miniaturized instrument is expected to be used on future multi-spacecraft and/or planetary exploration missions.

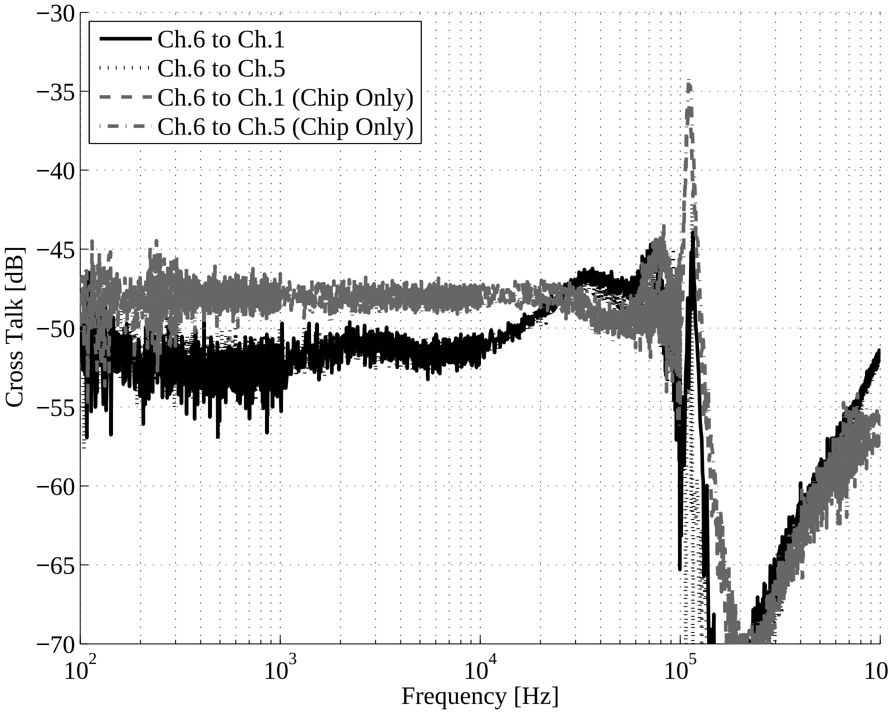

Figure 4.8: Crosstalk of the waveform receiver and the system chip from channel 6 to channels 1 and 5.

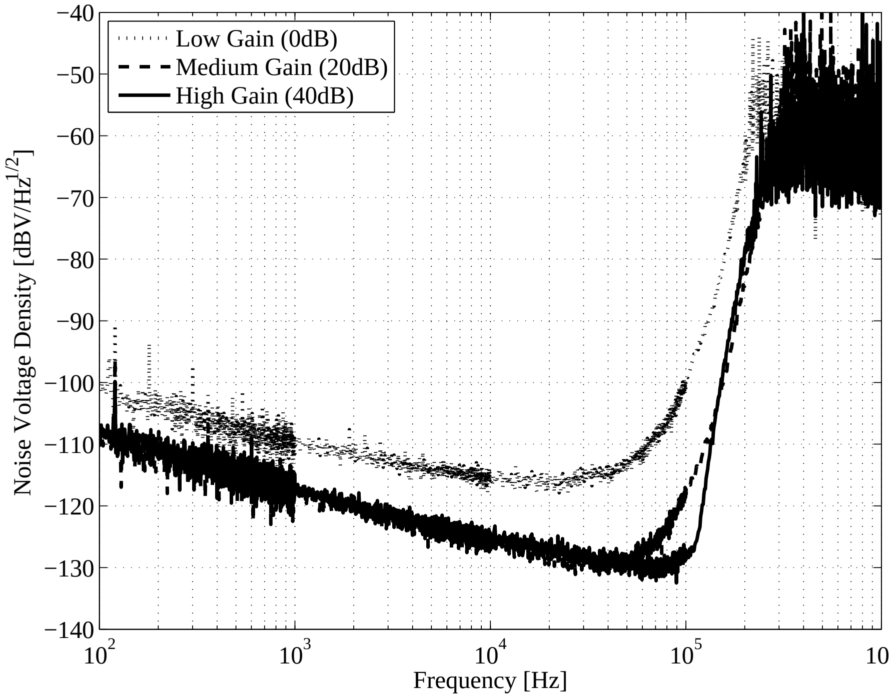

Figure 4.9: Sensitivities of the circuit board.

Chapter 5

Applications with Miniaturized Receivers

5.1 Introduction

In the present paper, we describe an attempt to develop a very small analog component for the plasma wave receiver using analog application specific integrated circuit (ASIC) technology. As described in the previous chapters, the analog ASIC enables several channels of plasma wave receivers to be installed in a small chip having dimensions of a few millimeters by a few millimeters. However, the design of the circuit is completely different from those realized with discrete electronic parts. The system chip for the waveform receiver with the ASIC was newly developed and installed on the tiny waveform receiver in Chapter 4. Six channels of analog components were implemented on the small system chip. The results revealed the analog ASIC promises for use in the miniaturization of plasma wave receivers.

New two applications with the miniaturized plasma wave receiver using ASIC are introduced in this chapter. The first is a monitoring system for variation and disturbance of local electromagnetic environment by a number of small sensor nodes, which observe plasma waves and work as a part of sensor network. Small sensor nodes of the sensor network are distributed throughout the target area. This system simultaneously monitors plasma wave activities at multiple points. Each small sensor node carries a very small plasma wave receiver with small sensors. The spectrum receiver based on analog ASIC technology such as the sweep frequency analyzer (SFA) introduced in Chapter 2 is suitable to the small plasma wave receiver for the sensor node. The following sections describe the sensor network system in space as an application of small plasma wave receivers.

The second application is a measurement system to determine a location of the plasmapause. The plasmapause is the boundary of the plasmasphere which more cold electrons and ions exist than other regions in the magnetosphere. For the measurement, actively radiated radio waves are received at several small satellite with onboard small plasma wave receiver. Following sections introduce and discuss these systems.

5.2 Sensor Network System in Space

Since the limitation of single-point observations in space is easily understood, missions such as the Cluster or THEMIS satellites, which involve multiple satellites, have become the trend in recent scientific missions. However, even if multiple satellites observations can be expected, the number of the observation points is limited, because the number of the satellites is limited by cost and the mass budget of the launch vehicles, for example. Such multiple satellite missions are not particularly well suited to the observation of inhomogeneous phenomena localized in relatively small regions. One example of inhomogeneous phenomena in space plasmas is the interaction between space plasmas and artificial structures. *Gurnett et al.* (1988) reported the existence of localized plasma wave turbulence and its inhomogeneity caused by the interaction between space plasmas and the space shuttle [54]. The spatial distribution of such plasma wave turbulence is not easily identified by single-point observations nor multiple-point observations with a limited number of satellites. However, knowledge about the turbulence around the artificial structures is crucial from a scientific point of view, as well as from the viewpoint of space development.

Based on the progress in the miniaturization of plasma wave receivers described in the previous chapters, a new system for monitoring the electromagnetic environment in space is proposed. This system provides one solution to resolve the above problem concerning the observation of spatial inhomogeneous phenomena in space. This system is referred to as the monitor system for space electromagnetic environments (MSEE). The MSEE is a sensor network system in space.

Figure 5.1 shows a schematic illustration of the MSEE, which consists of palm-sized sensor nodes. The sensor nodes are randomly distributed throughout the target area and simultaneously monitor plasma waves at multiple points. Each sensor node carries a compact plasma wave receiver as well as other necessary components, such as communications and digital processing units. The observed data are transferred to the central station, such as a space station or a satellite/rocket, through the ad-hoc network system. The objective of the MSEE is to observe plasma wave activities in multiple points. The targets of the MSEE are the artificial disturbances caused by human activities in space as well as natural plasma waves.

Figure 5.2 shows a schematic illustration of the MSEE sensor node. Tri-axes electric and magnetic field sensors are attached outside the body. The body is a cubic structure with sides of 7 cm. The body contains all of the necessary electrical components, such as a digital processing unit and a telemetry communication system, as well as a compact

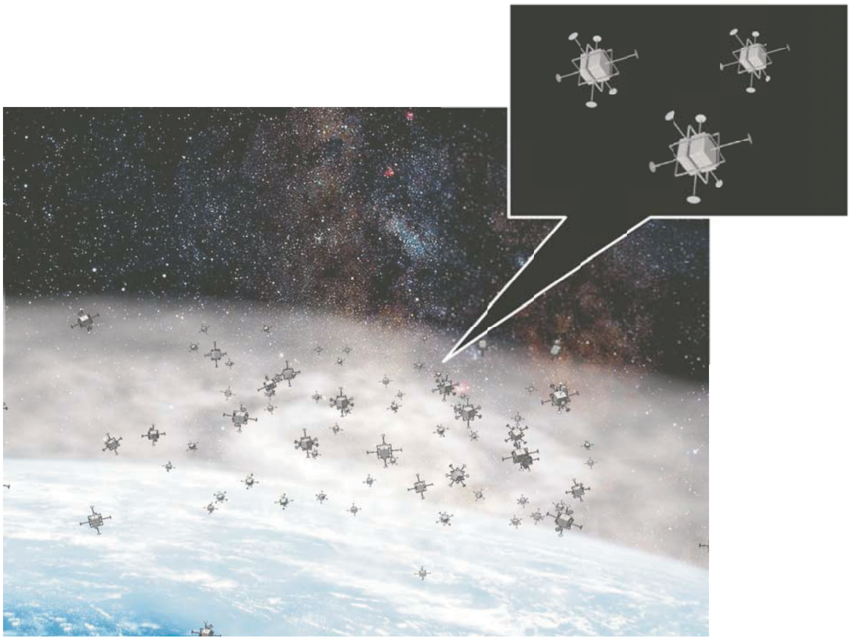

Figure 5.1: Schematic illustration of the MSEE sensor network system. The system consists of several small sensor nodes.

plasma wave receiver. The body is made of aluminum plates, the surfaces of which are covered by permalloy. The plates suppress the noise radiating from the inner electronic circuits. The sensors of the electric field and the magnetic field are installed outside the body. While the electric field sensors are top-hat type dipole antennas with a tip-to-tip length of 0.4 m, the magnetic sensors are square loop antennas with 15 turns with edges of 10 cm. The sensors observe full sets of electromagnetic components (three for electric and three for magnetic field components).

The target specifications of the MSEE sensor node are shown in Table 5.1. The concept of the MSEE sensor network is completely different from that of scientific satellites. The design of each sensor node is identical and the production costs are much cheaper than those of satellites. A few hours of the lifetime is enough for each sensor node after the distribution and the nodes are completely disposal. However, we can repeatedly distribute the nodes in the target area. This system is similar to the radiosonde, which is used for monitoring meteorological phenomena in the earth's atmosphere.

Figure 5.3 shows a block diagram of the MSEE sensor node in the present design. The power is supplied by a dry battery. The core part of the sensor node is the one-chip plasma wave receiver, which is realized by the analog ASIC. The design of the ASIC has not been fixed yet. Considering the total power consumption and signal-to-noise ratio (SNR), the sweep frequency analyzer (SFA) is suitable to the receiver for the MSEE sensor node. The prototypes of the necessary components of the SFA such as a bandpass filter, and mixer, have already been manufactured and tested.

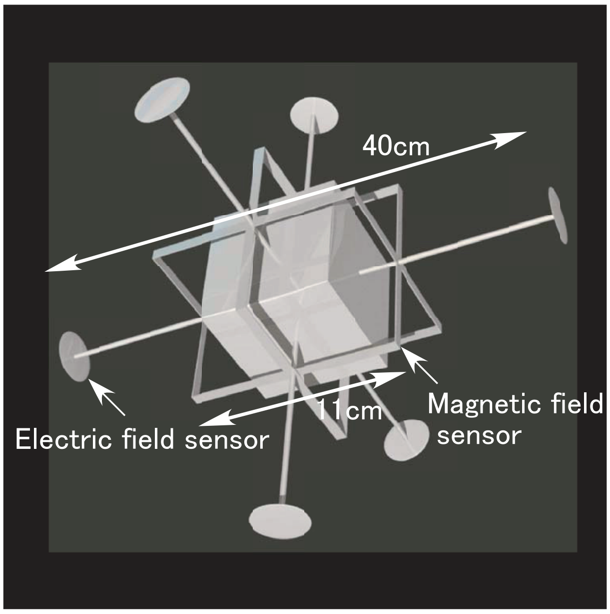

Figure 5.2: Schematic illustration of the MSEE sensor node.

The signals picked up by six sensors are fed into the one-chip plasma wave receiver through their preamplifiers. The preamplifiers are required to have high input impedance and to have very low noise at the input. Hence, they are not incorporated onto the analog ASIC.

The preamplifiers is specifically designed for the MSEE sensor node. They should be compact and low-noise amplifiers with sufficient gain to compensate for the disadvantage of the sensitivities of compact electromagnetic sensors. Figure 5.4 shows the measured equivalent input noise of the preamplifier of the electric field sensor. The lowest noise level is approximately equal to 10 nV/$\sqrt{\text{Hz}}$ at 500 kHz. The electronic circuit is very simplified so that it can be installed inside the small body. However, its performance is sufficient for use in scientific missions.

The digital part of the MSEE sensor node performs any necessary digital processing, such as the frequency analysis, in addition to the control of the MSEE sensor node system. The design of the digital part is under way, and we use the PIC device of Microchip Technology Inc. Since the system of the MSEE sensor node does not require a powerful processor, the PIC with several channels of inner A/D converters is appropriate for this system.

Figure 5.5 shows a prototype MSEE sensor node. The electric field and magnetic field sensors, along with their preamplifiers and a power supply system, are installed in this model. The equivalent input noise shown in Fig. 5.4 is measured in this prototype sensor node.

Whereas the length of the MSEE electric field sensor is 0.4 m tip-to-tip, the length

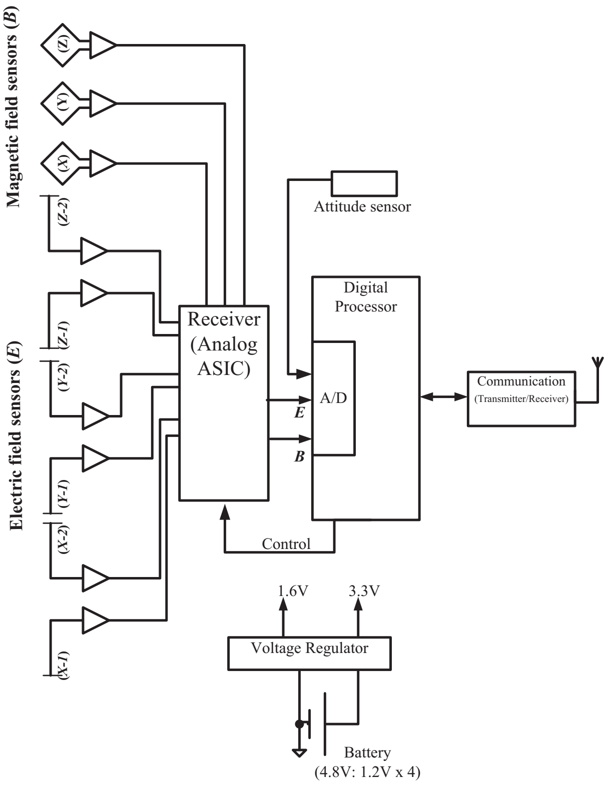

Figure 5.3: Block diagram of the MSEE sensor node in the current design.

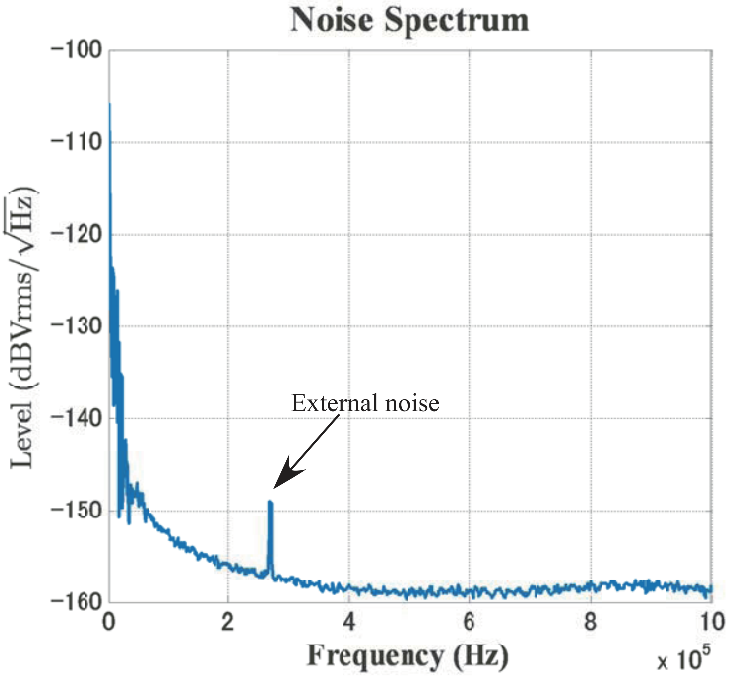

Figure 5.4: Equivalent input noise of the preamplifier for the electric field component.

Table 5.1: Specifications of the MSEE sensor node.

Sensors	
Dipole antenna (for the electric field)	
Length (radius)	40 cm (0.25 cm)
Sensitivity	$\sim 1\ \mu\mathrm{V/m}/\sqrt{\mathrm{Hz}}$ at 100 kHz
Loop antenna (for the magnetic field)	
Size	10 cm × 10 cm (15 turns)
Sensitivity	$\sim 0.1\ \mathrm{pT}/\sqrt{\mathrm{Hz}}$ at 100 kHz
Receiver	
Frequency	< 100 kHz
Output data	Spectrum
Time resolution	a few seconds
Power supply	Dry battery (4.8 V)
Attitude detection	Magnetometer and Sun sensor
Location estimation	GPS
Life time	> a few hours
Digital processor	PIC, Microchip Technology Inc.
Communication	2.4 GHz (Zigbee Standard)

of electric field sensors mounted on the GEOTAIL spacecraft launched in 1992 is 100 m tip-to-tip [12]. The disadvantage of the MSEE electric field sensor, as compared to the electric field sensors used in scientific satellites, is its short antenna length. Thus, it is important to evaluate the sensitivity of the MSEE electric field sensors. In general, the antenna impedance of the short dipole antenna is capacitive in a vacuum. The capacitance of the dipole antenna is derived as follows: [7, 55]

$$C_{\mathrm{a}} = \frac{\pi l}{\eta_0 c \ln \dfrac{2l}{a}}, \tag{5.1}$$

where l, η_0, c, and a denote the length of one antenna element, the characteristics impedance in vacuum, the speed of light, and the radius of the antenna element, respectively. When we use $l = 0.2$ m and $a = 0.0025$ mm, the antenna capacitance of the MSEE electric field sensor is calculated to be approximately 1 pF. Since the small disk is installed at the top of the MSEE electric field sensor, its capacitance is added to the capacitance of the dipole antenna. For reference, the antenna capacitance of the GEOTAIL electric field sensor is 113 pF [7].

On the other hand, concerning the input capacitance at the input of the preamp, the MSEE has an advantage over scientific satellites. Because the small input circuit leads to a small input capacitance. By measuring the prototype shown in Fig. 5.5, the input capacitance of the electric field preamps was found to be approximately 4.0 pF [56]. (The input capacitance of the GEOTAIL electric field sensor preamp is approximately 40 pF.)

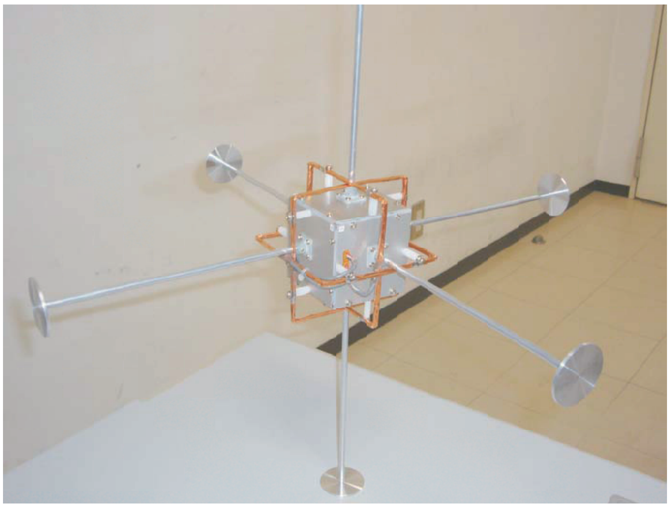

Figure 5.5: Second prototype of the MSEE sensor node.

The antenna impedance, the input circuits of the preamp, and the input capacitance determine the transfer function of $G_p(f)$ as the pick up factor:

$$G_{\mathrm{p}}(f) = \frac{V_{\mathrm{i}}(f)}{V_{\mathrm{a}}(f)} \tag{5.2}$$

where $V_{\mathrm{i}}(f)$ and $V_{\mathrm{a}}(f)$ denote the signal level at the input of the preamp and the signal level induced in the electric field sensor, respectively.

Applying the above pickup factor to the following equation, we can obtain the sensitivity of the electric field sensors, as follows:

$$E_{\mathrm{s}}(f) = \frac{N_{\mathrm{i}}(f)}{|G_{\mathrm{p}}(f)|} \cdot \frac{1}{l_{\mathrm{eff}}}. \tag{5.3}$$

where $N_{\mathrm{i}}(f)$ is the equivalent input noise level shown in Fig. 5.4, and l_{eff} is the antenna effective length, which is 0.2 m in the MSEE electric field sensor. The antenna impedance in a vacuum described above is more complex in plasmas. In addition to the capacitance, the resistive effect occurs, depending on plasma densities and temperatures. $G_{\mathrm{p}}(f)$ varied depending on the target region in space plasmas.

Figure 5.6 shows the summary of the sensitivities of electric field sensors in representative science missions (GEOTAIL and BepiColombo MMO) as well as the sensitivity of the MSEE compared with the typical intensities of plasma waves observed in the terrestrial magnetosphere. The antenna impedance of the MSEE is assumed to be that in the ionosphere. The sensitivity of the MSEE electric field sensor is worse than that of the scientific missions because of the shorter antenna length. Nevertheless, the MSEE electric field sensor has sufficient sensitivity to detect natural plasma wave phenomena. Since the plasma wave turbulence around the artificial structure, as shown by *Gurnett*

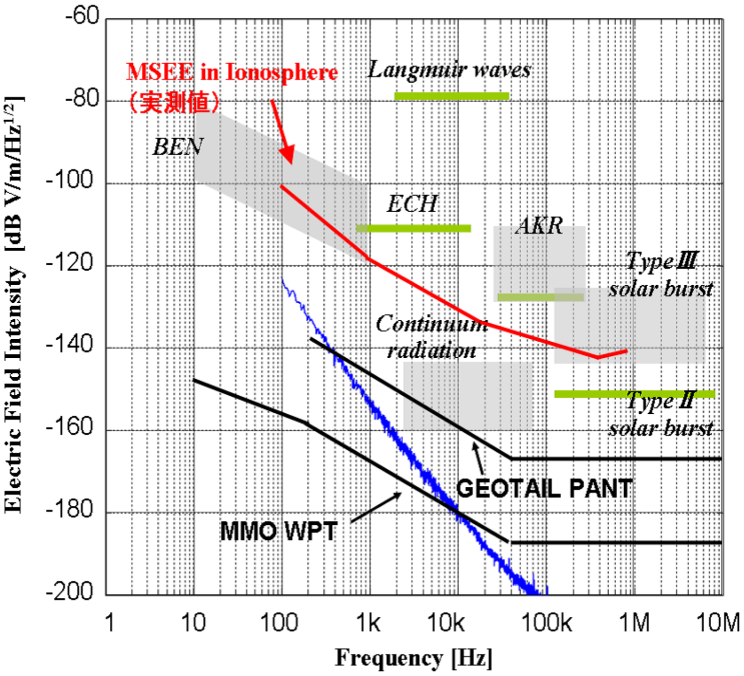

Figure 5.6: Summary of the sensitivities of electric field sensors (red line: MSEE, black lines: GEOTAIL and BepiColombo MMO) compared with the intensities of typical plasma waves observed in the terrestrial magnetosphere (green and gray boxes), and the electric field radiation from the breadboard model of the sensor node (blue line).

et al., (1988) [54], is expected to be more intense than that around natural phenomena, the MSEE electric field sensors are effective for observing both natural and artificial phenomena. The sensitivity of the MSEE magnetic field sensor was discussed and confirmed that the MSEE magnetic field sensor has sufficient sensitivity to observe natural plasma waves in space by *Yagitani et al.*, (2011) [57]. The breadboard design of the MSEE sensor node was partially developed by *Okada*, (2010) [56]. Electromagnetic compatibility (EMC) tests was also conducted by using the breadboard model of the sensor node. The background noise level of radiated electric fields from the breadboard model is also shown in Fig. 5.6 with the sensitivity of the sensor.

The location identification of each sensor node is very important to The sensor nodes are released and distributed randomly throughout the target area. The system is needed for identifying the location of each sensor node. The most convenient method of identifying the location of each sensor node is to use the GPS. There exist commercial small GPS receiver chips. Although such small GPS receivers can be used, the GPS is not always available in space. For instance, if the MSEE sensor nodes are distributed at a higher altitude than the GPS satellites, then the MSEE sensor node cannot identify its own location using the GPS.

The self-organizing map location (SOM) estimation provides a method of location identification without using the GPS [58]. The main feature of this method is to require only distance measurement among the neighborhood sensor nodes. The difference between the tentative location of a node and the measured distance is iterated in each sensor node. This means that the present SOM algorithm method does not require significant CPU resources for the location estimation of each sensor node. Since the SOM estimation was proposed for ad-hoc networks on the ground, it is basically two-dimensional. However, we have already succeeded in extending it to the three-dimensional algorithm and we have examined the efficiency of the three-dimensional SOM algorithm using computer simulations. The results indicate that the three-dimensional SOM is promising for the location estimation of each sensor node. However, an important issue that remains to be addressed is the development of a small distance measurement device. Therefore, the location estimation will depend on the GPS system until the SOM system can be completed.

5.3 Plasmapause Location Determination

5.3.1 Outline

Plasmasphere is an interesting region in Geospace, the inner region of terrestrial magnetosphere, and has been studied by a number of scientists. The plasmasphere is located above ionosphere and consists of cold electrons, ions, and slight amount of neutral atoms. The boundary of the plasmasphere is called plasmapause, which is typically located from 3 to 4 R_{E} of geocentric distance (R_{E}: Earth radii). The location of the plasmapause depends of local time and solar activity. It has been considered that the other regions in Geospace, inner plasmasheet, ring current, and radiation belt, interact with the plasmasphere during geomagnetic storms, and magnetospheric substorms.

In this decade, the IMAGE mission tried to reveal the characteristics, relations between the each region, and mechanism of the interactions by taking images with the extreme ultraviolet ray [59], and the radio wave [60]. Then, how the plasmasphere exists and can be modelled are emerged. For example, *Goldstein et al.*, (2003) identified the shape of the plasmasphere for several cases [61]. Global models of the plasmasphere have been developed [62, 63].

Recently, small and short-time scale phenomena have been thought very important processes to consider global scale dynamics in the magnetosphere. Besides, it is not unclear whether the location of the plasmapause moves more quickly and drastically than limitation of the detection by the conventional methods. An *in-situ* observation system is proposed to detect a local electron density structure in the plasmasphere. The detection of the local electron density structure lead determination of the plasmapause location. The objective of the presented system in this section is to find out whether the smaller structures exist than the spatial resolution of conventional techniques. The system is realised with nanosatellite constellation. It is very significant for solar-terrestrial physics that a scientific mission using the nanosatellite constellation is drummed up since nanosatellite will have taken important roles for any space science fields in this coming decade.

The observation system is proposed for the local electron density structure of the plasmasphere with the nanosatellite constellation. A nanosatellite is defined as a 50 kg-class satellite. The schematic illustration of the system is shown in Fig. 5.7.

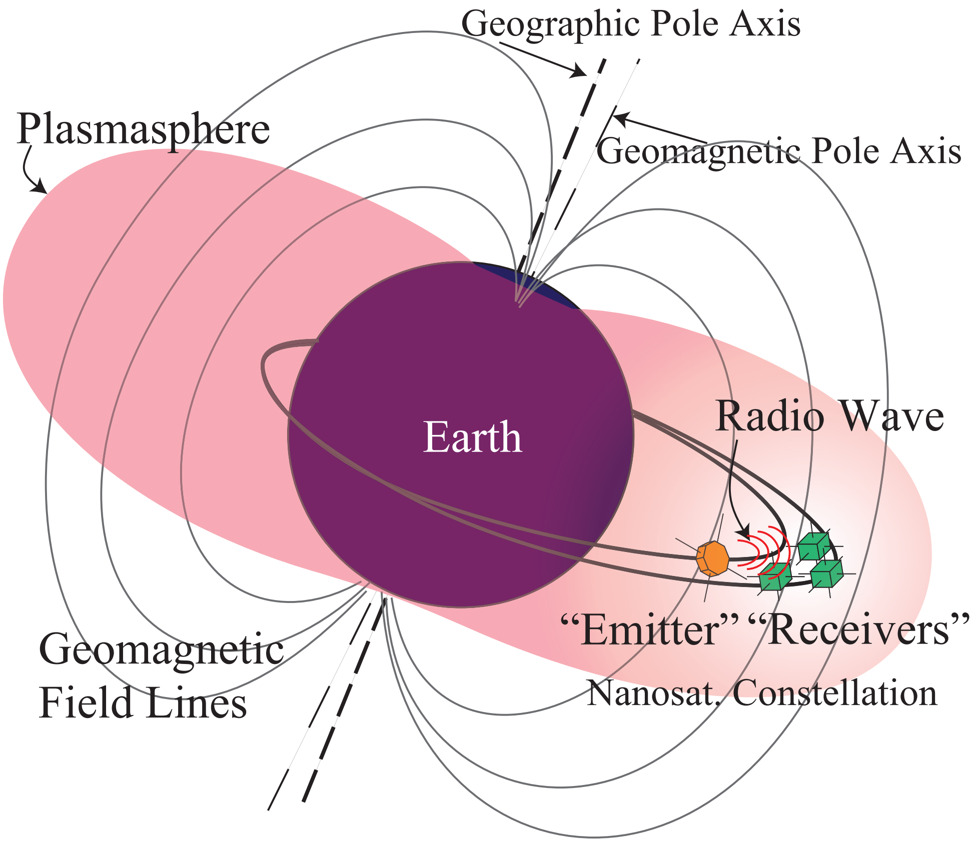

Figure 5.7: The schematic illustration of the nanosatellite constellation to observe the plasmasphere structure with a radio wave.

The constellation consists of two kinds of satellites, "Emitter," and "Receivers." "Emitter" and "Receivers" elliptically go around the Earth in the same orbital plane. "Emitter" transmits linearly-polarized radio wave pulses with cross dipole antennas mounted on the satellite. Each "Receiver" has orthogonal triaxial dipole antennas and receives the radio wave pulses from "Emitter." As further the transmitted radio wave propagates in the plasmasphere, the polarization direction of the radio wave has been changing since the phenomenon, so-called Faraday rotation, occurs in plasmas. The electron density in the plasmasphere affects the Faraday rotation angle. Then, the variation of the rotation angle would change if the electron density is different from that of the modelled density distribution. The observation system proposed in this paper measures the polarization direction of the radio wave, transmitted from “Emitter,” and received by “Receivers.” Then, we can know the local electron density distribution in the plasmasphere.

The largest advantage of this system is the capability to observe electron density with the radio wave simultaneously at multi-point. Besides, the onboard radio wave receiver does not need to be a receiver with sweeping frequency for observation. Generally, plasma measurement instruments are difficult to downsize in principle. The plasma wave receiver with SFA has been used to measure the antenna impedance of spacecraft. Since the antenna impedance denotes the electron density, the SFA can measure the electron density. However, the SFA also requires a certain dimensions because SFA should receive waves in wide-band and have low-noise, high-sensitivity, wide dynamic range characteristics. On the other hand, the proposed system receives just a monochromatic wave and requires moderate system requirements for the receiver. Thus, the satellites can be smaller than conventional scientific satellites.

Inclination and orbit period of all of the satellites are assumed to be 28°, and 7,448 seconds, respectively. The satellites go around the Earth 58 periods in five days. The apogee of “Emitter” is 9,555 km (= 1.5 R_{E}). The apogees of “Receivers” are a few hundred kilometres further from “Emitter.” The observation is conducted once for every orbit at midnight in local time. All satellites are on a line in the midnight, therein a radio wave pulse is transmitted from “Emitter.”

5.4 Radio Wave Propagation in Space Plasma

Since plasma is a dispersive medium, both of phase and group velocities of a plasma wave and a radio wave are different from those of light in vacuum. Frequency is not proportional to wave number, but depends on it. We have an essential parameter, which indicates radio waves are affected by plasma, the plasma frequency denoted in the following equation.

$$\omega_{ps} = \sqrt{\frac{n_s {q_s}^2}{m_s \varepsilon_0}}, \tag{5.4}$$

where ε_0, n_s, q_s, and m_s are permittivity in vacuum, density, electricity, and mass of one species (s) in plasmas (s becomes e for, electron, and i for proton and other species of ions). If frequency is not much higher than the plasma frequency, the plasma wave interacts with the plasma and leads cut-off, and resonance. The cyclotron frequency denoted in the following equation is another important parameter which tells the strength of the ambient magnetic field B_0.

$$\omega_{cs} = \frac{q_s B_0}{m_s} \tag{5.5}$$

In Fig. 5.8, ψ is the angle between the ambient magnetic field vector $\boldsymbol{B_0}$, and wave number vector $\boldsymbol{k}$, is also important.

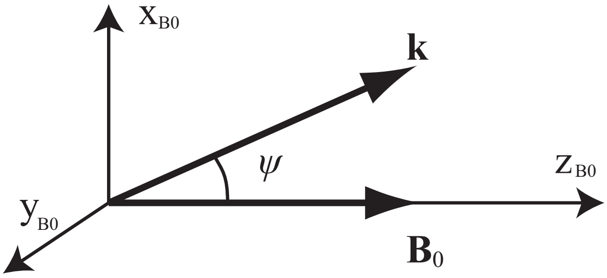

Figure 5.8: The z$_{B0}$ axis is parallel to $\boldsymbol{B_0}$, and $\boldsymbol{k}$ exists in x$_{B0}$-z$_{B0}$ plane.

The dispersion relations for electromagnetic waves in plasma are derived from Maxwell's equations and the equation of motion on magnetohydrodynamics shown in Eqs. (5.6) to (5.8).

$$\nabla \times \boldsymbol{B} = \mu_0\Big(\boldsymbol{J} + \varepsilon_0 \frac{\partial \boldsymbol{E}}{\partial t}\Big), \tag{5.6}$$

$$\nabla \times \boldsymbol{E} = -\frac{\partial \boldsymbol{B}}{\partial t}, \tag{5.7}$$

$$m_s n_s \frac{d\boldsymbol{v_s}}{dt} = q_s(\boldsymbol{E} + \boldsymbol{v}_s \times \boldsymbol{B}), \tag{5.8}$$

where the current density $\boldsymbol{J}$ is shown as

$$\boldsymbol{J} = \sum_s q_s n_s \boldsymbol{v}_s \tag{5.9}$$

μ_0 is the magnetic permeability in vacuum. $\boldsymbol{E}, \boldsymbol{B}$, and $\boldsymbol{v_s}$ are the electric field, magnetic field and fluid velocity of species s, respectively. Herein, we ignore the static electric field and fluid velocities, linearize and apply Fourier transform to $\boldsymbol{E}, \boldsymbol{B}$, and $\boldsymbol{v}_s$. That is, $\boldsymbol{E} = \boldsymbol{E}_1, \boldsymbol{B} = \boldsymbol{B}_0 + \boldsymbol{B}_1, \boldsymbol{v}_s = \boldsymbol{v}_{s1}, \nabla = j\boldsymbol{k}$, and $\partial/\partial t = -j\omega$, respectively. Removing $\boldsymbol{B}_1$ and $\boldsymbol{v}_{s1}$ from the above equations,

$$\begin{pmatrix} S - \mu^2\cos^2\psi & -jD & \mu^2\sin\psi\cos\psi \\ jD & S - \mu^2 & 0 \\ -\mu^2\sin\psi\cos\psi & 0 & S - \mu^2\sin^2\psi \end{pmatrix} \boldsymbol{E} = 0 \tag{5.10}$$

is obtained, where, μ is the real part of the complex refractive index. S, D, and P are denoted as follows:

$$\begin{aligned} S &= \frac{1}{2}(R+L), &(5.11)\\ D &= \frac{1}{2}(R-L), &(5.12)\\ R &= 1-\sum_s \frac{\omega_{ps}^2}{\omega(\omega+\omega_{cs})}, &(5.13)\\ L &= 1-\sum_s \frac{\omega_{ps}^2}{\omega(\omega-\omega_{cs})}, &(5.14)\\ P &= 1-\sum_s \frac{\omega_{ps}^2}{\omega^2}. &(5.15) \end{aligned}$$

If Eq. (5.10) has a solution without $\boldsymbol{E} = 0$, the determinant of the matrix should be equal to zero. Then, the squared refractive index μ^2 is given as shown in Eq. (5.16).

$$\begin{aligned} \mu^2 &= \frac{C_1 \pm C_2}{2C_3}, &(5.16)\\ C_1 &= RL\sin^2\psi + PS(1+\cos^2\psi), &(5.17)\\ C_2 &= \sqrt{(RL-PS)^2\sin^4\psi + 4P^2D^2\cos^2\psi}, &(5.18)\\ C_3 &= S\sin^2\psi + P\cos^2\psi. &(5.19) \end{aligned}$$

The refractive index has only the real part when μ^2 is positive. An example of the squared refractive index, where $\psi = 0$, $\omega_{pe} = 1.26$ Mrad/s, and $\omega = -1.76$ Mrad/s, is shown in Fig. 5.9.

The refractive index has two mode, R-X (Right-hand eXtraordinary), and L-O (Left-hand Ordinary). For the R-X mode, the sign in front of C_2 is positive. For the L-O mode, the sign is negative. The R and L modes in Fig. 5.9 are the special case, where ψ is equal to zero.

The both refractive indices of R-X and L-O modes differently depend on the plasma frequencies and the cyclotron frequencies. The norm of wave number vector is expressed with the refractive index as shown in Eq. (5.20).

$$\left.\begin{aligned} k_{\mathrm{RX}} = &\ |\boldsymbol{k}_{\mathrm{RX}}| = \frac{\omega}{c}\mu_{\mathrm{RX}} \\ k_{\mathrm{LO}} = &\ |\boldsymbol{k}_{\mathrm{LO}}| = \frac{\omega}{c}\mu_{\mathrm{LO}} \end{aligned}\right\}, \tag{5.20}$$

where c is speed of light in vacuum, and ω is angular frequency of the radio wave. Subscriptions, RX and LO, represent R-X and L-O mode, respectively. Assuming a linear

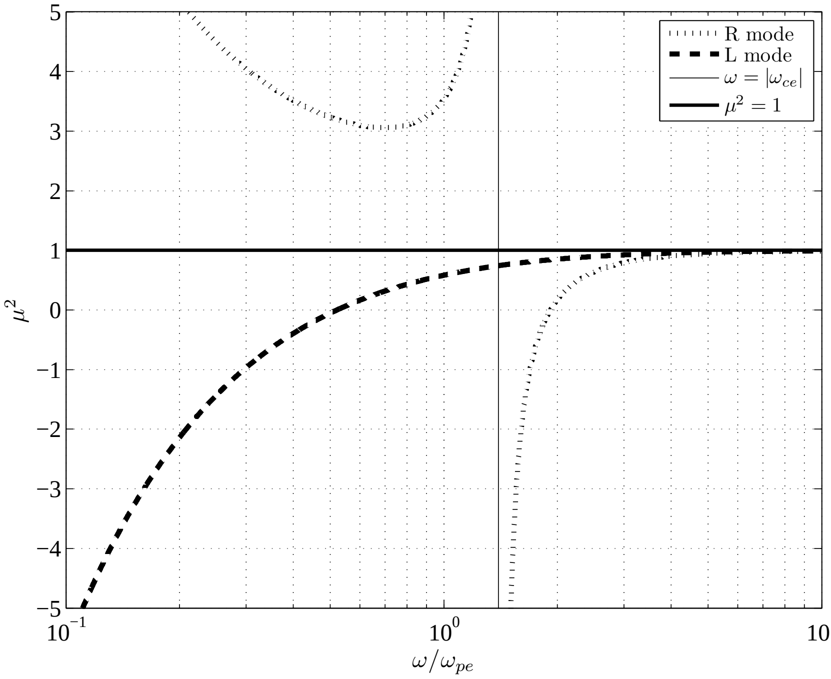

Figure 5.9: The square refractive index versus normalized frequency with plasma frequency.

polarized wave, the wave has the both mode of which the amplitudes are equal. When the propagation direction is assumed to be parallel to z-axis, the linear polarized wave is expressed in Eq. (5.23).

$$\boldsymbol{E} = \boldsymbol{E}_{\mathrm{RX}} + \boldsymbol{E}_{\mathrm{LO}} \tag{5.21}$$

$$= \frac{E_0}{2}\begin{pmatrix} \cos(\boldsymbol{k}_{\mathrm{RX}} \cdot \boldsymbol{r} - \omega t) \\ \sin(\boldsymbol{k}_{\mathrm{RX}} \cdot \boldsymbol{r} - \omega t) \\ 0 \end{pmatrix} + \frac{E_0}{2}\begin{pmatrix} \cos(\boldsymbol{k}_{\mathrm{LO}} \cdot \boldsymbol{r} - \omega t) \\ -\sin(\boldsymbol{k}_{\mathrm{LO}} \cdot \boldsymbol{r} - \omega t) \\ 0 \end{pmatrix} \tag{5.22}$$

$$= E_0 \cos\left\{\frac{(\boldsymbol{k}_{\mathrm{RX}} + \boldsymbol{k}_{\mathrm{LO}}) \cdot \boldsymbol{r}}{2} - \omega t\right\}\begin{pmatrix} \cos\frac{(\boldsymbol{k}_{\mathrm{RX}} - \boldsymbol{k}_{\mathrm{LO}}) \cdot \boldsymbol{r}}{2} \\ \\ \sin\frac{(\boldsymbol{k}_{\mathrm{RX}} - \boldsymbol{k}_{\mathrm{LO}}) \cdot \boldsymbol{r}}{2} \\ \\ 0 \end{pmatrix}, \tag{5.23}$$

where $\boldsymbol{r}$ and E_0 is a positional vector and the amplitude of the electric field vector of the waves, respectively. $\boldsymbol{E}$ is also expressed as $(E_{\mathrm{x}}\ E_{\mathrm{y}}\ E_{\mathrm{z}})^T$. The polarization direction ζ is defined as

$$\zeta = \arctan\frac{E_{\mathrm{y}}}{E_{\mathrm{x}}} = \frac{(\boldsymbol{k}_{\mathrm{RX}} - \boldsymbol{k}_{\mathrm{LO}}) \cdot \boldsymbol{r}}{2}. \tag{5.24}$$

Equation (5.24) means that a half of the phase difference between R-X mode and L-O mode waves at position indicated by $\boldsymbol{r}$ is equal to the angle of the polarization to the reference direction. If the each path of R-X and L-O mode waves is much different each other, the propagation time difference should also be considered. When frequency of radio waves is much higher than the electron plasma frequency, the radio waves act as radio waves in vacuum. Then, the both refractive indices of R-X and L-O mode become close to 1 for the high frequency radio waves. In the plasmasphere, electron plasma frequency is typically from $2\pi \times 100$ kHz to 1 MHz, approximately corresponding to electron density from 10^2 to 10^4 cm^{-3}. Changing the polarization of the linear polarized wave propagating in a certain medium is known as Faraday Rotation. The rotation angle can be calculated for a wave propagating from a position $\boldsymbol{r}_{\mathrm{A}}$ to $\boldsymbol{r}_{\mathrm{B}}$ as shown in the following equation. Here, δ indicates the angle between the radial and propagation directions. θ is elevation angle in the meridian plane.

$$\tilde{\zeta}_{\mathrm{AB}} = \int_{\boldsymbol{r}_{\mathrm{A}}}^{\boldsymbol{r}_{\mathrm{B}}} \nabla\zeta \cdot d\boldsymbol{r}, \tag{5.25}$$

$$d\boldsymbol{r} = \begin{pmatrix} dr \\ rd\theta \end{pmatrix} \tag{5.26}$$

$$\nabla = \begin{pmatrix} \dfrac{\partial}{\partial r} \\ \dfrac{1}{r}\dfrac{\partial}{\partial\theta} \end{pmatrix} \tag{5.27}$$

$$\nabla\zeta = \nabla\left(\frac{\boldsymbol{k}_{\mathrm{RX}}\cdot\boldsymbol{r} - \boldsymbol{k}_{\mathrm{LO}}\cdot\boldsymbol{r}}{2}\right) \tag{5.28}$$

$$\begin{aligned}
&= \nabla\left\{\frac{\omega}{2c}\left(\mu_{\mathrm{RX}}\cos\delta_{\mathrm{RX}} - \mu_{\mathrm{LO}}\cos\delta_{\mathrm{LO}}\right) r\right\} \\
&= \frac{\omega}{2c}\{(\mu_{\mathrm{RX}}\cos\delta_{\mathrm{RX}} - \mu_{\mathrm{LO}}\cos\delta_{\mathrm{LO}})\nabla r + r\left[((\nabla\mu_{\mathrm{RX}})\cos\delta_{\mathrm{RX}} - (\nabla\mu_{\mathrm{LO}})\cos\delta_{\mathrm{LO}})\right. \\
&\qquad \left. +(\nabla(\cos\delta_{\mathrm{RX}})\mu_{\mathrm{RX}} - \nabla(\cos\delta_{\mathrm{LO}})\mu_{\mathrm{LO}})\right]\} \\
&= \frac{\omega}{2c}\begin{pmatrix}
\begin{aligned}&(\mu_{\mathrm{RX}}\cos\delta_{\mathrm{RX}} - \mu_{\mathrm{LO}}\cos\delta_{\mathrm{LO}}) + r\left(\cos\delta_{\mathrm{RX}}\frac{\partial\mu_{\mathrm{RX}}}{\partial r} - \cos\delta_{\mathrm{LO}}\frac{\partial\mu_{\mathrm{LO}}}{\partial r}\right)\\ &+r\left(\mu_{\mathrm{RX}}\frac{\partial\cos\delta_{\mathrm{RX}}}{\partial r} - \mu_{\mathrm{LO}}\cos\frac{\partial\delta_{\mathrm{LO}}}{\partial r}\right)\end{aligned} \\
\\
\left(\cos\delta_{\mathrm{RX}}\frac{\partial\mu_{\mathrm{RX}}}{\partial\theta} - \cos\delta_{\mathrm{LO}}\frac{\partial\mu_{\mathrm{LO}}}{\partial\theta}\right) + \left(\mu_{\mathrm{RX}}\frac{\partial\cos\delta_{\mathrm{RX}}}{\partial\theta} - \mu_{\mathrm{LO}}\cos\frac{\partial\delta_{\mathrm{LO}}}{\partial\theta}\right)
\end{pmatrix}
\end{aligned} \tag{5.29}$$

Then, the rotation angles is numerically calculated and demonstrated in the following section.

5.5 Polarization Calculation

In this section, we show how the Faraday rotation relates to the electron density with numerical calculation. We use the ray tracing technique, which had been developed since 1954 to calculate whistler ray paths in the magnetosphere. The latest version can provide ray paths of the both (R-X, and L-O) modes, assuming the diffusive equilibrium model for plasma distribution around the Earth and dipole geomagnetic field model. The program uses Adams-Bashforth predictor method and -Moulton corrector method to integrate the differential equations numerically. The source code of the ray tracing program mainly written with FORTRAN has been made available to public for free since 2010 [64].

The ray tracing program gives us the ray paths of the radio waves transmitted from an arbitrary point with refractive index for each propagating time. The polarization direction of the radio wave is not calculated by the ray tracing program. We need to calculate the phase difference and polarization direction according to Eqs. (5.20), (5.25), and (5.29) from the ray tracing results. We also have to assume that electron density is different from the model which has been assumed in the ray tracing program to investigate that the polarization direction is changed by the difference of the electron distribution. In short, the diffusive equilibrium model is defined with the density at an initial point of the ray path and the spatial gradient of the density. We modify the program to set a slightly different model which has peaks in the distribution every certain distance.

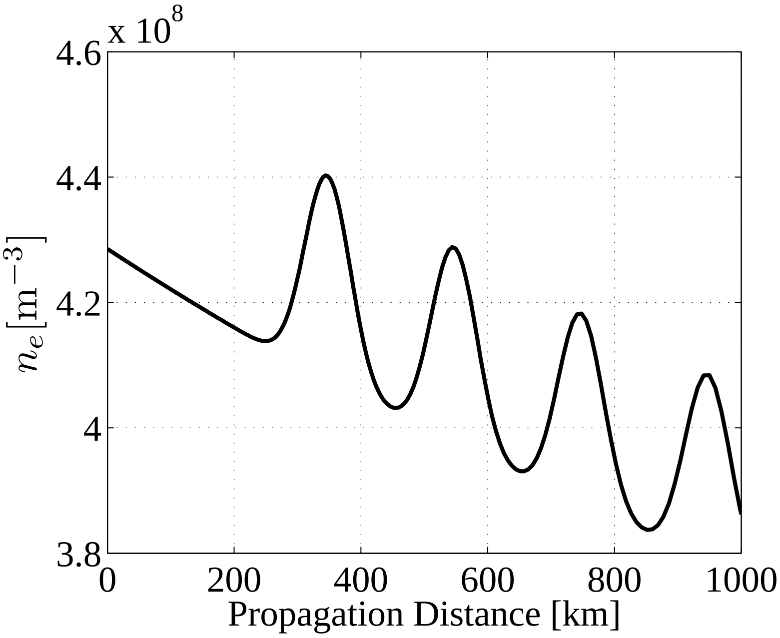

Figure 5.10: The electron density model for the geocentric radial direction which has peaks.

As a test case, we chose the electron density at the peaks is approximately 10 % larger than that of the native diffusive equilibrium model. The peak widths were set to several tens kilometers. Figure 5.10 shows the electron density model for the geocentric radial direction which has the peaks. The radio wave is transmitted from the position where the geocentric distance is equal to 1.5 R_{E} (= 9,555 km) toward the radial direction in each calculation of the ray tracing. The frequency is 12 MHz.

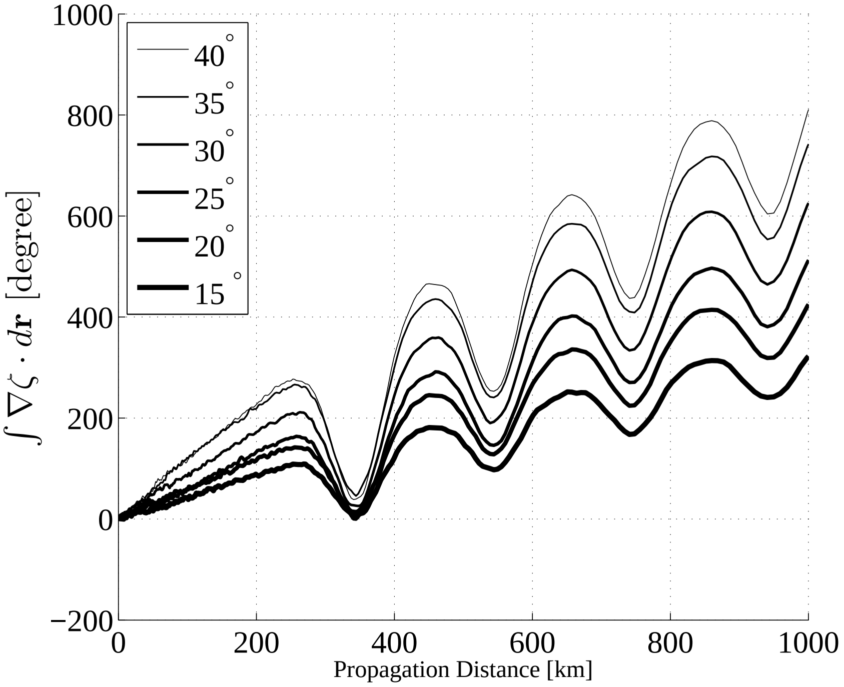

Figure 5.11: Rotation angle for six magnetic latitudes.

The refractive index at each point depends on not only the electron density but also magnetic field intensity and angle to the wave number vector. The geomagnetic field rotates in synchronization with the axial rotation. The axis of geomagnetic poles is 11° tilted against the axis of geographic poles. The geomagnetic latitude is in the range of the inclination of the satellite plus or minus 11°. The polarization direction for was calculated every 5° from 15° to 40° of the geomagnetic latitude. Figure 5.11 represents the Faraday rotations with the electron density model and several conditions of the geomagnetic latitude: every 5° from 15 to 40°. The horizontal axis is the geocentric distance. Each line indicates the result from the ray tracing for the each magnetic latitude. As the radio wave propagates, the electron density declines since the equilibrium model has the smaller density at the further position. It is obvious that the phase difference for any magnetic latitudes increases and decreases because of the peaks of the electron density profile. On the smaller geomagnetic latitude, the sensitivity of the Faraday rotation becomes smaller since the angle between the magnetic field line and wave number vector becomes close to 90°.

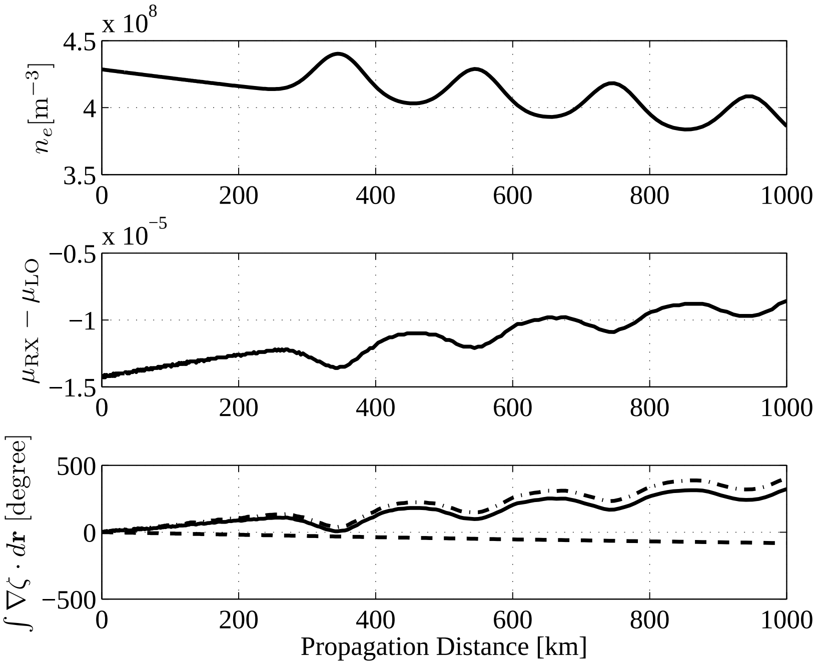

Figure 5.12: Upper panel: Electron density. Middle panel: refractive index difference. Lower panel: Rotation Angle (solid line: total, broken line: the first term in Eq. (5.29), and dotted line: the second term in Eq. (5.29).

The electron density, refractive index difference, and Faraday rotation on the magnetic latitude of 15° are shown in Fig. 5.12. Three lines in the lower panel indicate total Faraday rotation (solid line), the first (broken line) and second (dotted line) terms of the r-component in Eq. (5.29), respectively. The second terms (dotted line) mean Faraday rotation because of difference of refractive indices, and radial gradient difference of those, respectively. Comparing the electron density (upper panel) with the Faraday rotation (lower panel), when the electron density becomes large, the second term the total rotation angle (dotted and solid lines) decreases. On the other hand, the first term (broken line) negatively increases without relation to the electron density. Thus, the difference of radial gradient of the refractive indices conforms the positions of peaks and troughs of the electron density with those of the rotation angle.

Considering to detect the polarization direction, sampling points should be located close enough each other. When difference of the Faraday rotation between two sampling points is smaller than 180°, ambiguity of the Faraday rotation does not exist in observation results. In other words, the plasmapause, that has significant electron density gap, can be detected by measuring the Faraday rotation at multi-point. The spatial sampling interval should be several tens kilometers at most to detect electron density variation in this test case. In fact, how large perturbation exists in the electron density profile has not been observed and understood yet. Thus, the position of the sampling points should be decided from a requirement of spatial resolution. The IMAGE EUV, which is the instrument for imaging of the plasmasphere, had the spatial resolution of 630 km [59]. The spatial resolution of our system are set to tenth of the 630 km, 63 km. According to sampling theorem, the interval of the sampling points should be smaller than 31 km. In the next section, orbital elements of the constellation, and requirements for the system are introduced, referring to the above results.

5.6 System Design of Satellites

First, the number of constellation is assumed to be four, one for "Emitter" and other three for "Receiver." This is the minimal constitution to observe whether a peak or nadir exists. Of course, the number can be increased if budget permit extra satellites. Table 5.2 shows orbital elements for the four satellites.

Table 5.2: Orbital elements of "Emitter" and "Receivers."

	Emitter	Receiver 1	Receiver 2	Receiver 3
a [km]	8,243			
i [degree]	28			
T [s]	7,448			
ω [degree]	90			
e	0.1592	0.1835	0.1859	0.1883
r_p [km]	6,930	6,730	6,710	6,690
r_a [km]	9,555	9,755	9,775	9,795

In the upper four rows, a, i, T, ω, and e are semi-major axis, inclination, period, argument of perigee, and eccentricity, respectively. In the lower rows, r_p, and r_a are geocentric distances of perigee and apogee, respectively. "Receivers" are not more than 240 km distant from "Emitter" at apogee.

To realise the presented observation system, several subsystems listed below are indispensable to make the observation feasible.

"Emitter" Only

- Transmitter for the radio wave
- Communication with the Ground

"Receiver" Only

- Receiver for the radio wave

Both ("Emitter" and "Receivers")

- Time synchronization
- Precise attitude detection
- Communication in constellation
- Solar cells and Battery

From here, we discuss requirements for the subsystems and denote their feasibility.

The most essential part of transmitters and receivers is the antenna. The suitable type and length of antennas should be chosen to minimize necessary power to transmit and maximize receivable power. Assumptions about the transmitter and receiver are shown in Table 5.3 to estimate the minimum radiation power from the transmitter.

Table 5.3: Assumptions in transmitter and receiver.

Transmitter	
Type	Half wavelength dipole
Form	Wire
Axes	2
Length	12 m tip-to-tip
Gain (G_t)	1.64
Receiver	
Type	Small dipole
Form	Flexible CFRP
Axes	3
Length	3 m tip-to-tip
Gain (G_r)	1.5
Noise Density	100 nV/$\sqrt{\text{Hz}}$
SNR	5 dB
Bandwidth	120 kHz

The cross wire dipole antenna is suitable to deploy the half wavelength dipole antenna by spinning of "Emitter." Down-conversion technique is used for receiving the radio waves. Comparing the amplitudes of the picked-up triaxial signals, the polarization direction is obtained. The equivalent input noise level of the radio wave receiver is comparable to the results described in the Chapter 3.

$$P_r = \left(\frac{\lambda}{4\pi d}\right)^2 P_t G_t G_r \tag{5.30}$$

The Friss transmission equation is shown in Eq. (5.30), where λ, d, G_t, G_r, P_t and P_r are wave length, distance between the transmission and receiving points, gains of the antennas for the transmitter and the receiver, the transmission power and the received power, respectively. P_r is calculated as the necessary received power from the equivalent input noise level and SNR. Assuming d and λ are equal to 250 km and 25 m, the minimum power to be transmitted is 3.09 W with the parameters indicated in Table 5.3. If radiation efficiency is approximately 50 %, the total necessary power for the transmitter is need to be more than 6 W. Commercial items of the 10-W class HF-band transmitter within 10 kg are compassable and applicable for the transmitter in "Emitter." Time of each satellite has to be synchronized just relatively. Then, all "Receivers" are synchronized with "Emitter" in every orbit before starting observation by sending a reference signal in communication. Employing a small rubidium oscillator as a reference clock for each satellite, synchronization precision is equal to the stability of 10^{-10} s. Then, the precision of obtained phase is calculated as follows:

$$
\begin{aligned}
\Delta\zeta &= f\Delta T \times 360^\circ && (5.31)\\
&= 12 \times 10^6\text{Hz} \times 10^{-10}\text{s} \times 360^\circ && (5.32)\\
&= 0.43^\circ, && (5.33)
\end{aligned}
$$

where, ΔT is the stability of the oscillator.

Attitude detection should be comparable to $\Delta\zeta$ or better. We can find out a small sun sensor and magnetic field sensor with 1° resolution. This two kinds of the sensors are appropriate for the attitude sensors the satellites.

Each "Receivers" satellite should obtain observation start time and a data set of the polarization direction for one path. Then, the necessary data rate in communication can be estimated.

The observation start time is obtained by counting up the clock from the time synchronization to detection of the radio wave on the receiver. The temporal sampling rate of polarization direction should be high enough not to move larger distance for the satellite than wavelength of the radio wave during the observation. Assuming 1% of the wavelength is acceptable for the traveling distance, the sampling rate should be 30 ksample/s or higher.

The bit length of the polarization direction is 8 bits because of the precision of time synchronization and attitude detection. When number of sampling is 1000, one data set is 8 kbits. Including the attitude data with the same bit lengths, the data transmitted from one "Receiver" amounts 24 kbits for one path. Thus, each "Receiver" has to establish communication with "Emitter" and send data of 24 kbits at least every orbit.

"Emitter" collects data from all three "Receivers", therefore, the stored data in "Emitter" is equal to 72 kbits for one path. The orbit period is equal to 1/11.6 of a day. Therefore, the constellation can go back to a certain ground station every five days, which is 58 periods. Assuming only one specified ground station is always available, "Emitter" has to send 4.2 Mbits while "Emitter" is just above the ground station. If the bit-rate of 50 kbps is realized, it takes around 84 s to download all of the data.

5.7 Conclusion and Future Works

The miniaturized plasma wave receiver has the potential to expand its use in space science as well as space development. In this chapter, two novel applications with the miniaturized plasma wave receiver were discussed. A sensor network system for monitoring the status of the space electromagnetic environment was proposed as the application of the small plasma wave receiver. The multiple sensor nodes are randomly distributed with observing plasma waves of electric and magnetic field components and communicating each other. The architecture and specification of the sensor node were introduced. The sensitivity and its feasibility were also represented. Completing the development of the breadboard model are the most pressing issue for this application.

Another space scientific system to observe local electron density structures in the terrestrial plasmasphere was also proposed. The variation of the polarization direction of the linear polarized radio wave provides the electron density at an observation point. The observation is conducted with a constellation which consists of two kinds of satellite. One transmits radio waves every orbit, and the other receives the waves and detects the polarization direction. Orbital elements of the constellation and the required performance of the systems in the satellites were investigated. The performances of the satellites were feasible to realize the observation system with nanosatellites. It is very significant that the scientific observation system proposed here can be implemented with nanosatellite. As future works, design to establish connections with appropriate bandwidth between satellites or the ground is indispensable. Besides, power-supply design of the satellites and loss caused by impedance miss-matching in the transmitter should be discussed.

Chapter 6

One-chip Wave-Particle Interaction Analyzer

6.1 Introduction

Since space plasmas are essentially collisionless, their kinetic energies are altered mainly through wave-particle interactions. While plasma waves are destabilized by absorbing kinetic energy, the excited waves result in damping by energizing the plasma. Plasma wave receivers and plasma instruments onboard spacecraft take on the role of observing wave-particle interactions in space. Previous plasma wave receivers and plasma instruments were completely independent. In typical space missions, they were not controlled in coordinated ways and did not interact with each other. This independence made it difficult to quantitatively study wave-particle interactions. For example, direct correlation analyses using waveforms and velocity distribution functions were usually impossible by the difference in time resolutions.

Extensive attempts have been made in the past several decades to identify wave-particle interaction processes. There exist roughly two different methods for rocket or spacecraft observations. One is based on particle correlation techniques [65, 66]. It calculates an autocorrelation (or cross-correlation) function using the particle detection pulses. Since the results depend on velocity modulations in the plasmas in phase space due to wave-particle interactions, they enable one to identify the energy source of plasma waves by comparing enhancements in the autocorrelation functions in different energy ranges with the plasma wave frequencies. *Gough et al.*, (1998) reported the auto correlation function had been modulated with the upper hybrid frequency by an injection of electron beam into the ionosphere [66]. *Buckley et al.*, (2000) introduced an outline of the particle correlator for the Cluster mission and evidenced the capability of the correlator to detect wave particle interactions by simulation [67]. Furthermore, the flight data of the particle correlator on board the Cluster spacecraft show the good correlation of the detected particle modulation frequencies with the frequencies of the observed plasma waves in the magnetosheath [68].

The other system is the so-called "Wave-Particle Correlator (WPC)" [69, 70]. The preceding correlator makes use of only the data from particle instruments, whereas the wave-particle correlator uses data from both plasma waves and particle instruments. It counts particle events detected by plasma instruments taking into account the phase observed by the plasma wave receivers. The advantage of this technique is it allows one to identify the direction of energy flow between plasma waves and plasmas, as well as to find out the wave energy sources. *Kletzing et al.*, (2005) developed a new wave-particle correlator, which counts up detected particles, according to phase divided into 16 bins [71]. These wave-particle correlators showed the correlation between the phase of the Langmuir waves and the observed electron counts in the polar region. Of course, their technique can be applied to other waves in other regions.

In summary, the particle correlator provides autocorrelation functions, which are equivalent to the modulation frequency of plasmas in phase space, whereas the wave-particle correlator provides the number of particles detected during the period of a specific wave phase. In the present chapter, we propose a new type of instrument with the capability to conduct direct and quantitative measurements of wave-particle interactions. We name it the "Wave-Particle Interaction Analyzer (WPIA)." The WPIA quantifies the kinetic energy flow by the inner product of the amplitudes of the observed waves and velocities of the detected particles. The other methods do not consider all of the properties of the observed waveforms and particles. However, the WPIA considers instantaneous wave amplitudes and velocities of particles, as well as the phase relations between the waves and particles. Furthermore, since the wave-particle interactions are confined to specific directions relative to the ambient magnetic field, the WPIA also accounts for the direction of the ambient magnetic field in the above calculations. These calculations should be conducted onboard spacecraft since sending all of the data for the calculations needs a wide communication band of telemetry, which is actually not available.

The detailed principle of the WPIA is described in section 6.2 and consists of complicated processes in its function. One of the easiest way to realize the WPIA is to develop software running on a digital processor onboard a spacecraft. However, the heavy load of the WPIA requires a dedicated processor on a real-time basis. This requirement does not always meet the capabilities of a spacecraft. Therefore, we have developed a Field Programmable Gate Array (FPGA) with all of the necessary functions of the WPIA. We call it the "One-chip Wave-Particle Interaction Analyzer (O-WPIA)." The O-WPIA realizes the capability of the WPIA with real-time processing and low-power consumption.

A proposal of the SCOPE (cross-Scale COupling in the Plasma universE) mission was submitted to JAXA (Japan Aerospace Exploration Agency) [72]. The SCOPE targets the investigation of the cross-scale coupling in the terrestrial magnetosphere. In this mission, since the wave-particle interaction is the key observational subject, we believe that the quantitative data of the O-WPIA will be exceedingly significant in this mission. On the other hand, another proposal of the mission called "ERG (Energization and Radiation in Geospace)" [73] was also submitted. It is a small satellite mission, which focuses on the observation of the radiation belts of the Earth. In this mission, we propose the software-type WPIA (S-WPIA). In the S-WPIA, the functions and logics of the WPIA are realized by the software running on the on board general purpose processor. Since the S-WPIA does not have exclusive hardware, we cannot expect real-time operations of the WPIA. However, it is very efficient in the small satellite mission, in which the available resources of the satellite are very limited.

6.2 Principle and significance of the WPIA

The present section demonstrates the principle and significance of the WPIA by comparing it with the conventional methods used in earlier studies. In the conventional method for the study of wave-particle interactions using spacecraft observation data, one calculates the correlation of plasma wave data (such as frequency spectra) with plasma particle data (such as energy spectra). When attempting to identify physical mechanisms of plasma wave instabilities in detail, the reduced velocity distribution functions are examined in the periods of notable plasma wave activities. Since the correlation is visually examined in such methods, qualitative results are unavoidable. Moreover, one frequently faces a lack of time resolution in this conventional method. Since the energies of the particles fluctuate at a characteristic timescale in wave-particle interactions such as at an electron beam instability, the time resolution of the data should be high enough to trace the phenomenon.

An electron beam instability is a good example to demonstrate the advantage of the WPIA. Figure 6.1 schematically shows the relation between the velocity distribution (a), and phase space trajectories for beam particles (b) in the nonlinear stage. The vertical axis in Fig. 6.1 (b) denotes the velocity component parallel to the ambient magnetic field, and the horizontal axis represents the phase relation of the particles and plasma waves (that is, the position of particles relative to the spatial structure of the electrostatic potentials). The center of the trajectories is aligned with the phase velocity (v_ϕ) of destabilized plasma waves. As the wave growth in the linear phase leads to the formation of an electrostatic potential, beam particles start getting trapped in the hatched region in Fig. 6.1 (b) by losing their kinetic energies. The velocity width in the trapping region is defined by the trapping velocity (V_t),

$$V_t = 2\sqrt{\frac{eE_w}{m_0 k}} = 2\sqrt{\frac{ev_\phi E_w}{m_0 \omega_p}}, \qquad \left(\frac{\omega_p}{k} \sim v_\phi\right), \tag{6.1}$$

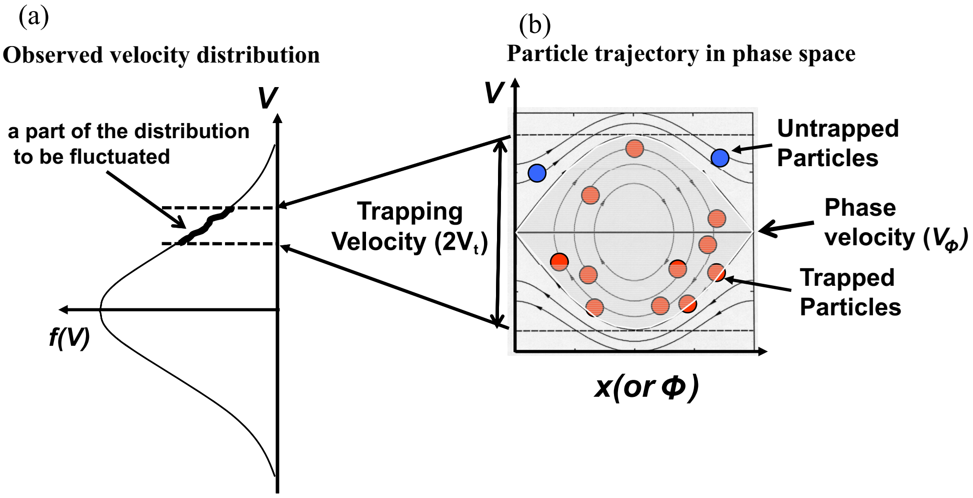

Figure 6.1: Classical method in studying wave-particle interactions. The phase relation of the plasmas and plasma waves disappear in the reduced velocity distributions.

where E_w and ω_p are the wave amplitude and the electron plasma frequency, respectively. Once particles are trapped, their kinetic energies are exchanged with plasma wave energies, and the direction of energy flow (waves to particles or vice versa) is defined by the phase relation between the particles and plasma waves. A series of these processes results in the appearance of fluctuations with a width of $2V_t$ around v_ϕ in the reduced velocity distribution shown in Fig. 6.1 (b). In conventional data processing for calculating velocity distributions, data integration of longer than a few seconds is necessary. This data integration process averages the fluctuations, resulting in the disappearance of the variations in the velocity distribution. Furthermore, despite the importance of the phase relation between the plasma waves and particles, the reduced velocity distribution loses the phase information.

The Japanese spacecraft GEOTAIL succeeded in showing the importance of time domain observations of plasma waves, as realized by the Wave-Form Capture receiver [12, 13]. It directly samples waveforms with an analog-digital converter of high sampling frequency. The time domain observations allow one to examine phase information of the waveforms. They also provide an opportunity to examine quick changes in wave features, because they do not require data accumulation, in contrast to the spectral analysis. On the other hand, high time resolutions in the velocity distribution measurements remain an important issue for future missions. The realization of superior plasma instruments with high time resolution is an excellent solution for quantitative research on wave-particle interactions in space plasmas. However, we believe that the WPIA provides another solution for future work. The WPIA measures an important physical quantity, $\boldsymbol{E}_w \cdot \boldsymbol{v}$, which quantitatively represents the wave-particle interaction, where $\boldsymbol{E}_w$ is the instantaneous electric field vector and $\boldsymbol{v}$ is the velocity vector of a plasma particle. Note that $\boldsymbol{E}_w \cdot \boldsymbol{v}$ is equivalent to a time variation in the kinetic energy of a single particle according to

$$\frac{d}{dt}\left(m_0 c^2(\gamma - 1)\right) = q\boldsymbol{E}_w \cdot \boldsymbol{v}, \tag{6.2}$$

where m_0, q, c, and γ denote the rest mass, charge of a particle, light speed, and Lorentz factor, respectively. The calculation of this physical value at the source region allows us to do quantitative studies of the wave-particle interaction. Since it is not enough to do the calculation for only one particle, we need some accumulation over a time period of at least several characteristic timescales in the target phenomenon as follows,

$$I = q \sum_i \boldsymbol{E}_{w_i} \cdot \boldsymbol{v}_i. \tag{6.3}$$

Equation (6.3) is valid for the kinetic energy transfer in any wave-particle interaction process. The most significant difference between this method and the conventional one is that the data accumulation is conducted after considering the phase relation of $\boldsymbol{E}_w$ and $\boldsymbol{v}$ (see Fig. 6.2) as well as amplitude and velocities. Furthermore, the accumulation method is flexible. For example, we can examine the results with fixed phase differences between the plasma waves and particles. In short, the main function of the WPIA is to calculate the physical quantity $\boldsymbol{E}_w \cdot \boldsymbol{v}$ and to accumulate it for a specific time period, i.e., the quantity "I" from Eq. (6.3), in various ways.

In order to calculate $\boldsymbol{E}_w \cdot \boldsymbol{v}$ without any integration or averaging processes, the WPIA simultaneously collects digitized waveforms picked up by a plasma wave receiver and pulses corresponding to the detection of plasma particles. Plasma wave observations and plasma measurements are essentially independent. However, the WPIA links these two instruments and generates the physical quantity $\boldsymbol{E}_w \cdot \boldsymbol{v}$. While the waveform data are continuously input to the WPIA, output pulses with information on the arrival time and equivalent energy are impulsively input to the WPIA. The WPIA can also accumulate $\boldsymbol{E}_w \cdot \boldsymbol{v}$ in various ways.

Similar attempts to focus on the phase relation between the observed waves and timing of particle detection pulses have been conducted in previous rocket and satellite missions [69, 71].They counted up the number of particle detection pulses in reference to the phase of the observed Langmuir waves. In keeping the phase relation of waves and particles, their principle is similar to that of the WPIA. However, because they do not take into account the phase relation between the electric field vector and the particle velocity vector, their outputs are not quantitative physical values. In contrast, the WPIA provides $\boldsymbol{E}_w \cdot \boldsymbol{v}$, which is equivalent to the time variation of the kinetic energies. This is the significant and unique point of the WPIA compared with previous instruments.

The detailed inner processes of the WPIA are described in section 6.3. The most important issue in realizing the WPIA is that it requires high-performance digital pro-

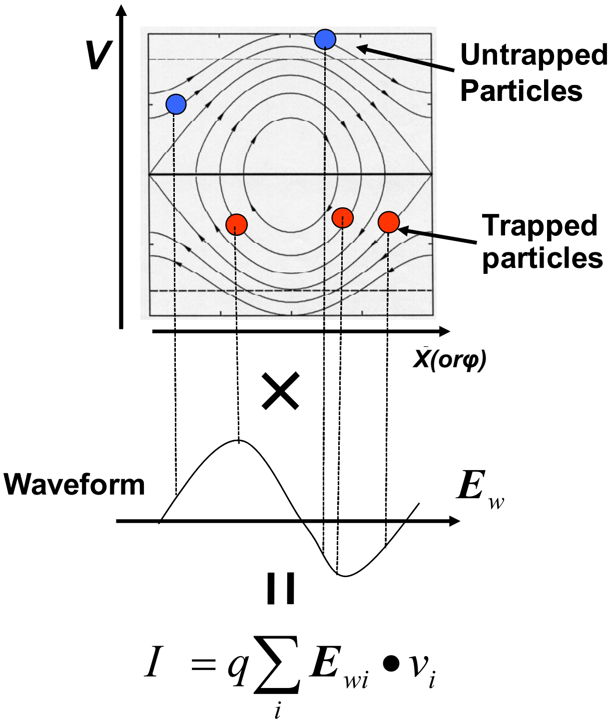

Figure 6.2: Principle of the WPIA. The WPIA calculates $\boldsymbol{E}_w \cdot \boldsymbol{v}$ before accumulating the observed data.

cessing. For example, the WPIA needs the functions of FFT (Fast Fourier Transform) and IFFT (Inverse Fast Fourier Transform) as well as the calculation of $\boldsymbol{E}_w \cdot \boldsymbol{v}$. Since the WPIA needs to calibrate the observed waveforms before calculating $\boldsymbol{E}_w \cdot \boldsymbol{v}$, the FFT and IFFT processes are essential. The one-chip WPIA provides a solution for realizing a WPIA by keeping its mass and power consumption as small as possible.

6.3 Wave-Particle Interaction Analyzer (WPIA)

6.3.1 Interconnections with necessary sensors

In section 6.2, we described the principle of the Wave-Particle Interaction Analyzer (WPIA) and stressed its advantage in studying wave-particle interactions via spacecraft observations. In conducting onboard calculations of energy exchanges among plasma particles and waves by the WPIA, it is indispensable to coordinate the plasma wave receivers with the plasma and magnetic field instruments.

Figure 6.3 shows the interconnection of the WPIA with other sensors. Since the WPIA system calculates $\boldsymbol{E}_w \cdot \boldsymbol{v}$ onboard a spacecraft, it requires input of data from plasma sensors and fluxgate magnetometers as well as plasma wave sensors. Although scientific instruments onboard spacecraft are usually operated independently of other observation

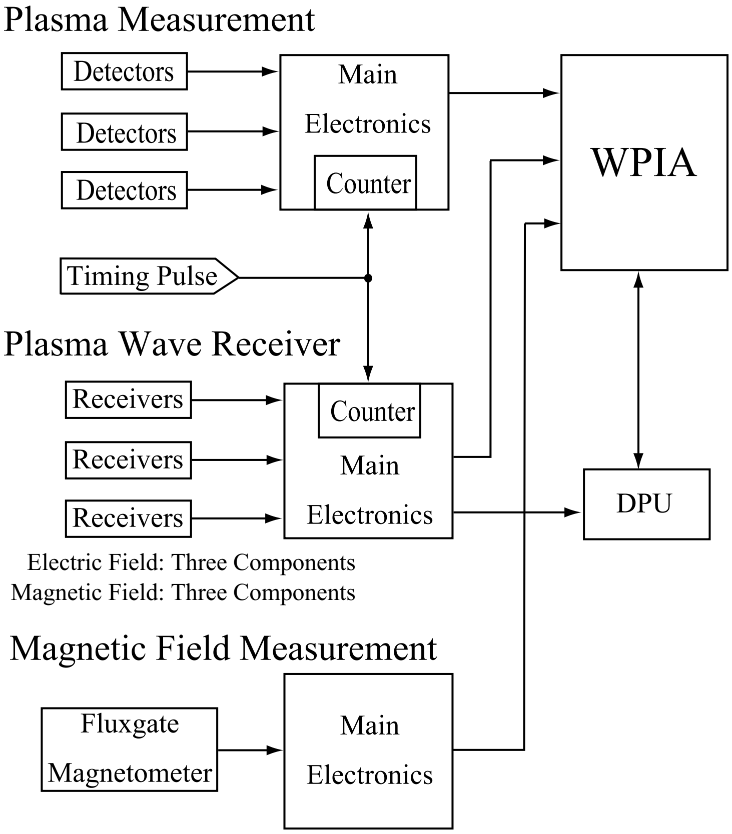

Figure 6.3: Interconnection of the WPIA with other instruments.

instruments, the WPIA works cooperatively with plasma wave, plasma, and magnetic field measurement instruments. Plasma wave receivers and plasma instruments transfer their observed data to the WPIA including their phase information. This means that plasma wave receivers and particle instruments should transmit the observed waveform data and the timing of the particle detection pulses with their energy information. Additional information such as the incoming directions of the detected particles are also sent to the WPIA. Further, the wave-particle interactions should be referred to the direction of the ambient magnetic field. For example, in the case of the interaction of electron beams and Langmuir waves, the calculation of $\boldsymbol{E}_{\parallel} \cdot \boldsymbol{v}_{\parallel}$ is essential, where $\boldsymbol{E}_{\parallel}$ and $\boldsymbol{v}_{\parallel}$ denote the instantaneous electric field vector and the detected particle velocity vector relative to the ambient magnetic field, respectively. For this transformation of the coordinate system in wave vectors and velocity vectors of particles, the data of the fluxgate magnetometer are used. Real-time operation of the WPIA requires the data transmission line to have a large enough capacity to send all of the data without any delays to the WPIA. If the system cannot provide enough data transmission capacity to the WPIA, some data buffers for storing the observed waveforms and particle information should be prepared. In that case, it is difficult to guarantee the real-time calculation of $\boldsymbol{E} \cdot \boldsymbol{v}$.

6.3.2 Blocks to be implemented

Figure 6.4 shows a block diagram of the WPIA. It describes the necessary functions to be implemented in the WPIA. As already mentioned, knowing the precise phase relation between the waveforms and the timing of the pulses is very important. Therefore, waveform calibration and data conversion such as transformation of the coordinate system are essential functions of the WPIA. In addition, as particle data are asynchronously obtained with respect to waveform data, we need information on their relative time difference to calculate $\boldsymbol{E}_w \cdot \boldsymbol{v}$ accurately.

Because the characteristics of wave receivers and sensors affect the amplitude and phase of the observed waveform, we need to calibrate the waveforms. The “Waveform Calibration” block shown in Fig. 6.4 takes the role of canceling the effects of analog circuits and sensors. The importance of the phase relation between the observed electric field vector and particle velocity vector is stressed. It is essential to obtain calibrated phase in the WPIA. The calibration is conducted by the FFT ($\mathscr{F}$) and IFFT ($\mathscr{F}^{-1}$) calculations using the calibration values of the plasma wave receivers and sensors,

$$X(f) = \mathscr{F}[x(t)], \tag{6.4}$$

$$x_{\mathrm{cal}}(t) = \mathscr{F}^{-1}[G^{-1}(f)X(f)], \tag{6.5}$$

where $x(t)$ denotes a time series of sampled raw waveform data, $G(f)$ is the transfer function of the plasma wave receiver including its sensor characteristics measured in ground

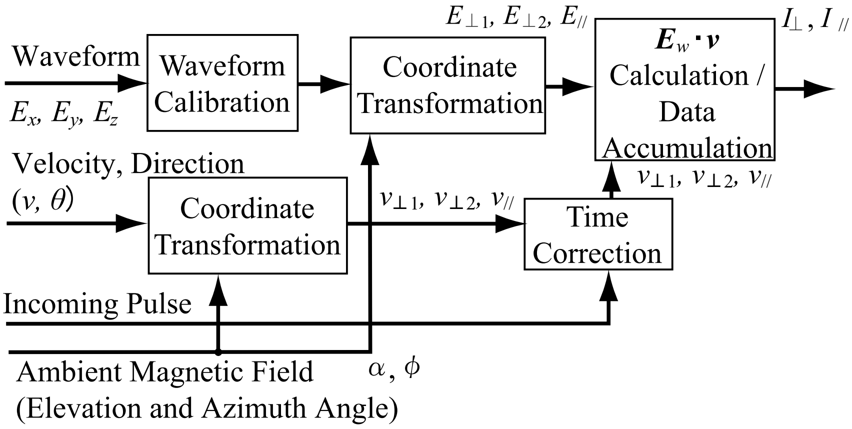

Figure 6.4: Data flow diagram of the WPIA.

tests, and $x_{\text{cal}}(t)$ is the time series data of calibrated waveforms. This calibration process should be applied to each component of a waveform. When the plasma wave receiver observes six components of waveforms simultaneously (i.e., three components for electric fields and three components for magnetic fields), six calibration processes will run on the WPIA in parallel. Thus, the calibration process causes the heaviest load on the WPIA. In the SCOPE mission including the one-chip type of the WPIA, satellites are spin-stabilized and have short rigid electric antennas along the satellite spin axis. Though the sensitivity of the short rigid antenna is generally much worse than a long wire antenna deployed perpendicular to the spin axis, the spin-axis antenna will have enough sensitivity for observing target plasma waves because of the low noise preamplifier. Hence, there is a difference of characteristics between the spin-axis antenna and wire antennas. The WPIA can calibrate waveforms using the independent calibration data for each axis of the antennas to provide measurements of the three components of the electric field with good precision.

The physical properties of the wave-particle interactions should be referenced to the local ambient magnetic field direction. The “Coordinate Transformation” block transforms the observed waveforms and particles relative to the ambient magnetic field. Figure 6.5 shows a typical coordinate system in a spin-stabilized spacecraft. $\boldsymbol{B}$ in the Fig. 6.5 is the local ambient magnetic field vector. The transform matrix is given by

$$\boldsymbol{r}_{\text{LM}} = [\hat{\alpha}][\hat{\phi}]\boldsymbol{r}_{\text{SC}}, \tag{6.6}$$

$$\boldsymbol{r}_{\text{LM}} = (r_{\perp 1}, r_{\perp 2}, r_{\|})^T, \quad \boldsymbol{r}_{\text{SC}} = (r_x, r_y, r_z)^T,$$

$$[\hat{\phi}] = \begin{pmatrix} \cos\phi & \sin\phi & 0 \\ -\sin\phi & \cos\phi & 0 \\ 0 & 0 & 1 \end{pmatrix}, [\hat{\alpha}] = \begin{pmatrix} \cos\alpha & 0 & -\sin\alpha \\ 0 & 1 & 0 \\ \sin\alpha & 0 & \cos\alpha \end{pmatrix},$$

where $\boldsymbol{r}_{\text{LM}}$ and $\boldsymbol{r}_{\text{SC}}$ are given vectors fixed in the local magnetic coordinate system and in

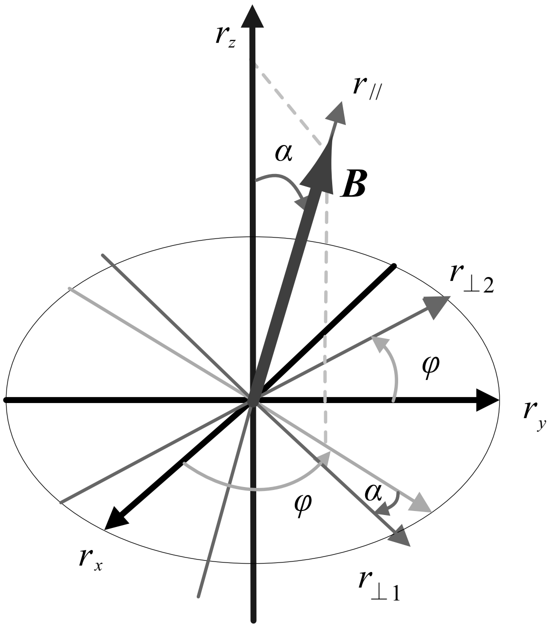

Figure 6.5: Relation between the coordinate system of the spacecraft and the ambient magnetic field.

the spacecraft coordinate system, respectively. Both suffixes 'LM' and 'SC' are appended to electric field vector $\boldsymbol{E}$, and particle velocity vector $\boldsymbol{v}$. In the local ambient magnetic field coordinate system, $\perp 1$ and $\perp 2$ are two orthogonal components in the plane perpendicular to the ambient magnetic field, $\|$ means the direction parallel to the magnetic field $\boldsymbol{B}$, ϕ and α are an azimuth and elevation angle, respectively.

Moreover, since plasma sensors are independently located in different positions on the spacecraft, we need another transformation calculation. If we obtain particle data as shown in Fig. 6.6, the transformation for particle data is given by Eq. (6.7), where ξ is the constant angle between the particle sensor and the r_x-axis of the spacecraft coordinate system,

$$\begin{aligned}\boldsymbol{v}_{\mathrm{SC}} &= (v_x, v_y, v_z)^T \\ &= v\begin{pmatrix}\cos\xi & -\sin\xi & 0\\ \sin\xi & \cos\xi & 0\\ 0 & 0 & 1\end{pmatrix}\begin{pmatrix}0\\ \cos\theta\\ \sin\theta\end{pmatrix} = \begin{pmatrix}-v\sin\xi\cos\theta\\ v\cos\xi\cos\theta\\ v\sin\theta\end{pmatrix}. \end{aligned} \tag{6.7}$$

The timing of particle detection pulses is not synchronized with the sampled waveforms of the plasma waves. The "Time Correction" block corrects the time difference in the observations of the waveforms and incoming particle pulses as shown in Fig. 6.7. To conduct the time correction, we need to know the precise relative time difference. The "Time Correction" block works as a controller to calculate $\boldsymbol{E}_w \cdot \boldsymbol{v}$ with enough accuracy in view of the relative time difference.

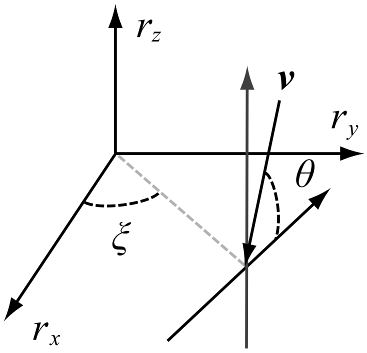

Figure 6.6: Relation between the coordinate system of the spacecraft and the coordinate system of a particle detector on a spacecraft which has a constant angle ξ relative to the r_x-axis. A particle with velocity v comes from a direction at angle θ to the $r_x r_y$-plane.

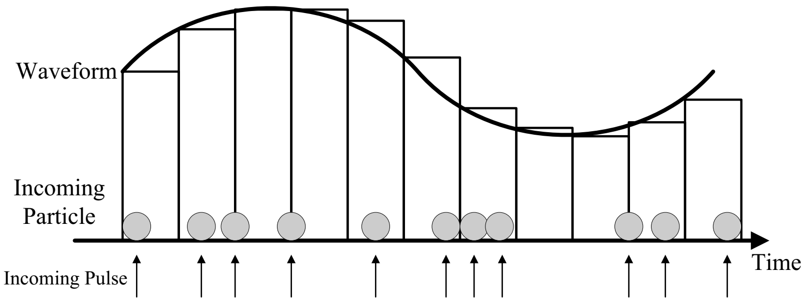

Figure 6.7: Schematic illustration indicating that a waveform is sampled and held at a sampling frequency although the particles are asynchronously caught by the particle detector.

The "$\boldsymbol{E}_w \cdot \boldsymbol{v}$ Calculation/Data accumulation" block calculates $\boldsymbol{E}_w \cdot \boldsymbol{v}$ and sums up the results in the parallel and perpendicular directions relative to the ambient magnetic field,

$$\tilde{I_\perp} = E_{\perp 1} v_{\perp 1} + E_{\perp 2} v_{\perp 2}, \tag{6.8}$$

$$\tilde{I_\parallel} = E_\parallel v_\parallel, \tag{6.9}$$

where $\tilde{I_\perp}$ and $\tilde{I_\parallel}$ are the perpendicular and parallel components relative to the magnetic field, respectively, $E_{\perp 1}, E_{\perp 2}, v_{\perp 1}, v_{\perp 2}$ are the electric fields and particle velocities in the perpendicular directions, and $E_\parallel, v_\parallel$ are the parallel components. Furthermore, "$\boldsymbol{E}_w \cdot \boldsymbol{v}$ Calculation" accumulates $\tilde{I_\perp}$ and $\tilde{I_\parallel}$ to detect the wave-particle interactions,

$$I_\perp = \sum \tilde{I_\perp} = \sum (E_{\perp 1} v_{\perp 1} + E_{\perp 2} v_{\perp 2}), \tag{6.10}$$

$$I_\parallel = \sum \tilde{I_\parallel} = \sum E_\parallel v_\parallel. \tag{6.11}$$

The accumulated values of $I_\perp$ and $I_\parallel$ are obtained as the physical measure of the wave-particle interactions.

6.4 One-Chip WPIA

6.4.1 Advantages of the One-Chip WPIA

The fundamental functions and interconnections of the WPIA with other sensors were described in section 6.3. The major functions of the WPIA can be realized by software running on a high-performance Central Processing Unit (CPU) or Digital Signal Processor (DSP). However, almost every computational resource of CPU or DSP is assigned to the WPIA due to the heavy load in the waveform calibrations and management of the data transfer from other sensors. We propose a one-chip WPIA as a solution for this difficulty. The one-chip WPIA possesses all of the necessary functions described in section 6.3. All of the functions are installed in the Field Programmable Gate Array (FPGA). The one-chip WPIA has such advantages as real-time processing and low power consumption.

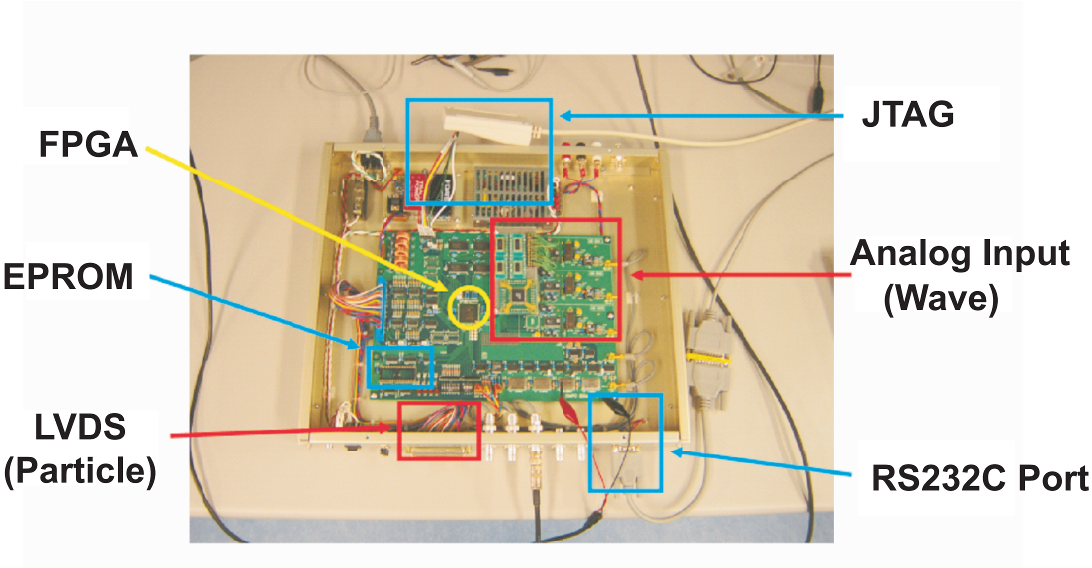

Figure 6.8: Evaluation board for developing the one-chip WPIA. It contains the FPGA device (located in the center of the figure) and peripheral circuits including simple plasma wave receivers and simulators of plasma and magnetic field sensors.

Figure 6.8 shows an evaluation board used in the development of the one-chip WPIA. It contains three channels of plasma wave receivers, input channels of the magnetic field and plasma instruments, as well as the FPGA. The three channels of plasma wave receivers collect waveforms at a sampling frequency of 62.5 kHz and transfer the waveform data with 16 bits to the WPIA through First-In First-Out (FIFO) memories. The frequency range to be observed in the plasma wave receivers is assumed to be from several hundred Hz to around a dozen kHz in the SCOPE mission. Thus, the O-WPIA is expected to observe wave particle interactions involving plasma waves such as whistler-mode chorus, Langmuir wave, or etc., which have a frequency of less than a dozen kHz. These specifications of the plasma wave receivers are almost the same as those of typical ones for targeting observations in the terrestrial magnetosphere.

A top-hat type particle detector utilizing the spacecraft spin will be installed in the mission. Although the field of view of the particle detector is limited in a very short time duration, the phase of the observed waves in the frequency range from several hundreds of Hz to several kHz rotates much faster than the spacecraft spin velocity. This means the O-WPIA can accumulate a lot of data on the phase relation of $\boldsymbol{E}_w \cdot \boldsymbol{v}$ even if the phase resolution of the particle detector is coarse. Thus, it can keep enough signal-to-noise ratio with limitation of the field of view.

We adopt the FPGA of the Xilinx XC2V1000 with 1 million gates. The operational clock frequency can be selected with an onboard switch as 1.920, 4.096, 40, or 100 MHz or by the external optional clock signal. In the present thesis, we set the clock frequency to 4 MHz by feeding in an external clock signal. Constant values such as the calibration data of the waveforms can be loaded onto the FPGA from the Erasable Programmable Read-Only Memory (EPROM) installed on the evaluation board. Detailed specifications of the FPGA applied to the one-chip WPIA are summarized in Table 6.1.

Table 6.1: Logic cells of Virtex-II XC2V1000 FG456.

Function	Number
Logic Cells	11,520
Block Select RAM (kb)	720
18×18 Multipliers	40
Digital Clock Management Blocks	8
Max Dist RAM (kb)	160
Max Available User I/O	432

6.5 Design of the One-chip WPIA

6.5.1 Waveform Calibration

Figure 6.9 shows the state transition diagram of the “Waveform Calibration” block. As mentioned in section 6.3, we make use of the FFT and IFFT functions in the “Waveform Calibration” block. The transforms are implemented as complex FFT and IFFT which can concurrently transform two components of waveforms by inputting two data sets into their real and imaginary parts. Therefore, two pairs of FFT and IFFT blocks are enough to conduct the calibration of three components of waveforms at once. We show a block diagram of the “Waveform Calibration” in Fig. 6.10.

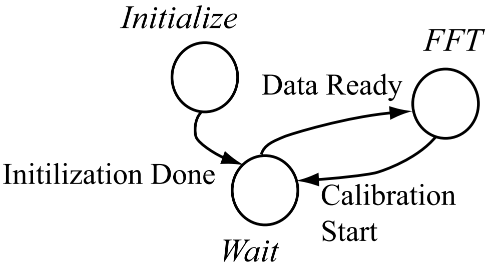

Figure 6.9: State transition diagram of the “Waveform Calibration” block.

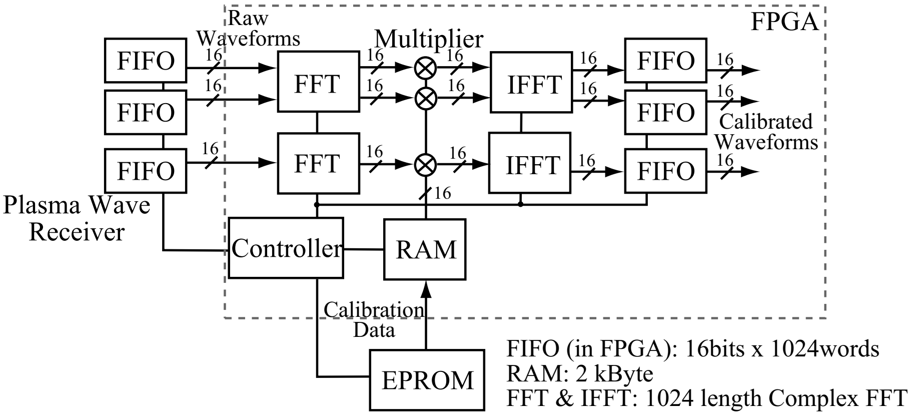

Figure 6.10: Block diagram of the “Waveform Calibration”.

The forward FFT blocks read the sampled raw waveforms from the FIFOs of the plasma wave receiver and obtain the results of the FFT corresponding to $X(f)$ in Eq. (6.4). The multipliers calculate the product of the results of the FFT and calibration data which are loaded from the onboard EPROM into Block Select RAM memory (inside the FPGA) at the initialization stage of the system. The inverse FFT block calculates the inverse transform of the product and outputs the calibrated waveforms. The calibrated waveforms are stored in FIFOs on the FPGA and read out the sampling frequency at the next block.

In the FFT, the discrete frequency is

$$f_k = \frac{f_s}{L} k (k = 0, 1, 2, \cdots L - 1), \tag{6.12}$$

where L is the number of sampled data points and f_s is the sampling frequency, respectively. Note that $X(k)$ is symmetrical, as indicated by Eqs. (6.14) and (6.15),

$$X(k) = \sum_{n=0}^{L-1} x(n) e^{-j\frac{2\pi k}{L}n}, \quad (n = 0, 1, 2, \cdots L - 1) \tag{6.13}$$

$$\mathrm{Re}[X(L-k)] = \mathrm{Re}[X(k)], \tag{6.14}$$

$$\mathrm{Im}[X(L-k)] = -\mathrm{Im}[X(k)], \tag{6.15}$$

where $X(k)$ can be obtained from $X(0)$ to $X(L-1)$ sequentially and is multiplied by $H(k)$ which is the calibration data given by

$$H(k) = G^{-1}(f)|_{f=f_k} = \frac{e^{-j\varphi(f_k)}}{A(f_k)}, \tag{6.16}$$

$$= \begin{cases} H_{\mathrm{real}}(k) + jH_{\mathrm{imag}}(k) & (0 \leq k < L/2 - 1) \\ H_{\mathrm{real}}(L-k) - jH_{\mathrm{imag}}(L-k) & (L/2 \leq k < L-1), \end{cases} \tag{6.17}$$

where $A(f_k)$, and $e^{-j\varphi(f_k)}$ denote the calibration data of the plasma wave receiver in gain and phase, respectively. The calibrated waveform $x_{\mathrm{cal}}(n)$ is obtained from the following IFFT,

$$x_{\mathrm{cal}}(n) = \frac{1}{L}\sum_{k=0}^{L-1} H(k)X(k)e^{j\frac{2\pi n}{L}k}. \tag{6.18}$$

The sampled waveform data are transmitted to the one-chip WPIA through the FIFO with a capacity of 4096 words. Since a series of data is continuously input to the forward FFT at the clock frequency, we need to choose L to be less than or equal to 4096 to avoid overflow of the FIFO. The number of data L affects the frequency resolution as well as the processing time (equivalent to the time resolution). We need to choose it by considering the target phenomena from the point of view of frequency and time resolution. We also need to take into account the available logic gates of the FPGA in determining L. In this thesis, L is fixed at 1024, which is equivalent to a frequency resolution of 61 Hz.

Since the load of the FFT calculations is the heaviest in the one-chip WPIA system, an estimation of the processing time of the FFT including the coordinate transformation is important. The period (T_{in}) required to obtain the waveforms depends on the number of data L. Further, the period to calculate the forward and inverse FFTs (T_{cal}) also depends on L. The “Coordinate Transformation” block processes the data in T_{trans} equivalent to three cycles of the system clock. Thus, the total time (T_{total}) can be estimated as the sum of T_{in}, T_{cal}, and T_{trans}. The particle data to be processed with the waveform data are kept in the Block Select RAM during the period of T_{total} in order to make it possible to conduct a series of calculations without delay. These periods are given by

$$T_{\mathrm{in}} = \frac{L}{f_s}, \tag{6.19}$$

$$T_{\mathrm{cal}} = \frac{N_{\mathrm{cal}}}{f_c}, \tag{6.20}$$

$$T_{\mathrm{trans}} = \frac{N_{\mathrm{trans}}}{f_c} = \frac{3}{f_c}, \tag{6.21}$$

$$\begin{aligned} T_{\mathrm{total}} &= T_{\mathrm{in}} + T_{\mathrm{cal}} + T_{\mathrm{trans}}, \\ &= \frac{L}{f_s} + \frac{N_{\mathrm{cal}} + 3}{f_c}, \end{aligned} \tag{6.22}$$

where $f_s = 62.5$ kHz is the sampling frequency, $f_c = 4$ MHz is the clock frequency of the FPGA, and N_{cal} and N_{trans} are the number of clock cycles of calibration and coordinate transformation, respectively. In the case of $L = 1024$, $N_{\mathrm{cal}} = 12542$ cycles are needed to complete the whole calibration process (data load and transformation : 6264 cycles / FFT, delay to output : 7 cycles / FFT; determined by specification of applied Intellectual Property (IP) core). Thus, the period and number of clock cycles are calculated to be

$$\begin{aligned} T_{\mathrm{in}} &= 16.384 \text{ ms}, && (6.23)\\ T_{\mathrm{cal}} &= 3.1355 \text{ ms}, && (6.24)\\ T_{\mathrm{trans}} &= 0.75\ \mu\text{s}, && (6.25)\\ T_{\mathrm{total}} &= 19.52025 \text{ ms}, && (6.26)\\ N_{\mathrm{total}} &= f_c T_{\mathrm{total}} = 78081\text{cycles}. && (6.27) \end{aligned}$$

Equation (6.27) implies that the calibrated waveforms are obtained after 78081 clock cycles.

The count rate of the plasma detectors should also be considered in the design of the one-chip WPIA. It strongly depends on the plasma flux and on the sensitivity of the plasma sensors. In our current design of the one-chip WPIA, we assume the maximum count rate is expected to be 10^5/s in the SCOPE mission along its orbit inside the magnetosphere. Therefore the expected number of particle count pulses for the period of $T_{\mathrm{total}} = 19.52025$ ms is 1952. The bit width of the Block Select RAMs for particle data is 65, since we need to store 16-bit velocity data for particles in three dimensions and 17-bit time information at which each particle is detected. In considering the amount of RAM to keep the particle data, we must set L to be less than or equal to 1024.

6.5.2 Coordinate Transformation

The "Coordinate Transformation" blocks calculate the parallel and perpendicular components of the waves and velocities of the particles in reference to the ambient magnetic field,

$$\boldsymbol{E}_{\mathrm{LM}} = [\hat{\alpha}][\hat{\phi}]\boldsymbol{E}_{\mathrm{SC}} \tag{6.28}$$

$$\boldsymbol{v}_{\mathrm{LM}} = [\hat{\alpha}][\hat{\phi}]\boldsymbol{v}_{\mathrm{SC}}, \tag{6.29}$$

where $\boldsymbol{E}_{\mathrm{LM}} = (E_{\perp 1}, E_{\perp 2},\ E_{\parallel})^T, \boldsymbol{E}_{\mathrm{SC}} = (E_x, E_y, E_z)^T$, $\boldsymbol{v}_{\mathrm{LM}} = (v_{\perp 1}, v_{\perp 2}, v_{\parallel})^T$, and $\boldsymbol{v}_{\mathrm{SC}} = (v_x, v_y, v_z)^T$.

It is necessary to calculate the product of the two matrices $[\hat{\alpha}]$ and $[\hat{\phi}]$. The number of available multipliers are limited and the multiplication needs two clock cycles at least in the FPGA because of specification of applied multipliers. To decrease them, the one-chip

WPIA calculates the multiplication by one matrix, as shown in Eqs. (6.30), (6.31), and (6.32). The diagram in Fig. 6.11 shows the operation of the multiplication,

$$\boldsymbol{E}_{\mathrm{LM}} = [\widehat{\alpha\phi}]\boldsymbol{E}_{\mathrm{SC}}, \tag{6.30}$$

$$\boldsymbol{v}_{\mathrm{LM}} = [\widehat{\alpha\phi}]\boldsymbol{v}_{\mathrm{SC}}, \tag{6.31}$$

$$[\widehat{\alpha\phi}] = \begin{pmatrix} \dfrac{\cos(\alpha+\phi)+\cos(\alpha-\phi)}{2} & \dfrac{\sin(\alpha+\phi)-\sin(\alpha-\phi)}{2} & \sin\alpha \\ -\sin\phi & \cos\phi & 0 \\ \dfrac{\sin(\alpha+\phi)+\sin(\alpha-\phi)}{2} & \dfrac{-\cos(\alpha+\phi)+\cos(\alpha-\phi)}{2} & \cos\alpha \end{pmatrix}, \tag{6.32}$$

where $\sin\alpha$, $\cos\alpha$, $\sin\phi$, $\cos\phi$, $\sin(\alpha+\phi)$, $\cos(\alpha+\phi)$, $\sin(\alpha-\phi)$, and $\cos(\alpha-\phi)$ are obtained from sine and cosine lookup tables.

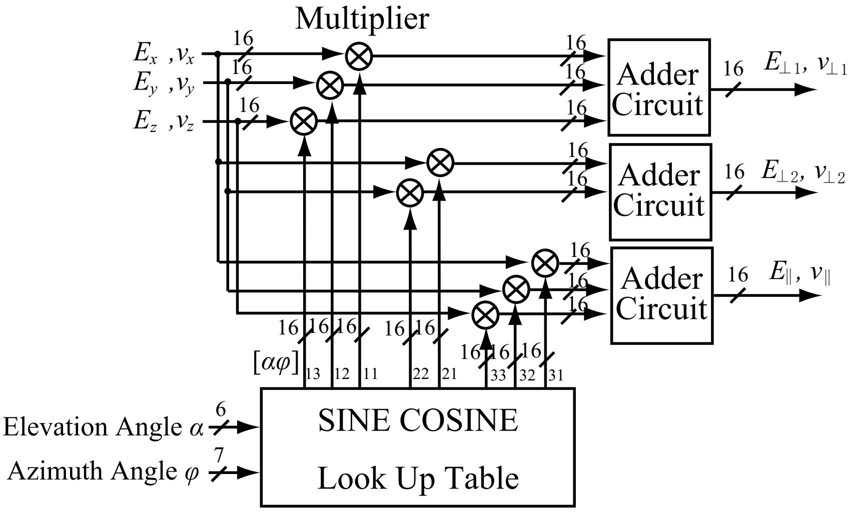

Figure 6.11: Block diagram of the "Coordinate Transformation" for the ambient magnetic field coordinate system.

The "Coordinate Transformation" needs three clock cycles. Two clock cycles are necessary for the multiplication and one clock cycle is necessary for loading the values from the tables.

The design of the "Coordinate Transformation" block for the spacecraft coordinate system is shown in Fig. 6.12. This block transforms the speed of a particle and its incoming direction into the velocities (v_x, v_y, v_z) before the other transformation is performed.

6.6 Time Correction

The waveforms and particle data are asynchronously obtained. Moreover, the particle data must wait for the end of the "Wave Calibration" and "Coordinate Transformation"

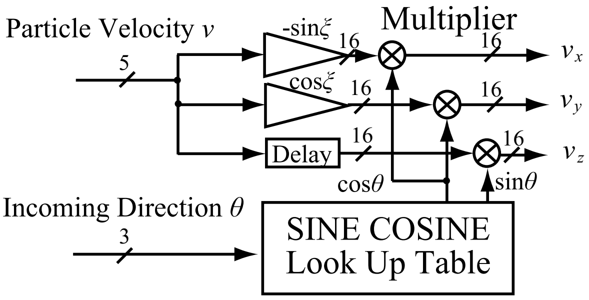

Figure 6.12: Block diagram of the "Coordinate Transformation" for the spacecraft coordinate system.

processes as shown in Fig. 6.13. The "Time Correction" is a controller that synchronizes the waveform and particle data, as sketched in Fig. 6.14.

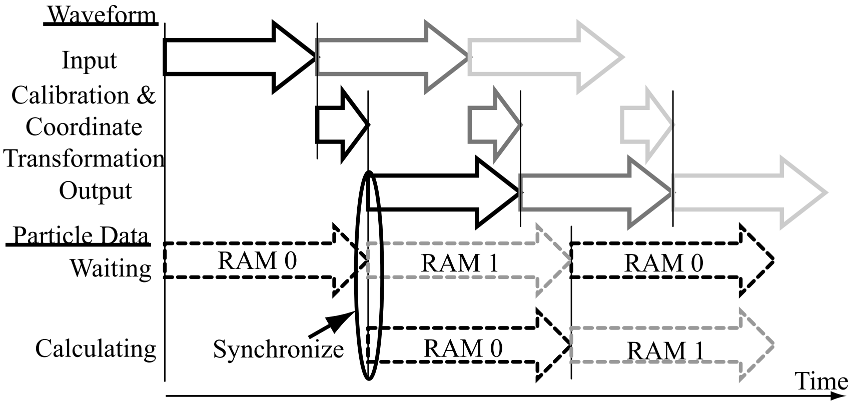

Figure 6.13: Timing chart for the time correction. After the first input of waveform data, calculations of the waveform calibration and coordinate transformation start while the second input starts. The first particle data set is written in RAM0 and waits for the end of the calculations of the first waveform data set. When the calculations are finished, RAM0 transfers the first data set and RAM1 takes the role of RAM0.

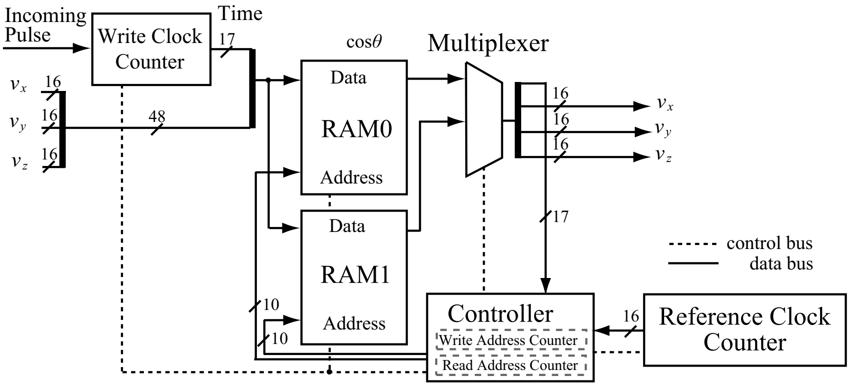

Figure 6.14: Block diagram of the “Time Correction”.

In the “Time Correction” block, the one-chip WPIA has two clock counters, which indicate the relative time difference of the sampled waveforms and the detected plasma pulses. Both counters count at the clock frequency of the FPGA. One of the clocks is called the “Write Clock” and the other is the “Reference Clock.” While the “Write Clock” starts counting when the sampling of the raw waveforms starts, the “Reference Clock” begins when the first calibrated waveforms are generated. The “Write Clock” and “Reference Clock” are reset to zero if the count of each clock reaches N_{total} of 78081 clock cycles. Since two Block Select RAMs are prepared inside the FPGA, they are switched between reading and writing by so-called switching buffers. Both RAMs have individual address counters and they are reset to zero when the RAMs are switched. The transformation for the particle data needs seven clock cycles (load trigonometric function values : 2 cycles, twice multiplication: 2 × 2 cycles, hold sum of the products, 1 cycles). The “Reference Clock” is reset every seven clock cycles behind the reset of the “Write Clock” to synchronize accurately, as shown in Fig. 6.15.

When an incoming pulse from the plasma instruments is detected, the count number of the “Write Clock” is held in a temporary memory and the address counter of the writing RAM process is incremented. The held count is stored again with the transformed velocity $(v_{\perp 1}, v_{\perp 2}, v_{\parallel})$, in the area which the writing RAM address indicates. After switching the roles of the RAMs, the stored count is compared with the “Reference Clock” count. If the stored count and the “Reference Clock” are equal to each other, the stored velocity is read out from the RAM and the RAM address is incremented. We can thereby obtain synchronized particle data with calibrated waveforms and calculate $\boldsymbol{E}_w \cdot \boldsymbol{v}$.

6.6.1 Calculation of $\boldsymbol{E}_w \cdot \boldsymbol{v}$/Accumulation

In the “Calculation of $\boldsymbol{E}_w \cdot \boldsymbol{v}$/Accumulation” block, $I_\perp$, and $I_\parallel$ are calculated and accumulated for a given period represented by Eqs. (6.10) and (6.11). The accumulation

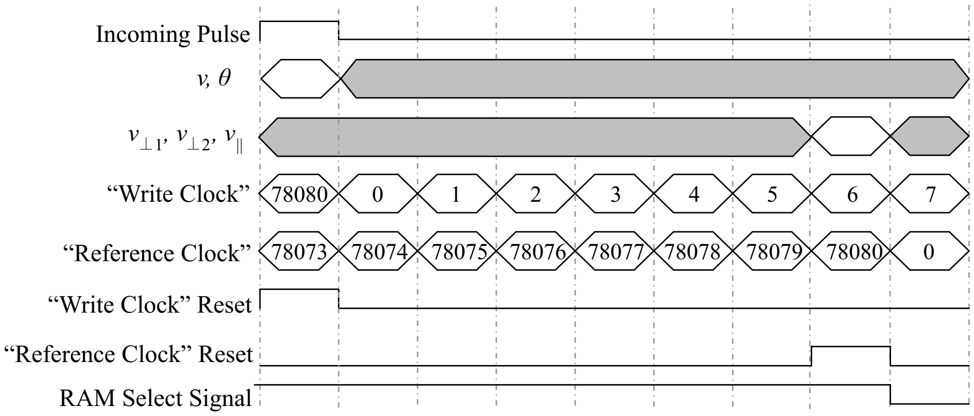

Figure 6.15: Data v and θ are captured when the incoming pulse becomes 'High'. It takes seven clock cycles to transform v and θ into $v_{\perp 1}$, $v_{\perp 2}$, and $v_{\|}$. The incoming pulse is held in seven clock cycles to save information about time. Thus, the "Reference Clock" is reset and the RAM select signal is inverted seven clock cycles behind the reset of the "Write Clock."

time depends on the required time resolution. The amount of time needed to accumulate $I_{\|}$ and $I_{\perp}$ should be a few times larger than one period of the observed waves since we should consider phase relation between the plasma waves and particles for various phases of the plasma waves. The frequency of observed plasma waves is assumed to be less than a dozen kHz in the SCOPE mission. In this study, we use a period of 64 times the $\boldsymbol{E}_w \cdot \boldsymbol{v}$ calculation. Assuming a particle count rate of 10^5/s, the time resolution is 640 μs. This value is sufficient since it is equal to a few times larger than than one period of the waves.

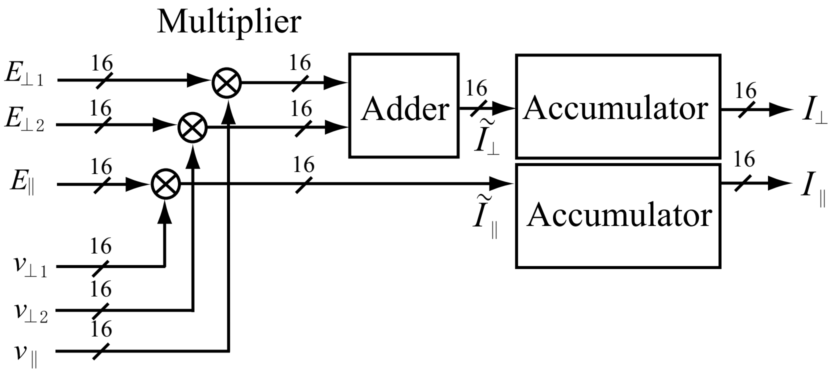

Figure 6.16: Block diagram of the "$\boldsymbol{E}_w \cdot \boldsymbol{v}$ Calculation".

The design of the "Calculation of $\boldsymbol{E}_w \cdot \boldsymbol{v}$" block is shown in Fig. 6.16. Three multipliers independently calculate the product of the electric field and the particle velocity, $E_{\perp 1}v_{\perp 1}, E_{\perp 2}v_{\perp 2}$, and $E_{\|}v_{\|}$. Products in two perpendicular directions ($E_{\perp 1}v_{\perp 1}$, and

$E_{\perp 2}v_{\perp 2}$) are added before accumulation. The calculations of $\tilde{I_{\perp}}$ and $\tilde{I_{\parallel}}$ are held in two separate accumulators. The multipliers are enabled every time that particle data are read out from the "Time Correction" and the accumulators are enabled two clock cycles later.

6.7 Performance

In this section, we demonstrate that the one-chip WPIA properly functions on the FPGA. We also estimate the power consumption of the one-chip WPIA with application to future missions in mind.

6.7.1 Operational Accuracy

We checked the one-chip WPIA functions by giving it $\boldsymbol{E}_w(t)$ and $\boldsymbol{v}(t)$ dummy data, which are time series of electric field and particle velocity vectors, respectively. In order to make it easy to examine the functions, we use the following simple dummy data,

$$\boldsymbol{E}_w(t) = (E_0 \sin(2\pi f t + \varphi), 0, 0)^T, \tag{6.33}$$

$$\boldsymbol{v}(t) = \Big(v_0 \sum_k \delta(t - \frac{k}{f_v}), 0, 0\Big)^T. \tag{6.34}$$

Here $\boldsymbol{E}_w$ is a sinusoidal wave with frequency f, and $\boldsymbol{v}$ is a series of periodic pulses at a cycle of $1/f_v$ expressed as a sum of delta functions, respectively. Both $\boldsymbol{E}_w$ and $\boldsymbol{v}$ are generated within the FPGA.

Assuming the ratio of f/f_v is equal to an integer, the output of the one-chip WPIA should be

$$I(t) \propto t. \tag{6.35}$$

By using these dummy data, we can confirm the functions of the whole one-chip WPIA including the "Waveform Calibration", "Time Correction", "Coordinate Transformation", and "Calculation of $\boldsymbol{E}_w \cdot \boldsymbol{v}$."

Figure 6.17 shows the output $I(t)$ of the one-chip WPIA for the above check configuration. Both of the frequencies f and f_v are set to 3.90625 kHz, which is equal to exactly 1/16 of the sampling frequency of the wave receiver. The output $I(t)$ is reset every 524 ms in order to avoid overflow of the accumulators in the "Calculation of $\boldsymbol{E}_w \cdot \boldsymbol{v}$." The results show that the output is proportional to the time step number without distortions, and therefore the one-chip WPIA on the FPGA operates as designed. Notably it is confirmed that the functions of the time correction and the calculation of $\boldsymbol{E}_w \cdot \boldsymbol{v}$ work properly.

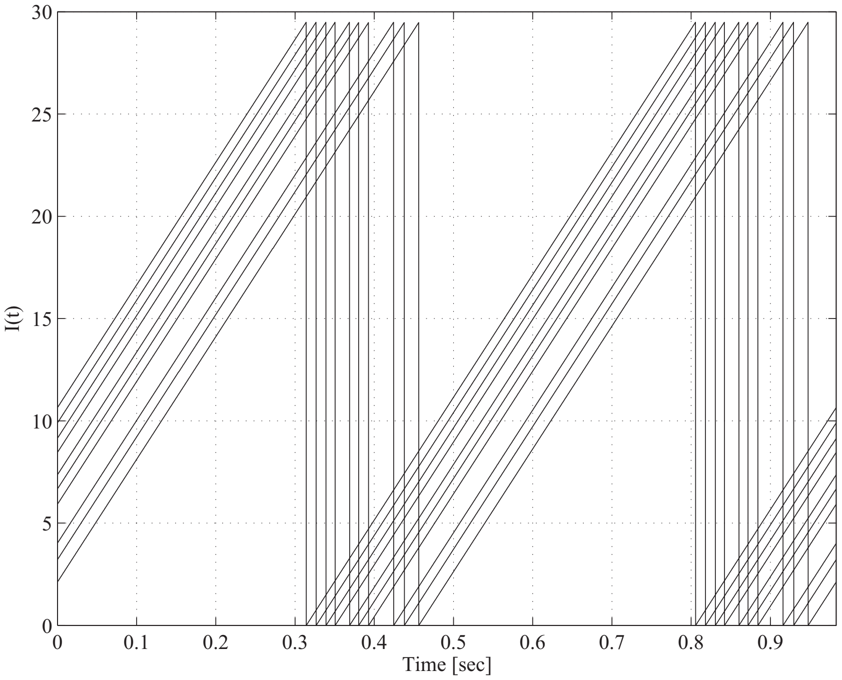

Figure 6.17: Ten results of $I(t) = \sum \boldsymbol{E}(t) \cdot \boldsymbol{v}(t)$. There is only a time distinction between the curves.

6.7.2 Calibration errors

The phase of the collected waveforms are important in calculating $\boldsymbol{E}_w \cdot \boldsymbol{v}$. We therefore need to evaluate the expected phase errors depending on the signal-to-noise-ratio (SNR). To do so, we measure the errors in the “Waveform Calibration” to examine the influence of noise.

The errors in the “Waveform Calibration” are measured as follows: **1.** A sinusoidal waveform with a fixed frequency is fed to the plasma wave receiver on the evaluation board. **2.** The digitized waveform from the A/D converter is input to the one-chip WPIA through the FIFO. **3.** The waveforms at the input and output of the “Waveform Calibration” block are transfered to the workstation through the Joint Test Action Group (JTAG) cable. **4.** The phase errors are measured by comparing the phases of the input and output waveforms on the workstation.

In these measurements, we make use of the calibration table in the whole frequency range at a gain of 0 dB and phase of 90°. The frequencies are 5 kHz, 10 kHz, 15 kHz, 20 kHz, and 3.90625 kHz ($= f_s/16$), which is chosen to investigate the influence of the discretization. The measurements are conducted twenty times under the same conditions except for the initial phase of the raw waveforms. The average and standard deviation are calculated at each frequency.

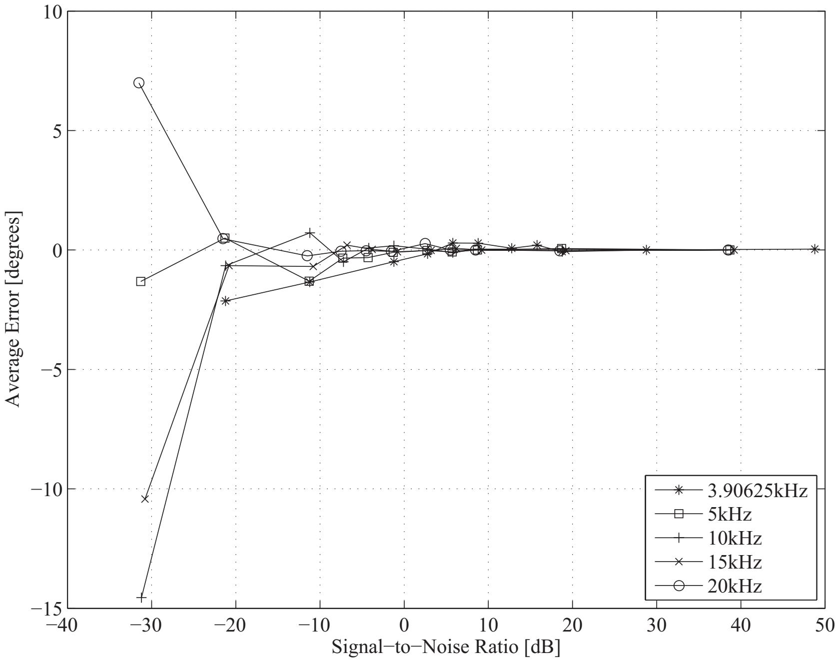

Figure 6.18: Average errors in the "Waveform Calibration" are plotted against the signal-to-noise ratio at the frequencies of the input waveform of 3.90625 kHz, 5 kHz, 10 kHz, 15 kHz, and 20 kHz.

In Figs. 6.18 and 6.19, these errors are plotted versus the SNR, at the indicated frequencies. The average errors are larger than 0 dB at small SNR because of the increased noise. The standard deviation of the errors becomes large when the SNR is smaller than 10 dB. Furthermore, at low frequency the standard deviation increases. The relative difference between the true frequency of the raw waveform and the discrete frequency of the calibrated waveforms is not related to the increase in the standard deviation at 3.90625 kHz. Therefore, since the waveform period in a fixed length FFT decreases with decreasing frequency, the larger standard deviation is caused by the growing data spread due to the difference in the initial phase of the waveform.

In general, the angular resolution of a plasma detector is 20°. If we assume that the errors have a normal distribution and less than 1% fall outside of the angular resolution range, then the SNR has to reduce the standard deviation to less than 1/2.576 of 10°. That is, the SNR needs to be not less than −3 dB (at 3.90625 kHz) to realize the assumed precision. If less than 0.1 % of the errors are to be out of the range, then the SNR should be at least 0 dB.

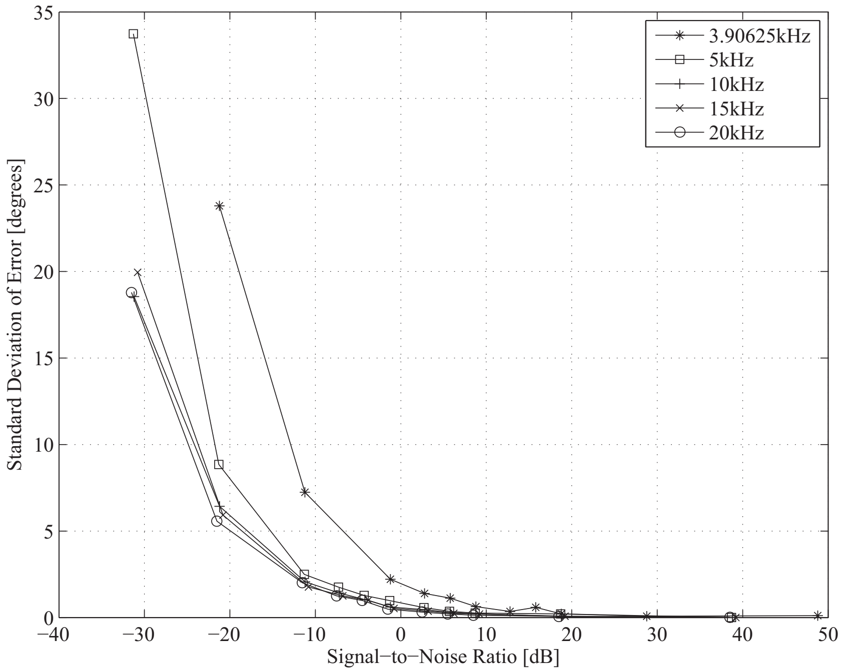

Figure 6.19: Standard deviation of the errors in the "Waveform Calibration" are plotted against the signal-to-noise ratio at the frequencies of the input waveform of 3.90625 kHz, 5 kHz, 10 kHz, 15 kHz, and 20 kHz.

6.7.3 Power consumption

The power budget is a critical issue to be resolved in space missions. The allocation to each instrument depends on the spacecraft configuration. It is important to estimate the power consumption of the one-chip WPIA and its dependence on variations in its design.

The power consumption of the FPGA can be calculated using Xilinx Virtex-II Web Power Tool by inputing the number of logic gates and the system clock frequency. The power consumed by the FPGA is 410 mW with the one-chip WPIA configured by the "Waveform Calibration" containing two pairs of FFT-IFFT for three components of the waveforms, and the "Time Correction" with the allocation of 2048 words in the Block Select RAMs. The toggle rates are set to 20% and 5% for the "Waveform Calibration" and other components, respectively. These use a FFT data length of 1024 and a particle count rate of 10^5/s. In addition, one must take into account the power consumption of the three onboard FIFO memories, which is approximately 90 mW. Therefore, the total power of the one-chip WPIA is estimated to be 500 mW. Noting that the one-chip WPIA does not require other components such as a CPU or DSP, this total power consumption of 500 mW is feasible for the SCOPE mission.

6.8 Conclusion

Conventionally, the study of wave-particle interactions using observational data has been conducted by comparing the spectra of plasma waves with energy spectra or velocity distributions of plasmas. However, the relation between the phase and timing of the detected particles has been ignored, despite its importance in wave-particle interactions. Some attempts at directly measuring the wave-particle interactions have been made by rocket experiments and spacecraft observations [e.g., *Ergun et al.*, (1991); *Kletzing et al.*, (2005)]. They have focused on the relationship between the observed phase and the timing of the particle detections. However, since they counted particles by considering the observed wave phase, they did not obtain the physical energy flows. The WPIA provides $\boldsymbol{E}_w \cdot \boldsymbol{v}$, incorporating the time variation of the kinetic energies during the interactions of the waves and particles.

The calculation of $\boldsymbol{E}_w \cdot \boldsymbol{v}$ requires several procedures including waveform calibration and coordinate transformation. The waveform calibration is essential to obtain the correct phase from the observed data. The calibration consists of a calculation of the FFT and IFFT. It requires a dedicated digital processing component with high performance to accomplish real-time operation of the WPIA.

We succeeded in developing a new scientific instrument for studying wave-particle interactions in space. We called it the one-chip WPIA. It provides a solution for realizing the WPIA on a real-time basis with minimum resources. The one-chip WPIA is the FPGA which implements all of the necessary functions. The one-chip WPIA has been proposed for SCOPE (cross-Scale COupling in the Plasma universE) mission which targets the investigation of the cross-scale coupling in the terrestrial magnetosphere. In the present chapter, we demonstrated the design, functions, and performance of the one-chip WPIA. It consists of four blocks for individual functions of waveform calibration, coordinate transformation, time correction, and calculation of $\boldsymbol{E}_w \cdot \boldsymbol{v}$. These blocks operate in cooperation with other necessary sensors. Since the one-chip WPIA calculates $\boldsymbol{E}_w \cdot \boldsymbol{v}$ in reference to the ambient magnetic field, it needs data from the particle and magnetic field instruments as well as from the plasma wave receivers. The WPIA directs the processes in the above blocks by coordinating the data flows from these sensors.

We realized a one-chip WPIA on an evaluation board containing a plasma wave receiver and an interface with plasma instruments and other components needed in the development of the one-chip WPIA. By using this evaluation board, we confirmed that the one-chip WPIA works as designed. We showed that it continuously calculated $\boldsymbol{E}_w \cdot \boldsymbol{v}$ with enough precision and without delays.

Furthermore, we examined the accuracy of the waveform calibration by comparing the phase angles of the raw and calibrated waveforms. The accuracy was determined by the average and standard deviation of the error. The average and standard deviation explicitly increase when the SNR is smaller than 0 dB and 10 dB, respectively. Assuming an error range of 20° and a probability that the errors arising from the waveform calibration are out of range by 1 % or 0.1 %, a respective SNR of greater than −3 dB or 0 dB is required. Though the large errors at lower frequency have to be reduced by using several different numbers of FFTs or by setting a lower sampling frequency, we achieved good accuracy in the major range of frequency to be observed (several hundred Hz to around a dozen kHz) in the SCOPE mission.

The one-chip WPIA enables the study of various wave-particle interactions using spacecraft observation data. The power consumption is estimated to be 500 mW when processing three components of waveforms sampled at 62.5 kHz and reading plasma data at a maximum count rate of 10^5/s. This specification is comparable to that of space missions for observing the terrestrial magnetosphere. Therefore, the one-chip WPIA is feasible for the SCOPE mission.

The most important feature of the one-chip WPIA is to guarantee real-time observations. Although the function of the one-chip WPIA can be realized by software running on a CPU, continuous operation in real time would be difficult. The software-type WPIA has been proposed for ERG (Energization and Radiation in Geospace), which is a small satellite mission focusing on the observation of the radiation belt of the Earth. On the other hand, a disadvantage of the one-chip WPIA compared to software WPIA is its smaller flexibility in the calculation and accumulation of $\boldsymbol{E}_w \cdot \boldsymbol{v}$. For example, software WPIA can change accumulation procedures depending on the wave-particle interactions. We have not examined how much flexibility one can expect in a one-chip WPIA. Since there exist various types of wave-particle interactions in space, flexibility in the calculation and data accumulation is important. The next goal in the development of the one-chip WPIA is to incorporate as much flexibility as possible.

Chapter 7

Concluding Remarks

7.1 Summary and Conclusions

In the present thesis, the miniaturization and integration of measurement instruments for space plasma physics were reported. The electromagnetic environment in space is characterized by plasma waves since the space plasmas are essentially collisionless. A plasma wave receiver and the wave-particle interaction analyzer (WPIA), which cooperates with the instrument for plasma measurement and the magnetometer, were considered for miniaturization and integration. Although digital circuits have reduced their size and mass, the plasma wave receiver still uses analog front-end circuits without downsizing. Analog application specific integrated circuits (ASIC) have been developed for the miniaturization of the plasma wave receiver. A circuit board was developed for the waveform receiver chip with peripheral circuits i.e., a power circuit, a clock generator, and analog-to-digital converters. Applications using the miniaturized receivers were also introduced. The WPIA is a novel instrument for measuring energy transport between plasmas and plasma waves. A one-chip WPIA was demonstrated using a field programmable gate array (FPGA). This instrument provides kinetic energy variation of a plasma in real-time.

In Chapter 1, the natural space environments around the Earth are introduced. The Earth's magnetism interacts with the solar wind, which is a supersonic plasma flow and forms the magnetosphere. The solar wind and upper atmosphere produce plasmas around the Earth. Since the space plasmas are very subtle, plasma waves are important for space plasma physics. Therefore, electric and magnetic field sensors and plasma detectors are used to investigate the space environment. The weight and size of the onboard instruments connected to the sensors, especially plasma wave receivers, have recently undergone further reduction for forthcoming scientific missions. The effect of miniaturization and integration of the plasma wave receiver and the cooperative instrument with different kinds of the sensors are described.

In Chapter 2, the methods for achieving miniaturization and integration are introduced with the plasma wave receivers used in previous scientific missions. Replacing the analog circuits with digital hardware and software have reduced the size and weight budget of the plasma wave receiver. However, the power consumption increases and hence analog electronics continue to be used at the front-end of the receiver. The ASIC technology, which enables the receiver to be reduced in size, was presented. The circuits to be downsized with the ASIC were described. Two kinds of receiver, waveform receiver and spectrum analyzer, are introduced as the targets of the miniaturization and integration. A waveform receiver of six-channel filters and amplifiers is integrated on one chip. The spectrum receiver inside the ASIC is a double super heterodyne receiver where the timer resolution is improved by combining digital signal processing.

In Chapter 3, circuits for the waveform receiver and the spectrum analyzer are designed and tested. For the waveform receiver, low-noise and manufacturing accuracy are necessary. A $\mathrm{G_m}$–C filter was applied to the low-noise filter and a switched capacitor filter was employed as the anti-aliasing filter. A differential amplifier with switchable gains of 0, 20, and 40 dB was designed. Noise eliminating filters were also inserted in front and behind the switched capacitor filter. The performances of these circuits were confirmed as being acceptable. A mixer, bandpass filter to reject images of mixing, and frequency synthesizer with phase-locked loop (PLL) were designed for the spectrum analyzer. Prototypes of a double-balanced mixer, eighteenth-order switched capacitor filter, voltage-controlled oscillator, and loop filter for the PLL were manufactured and tested. The operation and characteristics of the overall PLL and the frequency conversion with image rejection were confirmed in simulations.

In Chapter 4, the developed circuits in the ASIC for the waveform receiver is integrated into a system chip. The physical layout design of the entire receiver is introduced. A circuit board of 45×50 mm^2 was designed and the system chip was installed on the circuit board. Switchable gains were obtained with errors less than -3 dB. The cross talks were approximately -50 dB between two channels. The sensitivity was improved for the medium and high gain setting, sufficient for scientific observations. The waveform receiver has been successfully miniaturized to a twentieth of the size of instruments developed for previous missions.

In Chapter 5, two different applications using the miniaturized plasma wave receiver are presented. A measurement system for the space electromagnetic environment (MSEE) was introduced. The MSEE consists of a sensor network system with a number of plasma wave sensor nodes. Each sensor node has triaxial electric and magnetic field sensors, a dry battery, a communication transceiver, and attitude detection sensors. Each sensor node is distributed in the region of space to be studied and observes the local plasma waves. The spatial distribution of the plasma wave is obtained by collecting the observed data. The design of the sensor node is introduced and the evaluation of the electric field sensor is described. The other application is a constellation for plasmapause detection. The position of the plasmapause is considered to move because of magnetic storms and magnetospheric substorms. The measured electron density reduction indicates the position of the plasmapause. The propagation of radio waves in the MF and HF bands is strongly affected by electron density and static magnetic field intensity. It is demonstrated that a multi-point observation of the Faraday rotation of the radio waves reflects the spatial distribution of electron density. The principle and system design of this application are described. The used frequency was 12 MHz. Using a miniaturized receiver, the presented system can be realized with very small satellites, so-called nanosatellites.

In Chapter 6, the WPIA is introduced and developed, including the hardware. Commonly, the telemetry capacity of a spacecraft is severely limited. The instruments on a spacecraft can provide measured physical quantities with poor time resolution or low dimensions because of integration by time and other physical limitations. Hence, the basic physical processes of the wave-particle interaction have not been observed directly. The WPIA calculates the inner products of the instantaneous electric field vector and velocity vectors detected in plasma measurement instruments. The inner product is proportional to the time derivative of the kinetic energies of the plasmas. The total amount of variation of the kinetic energies is obtained by accumulating the inner product. The instrument must work with the plasma wave receiver, plasma detector and magnetometer. Preprocessing for the WPIA is required before calculating the inner product. Since the phase relation between the electric field vector and the velocity vectors are essential in the WPIA, calibration of the waveform of the electric field is indispensable. Frequency domain calibration was implemented using FFT and IFFT. Because of the delay from the calibration, it is necessary to perform a timing correction for the velocity data. A time tag was added to the velocity data for the timing correction. A coordinate transformation from the satellite coordinate system to the ambient magnetic field coordinate system was also implemented. The development of a one-chip WPIA was successful for real-time operation using a FPGA with 4-MHz clock frequency. The WPIA algorithm presented here has been adopted for the ERG (Energization and Radiation in Geospace) mission.

In conclusion, the miniaturization of the waveform receiver was completely successful. A waveform receiver without a spectrum receiver can work as a plasma receiver, though the signal-to-noise ratio is inadequate to measure very weak plasma waves. The spectrum analyzer was partially miniaturized in the ASIC. However, the developed components of the spectrum receiver are critical for the sweep frequency analyzer. The other components can be realized with modifications of already developed circuits. Thus, the present study has contributed significantly to the miniaturization of the spectrum analyzer. Two applications are proposed and the detail of the systems are discussed, with the required specifications of these applications being clarified. The most important finding of this study is that these systems can be realized with miniaturized plasma wave receivers. Finally, a novel instrument for studying space plasma physics is designed and developed. With regard to both hardware and software, the WPIA suffers from a trade-off between processing speed and flexibility. The hardware-type one-chip WPIA was successfully developed. The algorithm of the present work has contributed to development of the software WPIA for the ERG mission, that will become the first demonstration of the WPIA in space.

7.2 Suggestions for Future Work

Several suggestions for further miniaturization and integration efforts can be made. Although the waveform receiver has been successfully miniaturized, the preamps and A/D converters were not included in the ASIC. Ideally, the preamp should have noise at a level less than a hundredth of the presented G_m–C filter. Such low noise performance can be realized inside the ASIC by employing a very large aspect ratio (W/L) MOSFET at the differential input pair. This would increase the size of, the chip however. A BiCMOS process would also allow low noise performance. An A/D converter with similar specifications to those used in Chapter 4 could be implemented with the ASIC. However, the six A/D converters would occupy a large exclusive area inside the ASIC. In other words, implementing a preamp and A/D converters would only be appropriate if the chip size is acceptable. Considering the role of the preamp, i.e., impedance conversion without loss of signal, it is not appropriate for the preamp function to be entirely inside one chip. One preamp is realized in one chip and placed very close to each sensor. Each chip contains a single channel of the waveform receiver with the A/D converter.The detected signals are digitally sent from the electronics adjacent to the sensor to a data handling unit of the spacecraft. Then, the analog electronics of the plasma wave receivers can be removed from the spacecraft body. This suggestion is applicable for the spectrum receiver.

A one-chip WPIA has an advantage in real-time processing over the software-type WPIA to be implemented in the ERG satellite. The WPIA must have several bins in the calculation in order to identify the interacting energy and pitch angle range of the particles, and the frequency and polarization of the plasma waves. This dividing process needs more resources for both hardware and software. Hence, a hybrid-type WPIA might be suitable. The signal processing introduced in the present thesis (e.g., FFT and matrix operation) is more appropriate for hardware implementation. The specific requirements of a study can be set using software. Exploiting the strength of each kind of WPIA leads to the best results. It is hoped that the present study will contribute to further developments of the technology for space instrumentation and the evolution of space plasma physics and related disciplines.

References

[1] NOAA Space Weather Prediction Center. “ACE Real Time Solar Wind Data Page”, May 19, 2012. URL: `http://www.swpc.noaa.gov/ace/ace_rtsw_data.html`.

[2] Van Allen, J. A., C. E. McIlwain, and G. H. Ludwig. “Radiation Observations with Satellite 1958 ε”. *J. Geophys. Res.*, 64(3):271–286, 1959. `doi:10.1029/JZ064i003p00271`.

[3] Miyoshi, Y., A. Morioka, H. Misawa, T. Obara, T. Nagai, and Y. Kasahara. “Rebuilding process of the outer radiation belt during the 3 November 1993 magnetic storm: NOAA and Exos-D observations”. *J. Geophys. Res.*, 108(A1):1004, 2003. `doi:10.1029/2001JA007542`.

[4] Acuna, M. H. and C .J. Pellerin. “A Miniature Two-Axis Fluxgate Magnetometer”. *IEEE Trans. Geosci. Electron.*, 7(4):252–260, 1969. `doi:10.1109/TGE.1969.271360`.

[5] Gloeckler, G., F.M. Ipavich, W. Studemann, B. Wilken, D.C. Hamilton, G. Kremser, D. Hovestadt, F. Gliem, R.A. Lundgren, W. Rieck, E.O. Tums, J.C. Cain, L.S. Masung, W. Weiss, and P. Winterhof. “The Charge-Energy-Mass Spectrometer for 0.3-300 keV/e Ions on the AMPTE CCE”. *IEEE Trans. Geosci. Remote Sens.*, GE-23(3):234–240, 1985. `doi:10.1109/TGRS.1985.289519`.

[6] Young, D. T., S. J. Bame, M. F. Thomsen, R. H. Martin, J. L. Burch, J. A. Marshall, and B. Reinhard. “2π-radian Field-Of-View Toroidal Electrostatic Enalyzer”. *Rev. Sci. Instrum.*, 59(5):743–751, 1988. `doi:10.1063/1.1139821`.

[7] Tsutsui, M., I. Nagano, H. Kojima, K. Hashimoto, H. Matsumoto, S. Yagitani, and T. Okada. “Measurements and Analysis of Antenna Impedance Aboard the Geotail Spacecraft”. *Radio Sci.*, 32(3):1101–1126, 1997. `doi:10.1029/97RS00396`.

[8] Pfaff, R. F., J. E. Borovsky, and D. T. Young. *Measurement Techniques in Space Plasmas: Fields*, chapter Principles of Space Plasma Wave Instrument Design, page 132. Geophysical Monograph. American Geophysical Union, 1998.

[9] Escoubet, C.P., R. Schmidt, and M.L. Goldstein. “CLUSTER - Science and Mission Overview”. *Space Sci. Rev.*, 79:11–32, 1997. 10.1023/A:1004923124586.

[10] Angelopoulos, V. “The THEMIS Mission”. *Space Sci. Rev.*, 141:5–34, 2008. 10.1007/s11214-008-9336-1.

[11] SCOPE Working Group, Japan Aerospace Exploration Agency. “Proposal of the scope mission”, 2008. (in Japanese).

[12] Matsumoto, H., I. Nagano, R. R. Anderson, H. Kojima, K. Hashimoto, M. Tsutsui, T. Okada, I. Kimura, Y. Omura, and M. Okada. “Plasma Wave Observations with GEOTAIL Spacecraft”. *J. Geomag. Geoelectr.*, 46(1):59–95, 1994.

[13] Matsumoto, H., H. Kojima, T. Miyatake, Y. Omura, M. Okada, I. Nagano, and M. Tsutsui. “Electrostatic Solitary Waves (ESW) in the Magnetotail: BEN Wave Forms Observed by GEOTAIL”. *Geophys. Res. Lett.*, 21(25):2915–2918, 1994. `doi:10.1029/94GL01284`.

[14] Bougeret, J. L., M. L. Kaiser, P. J. Kellogg, R. Manning, K. Goetz, S. J. Monson, N. Monge, L. Friel, C. A. Meetre, C. Perche, L. Sitruk, and S. Hoang. “Waves: The Radio and Plasma Wave Investigation on the WIND Spacecraft”. *Space Sci. Rev.*, 71:231–263, 1995. `doi:10.1007/BF00751331`.

[15] Gurnett, D. A., R. L. Huff, and D. L. Kirchner. “The Wide-Band Plasma Wave Investigation”. *Space Sci. Rev.*, 79:195–208, 1997. `doi:10.1023/A:1004966823678`.

[16] Bonnell, J., F. Mozer, G. Delory, A. Hull, R. Ergun, C. Cully, V. Angelopoulos, and P. Harvey. “The Electric Field Instrument (EFI) for THEMIS”. *Space Sci. Rev.*, 141:303–341, 2008. `doi:10.1007/s11214-008-9469-2`.

[17] Kasahara, Y., Y. Goto, K. Hashimoto, T. Imachi, A. Kumamoto, T. Ono, and H. Matsumoto. “Plasma Wave Observation Using Waveform Capture in the Lunar Radar Sounder On Board the SELENE Spacecraft”. *Earth Planets Space*, 60(4):341–351, 2008.

[18] Moore, G. E. “Cramming More Components Onto Integrated Circuits”. *Electronics*, 38(8):114–117, 1965. `doi:10.1109/JPROC.1998.658762`.

[19] Wikipedia.org. “Moore’s law”, May 12, 2012. URL: `http://en.wikipedia.org/wiki/Moore's_law`.

[20] Ono, T., A. Kumamoto, Y. Yamaguchi, A. Yamaji, T. Kobayashi, Y. Kasahara, and H. Oya. “Instrumentation and Observation Target of the Lunar Radar Sounder (LRS) Experiment On-Board the SELENE Spacecraft”. *Earth Planets Space*, 60(4):321–332, 2008.

[21] Ueda, Y., H. Kojima, H. Iwai, R. Fujiwara, K. Hashimoto, H. Matsumoto, I. Nagano, and T. Okada. “Development of Plasma Wave Analyzer with the Digital Control System for the Rocket Experiment in the Polar Region”. *IEICE Trans. Commun. Japenese Edtion*, 84(10):1808–1818, 2001. (in Japanese).

[22] Hashimoto, K., H. Iwai, Y. Ueda, H. Kojima, and H. Matsumoto. “Software Wave Receiver for the SS-520-2 Rocket Experiment”. *IEEE Trans. Geosci. Remote Sensing*, 41(11):2638–2647, Nov. 2003. `doi:10.1109/TGRS.2003.815410`.

[23] Brauninger, H., R. Danner, D. Hauff, P. Lechner, G. Lutz, N. Meidinger, E. Pinotti, C. Reppin, L. Struder, J. Trumper, E. Kendziorra, J. Kramer, M. Mohan, R. Staubert, N. Findeis, P. Holl, J. Kemmer, and C. vonZanthier. "First Results with the PN-CCD Detector System for the XMM Satellite Mission". *Nucl. Instrum. Methods Phys. Res. Sect. A-Accel. Spectrom. Dect. Assoc. Equip.*, 326(1-2):129–135, 1993. `doi:10.1016/0168-9002(93)90342-F`.

[24] Krizmanic, J. F. "GLAST: The Gamma-ray Large Area Space Telescope". *Nucl. Instrum. Methods Phys. Res. Sect. A-Accel. Spectrom. Dect. Assoc. Equip.*, 418(1):161–172, 1998. `doi:10.1016/S0168-9002(98)00730-X`.

[25] Paschalidis, N., N. Chrissostomidis, N. Stamatopoulos, P. Houlis, E. Sarris, S. Jaskulek, M. Mitchell, B. Tossman, and S. Krimigis. "A Commandable Pulse Height Analysis System Based on Custom VLSI ASICs for the Cassini Space Mission". *IEEE Trans. Nucl. Sci.*, 44(3):1023–1027, June 1997. `doi:10.1109/23.603797`.

[26] Paschalidis, N., N. Stamatopoulos, K. Karadamoglou, G. Kottaras, V. Paschalidis, E. Sarris, R. McNutt, D. Mitchell, and R. McEntire. "A CMOS Time-of-flight System-on-a-chip for Spacecraft Instruments". *IEEE Trans. Nucl. Sci.*, 49(3):1156–1163, June 2002. `doi:10.1109/TNS.2002.1039630`.

[27] Paschalidis, N. "A Family of Analog and Mixed Signal VLSI ASICs for NASA Science Missions". *Acta Astronaut.*, 59(8-11):974–980, 2006. `doi:10.1016/j.actaastro.2005.07.044`.

[28] Ezawa, H., M. Hirayama, T. Kamae, H. Kubo, K. Matsuzaki, K. Nagata, Y. Saito, H. Ikeda, K. Tsukada, H. Ozawa, T. Takahashi, H. Murakami, Y. Sano, and K. Shimizu. "Development of the Pulse-shape Discrimination LSI for Astro-E Hard X-ray Detector". *IEEE Trans. Nucl. Sci.*, 43(3):1521–1526, June 1996. `doi:10.1109/23.507096`.

[29] Takahashi, T., K. Abe, M. Endo, Y. Endo, Y. Ezoe, Y. Fukazawa, M. Hamaya, S. Hirakuri, S. Hong, M. Horii, H. Inoue, N. Isobe, T. Itoh, N. Iyomoto, T. Kanae, D. Kasama, J. Kataoka, H. Kato, M. Kawaharada, N. Kawano, K. Kawashima, S. Kawasoe, T. Kishishita, T. Kitaguchi, Y. Kobayashi, M. Kokubun, J. Kotoku, M. Kouda, A. Kubota, Y. Kuroda, G. Madejski, K. Makishima, K. Masukawa, Y. Matsumoto, T. Mitani, R. Miyawaki, T. Mizuno, K. Mori, M. Mori, M. Murashima, T. Murakami, K. Nakazawa, H. Niko, M. Nomachi, Y. Okada, M. Ohno, K. Oonuki, N. Ota, H. Ozawa, G. Sato, S. Shinoda, M. Sugiho, M. Suzuki, K. Taguchi, H. Takahashi, I. Takahashi, S. Takeda, K. Tamura, T. Tamura, T. Tanaka, C. Tanihata, M. Tashiro, Y. Terada, S. Tominaga, Y. Uchiyama, S. Watanabe, K. Yamaoka, T. Yanagida, and D. Yonetoku. "Hard X-ray Detector (HXD) on board Suzaku". *Publ. Astron. Soc. Jpn.*, 59(1):35, 2007.

[30] Matsuura, D., H. Nakajima, E. Miyata, H. Tsunemi, J.P. Doty, and H. Ikeda. "Development of an ASIC for Multi-readout X-ray CCDs". In *2007 IEEE Nucl. Sci.*

Symposium Conf. Record, volume 2, pages 1073–1077, 2007. `doi:10.1109/NSSMIC.2007.4437195`.

[31] Nakajima, H., D. Matsuura, N. Anabuki, E. Miyata, H. Tsunemi, J. P. Doty, H. Ikeda, and H.Katayama. “Development of X-ray CCD Camera System with High Readout Rate Using ASIC”. *Nucl. Instrum. Methods Phys. Res. Sect. A-Accel. Spectrom. Dect. Assoc. Equip.*, 610(1):78–82, 2009. `doi:10.1016/j.nima.2009.05.049`.

[32] Kokubun, M., S. Watanabe, K. Nakazawa, H. Tajima, Y. Fukazawa, T. Takahashi, J. Kataoka, T. Kamae, H. Katagiri, G.M. Madejski, K. Makishima, T. Mizuno, M. Ohno, R. Sato, H. Takahashi, T. Tanaka, M. Tashiro, Y. Terada, and K. Yamaoka. “Hard X-ray and Gamma-ray Detector for ASTRO-H Based on Si and CdTe Imaging Sensors”. *Nucl. Instrum. Methods Phys. Res. Sect. A-Accel. Spectrom. Dect. Assoc. Equip.*, 623(1):425–427, 2010. `doi:10.1016/j.nima.2010.03.024`.

[33] Kishishita, T., G. Sato, H. Ikeda, M. Kokubun, T. Takahashi, T. Idehara, H. Tsunemi, and Y. Arai. “Development of an SOI Analog Front-end ASIC for X-ray Charge Coupled Devices”. *Nucl. Instrum. Methods Phys. Res. Sect. A-Accel. Spectrom. Dect. Assoc. Equip.*, 636(1, Supplement):S143–S148, 2011. `doi:10.1016/j.nima.2010.04.099`.

[34] Magnes, W., M. Oberst, A. Valavanoglou, H. Hauer, C. Hagen, I. Jernej, H. Neubauer, W. Baumjohann, D. Pierce, J. Means, and P. Falkner. “Highly Integrated Front-end Electronics for Spaceborne Fluxgate Sensors”. *Measurement Science and Technology*, 19(11):115801, 2008. `doi:10.1088/0957-0233/19/11/115801`.

[35] Mossawir, B., I. R. Linscott, U. S. Inan, J. L. Roeder, J. V. Osborn, S. C. Witczak, E. E. King, and S. D.— LaLumondiere. “A TID and SEE Radiation-Hardened, Wideband, Low-Noise Amplifier”. *IEEE Trans. Nucl. Sci.*, 53(6):3439–3448, 2006. `doi:10.1109/TNS.2006.886219`.

[36] Li, W., F. Li, D. Guo, C. Zhang, and Z. Wang. “An Undersampling 14-bit cyclic ADC with Over 100-dB SFDR”. *J. Semicond.*, 31(2):025008, 2010. `doi:doi:10.1088/1674-4926/31/2/025008`.

[37] Matsumoto, H., T. Okada, K. Hashimoto, I. Nagano, S. Yagitani, . Tsutsui, Y. Kasaba, K. Tsuruda, H. Hayakawa, A. Matsuoka, S. Watanabe, H. Ueda, I. Kimura, Y. Kasahara, Y. Omura, T. Matsumura, T. Imachi, K. Ishisaka, and Y. Tateno. “Low Frequency Plasma Wave Analyzer (LFA) Onboard the PLANET-B Spacecraft”. *Earth Planets Space*, 50(3):223–228, 1998.

[38] Krummenacher, F. and N. Joehl. “A 4-MHz CMOS Continuous-Time filter with On-Chip Automatic Tuning”. *IEEE J. Solid-State Circ.*, 23(3):750–758, 1988. `doi:10.1109/4.315`.

[39] Taniguchi, K. *Introduction to CMOS Analog Integrated Circuit.* CQ Publishing Co.,Ltd., 2004. (in Japanese).

[40] Johns, D. and K. W. Martin. *Analog Integrated Circuit Design.* John Wiley & Sons, Inc., 1996.

[41] Banu, M. and Y. Tsividis. "An Elliptic Continuous-Time CMOS Filter with On-Chip Automatic Tuning". *IEEE J. Solid-State Circ.*, 20(6):1114–1121, 1985. `doi:10.1109/JSSC.1985.1052448`.

[42] Razavi, B. and T. Kuroda (Translation Supervisor). *Design of Analog CMOS Integrated Circuit.* Maruzen Publishing Co.,Ltd., 2003. (in Japanese).

[43] Agawa, K., H. Majima, H. Kobayashi, M. Koizumi, S. Ishizuka, T. Nagano, M. Arai, Y. Shimizu, G. Urakawa, N. Itoh, M. Hamada, and N. Otsuka. "A −90 dBm sensitivity 0.13 μm CMOS Bluetooth Transceiver Operating in Wide Temperature Range". In *2007 IEEE Proc. CICC*, pages 655–658, Sept. 2007. `doi:10.1109/CICC.2007.4405817`.

[44] Okada, S. "Study on Integration of Analog Downconversion Circuits toward Small Plasma Wave Spectrum Receivers". Master's thesis, Kyoto University, 2012.

[45] Fried, D. L. "Analog Sample-Data Filters". *IEEE J. Solid-State Circ.*, 7(4):302–304, 1972. `doi:10.1109/JSSC.1972.1050305`.

[46] Hosticka, B. J., R. W. Brodersen, and P. R. Gray. "MOS Sampled Data Recursive Filters Using Switched Capacitor Integrators". *IEEE J. Solid-State Circ.*, 12(6):600–608, 1977. `doi:10.1109/JSSC.1977.1050967`.

[47] Caves, J. T., S. D. Rosenbaum, M. A. Copeland, and C. F. Rahim. "Sampled Analog Filtering Using Switched Capacitors as Resistor Equivalents". *IEEE J. Solid-State Circ.*, 12(6):592–599, 1977. `doi:10.1109/JSSC.1977.1050966`.

[48] Young, I. A. and D. A. Hodges. "MOS Switched-Capacitor Analog Sampled-Data Direct-Form Recursive Filters". *IEEE J. Solid-State Circ.*, 14(6):1020–1033, 1979. `doi:10.1109/JSSC.1979.1051311`.

[49] Arreola, J. I., E. SÃ nchezSinencio, Y. P. Tsividis, and P. E. Allen. "Simple Implementation of Sampled-Data Filters Using Current Multipliers, Switches and Capacitors". *Electron. Lett.*, 15(24):780–782, 22 1979. `doi:10.1049/el:19790555`.

[50] Allen, P. E. and D. R. Holberg. *CMOS Analog Circuit Design*, page 644. The Oxford Series in Electrical and Computer Engineering. Oxford University Press, 2011.

[51] Gilbert, B. "A Precise Four-Quadrant Multiplier with Subnanosecond Response". *IEEE J. Solid-State Circ.*, 3(4):365–373, 1968. `doi:10.1109/JSSC.1968.1049925`.

[52] Sato, H., A. Hyogo, and K. Sekine. "A Low Voltage OTA Using MOSFET in the Triode Region and Cascode Current Mirror". In *IEEE Proc. ECCTD 2005*, volume 3, pages III/453–III/456, 2005. `doi:10.1109/ECCTD.2005.1523158`.

[53] Kasaba, Y., J.-L. Bougeret, L.G. Blomberg, H. Kojima, S. Yagitani, M. Moncuquet, J.-G. Trotignon, G. Chanteur, A. Kumamoto, Y. Kasahara, J. Lichtenberger, Y. Omura, K. Ishisaka, and H. Matsumoto. "The Plasma Wave Investigation (PWI) onboard the BepiColombo/MMO: First Measurement of Electric Fields, Electromagnetic Waves, and Radio Waves around Mercury". *Planetary and Space Science*, 58:238–278, 2010. `doi:10.1016/j.pss.2008.07.017`.

[54] Gurnett, D. A., W. S. Kurth, J. T. Steinberg, and S. D. Shawhan. "Plasma Wave Turbulence around the Shuttle: Results from the Spacelab–2 Flight". *Geophys. Res. Lett.*, 15(8):760–763, 1988. `doi:10.1029/GL015i008p00760`.

[55] Elliott, R. S. *Antenna Theory and Design*, pages 301–302. Prentice Hall, Englewood Cliffs, 1981.

[56] Okada, S. "Study on the Small Sensor Node System for Measuring Space Electromagnetic Environment". Bachelor's Thesis, Kyoto University, 2010.

[57] Yagitani, S., M. Ozaki, and H. Kojima. "A Compact Loop Antenna System for Monitoring Local Electromagnetic Environments in Geospace". *IEICE Trans. Commun.*, 94(6):1744–1747, 2011. `doi:10.1587/transcom.E94.B.1744`.

[58] Takizawa, Y., P. Davis, M. Kawai, H. Iwai, A. Yamaguchi, and S. Obana. "Self-Organizing Location Estimation Method Using Received Signal Strength". *IEICE Trans. Commun.*, 89(10):2687–2685, 2006.

[59] Sandel, B. R., A. L. Broadfoot, C. C. Curtis, R. A. King, T.C. Stone, R. H. Hill, J. Chen, O. H. W. Siegmund, R. Raffanti, DAVID D. Allred, R. STEVEN Turley, and D. L. Gallagher. "The Extreme Ultraviolet Imager Investigation for the IMAGE Mission". *Space Sci. Rev.*, 91:197–242, 2000. `doi:10.1023/A:1005263510820`.

[60] Reinisch, B. W., D. M. Haines, K. Bibl, G. Cheney, I. A. Galkin, X. Huang, S. H. Myers, G. S. Sales, R. F. Benson, S. F. Fung, J. L. Green, S. Boardsen, W. W. L. Taylor, J. L. Bougeret, R. Manning, N. Meyer-Vernet, M. Moncuquet, D. L. Carpenter, D. L. Gallagher, and P. Reiff. "The Radio Plasma Imager Investigation on the IMAGE Spacecraft". *Space Sci. Rev.*, 91:319–359, 2000. `doi:10.1023/A:1005252602159`.

[61] Goldstein, J., M. Spasojevic, P. H. Reiff, B. R. Sandel, W. T. Forrester, D. L. Gallagher, and B. W. Reinisch. "Identifying the Plasmapause in IMAGE EUV Data Using IMAGE RPI in situ Steep Density Gradients". *J. Geophys. Res.*, 108(1147):1–13, 2003. `doi:10.1029/2002JA009475`.

[62] X., B. W. Reinisch, P. Song, J. L. Green, and D. L. Gallagher. "Developing an empirical density model of the plasmasphere using IMAGE/RPI observations". *Adv. Space Res.*, 33(6):829–832, 2004. `doi:10.1016/j.asr.2003.07.007`.

[63] Pierrard, V. and K. Stegen. "A three-dimensional dynamic kinetic model of the plasmasphere". *J. Geophys. Res.*, 113(A10209):1–15, 2008. `doi:10.1029/2008JA013060`.

[64] Kimura, I. and Y. Goto. "Ray tracing", May 12, 2012. URL: `http://waves.is.t.kanazawa-u.ac.jp/index.php`.

[65] Gough, M. P., D. A. Hardy, M. R. Oberhardt, W. J. Burke, L. C. Gentile, B. McNeil, K. Bounar, D. C. Thompson, and W. J. Raitt. "Correlator Measurements of Megahertz Wave-Particle Interactions During Electron Beam Operations on STS". *J. Geophys. Res.*, 100(A11):21,561–21,575, 1995. `doi:10.1029/95JA00679`.

[66] Gough, M. P. "Particle Correlator Instruments in Space: Performance; Limitation, Successes, and the Future". In *Measurement Techniques in Space Plasmas: Particles (Geophysical Monograph)*, pages 333–338. American Geophysical Union, 1998.

[67] Buckley, A. M., M. P. Gough, H. Alleyne, K. Yearby, and I. Willis. "Measurement of Wave-Particle Interactions in the Magnetosphere using the DWP Particle Correlator". In *Proc. Cluster-II Workshop: Multiscale/Multipoint Plasma Measurements*, pages 303–306. European Space Agency, Sept. 2000.

[68] Buckley, A. M., M. P. Gough, H. Alleyne, K. Yearby, and S. N. Walker. "First Measurements of Electron Modulations by the Particle Correlator Expeiments on Cluster". In *Proc. Les Woolliscroft Memorial Conf. / Sheffield Space Plasma Meeting: Multipoint Measurements versus Theory*, pages 19–26. European Space Agency, April 2001.

[69] Ergun, R. E., C. W. Carlson, J. P. McFadden, J. H. Clemmons, and M. H. Boehm. "Langmuir Wave Growth and Electron Bunching: Results From a Wave-Particle Correlator". *J. Geophys. Res.*, 96(A1):225–238, 1991. `doi:doi:10.1029/90JA01596`.

[70] Ergun, R. E., J. P. McFadden, and C. W. Carlson. "Wave-particle Correlator Instrument Design". In *Measurement Techniques in Space Plasmas: Particles (Geophysical Monograph)*, pages 325–331. American Geophysical Union, 1998.

[71] Kletzing, C. A., S. R. Bounds, J. Labelle, and M. Samara. "Observation of the Reactive Component of Langmuir Wave Phase Bunched Electrons". *Geophys. Res. Lett.*, 32(L05106), 2005. `doi:10.1029/2004GL021175`.

[72] SCOPE Working Group. "One-chip Wave-particle Interaction Analyzer". In *Proposal of the SCOPE mission*, pages 449–458. Japan Aerospace Exploration Agency, 2008. (in Japanese).

[73] ERG Working Group. "Software-type Wave-particle Interaction Analyzer". In *Proposal of the ERG mission*, pages 62–65. Japan Aerospace Exploration Agency, 2008. (in Japanese).

Publication List

Major Publications

1. Fukuhara, H., H. Kojima, Y. Ueda, Y. Omura, Y. Katoh, and H. Yamakawa, “A New Instrument for the Study of Wave-Particle Interactions in Space: One-Chip Wave-Particle Interaction Analyzer”, *Earth, Planets and Space*, 61, 756–778, 2009.

2. Kojima, H., H. Fukuhara, Y. Mizuochi, S. Yagitani, H. Ikeda, Y. Miyake, H. Usui, H. Iwai, Y. Takizawa, Y. Ueda and H. Yamakawa, “Miniaturization of Plasma Wave Receivers Onboard Scientific Satellites and its Application to the Sensor Network System for Monitoring the Electromagnetic Environments in Space”, *Advances in Geosciences*, 34(5), 2094–2102, doi:10.1109/TPS.2006.883290, 2010.

3. Fukuhara, H., H. Kojima, S. Okada, H. Ikeda, and H. Yamakawa, “Toward a Waveform Receiver on-a Chip Dedicated to Plasma Wave Instrument Onboard Scientific Spacecraft”, *Aerospace Conference, 2011 IEEE*, 1–9, doi:10.1109/AERO.2011.5747462, 2011.

4. Fukuhara, H., H. Kojima, H. Ikeda, and H. Yamakawa, “Temperature Compensated $\mathrm{G_m}$–C Filter for Plasma Wave Receivers Onboard Scientific Spacecraft (in Japanese)”, *IEICE Transaction on Electronics Japanese Edition*, J94–C(6), 155–162, 2011.

5. Fukuhara, H., H. Kojima, H. Ishii, S. Okada, and H. Yamakawa, “Tiny Waveform Receiver with a Dedicated System Chip for Observing Plasma Waves in Space”, *Measurement Science and Technology*, accepted for publication in August, 2012.

Presentations in International Meetings

1. Fukuhara, H., Y. Ueda, H. Kojima, and H Yamakawa, “System Design of One-chip Wave Particle Interaction Analyzer for SCOPE mission”, *The 37th COSPAR Scientific Assembly*, Montreal, Canada, 2008.

2. Fukuhara, H, “System Design of One-Chip Wave Particle Interaction Analyzer for Future Space Plasma Observations”, *The 59th International Astronautical Congress*, Glasgow, U.K., 2008.

3. Fukuhara, H., H. Kojima, S. Okada, H. Ikeda and H. Yamakawa, "Development of Analog Circuits for Miniaturized Plasma Wave Receiver Using Analogue ASIC Devices", *2010 Taiwan-Japan Space Instrument Workshop*, Tainan, Taiwan, 2010.
4. Fukuhara, H., S. Okada, H. Kojima, H. Ikeda, and H. Yamakawa, "Development of Miniaturized Observation System for PlasmaWave Using Analog ASIC for Small Scientific Satellite Missions", *2010 Asia-Pacific Radio Science Conference*, Toyama, Japan, 2010.
5. Fukuhara, H., H. Kojima, H. Ikeda, and H. Yamakawa, "Toward a Waveform Receiver on-a Chip Dedicated to Plasma Wave Instrument Onboard Scientific Spacecraft", *2011 IEEE Aerospace Conference*, Montana, U.S.A., 2011.
6. Fukuhara, H., H. Kojima, S. Okada, H. Ikeda, H. Yamakawa, "Development of the Analog ASIC for Miniaturized Waveform Receiver", *2011 Japan Geoscience Union Meeting*, Chiba, Japan, 2011.
7. Fukuhara, H., H. Kojima, Y. Kasahara, Y. Goto, and H. Yamakawa, "Nanosatellite Constellation for Measuring the Terrestrial Plasmasphere Structure", *The 62nd International Astronautical Congress*, Cape Town, South Africa, 2011.
8. Fukuhara, H., H. Kojima, H. Ishii, S. Okada, and Yamakawa, "Development of Small Plasma Wave Receiver with a Dedicated Chip for Scientific Spacecraft", *European Geophysical Union*, Wien, Austria, 2012.
9. Fukuhara, H., S. Okada, H. Ishii, H. Kojima, and H. Yamakawa, "Development of Miniaturized Plasma Wave Receiver using analog ASIC", *2012 Japan Geoscience Union Meeting*, Chiba, Japan, 2012.

Awards

1. "British Interplanetary Society Prize for Best Technical Paper", System Design of One-Chip Wave Particle Interaction Analyzer for Future Space Plasma Observation, *The 59th International Astronautical Congress*, 2008.
2. "Inose Academic Encouraging Prize", Development, Miniaturization and Integration of Measurement System of Space Electromagnetic Environemts, *Foundation for Promotion of Electrical and Electronic Engineering and Information Science*, 2009.
3. "IEEE Kansai Section Student Paper Award", Toward a Waveform Receiver on-a Chip Dedicated to Plasma Wave Instrument Onboard Scientific Spacecraft, *IEEE Kansai Section*, 2012.